Linear and nonlinear characterization of monolithically integrated GaP microdisks on Si and GaP substrates

Rasool Saleem Urothodi

UNIVERSITÉ DE RENNES 1

THESE DE DOCTORAT DE

L'UNIVERSITE DE RENNES 1

ECOLE DOCTORALE N° 596
Matière, Molécules, Matériaux
Spécialité : *Photonique*

Par

Rasool Saleem UROTHODI

Linear and nonlinear characterization of monolithically integrated GaP microdisks on Si and GaP substrates

Thèse présentée et soutenue à ENSSAT-Lannion, le 09/12/2022
Unité de recherche : Fonctions Optiques pour les Technologies de l'informatiON-CNRS UMR 6082

Rapporteurs avant soutenance :

Isabelle SAGNES Directrice de Recherche CNRS, C2N, Université Paris Saclay, France
Stéphane CALVEZ Chargé de Recherche CNRS HDR, LAAS-CNRS, Université de Toulouse, France

Composition du Jury :

Président :	Charles CORNET	Professeur, Institut FOTON, INSA de Rennes, France
Examinateurs :	Emmanuel CENTENO	Professeur, Université Clermont Auvergne, France
	Christian GRILLET	Chargé de Recherche CNRS HDR, INL-CNRS, France
Dir. de thèse :	Yannick DUMEIGE	Professeur, Institut FOTON, Université de Rennes 1, France
Co-dir. de thèse :	Yoan LÉGER	Chargé de Recherche CNRS HDR, Institut FOTON, INSA de Rennes, France

This thesis work is dedicated to my wife,

Dr.Riya Thanzeela KORAKKOTTIL SHAREEF

Acknowledgments

First of all, I would like to express my sincere thanks to my supervisors Yoan LÉGER (Chargé de Recherche-CNRS, HDR, UMR 6082-Institut FOTON, Université de Rennes 1, France) and Yannick DUMEIGE (Professeur des Universités, UMR 6082-Institut FOTON, Université de Rennes 1, France) for offering me an opportunity to pursue my Ph.D. under their guidance as part of the ORPHEUS-ANR project. The encouragement and support they offered throughout the period were immense and memorable. Thanks a ton for their valuable advice in many difficult situations and for making themselves available whenever I needed to discuss physics. They are excellent researchers and teachers who share their knowledge with patients. They taught me how good a supervisor can become in every aspect. Thank you so much from the bottom of my heart.

I would like to extend my thanks to the CSI committee members Olivier DURAND (Professor-INSA, Head of the OHM team) and Daniel CHILLET (Enseignant/Chercheur, Enssat-Université de Rennes 1) for monitoring my thesis progress and timely responses. I appreciate the members of the OHM team and the NanoRennes platform who have worked on the fabrication of samples utilized for this thesis, a special thanks to Tony ROHEL, Julie LE POULIQUEN and Rozenn BERNARD for your efforts. Thank you very much to the collaborators Isabelle SAGNES (C2N laboratory, Head of the MOVPE team) and Bart Kuyken (Ghent university, Photonics research group) for the fabrication of advanced samples. I would also like to thank several persons in the Institut Foton for offering support on various occasions. A big thanks to the directors of the Institut Foton, Pascal BESNARD and Mehdi ALOUINI for the extensive support. Thank you Christelle VELLY and Laurent BRAMERIE for the technical assistance, Patrice FÉRON for the deep discussions in photonics, Stéphane TREBAOL for the kindness to share the beautiful French culture, Monique THUAL and Mohammed GUENDOUZ for the team management and meetings. I would like to remember and thank my colleagues Louis RUEL, Pierre Guillemé, Alejandro Lorenzo-Ruiz, and Nessim JEBALI for their friendly talks and discussions on experiments. Not to forget, Chloé DESCHAMPS and Isabelle POULARD for their tremendous administrative assistance. I must thank Charles CORNET, Cyril PARANTHOËN, Ronan LE PAGE, Sébastien LOBO and Luiz POFFO for their help.

Finally, I would like to thank my wife for her kind understanding and support. This thesis would not have been possible without her patience and perseverance. I can't thank you enough and I owe you everything in my life. My mom and dad, I will never forget their sacrifice and thanks to my brother for his tremendous support. Thank you very much, everyone.

Contents

List of Tables

List of Figures

General introduction

The research and developments are directed toward meeting the high demands of the modern world through photonic integrated circuits (PICs) by keeping Moore's law active [1]. The PIC is an optical chip that integrates a large number of optical components performing various optical functions. A major difference between a PIC and an electronic integrated circuit is that it performs functions for information signals carried on optical wavelengths. Innovations for micro/nanoelectronic components from the 1960s matured the silicon (Si) based complementary metal-oxide-semiconductor (CMOS) fabrication technology by exploiting the merits of silicon such as large wafer size, natural abundance and low cost [2]. Most electronic integrated circuits are thus based on the silicon substrate. Leveraging this well-known Si-CMOS infrastructure, silicon photonics became the leading PIC technology in the 20th century enabling the fabrication of ultra-fast, low cost and large-scale integrated photonic devices [3][4]. Hybrid devices containing monolithically integrated electronic and optical components are then fabricated [5][6]. In addition, all optical PICs are currently an active research topic [7]. The PICs have advancements in optical communication links [8], data center networks [9], single-chip microprocessors [10], memory chips [11], computing [12], lab-on-a-chip [13], nonlinear photonics [14][15], etc. Silicon photonics is predominantly based on a silicon-on-insulator (SOI) platform where patterning of the Si layer on top of a buried SiO_2 layer fabricated on a Si substrate forms the core of silicon photonic devices with high refractive index contrast for optical confinement [16]. Optical whispering gallery mode resonators are micro-nano scale sized cylindrical symmetric structures with a high refractive index compared to their surroundings that can confine light by total internal reflections [17]–[21]. They are one of the primary components in PICs [14], [22]–[25] capable of demonstrating various optical functions and have different geometries like disks, spheres, rings, etc [24], [26]–[32]. They are an ideal candidate for nonlinear photonics enhancing light-

matter interaction due to the confinement of light to a small volume for a long duration [14][33][34].

One of the main challenges in realizing PICs is the lack of semiconductor materials with suitable properties for demonstrating a variety of optical functions. Silicon is a centrosymmetric material with 3rd order nonlinear susceptibility and indirect bandgap. This makes silicon an inefficient candidate for light emission and nonlinear optical functions requiring high power operation. Most III-V semiconductors show excellent optoelectronic performances due to their direct bandgap and high electron mobility properties [35][36]. The binary III-V compound semiconductor gallium phosphide (GaP) entered the photonics industry in the 1960s in the form of green light emitting diodes and lagged behind due to its indirect bandgap [37]. Recently, GaP found back its track as a potential material for nanophotonic devices [14][23][38]. It has numerous merits for competing with its commercial counterparts (GaAs, $LiNbO_3$, InP, etc.) such as a wide-indirect bandgap for high power nonlinear process, non-centrosymmetric with competitive second order nonlinear susceptibility, a cubic crystal of zinc-blende type offering $\bar{4}$-QPM [39][40], largest linear refractive index among visibly transparent III-V materials for high optical confinement and possesses a higher nonlinear refractive index for realizing third order nonlinearity [14]. In addition, the least lattice parameter mismatch with Si among all binary III-V semiconductors [41] allows the monolithic integration of GaP on Si substrates [42]. However, polar-on-nonpolar heteroepitaxy results in growth defects [43]–[47] such as antiphase domains (APDs)/antiphase boundaries (APBs) propagating in the GaP layer unless otherwise annihilated or controlled [43], [48]–[50]. The APDs were reported to act as deep centers, resulting in light absorption within the semiconductor band gap [51]. In the epitaxy community, efforts thus first concentrated on their annihilation in the quest to realize lasers on silicon [52][53]. However, if APDs are tailored, these defects could become an advantage for the GaP/Si platform in the field of nonlinear silicon photonics with the concept of random quasi phase matching [34][54][48]. The main goal of this thesis is thus to explore the optical properties of GaP/Si microdisks and compare their suitability for random quasi phase matching assisted nonlinear frequency conversion with the most efficient $\bar{4}$-QPM schemes.

In this thesis, we have characterized monolithically integrated suspended GaP based microdisks on Si and GaP substrates linearly and nonlinearly. This investigation reports on the various loss mechanisms in the fabricated GaP/Si microdisks focussed on estimating APDs induced losses. It gives critical feedback for quality control of the fabrication process and development of future defect tailored PICs based on such materials. The nonlinear characterization of GaP/Si and GaP/$Al_{0.7}$GaP/GaP microdisks is then presented. For the first time, second harmonic generation with strict $\bar{4}$-QPM is demonstrated in a III-V zinc-blende microdisk resonator, on the GaP/$Al_{0.7}$GaP/GaP platform. Upconversion processes

are also observed on the GaP/Si platform, as a first step towards the realization of GaP/Si nonlinear PICs.

This thesis is organized into four chapters,

Chapter 1: Theoretical frameworks for explaining optical loss mechanisms and nonlinear processes in GaP based microdisks.

Chapter 2: Describing optical instruments and experimental configurations for characterizing microdisks.

Chapter 3: Experimental analysis of different optical loss contributions in the GaP/Si microdisks with tailored APDs.

Chapter 4: Nonlinear characterization demonstrating strict $\bar{4}$-QPM assisted second harmonic generation in GaP/$Al_{0.7}$GaP/GaP microdisks and frequency upconversion process in GaP/Si microdisks.

1 Theory of linear and nonlinear characterization of microdisks

Introduction

This chapter is dedicated to presenting the necessary theoretical formulation for understanding the linear and nonlinear characterization of our GaP microdisks grown on native substrates and Si substrates. We will begin with the basics of nonlinear optics focusing on the second harmonic generation and establishing the requirements for frequency mixing. Different phase matching schemes are also described for efficient frequency conversion. Then, the theory of a microdisk coupled with an access waveguide such as a fiber taper is discussed along with the WGM properties facilitating nonlinear interactions. Later, the material properties of GaP are analyzed as a potential competitor for nonlinear integrated photonics. The formation of growth defects during monolithic integration on Si and its tailoring for relaxed phase matching is explained. Finally, different loss contributions in the microdisks such as fabrication induced roughness and volume defects are theoretically covered.

1.1 Microresonator: optical confinement

The introduction to whispering gallery modes (WGM) occurred in 1877 when scientist Lord Rayleigh explained the mysterious phenomenon of whispering happening under the dome of St. Paul's cathedral in London as the refocusing effect of acoustic waves by curved symmetric structures [17][18][19]. Considering their optical counterpart [20][21], an optical WGM resonator is a tiny cylindrical symmetric structure with a high refractive index compared to its surrounding that can confine light by successive total internal reflections (TIR) near its periphery when properly excited. It can enhance the light intensity due to the constructive interferences after each in phase round trip. However, the number of round trips of

the photons can be limited due to the losses in the cavity. The optical WGM cavities can have different geometries like disks, rings, spheres, toroids, etc. and found many applications due to the confinement of light in a very small volume for a long duration, such as in optical sensing [26], optomechanics [27], lasing [28], nonlinear optics [14][33][34], filtering [29], quantum optics and quantum electrodynamics [30][31], optical signal processing [32], photonic integrated circuits [22][23][24], etc.

Let's consider a micrometer-sized disk WGM resonator of radius R, thickness h and made with a material of refractive index n_{disk} surrounded by a refractive index n_{clad} ($< n_{disk}$) as shown in Figure 1.1. For the parameters $R \gg \lambda$ and $h \ll R$, the light propagating very close to the inner wall of the microdisk by TIR returns to its initial point. If the initial phase is restored during a complete round trip, constructive interferences occur forming WGMs as given by the resonance condition:

$$2\pi n_{\text{eff}} R = m\lambda \qquad \text{Eq. 1.1}$$

where λ is the resonance wavelength of light, m is an integer (also known as the azimuthal quantum number of a WGM) and $n_{\text{eff}} = \beta\lambda/2\pi$ is the effective refractive index of the optical mode ($n_{\text{clad}} < n_{\text{eff}} < n_{disk}$) with the mode propagation constant β.

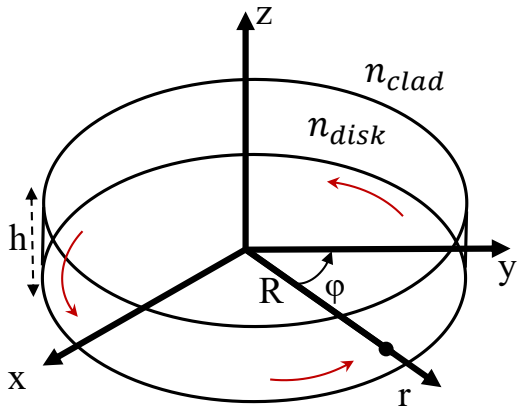

Figure 1.1: The 3D representation of microdisk in cylindrical coordinates (r, φ, z). The origin of coordinates is at the center of the microdisk where r is the radial distance, φ is the azimuthal angle and z is the axial distance.

1.2 Nonlinear optical process

The optical properties of a material system can be modified by the presence of intense light such as laser light [55][56]. In such cases, the response of the material will be nonlinear to the strength of the applied optical field. There are a lot of nonlinear optics effects and phenomena such as wavelength conversions which are further exploited by utilizing micron-scale optical structures like disk shaped cavities for developing photonic integrated devices [33], [57]–[59]. A detailed description of the microdisk resonator is given in section 1.3. The theoretical aspects of nonlinear optics explained in this section 1.2 are based on Ref.[60][61].

To describe the optical nonlinearities, let's consider the dipole moment per unit volume or macroscopic polarization $\vec{P}(t)$ of a lossless and dispersionless dielectric material which depends on the instantaneous strength of the applied optical field $\vec{E}(t)$. A weak applied optical field will lead to a linear variation of the induced polarization given by:

$$\vec{P}(t) = \varepsilon_0 \chi^{(1)} \vec{E}(t) \qquad \text{Eq. 1.2}$$

where ε_0 is the vacuum permittivity and $\chi^{(1)}$ is known as the linear optical susceptibility. If the applied field is intense, then the polarization is a complicated function of the applied electric field and can be expressed by generalizing Eq. 1.2:

$$\begin{aligned} \vec{P}(t) &= \varepsilon_0 \left[\chi^{(1)} \vec{E}(t) + \chi^{(2)} \vec{E}^2(t) + \chi^{(3)} \vec{E}^3(t) + \cdots \right] \\ &\equiv \vec{P}^{(1)}(t) + \vec{P}^{(2)}(t) + \vec{P}^{(3)}(t) + \cdots \end{aligned} \qquad \text{Eq. 1.3}$$

where $\chi^{(2)}$ and $\chi^{(3)}$ are known as the second order and third order nonlinear optical susceptibilities, respectively. In Eq. 1.3, the first term corresponds to the linear polarization $\vec{P}_L$ and the rest of them describe the nonlinear polarization $\vec{P}_{NL}$. The second order polarization $\vec{P}^{(2)}(t)$ occurs only in non-centrosymmetric crystals which do not show an inversion symmetry. In contrast, third order polarization $\vec{P}^{(3)}(t)$ occurs in both centrosymmetric and non-centrosymmetric crystals.

1.2.1 Introduction to 2nd order nonlinearity

Maxwell's equations can be solved to obtain the wave equation in a nonlinear optical medium. Considering a non-magnetic, isotropic and dielectric nonlinear optical medium with no free charges or currents modifies these relations as:

$$\vec{\nabla} \times \vec{E} = -\frac{\partial \vec{B}}{\partial t} \qquad \text{Eq. 1.4}$$

$$\vec{\nabla} \times \vec{H} = \frac{\partial \vec{D}}{\partial t} \qquad \text{Eq. 1.5}$$

where the magnetic flux density $\vec{B} = \mu_0 \vec{H}$ and the electric flux density $\vec{D} = \varepsilon_0 \vec{E} + \vec{P}$. The quantities $\vec{H}$ is the magnetic field intensity and μ_0 is the permeability of free space. Taking the curl of $\nabla \times \vec{E}$ results in an expression:

$$\begin{aligned}\nabla \times \nabla \times \vec{E} &= -\frac{\partial}{\partial t}\nabla \times \vec{B} \\ &= -\mu_0 \frac{\partial}{\partial t}\nabla \times \vec{H} \\ &= -\mu_0 \frac{\partial}{\partial t}\frac{\partial \vec{D}}{\partial t} \\ &= -\mu_0 \left(\varepsilon_0 \frac{\partial^2 \vec{E}}{\partial t^2} + \frac{\partial^2 \vec{P}}{\partial t^2}\right)\end{aligned} \qquad \text{Eq. 1.6}$$

Now, Eq. 1.6 can be rewritten using $\mu_0\varepsilon_0 = 1/c^2$ where c is the speed of light in vacuum:

$$\nabla \times \nabla \times \vec{E} + \frac{1}{c^2}\frac{\partial^2}{\partial t^2}\vec{E} = \mu_0 \frac{\partial^2 \vec{P}}{\partial t^2} \qquad \text{Eq. 1.7}$$

Utilizing the identity $\nabla \times \nabla \times \vec{E} = \nabla(\nabla \cdot \vec{E}) - \nabla^2\vec{E}$ from the vector calculus, we can write $\nabla \times \nabla \times \vec{E} = -\nabla^2\vec{E}$ for an isotropic medium under slowly varying amplitude approximation. The wave equation is finally obtained as:

$$\nabla^2\vec{E} - \frac{n^2}{c^2}\frac{\partial^2}{\partial t^2}\vec{E} = \frac{1}{\varepsilon_0 c^2}\frac{\partial^2 \vec{P}_{NL}}{\partial t^2} \qquad \text{Eq. 1.8}$$

where n is the linear refractive index. This relation shows that a time varying nonlinear polarization can act as the source of new electromagnetic field components [60]. The i^{th} cartesian component of the nonlinear polarization can be expressed as a function of the electric field components using the susceptibility tensors $\chi^{(m)}$ of order m ($m = 1,2,3 \ldots$):

$$P_{NL}^{i} = \varepsilon_0 \sum_{j,k} \chi_{ijk}^{(2)} E_j E_k + \epsilon_0 \sum_{j,k,l} \chi_{ijkl}^{(3)} E_j E_k E_l + \cdots \qquad \text{Eq. 1.9}$$

with $i,j,k,l = x,y,z$. Eq. 1.9 tells that the $\chi^{(m)}$ is a tensor of rank $(m+1)$. Thus, $\chi^{(2)}$ is a tensor of rank 3 and $\chi^{(3)}$ is a tensor of rank 4. In this thesis we will be primarily focusing on the $\chi^{(2)}$ induced nonlinear processes such as second harmonic generation (SHG) which can be described using the first term in Eq. 1.9. The 27-component $\chi^{(2)}$ tensor can be simplified by numerous symmetry conditions [60]. To represent it in a contracted notation, let's introduce a new tensor:

$$d_{ijk} = \frac{1}{2}\chi_{ijk}^{(2)} \qquad \text{Eq. 1.10}$$

where the factor $1/2$ comes from conventions. Considering a lossless medium and suppressing the frequency dependency of susceptibility for simplicity, the intrinsic permutation symmetry ($d_{ijk} = d_{ikj}$) can result in a 3×6 matrix d_{il}:

$$d_{il} = \begin{bmatrix} d_{11} & d_{12} & d_{13} & d_{14} & d_{15} & d_{16} \\ d_{21} & d_{22} & d_{23} & d_{24} & d_{25} & d_{26} \\ d_{31} & d_{32} & d_{33} & d_{34} & d_{35} & d_{36} \end{bmatrix} \qquad \text{Eq. 1.11}$$

Now, applying the Kleinman symmetry condition will leave us with 10 independent elements [62]:

$$d_{il} = \begin{bmatrix} d_{11} & d_{12} & d_{13} & d_{14} & d_{15} & d_{16} \\ d_{16} & d_{22} & d_{23} & d_{24} & d_{14} & d_{12} \\ d_{15} & d_{24} & d_{33} & d_{23} & d_{13} & d_{14} \end{bmatrix} \quad \text{Eq. 1.12}$$

The nonlinear polarization leading to SHG (frequency doubling) can be now represented in terms of d_{il} by the matrix equation (see section 1.2.2 for more details on SHG):

$$\begin{bmatrix} P_x(2\omega) \\ P_y(2\omega) \\ P_z(2\omega) \end{bmatrix} = \varepsilon_0 \begin{bmatrix} d_{11} & d_{12} & d_{13} & d_{14} & d_{15} & d_{16} \\ d_{21} & d_{22} & d_{23} & d_{24} & d_{25} & d_{26} \\ d_{31} & d_{32} & d_{33} & d_{34} & d_{35} & d_{36} \end{bmatrix} \begin{bmatrix} E_x(\omega)^2 \\ E_y(\omega)^2 \\ E_z(\omega)^2 \\ 2E_y(\omega)E_z(\omega) \\ 2E_x(\omega)E_z(\omega) \\ 2E_x(\omega)E_y(\omega) \end{bmatrix} \quad \text{Eq. 1.13}$$

where ω is the oscillation frequency of the electric field propagating through the nonlinear medium. If the medium also possesses $\bar{4}3m$ crystallographic symmetry such as GaP (zinc-blende type), then the number of independent non-zero components will reduce to 3 given as $d_{14} = d_{25} = d_{36}$ to express [60]:

$$\begin{bmatrix} P_x(2\omega) \\ P_y(2\omega) \\ P_z(2\omega) \end{bmatrix} = \varepsilon_0 \begin{bmatrix} 0 & 0 & 0 & d_{14} & 0 & 0 \\ 0 & 0 & 0 & 0 & d_{25} & 0 \\ 0 & 0 & 0 & 0 & 0 & d_{36} \end{bmatrix} \begin{bmatrix} E_x(\omega)^2 \\ E_y(\omega)^2 \\ E_z(\omega)^2 \\ 2E_y(\omega)E_z(\omega) \\ 2E_x(\omega)E_z(\omega) \\ 2E_x(\omega)E_y(\omega) \end{bmatrix} \quad \text{Eq. 1.14}$$

Eq. 1.14 describes the direction of SHG with a frequency of 2ω driven by the nonlinear polarization when the nonlinear medium interacts with a strong electric field of frequency ω. In the case of a microdisk resonator fabricated from $\bar{4}3m$ materials, the TM polarized SHG (electric field perpendicular to the plane of the microdisk) is expected for two TE polarized pump modes (electric field in the plane of the microdisk) through the relation [39]:

$$P_z(2\omega) = 2\varepsilon_0 d_{14} E_x(\omega) E_y(\omega) \quad \text{Eq. 1.15}$$

More details on the polarization of microresonator modes are included in section 1.3.1.

1.2.2 Second Harmonic Generation

The m-th order nonlinearity will lead to $(m+1)$-wave mixing. Thus, the $\chi^{(2)}$ nonlinearity controls the three-wave mixing processes in a nonlinear material with non-inversion symmetry. An intense optical field with two distinct frequency

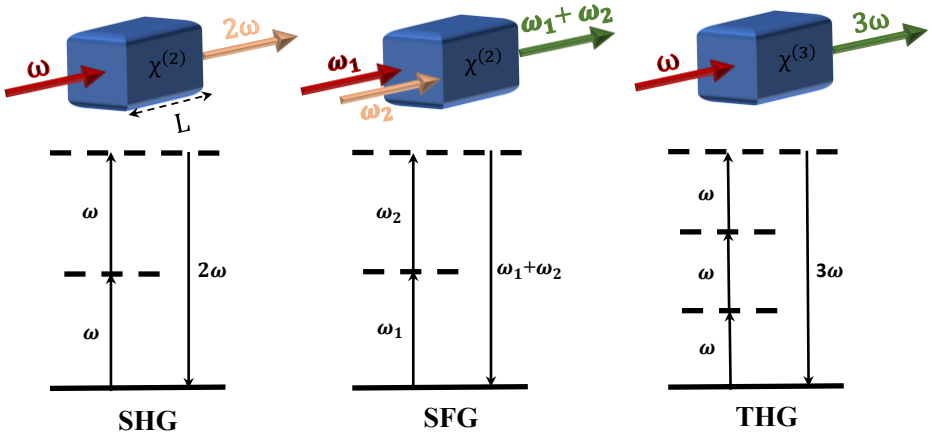

Figure 1.2: The geometry and the energy level description for the nonlinear interactions SHG, SFG and THG. The solid and dashed horizontal lines in the energy level diagrams represent atomic ground state and virtual levels, respectively.

components ω_1 and ω_2 incident on such materials can be expressed in scalar quantities for simplicity:

$$\tilde{E}(t) = E_1 e^{-i\omega_1 t} + E_2 e^{-i\omega_2 t} + \text{ c.c} \qquad \text{Eq. 1.16}$$

where c.c stands for the complex conjugate. Taking the second-order term from Eq. 1.3, we can rewrite it as:

$$\begin{aligned}\tilde{P}^{(2)}(t) = \varepsilon_0 \chi^{(2)} \big[& E_1^2 e^{-2i\omega_1 t} + E_2^2 e^{-2i\omega_2 t} + 2E_1 E_2 e^{-i(\omega_1+\omega_2)t} \\ & + 2E_1 E_2^* e^{-i(\omega_1-\omega_2)t} + \text{ c.c. } \big] + 2\varepsilon_0 \chi^{(2)} [E_1 E_1^* + E_2 E_2^*]\end{aligned} \qquad \text{Eq. 1.17}$$

and in a simplified notation with a summation that runs over $\pm\omega_n$:

$$\tilde{P}^{(2)}(t) = \sum_n P(\omega_n) e^{-i\omega_n t} \qquad \text{Eq. 1.18}$$

The general Eq. 1.17 includes all the possible nonlinear effects associated with $\chi^{(2)}$. The complex amplitudes of their frequency components are listed below:

$$\begin{aligned} P(2\omega_1) &= \varepsilon_0 \chi^{(2)} E_1^2 && \text{(SHG)} \\ P(2\omega_2) &= \varepsilon_0 \chi^{(2)} E_2^2 && \text{(SHG)} \\ P(\omega_1 + \omega_2) &= 2\varepsilon_0 \chi^{(2)} E_1 E_2 && \text{(SFG)} \\ P(\omega_1 - \omega_2) &= 2\varepsilon_0 \chi^{(2)} E_1 E_2^* && \text{(DFG)} \\ P(0) &= 2\varepsilon_0 \chi^{(2)} (E_1 E_1^* + E_2 E_2^*) && \text{(OR)} \end{aligned} \qquad \text{Eq. 1.19}$$

where the first two components correspond to the SHG. The remaining components SFG, DFG and OR stand for the sum frequency generation, difference frequency generation and optical rectification, respectively. The SHG can be found as a special case of the SFG.

In SHG, the two photons of frequency ω are annihilated to form a photon with double frequency 2ω. In terms of wavelength, this process can be written as $2\lambda_{2\omega} = \lambda_{\omega}$ where $\lambda_{\omega(2\omega)}$ is the wavelength of the pump (SH) wave. This is the first second order nonlinear effect ever reported [56]. If two photons of different frequencies ω_1 and ω_2 are annihilated to produce a photon of frequency $\omega_1 + \omega_2$, then the process is known as SFG. In $\chi^{(3)}$ effects, a simple case is the third harmonic generation (THG) where three photons of frequency ω are converted to a single photon of frequency 3ω. These frequency conversions obeying photon energy conservations are schematically illustrated in Figure 1.2. To describe the SHG process mathematically, let's consider a nonlinear medium of length L through which an intense field (pump wave) is propagating in the z-direction with an oscillating frequency of ω_1 and wave vector $k_\omega = n_\omega \omega_1 / c$. The second harmonic (SH wave) will be generated at a frequency of $\omega_2 = 2\omega_1$ with a wave vector $k_{2\omega} = n_{2\omega}\omega_2/c$. The medium is assumed to be lossless for both frequencies. Considering the slowly varying envelope approximation, solving Eq. 1.8 using Eq. 1.19 gives a general formula for SHG:

$$\frac{\partial E_{2\omega}(z)}{\partial z} = \frac{i4\pi\omega^2}{c^2 k_{2\omega}} \chi^{(2)} E_\omega(z)^2 e^{-i\Delta k z} \qquad \text{Eq. 1.20}$$

where $E_\omega(z)$ and $E_{2\omega}(z)$ are the amplitudes of pump wave (ω) and SH wave (2ω), respectively. Δk is the phase mismatch or momentum mismatch between the interacting waves defined as:

$$\Delta k = k_{2\omega} - 2k_\omega = \frac{2\omega}{c}(n_{2\omega} - n_\omega) \qquad \text{Eq. 1.21}$$

where n_ω and $n_{2\omega}$ are the refractive index of the pump and SH wave, respectively. If there is perfect phase matching ($\Delta k = 0$), then the intensity of the SH wave increases quadratically with pump wave intensity along the material length:

$$\begin{aligned} I_{2\omega}(L) &\propto E_\omega^4 \left(\chi_\omega^{(2)}\right)^2 L^2 \\ &\propto I_\omega^2 \left(\chi_\omega^{(2)}\right)^2 L^2 \end{aligned} \qquad \text{Eq. 1.22}$$

The internal SHG efficiency can be defined as the ratio of the optical power converted from one frequency to another without considering power injection and extraction expressed as:

$$\eta_{int} = \frac{P_{2\omega}}{P_\omega} \qquad \text{Eq. 1.23}$$

Now, integrating Eq. 1.22 based on Eq. 1.23 can express:

$$\eta_{int} \propto I_\omega \left(\chi_\omega^{(2)}\right)^2 L^2 \qquad \text{Eq. 1.24}$$

Eq. 1.24 implies that an efficient generation of SH wave requires a high pump wave intensity applied on a sufficiently long material possessing large second order

nonlinear susceptibility. The non-depleted pump approximation gives a normalized SHG efficiency which is often used in the literature to present experimental results:

$$\eta_{norm} = \frac{P_{2\omega}}{P_{\omega}^2} \qquad \text{Eq. 1.25}$$

The natural chromatic dispersion in materials will lead to phase mismatch ($\Delta k \neq 0$) and will affect the conversion efficiency. In this case, a phase shift will accumulate between the SH wave and the polarization driving it. This results in their constructive and destructive interferences through the material length which can be expressed as:

$$I_{2\omega}(L) \propto \frac{1}{\Delta k^2} I_{\omega}^2 \left(\chi_{\omega}^{(2)}\right)^2 \sin^2 \frac{\Delta k L}{2} \qquad \text{Eq. 1.26}$$

It shows that the SH wave intensity evolution becomes maximum after a certain distance known as coherence length given by:

$$\ell_{coh} = \frac{\pi}{\Delta k} \qquad \text{Eq. 1.27}$$

As soon as the ℓ_{coh} is passed, the $I_{2\omega}$ decreases to a minimum and then begins to rise again. Thus, phase matching techniques are explicitly developed to achieve efficient conversion.

1.2.3 Phase Matching techniques

The frequency mixing process requires to comply with energy and momentum conservations in addition to the polarization selection rules. Typically, no more than one of the frequency components given in Eq. 1.19 will be present with comparable intensity due to the phase matching criteria favoring only one effect. Thus, the dispersion of the nonlinear medium must be properly compensated to achieve phase matching. Depending on the material properties and applications many phase matching strategies are adapted. A widely used technique is to utilize the birefringence of the nonlinear crystal where the refractive index of the material is not only depends on the frequency but also on its polarization [63][64]. Adjusting the temperature and angular orientation of the birefringent crystal offer two kinds of phase matching. In type I, the two lower frequency waves have the same polarization and the high frequency wave has a polarization orthogonal to them. In type II, the two lower frequency waves have different orthogonal polarizations and the high frequency wave has a polarization same as one of the other two fields. However, this technique is not suitable while using isotropic III-V semiconductors lacking birefringence, such as for GaP [60]. This can be resolved by quasi phase matching (QPM) where the SHG intensity evolves quasi-quadratically with the propagation distance ($\propto 4L^2/\pi^2$) despite a finite phase mismatch [65][66]. To achieve QPM, the homogeneous crystal's nonlinear susceptibility is periodically reversed in sign with a period equal to twice the coherence length. In such an

engineered medium the destructive interference of the nonlinear polarization with the SH wave will be reversed to constructive. Different phase matching strategies are schematized in Figure 1.3. The QPM which is usually achieved by periodical poling cannot be implemented in III-V materials that are not ferroelectric [67]. However, orientation-patterned III-V crystals are fabricated in which the nonlinear susceptibility is periodically reversed by reversing the polarity of the semiconductor crystal. Recently, the SHG has been demonstrated in shallow-ridge waveguides fabricated with orientation-patterned GaP (OP-GaP) crystals, a promising candidate for nonlinear photonics [68]. In 2006, it was reported that a similar periodic reversal of the nonlinear susceptibility can be naturally accomplished in a microdisk resonator fabricated with materials possessing $\bar{4}3m$ point-group symmetry such as GaP. In this technique, every quarter turns for light around the [001] direction experience a periodical reversal in the sign of the nonlinear susceptibility [39]. A detailed description of its origin is included in section 1.4.2. In addition, this symmetry based QPM scheme can be further relaxed by a new method proposed with competitive performance where the spatial distribution of the opposite nonlinear susceptibility is random [34][69][70]. In section 1.5 we will elaborate on this novel technique based on our GaP microdisks grown on Si substrate.

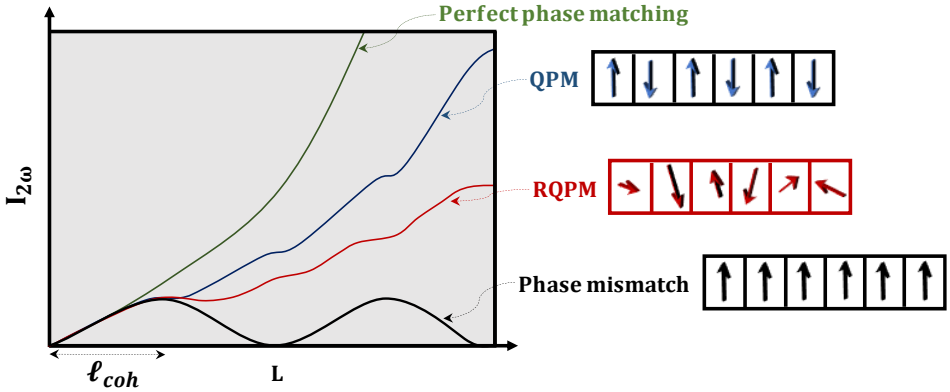

Figure 1.3: The evolution of the SHG intensity with the propagation distance for different phase matching scenarios. *L*: The length of the nonlinear medium.

1.3 Theory of WGMs in a microdisk

The WGMs in a microdisk is described here in details using a semi-analytical approach called the effective index method (EIM). Later, WGM parameters are explained and the exchange of energy between a waveguide and a microdisk is scrutinized. The theory part given in the following sections 1.3.1 to 1.3.3 are mainly extracted from Ref.[61], [71]–[76].

1.3.1 Modes in the cavity

The WGMs can be studied mathematically as a solution of the Helmholtz equation in curved coordinate geometry such as cylindrical for a microdisk. From the curl of Maxwell's equations (Eq. 1.4, Eq. 1.5) in the absence of free charges and currents for a linear piecewise homogeneous medium, the Helmholtz equation can be written as:

$$\vec{\nabla}^2\vec{F} + \frac{n_{disk}^2\omega^2}{c^2}\vec{F} = 0 \qquad \text{Eq. 1.28}$$

where $\vec{F} = \{\vec{E}, \vec{H}\}$, $\vec{\nabla}^2$ is the Laplacian operator and c is the speed of light. Let the cylindrical coordinates be (r, φ, z) as shown in Figure 1.1 (see section 1.1) and the corresponding Laplacian operator is given by:

$$\left(\frac{\partial^2}{\partial r^2} + \frac{1}{r}\frac{\partial}{\partial \mathrm{r}} + \frac{1}{r^2}\frac{\partial^2}{\partial \varphi^2} + \frac{\partial^2}{\partial z^2} + n_{disk}^2 k^2\right)\vec{F} = 0 \qquad \text{Eq. 1.29}$$

For a semiconductor microdisk with bulk a refractive index n_{disk} surrounded by a medium of refractive index n_{clad} ($< n_{\mathrm{disk}}$), the vertical confinement of the field is many times stronger than the horizontal one due to the refractive index contrast at the interface. This will restrict the photon movement to a plane rather than in three dimensions, effectively reducing the problem to a two dimensional one. We can thus use EIM in the vertical direction which is analogous to finding the optical mode's field distribution for a symmetric slab waveguide of the same thickness h as the microdisk with a refractive index n_{disk}. Such an assumption will help us to separate microdisk modes into two uncoupled and orthogonal sets of polarizations, TE (E field parallel to the microdisk plane) and TM (E field perpendicular to the microdisk plane). In other words, the TE modes have non-vanishing components $\{E_{\mathrm{r}}, E_{\varphi,} H_{\mathrm{z}}\}$ and for TM modes the non-vanishing components are $\{H_{\mathrm{r}}, H_{\varphi}, E_{\mathrm{z}}\}$.

Now using the separation of variables, Eq. 1.29 can be solved for F_{z} which is $\{H_{\mathrm{z}}, E_{\mathrm{z}}\}$ for {TE,TM} modes, respectively. The solutions take the form of $F_z = R(r)\Phi(\varphi)Z(z)$ and describe the axial, azimuthal and radial properties of the WGMs. The vertical dependence is given by:

$$\frac{\partial^2 Z}{\partial z^2} + k^2\left({n_{\mathrm{disk}}}^2 - n_{\mathrm{eff}}^2\right)Z = 0 \qquad \text{Eq. 1.30}$$

where k is the wave vector. This is the Helmholtz equation of slab waveguide with eigen functions Z of effective refractive index n_{eff}. Solving it gives the number of maxima of the Z function in the microdisk thickness, an integer labeled as planar number (q). The angular dependence is given by:

$$\frac{\mathrm{d}^2\Phi}{\mathrm{d}\varphi^2} + m^2\Phi = 0 \qquad \text{Eq. 1.31}$$

This can be integrated to get $\Phi(\varphi) = e^{\pm im\varphi}$ describing clockwise and counter-clockwise traveling waves where the integer m is the azimuthal number. The radial dependence is given by:

$$\frac{\mathrm{d}^2\mathrm{R}}{\mathrm{d}r^2} + \frac{1}{r}\frac{\mathrm{dR}}{\mathrm{d}r} + \left(k^2 n_{\mathrm{eff}}^2 - \frac{m^2}{r^2}\right)\mathrm{R} = 0 \qquad \text{Eq. 1.32}$$

This is Bessel's equation for the radial dependence of the electromagnetic field. The solutions of this equation can be written in terms of Bessel functions of the first kind inside the microdisk $(r \leq R)$ and Hankel functions of the second kind outside the microdisk $(r > R)$:

$$\mathrm{R}(r) = \begin{cases} NJ_m(\mathrm{k}n_{\mathrm{eff}}\, r) & r \leq R \\ NBH_m^{(2)}(\mathrm{k}r) & r > R \end{cases} \qquad \text{Eq. 1.33}$$

where N is a normalization constant and $B = J_m(kn_{\mathrm{eff}}R)/H_m^{(2)}(kR)$. If we impose the continuity of tangential components of $\vec{E}$ and $\vec{H}$ (for TE modes $\{H_z, E_\varphi\}$ and TM modes $\{H_\varphi, E_z\}$) at the interface, the dispersion relations are obtained:

$$\begin{aligned} &\mathrm{n}_{\mathrm{eff}}\frac{\mathrm{j_m}(\mathrm{kn_{eff}R})}{\mathrm{J_m}(\mathrm{kn_{eff}R})} - \frac{\dot{\mathrm{H}}_{\mathrm{m}}^{(2)}(\mathrm{kR})}{\mathrm{H}_{\mathrm{m}}^{(2)}(\mathrm{kR})} = 0 \qquad \text{TM modes} \\ &\frac{\mathrm{j_m}(\mathrm{kn_{eff}R})}{\mathrm{J_m}(\mathrm{kn_{eff}R})} - \mathrm{n}_{\mathrm{eff}}\frac{\dot{\mathrm{H}}_{\mathrm{m}}^{(2)}(\mathrm{kR})}{\mathrm{H}_{\mathrm{m}}^{(2)}(\mathrm{kR})} = 0 \qquad \text{TE modes} \end{aligned} \qquad \text{Eq. 1.34}$$

Now, solving Eq. 1.34 for k allows the determination of the microdisk resonant modes ω. Despite the analogous nature of the problem to an optical slab waveguide, the eigen frequency of a WGM is a complex number regardless of the real valued n_{eff}. The real part of k leads to the determination of resonance wavelength:

$$\lambda = \frac{2\pi}{\mathrm{Re}\,(k)} \qquad \text{Eq. 1.35}$$

The imaginary part of k corresponds to the curvature induced radiation losses experienced by all resonances in the cavity, which is linked to the intrinsic linewidth of the resonances (see section 1.6.1 for more details). We generally define the intrinsic quality factor of resonance as:

$$Q_{rad} = \frac{\mathrm{Re}\,(k)}{2\mathrm{Im}\,(k)} \qquad \text{Eq. 1.36}$$

For a given value of m, multiple solutions exist for Eq. 1.34. They are given by an integer labeled as radial mode numbers (p) which represents the number of field maxima along the radius of the microdisk. Once F_z is known, the other field components can be obtained by using Maxwell's equations as:

$$\begin{aligned} &\mathrm{H}_r = \frac{\mathrm{m}}{\mu_0 r\omega}\mathrm{E}_z \\ &\mathrm{H}_\varphi = -\frac{\mathrm{i}}{\mu_0\omega}\frac{\partial \mathrm{E}_z}{\partial \mathrm{r}} \end{aligned} \qquad \text{TM modes} \qquad \text{Eq. 1.37}$$

$$E_r = -\frac{m}{\varepsilon_0 \varepsilon_r r \omega} H_z \qquad \text{TE modes} \qquad \text{Eq. 1.38}$$
$$E_\varphi = \frac{i}{\varepsilon_0 \varepsilon_r \omega} \frac{\partial H_z}{\partial r}$$

Thus, every WGM is represented by a combination of mode numbers (m, p, q) for each polarization and possesses different dispersions and field distributions. The

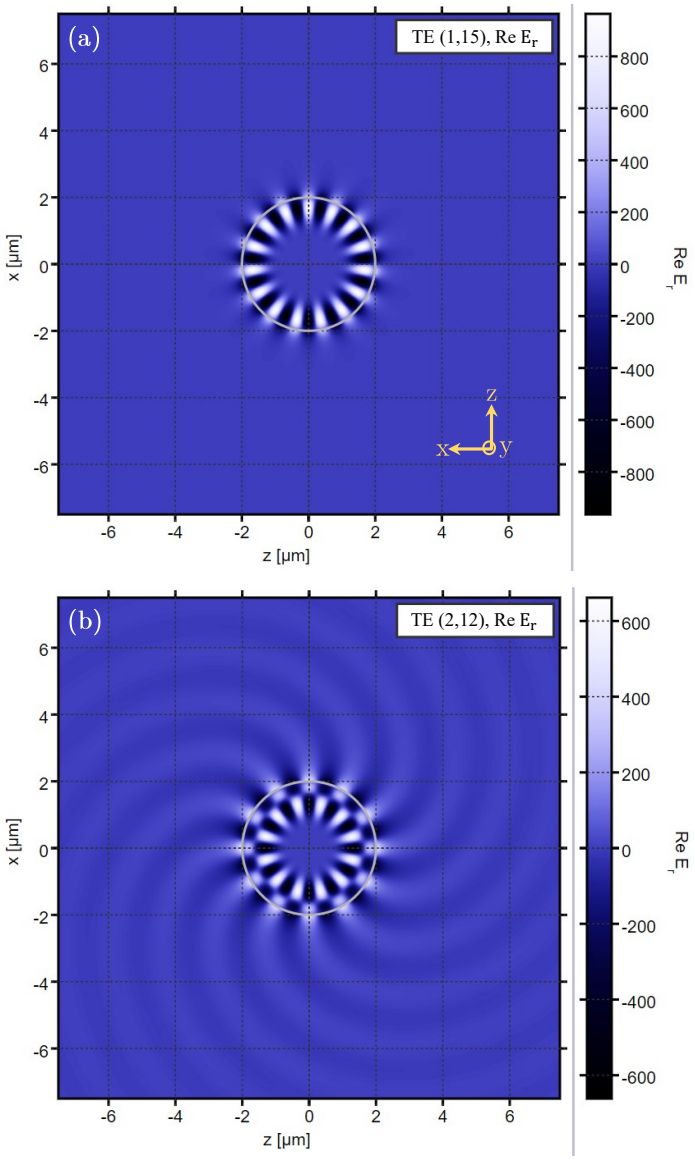

Figure 1.4: Top view of TE mode profiles of a WGM microdisk with (a) $p = 1$, $m = 15$ and (b) $p = 2$, $m = 12$. The white circular line represents the microdisk boundary. Images: Courtesy of mode solver in https://www.siio.eu/index.html based on Ref.[213].

distribution of the mode profile of a TE mode in a WGM microdisk of radius $2\ \mu m$ for different radial and azimuthal quantum numbers is shown in Figure 1.4.

1.3.2 WGM properties

Optical WGMs in microresonators are not only labeled by quantum numbers but also evaluated by different parameters detailed in the following subsections. These quantities can be simply extracted from the transmission spectra collected from the cavity. They will help us to understand the behavior of the microresonator fabricated and determine how good is a microresonator for its potential applications as a photonic device.

1.3.2.1 Quality factor (Q-factor)

The quality factor is a dimensionless quantity where the term has an origin in electronic circuits which is then extended to use in mechanical and acoustic resonators. Later, it becomes a common parameter in the characterization of optical resonators. In general, for all resonant elements with time-dependent stored energy U, frequency of oscillation ω, and power dissipation of P_{d}, the Q-factor is given by [77]:

$$Q \equiv \frac{\omega \cdot U}{P_{\mathrm{d}}} \qquad \text{Eq. 1.39}$$

where $U = U_0 e^{-\omega t/Q}$ with U_0 is the initial amount of energy stored in the resonator under the condition that there is no additional energy supplied. The energy decay rate $\mathrm{dU/dt} = -\omega U/Q$ describes that it is inversely proportional to the Q-factor, which means a resonator with a low energy decay rate will have a high Q-factor. Equivalently, the Q-factor is defined as 2π times the ratio of the total energy stored in the cavity to the energy dissipated per cycle:

$$Q \equiv 2\pi \times \frac{\text{Energy stored}}{\text{Energy dissipated per cycle}} \qquad \text{Eq. 1.40}$$

In the Fourier domain, the frequency distribution of the energy in the cavity takes a Lorentzian line shape and the Q-factor can be measured from the WGM spectrum as:

$$Q = \frac{\omega}{\Delta\omega} = \frac{\lambda}{\Delta\lambda} \qquad \text{Eq. 1.41}$$

where λ is the resonance wavelength. The $\Delta\omega$ and $\Delta\lambda$ in Eq. 1.41 are the frequency and wavelength separations, respectively, between half-power points, known as the full width at half maximum (FWHM). Apart from this conventional term, it is full width at half depth (FWHD) in transmission measurements (see Figure 1.5).

Let's rewrite the equation for the time dependence of energy stored in the cavity:

$$U(t) = U_0(t_0)e^{-t/(Q/\omega)} = U_0(t_0)e^{-t/\tau_{photon}} \qquad \text{Eq. 1.42}$$

where $\tau_{photon} = Q/\omega = 1/\Delta\omega$ is the cavity photon lifetime for a WGM of frequency ω. The photon lifetime is another common term in the optical resonators terminology which is the time required for the cavity stored energy to decay and become $1/e$ times its initial value.

There are two types of loss mechanisms controlling the performance of a resonator, intrinsic and extrinsic. The intrinsic losses are linked to the physical parameters of the resonator by which it is designed and fabricated. In general, it includes radiation losses due to the radius (curvature) (Q_{rad}), absorption in the material by which the resonator is fabricated (Q_{abs}), Rayleigh scattering by the rough surface and sidewalls (Q_R), and volume scattering/absorption due to defects and impurities formed in the cavity (Q_{bulk}). The sum of all these losses without an external coupling gives the unloaded or intrinsic Q-factor (Q_i) of the cavity:

$$\frac{1}{Q_i} = \frac{1}{Q_{rad}} + \frac{1}{Q_{abs}} + \frac{1}{Q_R} + \frac{1}{Q_{bulk}} \qquad \text{Eq. 1.43}$$

In addition, there is an extrinsic or coupling loss (Q_{cpl}) linked to the evanescent coupling of the resonator with a nearby access waveguide or other resonators for the selective excitation of modes. Then, the total Q-factor or loaded Q-factor can be expressed as:

$$\frac{1}{Q_{loaded}} = \frac{1}{Q_i} + \frac{1}{Q_{cpl}} \qquad \text{Eq. 1.44}$$

$$\frac{1}{Q_{loaded}} = \frac{1}{Q_{rad}} + \frac{1}{Q_{abs}} + \frac{1}{Q_R} + \frac{1}{Q_{bulk}} + \frac{1}{Q_{cpl}} \qquad \text{Eq. 1.45}$$

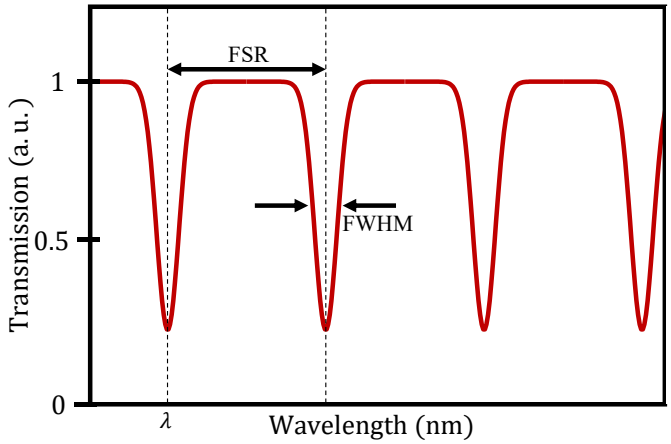

Figure 1.5: The transmission spectrum of a microresonator drawn schematically.

In section 1.6 we will discuss each of them in detail and loss analysis for our microdisks based on their values is included in chapter 3.

1.3.2.2 Free spectral range (FSR)

The free spectral range for a given refractive index value is the frequency (or wavelength) separation between the two consecutive resonant modes in the WGM spectrum along the frequency (or wavelength) axis (see Figure 1.5). From the formula for propagation constant $\beta = 2\pi n_{\text{eff}}/\lambda$, under the approximation of neglecting wavelength dependence of effective refractive index, we can write an expression for FSR in the wavelength domain as:

$$\text{FSR} = \frac{\lambda^2}{Ln_{eff}} = \frac{\lambda^2}{2\pi R n_{eff}} \qquad \text{Eq. 1.46}$$

where λ is the resonance wavelength, L and R are the effective circumference and radius of the resonator for a given mode. A more accurate expression can be also obtained for FSR accounting for the wavelength dependence of n_{eff}:

$$\frac{\partial \beta}{\partial \lambda} = -\frac{k}{\lambda} n_{\text{eff,grp}} \qquad \text{Eq. 1.47}$$

$$n_{\text{eff,grp}} = n_{\text{eff}} - \lambda \frac{\partial n_{\text{eff}}}{\partial \lambda} \qquad \text{Eq. 1.48}$$

where $k = 2\pi/\lambda$ is the wavevector and $n_{\text{eff,grp}}$ is the effective group refractive index of the resonant mode [78]. The FSR is then given by:

$$\text{FSR} = \frac{\lambda^2}{n_{eff,grp}\text{L}} = \frac{\lambda^2}{2\pi R n_{eff,grp}} \qquad \text{Eq. 1.49}$$

The FSR of the resonator is inversely proportional to the resonator radius, which indicates that a larger resonator possesses a smaller FSR and the denser the number of modes appears in the WGM spectrum. Also, it's worth noticing that the FSR is not the same at different wavelengths.

1.3.2.3 Effective mode volume

The effective mode volume is a measure of how much a mode spatially occupies the resonator cavity i.e., how much of the mode's intensity is tightly confined around its central maximum. The effective mode volume is given by:

$$V_{\text{eff}} = \frac{\int n_{disk}^2(\text{r})|\text{E(r)}|^2 dV}{max[n_{disk}^2(\text{r})|\text{E(r)}|^2]} \qquad \text{Eq. 1.50}$$

where $\int n_{disk}^2(\text{r})|\text{E(r)}|^2 dV$ is the total energy stored inside the resonator by a mode and $max[n_{disk}^2(\text{r})|\text{E(r)}|^2]$ is the maximum energy density of that mode. WGM resonators make use of their low mode volume which leads to a large energy density in favor of nonlinear optics.

The definition of the total Q-factor and the effective mode volume allows us to obtain an expression for the SHG conversion efficiency in a microdisk by taking into account the coupling of the injected and extracted power [61]:

$$\eta_{ext} \propto \frac{Q_{SH} Q_p^2}{\mathcal{V}_p} \left(\chi^{(2)}\right)^2 P_\omega^{ext} \qquad \text{Eq. 1.51}$$

where $Q_{p(SH)}$ is the loaded Q-factor of the pump (SH) mode and $\mathcal{V}_p$ is the pump mode volume. The high Q-factor to mode volume ratio offered by microresonators such as a microdisk not only enhances nonlinear frequency conversion efficiencies but also offers the advantage of integration [79][33][58].

1.3.3 Waveguide-microdisk coupling

The modes of an optical resonator can be excited by an access waveguide such as a tapered optical fiber used in our experiments for microdisk coupling. Light can be exchanged with the resonator by evanescent coupling when they are close in proximity. The Coupled Mode Theory (CMT) is the formalism that is commonly used to understand the energy transfer between the modes of both structures when they form a compound system. In such a system, the field is assumed to be a linear superposition of the eigenmodes of individual components which are perturbed by the presence of other modes [80][81][82].

Let's consider a simple waveguide-microdisk system as shown in Figure 1.6 separated by a physical gap of g. The κ_{int} is the intrinsic loss rate in the cavity and κ_{ext} is the external coupling loss rate due to the proximity of the waveguide. The normalized incident and outgoing field amplitudes traveling through the coupling waveguide are represented by S_{in} and S_{out}, respectively. The square of their magnitudes gives the power in the waveguide mode. If the normalized field amplitude in the resonator is $a(t)$, then its magnitude squared is equal to the stored resonator energy. The time dynamics of the fields can be expressed as [81]:

$$\begin{aligned} \frac{da(t)}{dt} &= -i\omega a(t) - \left(\frac{\kappa_{\text{int}}}{2} + \frac{\kappa_{ext}}{2}\right) a(t) + \kappa s_{in}(t) \\ s_{\text{out}}(t) &= s_{in}(t) - \kappa^* a(t) \end{aligned} \qquad \text{Eq. 1.52}$$

where $\kappa = i\sqrt{\kappa_{ext}}$ is a coefficient expressing the degree of coupling between the waveguide and resonator. The relations for the steady state WGM and waveguide outgoing field amplitudes for $S_{in} \propto e^{-i\tilde{\omega}t}$ are given by:

$$a = \frac{i\sqrt{\kappa_{ext}}}{-i\Delta + \left(\frac{\kappa_{\text{int}}}{2} + \frac{\kappa_{ext}}{2}\right)} s_{in} \qquad \text{Eq. 1.53}$$

and using Eq. 1.52 and Eq. 1.53:

$$s_{\text{out}} = \frac{-i\Delta + \left(\frac{\kappa_{\text{int}}}{2} - \frac{\kappa_{\text{ext}}}{2}\right)}{-i\Delta + \left(\frac{\kappa_{\text{int}}}{2} + \frac{\kappa_{\text{ext}}}{2}\right)} s_{\text{in}} \qquad \text{Eq. 1.54}$$

where $\Delta = \tilde{\omega} - \omega$ is the detuning in frequencies of WGM resonance (ω) and incident light $(\tilde{\omega})$. Then, the stored cavity energy can be written as:

$$|a|^2 = \frac{4\kappa_{\text{ext}}}{4\Delta^2 + (\kappa_{\text{int}} + \kappa_{\text{ext}})^2} |s_{\text{in}}|^2 \qquad \text{Eq. 1.55}$$

and the normalized transmission (T) through the waveguide in terms of frequency:

$$T_\Delta = \frac{|s_{\text{out}}|^2}{|s_{\text{in}}|^2} = \frac{4\Delta^2 + (\kappa_{\text{int}} - \kappa_{ext})^2}{4\Delta^2 + (\kappa_{\text{int}} + \kappa_{\text{ext}})^2} \qquad \text{Eq. 1.56}$$

If the detuning Δ=0 (on resonance) then Eq. 1.56 becomes:

$$T_{\text{on}} = \left(\frac{1 - \frac{\kappa_{\text{ext}}}{\kappa_{\text{int}}}}{1 + \frac{\kappa_{\text{ext}}}{\kappa_{\text{int}}}}\right)^2 = \left(\frac{1-K}{1+K}\right)^2 \qquad \text{Eq. 1.57}$$

where $K = \kappa_{\text{ext}} / \kappa_{\text{int}}$. Eq. 1.56 describes the Lorentzian shape spectral response of a resonator with FWHM controlled by $\kappa_{\text{int}} + \kappa_{\text{ext}} = \kappa_{\text{int}} (1 + K)$.

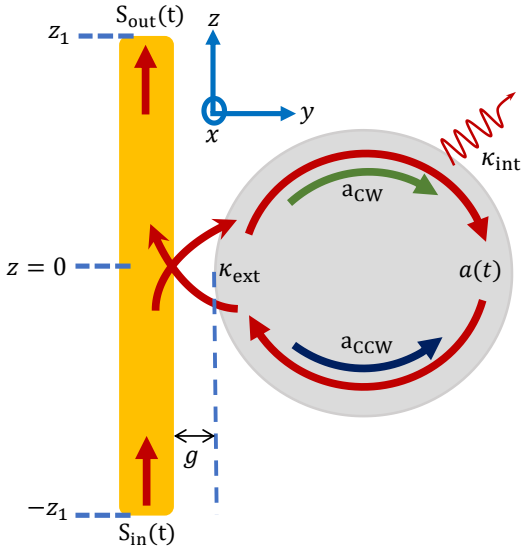

Figure 1.6: A schematic of the waveguide-microdisk coupled system.

1.3.3.1 Energy transfer regimes

It is now possible to define three different coupling regimes when an access waveguide interacts with the resonator, which depends on the relative strength of the external coupling loss rate to the intrinsic loss rate characterized by the parameter K. These regions of interest are,

- $K < 1$ (Under-coupled regime): The loss rate in the cavity predominates, $\kappa_{ext} < \kappa_{int}$. Thus, the injected power will be too low to overcome the intrinsic loss rate in the cavity resulting in weak coupling. The transmission becomes $0 < T_{on} < 1$ and the loaded Q-factor takes a value $Q_i/2 < Q_{loaded} < Q_i$. Experimentally, enlarging the value of g leads to this regime.
- $K = 1$ (Critical-coupled regime): The loss rates become equal, $\kappa_{ext} = \kappa_{int}$ and the waveguide output power $S_{out} = 0$ (i.e., $T_{on} = 0$). At this regime, optimal energy transfer occurs and the cavity will store maximum energy with $Q_{loaded} = Q^i/2 = Q^{cpl}/2$.
- $K > 1$ (Over-coupled regime): The injected power into the cavity is not dissipated fast enough, $\kappa_{ext} > \kappa_{int}$. The transmission becomes $0 < T_{on} < 1$. The resonance linewidth broadens due to increased coupling loss rate and Q_{loaded} lies between $Q_{cpl}/2$ and Q_{cpl}. This regime is achieved practically by reducing the value of g.

In general, it is preferable to work at or near the critical-coupled regime for optimal coupling strength between the waveguide and the resonator [83]. However, an over-coupled regime is helpful for injecting and/or extracting maximum power from the cavity despite the low Q_{loaded}. Experimentally, it is impossible to differentiate the under-coupling and over-coupling regimes from a single WGM spectrum [84].

1.3.3.2 Phase matching criterion for evanescent coupling

The coupling coefficient term κ in Eq. 1.52 is proportional to the overlap integral between the resonator and waveguide mode fields as mentioned in section 1.3.3. Thus, it is possible to write an expression for κ based on Ref.[85] as:

$$\kappa = i\frac{\widetilde{\omega}\varepsilon_0}{4}\int_{-z_1}^{z_1} dz \iint_{[resonator]} dxdy(n^2_{resonator} - 1)\vec{e}^*_{res}\vec{e}_{in}e^{-i\beta z} \qquad \text{Eq. 1.58}$$

where $\vec{e}_{res}(x,y,z)$ is the uncoupled resonator mode field normalized to unit energy. Then, inside the resonator, the electric field distribution can take the form of $a(t)\vec{e}_{res}(x,y,z)$. The $\vec{e}_{in}(x,y)$ term corresponds to the undisturbed waveguide mode profile normalized to unit power, β is the undisturbed waveguide propagation constant and $n_{resonator}$ is the refractive index of the resonator. In $\vec{e}_{res}$ the WGM has $e^{im\varphi}$ phase dependence. The guided waveguide mode has $e^{-i\beta z}$ spatial dependence. Then, for an efficient evanescent coupling of modes a phase matching condition of $m\varphi = \beta z$ should be met by waveguide and resonator fields. The κ also allows to rewrite the Q_{cpl} by [81]:

$$Q^{cpl} = \frac{\omega}{\kappa_{ext}} = \frac{\omega}{|\kappa|^2} \qquad \text{Eq. 1.59}$$

In order to tune the phase matching there are two ways, either by modifying the width of the waveguide or the gap between the waveguide and resonator.

1.3.3.3 Mode splitting by backscattering

Ideally, the rotational symmetry of a microdisk with no imperfections can support two degenerate modes resonating at a single frequency (ω) for each pair of (p, m) as represented by $a(t)$ in Figure 1.6. However, the fabrication process in practice leads to imperfections and thus the roughness formed will lift the cavity symmetry. A mode splitting (doublet) will then occur due to the modes propagating in clockwise (CW) and counter-clockwise (CCW) directions inside the microdisk with different resonance frequencies [86]–[92]. Their normalized field amplitudes are labeled by $a_{cw}(t)$ and $a_{ccw}(t)$ (see Figure 1.6). Using the same CMT formalism described in section 1.3.3, the normalized transmission for the doublets can be expressed as:

$$T_\Delta = \left| 1 + i\sqrt{\frac{\kappa_{ext}}{2}}\left(\frac{a_1}{s_{in}} - \frac{a_2}{s_{in}}\right)\right|^2 \qquad \text{Eq. 1.60}$$

where a_1 and a_2 are the stationary mode amplitudes of the doublet given by:

$$a_{1,2} = \frac{\pm i\sqrt{\frac{\kappa_{\text{ext}}}{2}}}{-i\left(\Delta \pm \frac{\kappa_\beta}{2}\right) + \left(\frac{\kappa_{\text{int}}}{2} + \frac{\kappa_{\text{ext}}}{2}\right)} s_{in} \qquad \text{Eq. 1.61}$$

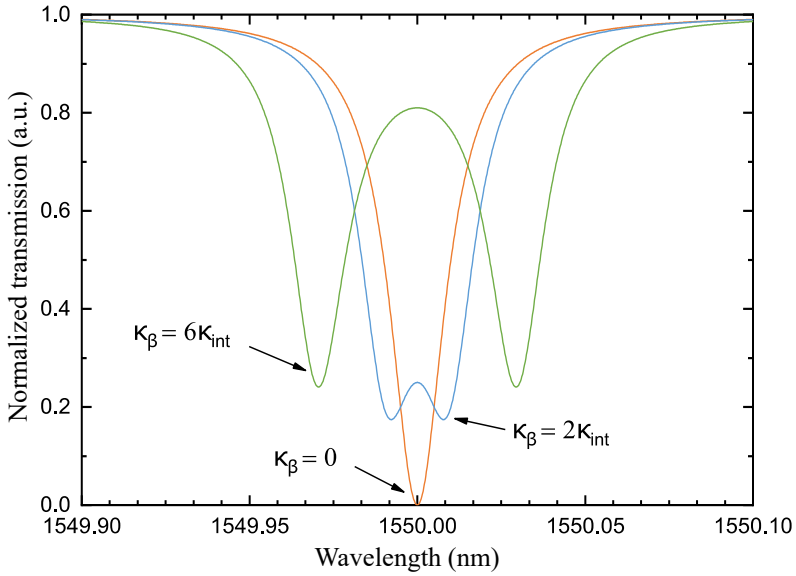

Figure 1.7: Normalized transmission spectra describing the evolution of doublet mode formation depending on the ratio $\kappa_\beta/\kappa_{int}$. Image (modified): Courtesy of Ref.[71].

The doublet response has a Lorentzian profile for each peak separated with frequencies $\omega - \kappa_\beta/2$ and $\omega + \kappa_\beta/2$, where κ_β is the term linked to the energy exchange between the counter propagating modes. Then a mode coupling optical quality factor Q_β can be defined:

$$Q_\beta = \frac{\omega}{\kappa_\beta} \qquad \text{Eq. 1.62}$$

The limiting cases are,

- $Q_\beta \ll Q_i$: The degeneracy is lifted and the transmission spectrum can resolve two largely separated peaks of the doublet mode formed.
- $Q_\beta \gg Q_i$: The degeneracy holds and no doublet splitting occurs due to the weaker coupling of counter propagating modes in comparison to the individual modes coupling with the surroundings.

Figure 1.7 shows the relative strength of κ_β and κ_{int} affecting a degenerated mode ($\kappa_\beta = 0$) in the critical coupling regime, $\kappa_{\text{ext}} = \kappa_{\text{int}}$. The doublet is observed when the ratio $\kappa_\beta/\kappa_{int}$ is greater than one, and the peak separation increases with this ratio.

1.4 Interests for monolithically integrated GaP/Si platform

The functionalities offered by photonic devices are not only determined by their geometrical design parameters but also by the properties of the chosen material for their construction. Silicon photonics technology can fabricate optical devices using Si material, thanks to the advancements in microelectronic processing technology. The III-V semiconductor materials are also proposed for fabricating optical devices intended for many specific applications such as a second order nonlinear frequency converter, where their non-centrosymmetry is a crucial advantage contrary to Si [57][58][33]. The binary III-V compound semiconductor GaP entered the photonics industry in the form of green light emitting diodes and lagged behind due to its indirect bandgap property [37]. Later, the GaP found back its track as a potential material for nanophotonic devices [23][14]. It has many merits as discussed in the following sections and can be monolithically integrated on a Si substrate to form an interesting platform GaP/Si for integrated photonics.

1.4.1 Indirect and wide bandgap

The GaP is an indirect bandgap compound semiconductor with a wide bandgap energy (E_{gap}) of $2.24\ eV$ at $300\ K$ as depicted in Figure 1.8. This limits its use as a light source unlike its competitors InP, GaAs and GaN. However, this shortcoming makes GaP a potential candidate for fabricating nonlinear devices by reducing photon absorption even at the edge of the bandgap ($554\ nm$). If we compare the $E_{gap} = 1.42\ eV$ of GaAs with the GaP, the two photon absorption

(TPA) in the case of a nonlinear frequency doubling process for a pump at $1.55\ \mu m$ ($0.8\ eV$ photon energy) is non-negligible for GaAs while merely impossible for GaP. In addition, the frequency doubled photons possessing $1.6\ eV$ energy get absorbed easily by GaAs in comparison to GaP.

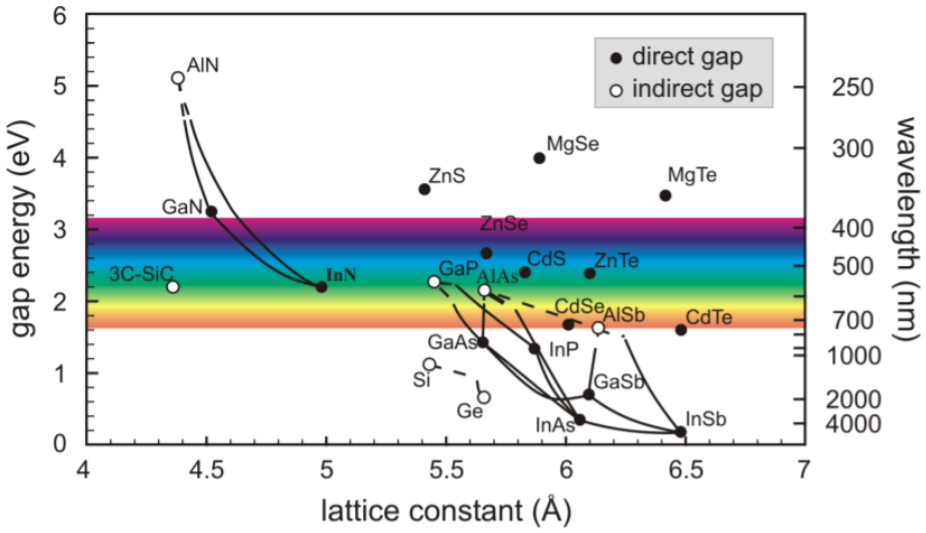

Figure 1.8: Direct and indirect bandgap energy (and corresponding wavelength) of different common semiconductor materials plotted as a function of their lattice constant.
Image: Courtesy of "III-V compound semiconductor material systems", http://web.tiscali.it/decartes/phd_html/node4.html

1.4.2 Natural $\bar{4}$-QPM in zinc-blende WGM resonators

The GaP semiconductor crystal has a zinc-blende type, a structure that is derived from the face centered cubic (FCC) unit cell consisting of two different atomic species. It is a non-centrosymmetric crystal lacking an inversion center. Most III-V semiconductors possess a blende structure, particularly interesting for the optoelectronic industry. To describe GaP, the FCC unit cell is formed by gallium (Ga) atoms and half of the tetrahedral interstitial sites (four of eight) are occupied by the phosphorus (P) atoms as shown in Figure 1.9(a). The space group of such a structure is called $F\bar{4}3m$ (in the Hermann–Mauguin notation). They hold $\bar{4}$-symmetry, which implies that after rotating the crystal around [001] axis by 90°, the atoms arrangements are the same as that obtained by a reflection through the plane (001) (see Figure 1.9). This material property can be effectively utilized as a natural phase matching technique where the nonlinear susceptibility experienced by photons can be naturally reversed in every quarter turn in a circular resonator, known as $\bar{4}$-QPM [39][40][93][33]. This is schematically presented for a microdisk in

Figure 1.10. The coherence length for $\bar{4}$-QPM in a microdisk of radius R can be defined as follows:

$$\ell_{coh} = \frac{2\pi R}{4} \qquad \text{Eq. 1.63}$$

The GaP possess a nonzero second order nonlinear optical susceptibility ($\chi^{(2)} \neq 0$) which controls its nonlinear behavior. The $\bar{4}$-symmetry of the zinc-blende group leads to a simplified expression for the $\chi^{(2)}$ tensor with three non-zero components as $d_{14} = d_{25} = d_{36}$ (see section 1.2.1 for a detailed description). In the case of SHG process in a microdisk based on natural $\bar{4}$-QPM, the polarization constraints require two TE polarized pump modes to generate a TM polarized SH mode as discussed under section 1.2.1. In cylindrical coordinates and considering the angular dependence of the nonlinear susceptibility, we can express the overlap between the pump and the SH WGMs as [94]:

$$K_{\pm} = \frac{\mp 1}{2\varepsilon_0 \omega_{\mathrm{SH}} n_p^4} \int_{-h/2}^{h/2} \tilde{Z}_{\mathrm{SH}} \tilde{Z}_p^2 \int_0^R \int_0^{2\pi} d_{14}(\mathrm{r}) \times e^{\mathrm{i}(\Delta m \pm 2)\varphi} r \tilde{\psi}_{\mathrm{SH}} \left(\frac{m_p}{r} \tilde{\psi}_p \pm \frac{\mathrm{d}\tilde{\psi}_p}{\mathrm{d}r} \right)^2 \mathrm{d}r\mathrm{d}\varphi\mathrm{d}z \qquad \text{Eq. 1.64}$$

where $\tilde{Z}(z)$ and $\tilde{\psi}(r)$ are the normalized dependence of the field along the disk axis and radius, respectively. The parameters ω_{SH} is the SH angular frequency, n_p is the refractive index for the pump mode, h is the thickness and R is the radius of the microdisk. The orbital momentum mismatch between the pump mode (m_p) and the SH mode (m_{SH}) is given by:

$$\Delta m = m_{\mathrm{SH}} - 2m_p \qquad \text{Eq. 1.65}$$

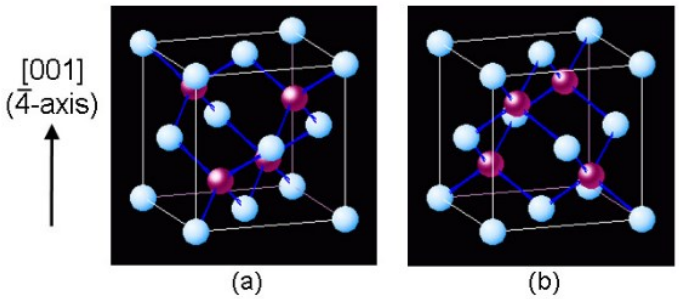

Figure 1.9: (a) Unit cell of zinc-blende structures such as GaP where pale blue is Ga atoms and dark purple is P atoms. (b) Obtained after rotating by 90° around $\bar{4}$-axis, which will be superimposable on a unit cell realized by (a) reflected through the plane (001). Image: Courtesy of Ref.[94].

Eq. 1.64 imposes phase matching rules in terms of the azimuthal numbers to achieve a non-zero SHG only if $\Delta m = \pm 2$. The $\Delta m = -2$ criterion is forbidden for the low value of p for pump and SH modes due to the chromatic dispersions of the TE and TM WGMs in a microdisk. Hence, only the $\Delta m = +2$ case can be achieved. However, the $\Delta m = -2$ is possible with high values of p both at pump and SH modes [39].

Recently, the physical origin of these additional quanta was unveiled in Ref.[40]. Using the transverse spin angular momentum (TSAM) formalism based on the fixed circular polarization (CP) frame, they demonstrated that these additional quanta appear due to the $\pm 2\pi$ Berry phase inherited by the transverse spin angular momentum components of the WGMs during their circulation within the resonator (see Figure 1.11) [40], [95]–[98]. Let's consider that E_+ and E_- are the spin-up and spin-down components of the TE modes electric field lying in the confinement plane of the microdisk. Assume that the TM modes have only a non-zero z component of the electric field (E_z) perpendicular to the microdisk plane, then only TE modes show TSAM behavior. Thus, the nonlinear polarization in the CP basis with contracted notation can be expressed as:

$$\begin{pmatrix} P_+ \\ P_- \\ P_z \end{pmatrix} = \varepsilon_0 d_{14} \begin{bmatrix} 0 & 0 & 0 & -i & 0 & 0 \\ 0 & 0 & 0 & 0 & i & 0 \\ i & -i & 0 & 0 & 0 & 0 \end{bmatrix} \begin{pmatrix} E_+E_+ \\ E_-E_- \\ E_zE_z \\ E_-E_z \\ E_+E_z \\ E_+E_- \end{pmatrix} \qquad \text{Eq. 1.66}$$

where the E_z SH field can be generated from the nonlinear polarization P_z driven by either E_+^2 or E_-^2. The E_+^2 and E_-^2combinations result in additional quanta of $+2$ ($\Delta m + 2 = 0$ and forbidden for $p = 1$ cases [39]) and -2 ($\Delta m - 2 = 0$), respectively. In addition, they directly lead to the evaluation of the integrals K_+

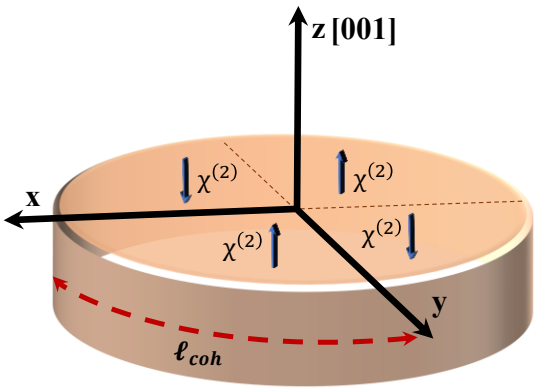

Figure 1.10: The natural periodic reversal of the nonlinear susceptibility tensor in a microdisk designed for $\bar{4}$-QPM.

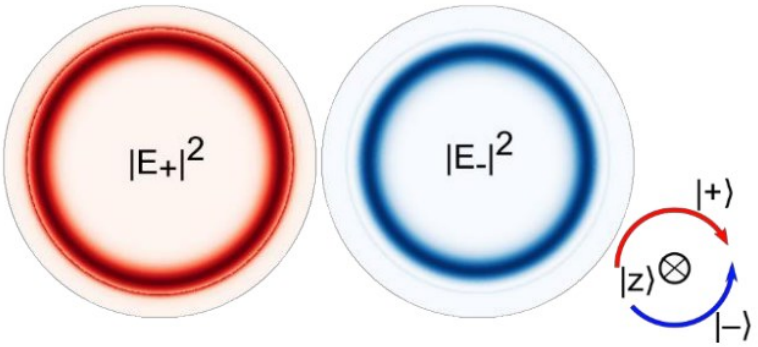

Figure 1.11: Squared magnitudes of the components $\boldsymbol{E_+}$ and $\boldsymbol{E_-}$ of a TE WGM in CP basis along the resonator axis obtained from FEM simulations. The unit vectors of the CP frame $|+\rangle$, $|-\rangle$ and $|\boldsymbol{z}\rangle$ correspond to spin-up polarization of photons, spin-down polarization of photons and spin 0 photons, respectively. Image: Courtesy of Ref.[40].

and K_- identified in Eq. 1.64. The demonstration of $\bar{4}$-QPM + modal phase matching based SHG in microdisks with an additional $+2$ quanta ($\Delta m = -2$) is reported in Ref.[33] and -2 quanta ($\Delta m = +2$) in Ref.[58].

Retuning to the cylindrical coordinate basis, the efficiency of the SHG in a microdisk offering $\bar{4}$-QPM can be expressed by taking into account the coupling of light using an access waveguide:

$$\eta = P_{\text{in}}|K_- + K_+|^2 \times \frac{\alpha_{\text{SH}}^2(1-|t_{\text{SH}}|^2)}{(1-\alpha_{\text{SH}}|t_{\text{SH}}|)^2} \times \left[\frac{\alpha_p^2\left(1-|t_p|^2\right)}{\left(1-\alpha_p|t_p|\right)^2}\right]^2 \qquad \text{Eq. 1.67}$$

where P_{in} is the pump power, $\alpha_{\text{p(SH)}}$ is the total scattering and radiation losses over a microdisk round trip for the pump (SH) mode, and $t_{p(SH)}$ is the transmission of the access waveguide for the pump (SH) mode. The parameters $\alpha_{\text{p(SH)}}$ and $t_{p(SH)}$ can be extracted from the intrinsic and the extrinsic Q-factors, respectively as follows [99]:

$$Q = \pi m \frac{\sqrt{y}}{1-y} \qquad \text{Eq. 1.68}$$

In Eq. 1.68, the parameter y is replaced with α for the Q_i and $|t|$ for the Q_{cpl}. The detailed mathematical treatment of Eq. 1.64 and Eq. 1.67 can be found in Ref.[94][61]. A computationally simple expression for the SHG efficiency can be obtained under the assumptions of critical coupling with large loaded Q-factors allowing us to consider $\alpha_{\text{p(SH)}}$ and $t_{p(SH)}$ close to one, then for a non-depleted pump approximation:

$$\eta \approx P_{in}|K|^2 \frac{Q_{SH}Q_p^2}{\pi^3 m_{SH} m_p^2} \qquad \text{Eq. 1.69}$$

where $Q_{p(SH)}$ stands for the loaded Q-factor of the pump (SH) mode. It is clear that for achieving high efficiencies, the interacting modes in the microdisk should possess lower azimuthal orders along with large Q-factors [61]. In addition, the efficiency also scales up with the strength of overlap between these modes and the power injected into the pump mode [39]. The conversion efficiency can be optimized by using microdisks that are doubly resonant for both pump and SH modes ($|\lambda_p - 2\lambda_{SH}| = 0$). In practice, the fabrication flaws that lead to the variation in the geometrical parameters and any modifications to the optical properties of the material can result in partially doubly resonant or singly resonant microdisks. Nonetheless, it is possible to tune the location of the resonant modes to convert a microdisk from singly to doubly resonant with enhanced efficiency [33][58][100].

1.4.3 Strength of GaP's second order nonlinear susceptibility

For GaP, the relevant non-zero element of the 2nd order nonlinear susceptibility tensor $d_{14} = 28.5\, pmV^{-1}$ at $1.55\, \mu m$ (C-band) [54], but for one of its commercial alternatives GaAs has a high value of $119\, pmV^{-1}$ around the same wavelength [101]. However, the former enables high power operation in all telecommunication bands, unlike the latter which is prone to TPA at infrared and visible wavelength regimes as discussed in section 1.4.1. We can also compare the values with another potential competitive nonlinear material $LiNbO_3$ which has a wide transmission window of $0.4\ \mu m$ to $5.5\ \mu m$ [102] where the $d_{33} = 19.5\, pmV^{-1}$ at a wavelength of $1.313\, \mu m$ (O-band) [101]. Then, the GaP with an operational spectral range of $0.57\, \mu m$ to $11\, \mu m$ [103] takes a larger value for $d_{14} = 36.8\, pmV^{-1}$ at the same wavelength [101]. For the wavelengths $1.064\ \mu m$ and $0.852\ \mu m$, the GaP can even achieve higher values for d_{14} with $70.6\, pmV^{-1}$ and $159\, pmV^{-1}$, respectively [101]. In this way along with many other properties [104], the GaP stands out as a material for emerging nonlinear photonics [14][34][105][68].

1.4.4 Refractive indices

The intensity dependent refractive index of materials N can be described by the relation:

$$N = n_0 + n_2 I \qquad \text{Eq. 1.70}$$

where n_0 is the linear refractive index, n_2 is the nonlinear refractive index and I denote the time averaged intensity of the optical field. The GaP has the largest linear refractive index ($n_0 > 3$) among visibly transparent III-V materials and also possesses a high nonlinear refractive index ($n_2 \sim 10^{-17} \mathrm{m^2 W^{-1}}$) [14]. Such high refractive index values for material not only offer strong optical confinement, a

favorable factor for the operation of integrated nonlinear devices but also enable large $\chi^{(3)}$ nonlinearity. The GaP dispersion curve is shown in Figure 1.12. The linear refractive index, bandgap energy at $300\,K$ and type of different semiconductors used in the nonlinear optics domain are listed in Table 1.

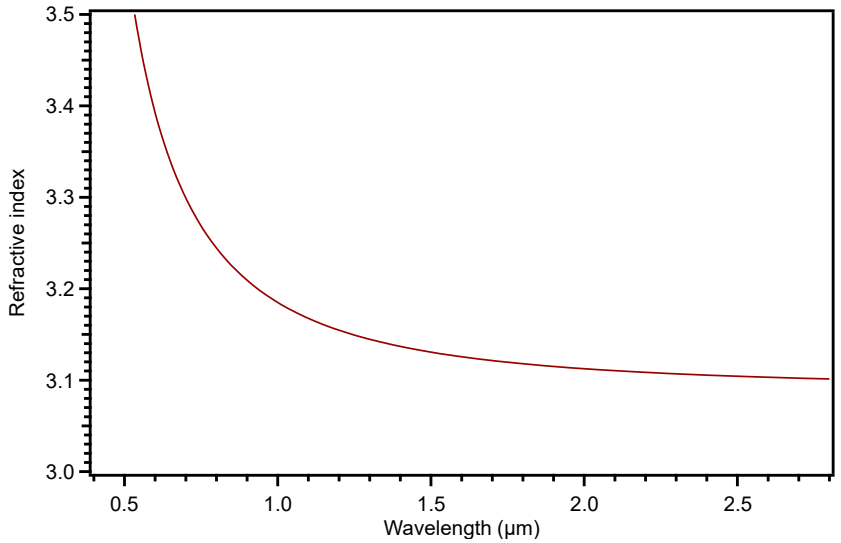

Figure 1.12: GaP linear refractive index versus wavelength.

Material	n_0	$E_{gap}\,(eV)$	Type
Si	3.482	1.11	Indirect
GaAs	3.383	1.42	Direct
InP	3.154	1.27	Direct
GaP	3.128	2.24	Indirect
GaN	2.317	3.4	Direct
$LiNbO_3$	2.211	3.77	Indirect
AlN	2.120	6.02	Direct

Table 1: Different nonlinear materials in integrated photonics and their properties. The refractive index values obtained at $1.55\,\mu m$ are based on Ref.[106] (Si), Ref.[107] (GaAs, InP, GaP), Ref.[108] (GaN), Ref.[109] ($LiNbO_3$), Ref.[110] (AlN). The bandgap energy values obtained at 300K are based on Ref.[111] (Si), Ref.[112] (GaAs), Ref.[111] (InP), Ref.[113] (GaP), Ref.[114] (GaN), Ref. [115] ($LiNbO_3$), Ref.[116] (AlN).

1.4.5 Lattice matching with Si

The heteroepitaxy consists of the epitaxial growth of a material different from the substrate such as fabricating integrated devices based on III-V semiconductors on a Si substrate. Directly growing III-V devices on Si by monolithic approach reduces the fabrication cost and time by avoiding expensive substrates and bonding along with large scale integration, unlike the hybrid method. An important concern in the growth process is a defect free high quality crystal interface that can affect the performance of devices made from it. One of the quantities under concern is the lattice parameter mismatch between the materials involved in epitaxy. If their lattice mismatch is large, then growth will be prone to defect formation and will extend along the interface and/or into the crystal volume in the form of dislocations. The lattice mismatch is quantified by [117]:

$$\Delta_{LM} = \frac{a_s - a_f}{a_s} \qquad \text{Eq. 1.71}$$

where a_s is the lattice constant of the substrate and a_f is the lattice constant of the semiconductor film deposited. Several direct bandgap materials among III-V semiconductors show a large lattice mismatch with Si $(5.43\ \text{A}°)$, a list of them is given in Table 2. Conversely, the indirect bandgap GaP has the least lattice mismatch at room temperature with Si among all binary III-V semiconductors, as can be seen in Figure 1.8 [41]. This makes GaP a suitable candidate for low defect and low cost pseudomorphic epitaxial growth on Si. In addition, good contrast in the chemical reactivity of GaP and Si can assist in their independent processing while fabricating integrated photonic circuits using lithography and etching techniques.

Material	Lattice constant (A°)	Mismatch Δ_{LM}(%)
GaSb	6.10(a)	12.24
AlN	4.98(c)	8.27
InP	5.87(a)	8.06
GaN	5.19(c)	4.53
GaAs	5.65(a)	4.09
GaP	5.45(a)	0.36

Table 2: III-V semiconductor materials and their lattice mismatch with Si. The lattice constant values (rounded figures) are obtained from Ref.[118].

The least lattice mismatch between GaP and Si at room temperature limits the formation of defects at the interface when the critical thickness of the GaP epilayer is below $90\,nm$ as reported in Ref.[119], between $45-95\,nm$ according to Ref.[120] and $64\,nm$ from the work of Ref.[121]. However, dislocations are not the only defects that can appear during the growth of III-V materials on Si. This is the case of APDs which are detailed in the next section 1.5. The OHM team of the Institut FOTON has developed unique know-how on the growth of GaP on Si and several research topics are effectively handled [34], [43], [48], [61], [95], [122]–[126].

1.5 Polar on non-polar epitaxy: Anti Phase Domains

The binary compound GaP is a polar material, which implies that each Ga atom is bounded to four P atoms. On the other hand, Si is a non-polar material which means each Si atom is bounded to the other four Si atoms. During the polar on non-polar epitaxy, crystal defects known as antiphase domains (APDs) can be formed within the GaP compound layer if there is a local inversion in the stacking order of the atomic planes [44][45][46]. From one APD to another, the Ga atomic planes will be opposite to P atomic planes and vice versa. These are regions where the lattice polarity is locally reversed and the junctions formed between adjacent antiphase domains are known as antiphase boundaries (APBs). The APDs/APBs formation can be attributed to different scenarios, such as a Si surface with mono atomic steps [49] (see Figure 1.13). A comprehensive state-of-the-art description of the APD formation in III-V/Si growth is provided in Ref.[43].

The APDs are thus growth defects featuring a random spatial distribution that can propagate along the growth axis throughout the epitaxial layer and affect the performance of devices carved out of such platforms. The potential of III-V materials on Si such as the GaP/Si platform enhanced the attraction of researchers towards this domain and they are trying to annihilate or tailor this defect in favor of them [43], [54], [69], [123], [127]–[131]. The main approaches towards APD-free growth for single phased III-V/Si platforms are listed below,

- Using different orientations of the substrate is proposed by Kroemer in 1987 where bi-step Si surfaces such as a Si(211) substrate can achieve APD free GaAs/Si layers [49].
- Using a vicinal Si substrate with a miscut of a few degrees towards the [110] direction where monolayer high steps on the surface of Si substrate are suppressed to generate even number layer high steps. A step doubling of off-oriented Si(001) occurs either through annealing [132] or misorienting towards the [110] direction by a few degrees [50]. This method can grow APD annihilated GaAs/Si [133], GaAs/Ge [134] and GaP/Si [135][136] layers. Researchers are also able to demonstrate APD

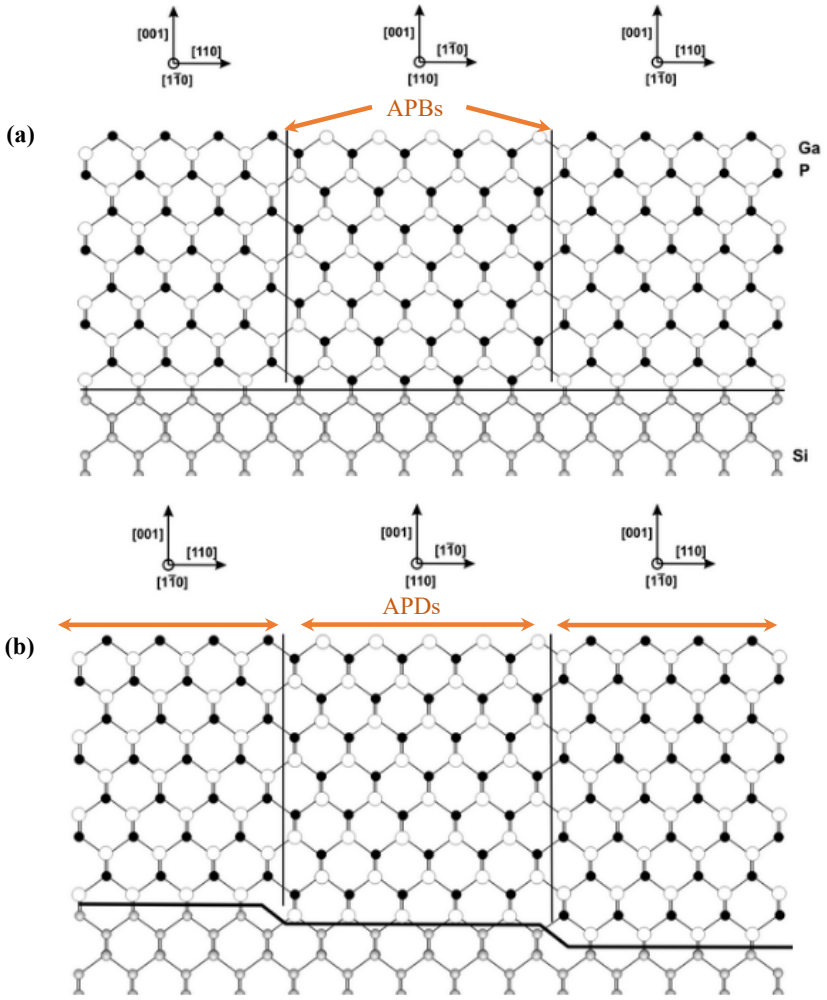

Figure 1.13: Antiphase domains in a GaP crystal formed by (a) non-uniformity of the first GaP atomic layer grown on Si substrate and (b) Si substrate surface with single atomic steps. Antiphase boundaries are lying on a {110} plane. Image (modified): Courtesy of Ref.[145].

free growth on exactly oriented Si(001) substrate [129]. However, the presence of single steps at the substrate surface itself cannot be the main reason for the APDs generation [123]. Recently, it has been reported by Cornet et al. [43] that the miscut impacts the initial antiphase domain distribution with "terraces-driven" and "nucleation-driven" for low miscut ($< 0.1°$) and large miscut ($> 1°$), respectively. This work also shows that the annihilation of APBs is the result of antiphase domains burying by the miscut induced growth rate imbalance between the two III-V crystal phases in III-V/IV epitaxy. According to their studies, for a given suitable growth temperature (high enough) the V/III ratio allows tuning the dominant phase at will as illustrated in Figure 1.14 for

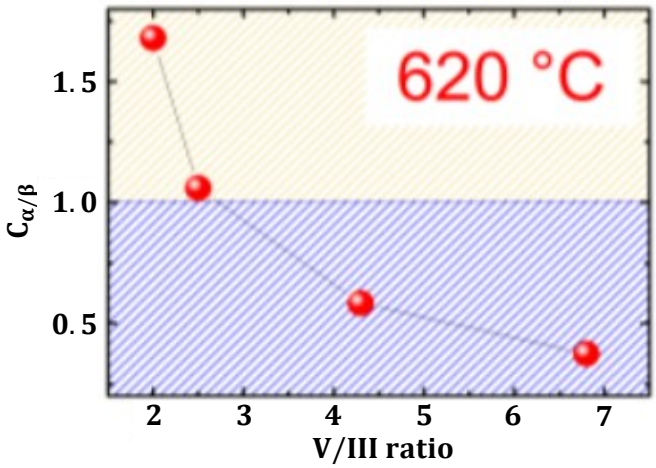

Figure 1.14: The variation of growth rate imbalance coefficient with V/III ratio for GaAs/Si at **620** ℃ where the dominant phase changes from $\boldsymbol{\alpha}$ (orange area) to $\boldsymbol{\beta}$ (blue area) by increasing the ratio. Image (modified): Courtesy of Ref.[43].

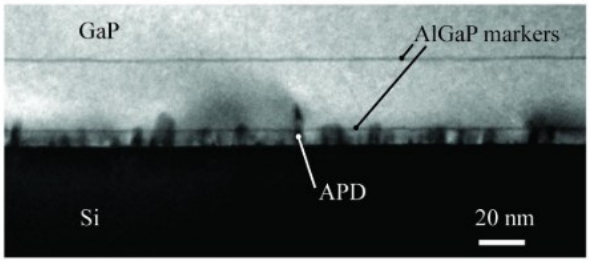

Figure 1.15: Cross-view transmission electron microscopy of GaP/Si platform with $Al_{0.2}GaP$ marker layers incorporated into the GaP epilayer. Image: Courtesy of Ref.[54].

GaAs/Si. Similar behavior is expected for other III-V semiconductors such as GaP/Si epitaxy. A growth rate imbalance coefficient ($C_{\alpha/\beta}$) can be defined as the ratio of the crystal growth rates of the phases α and β. The $C_{\alpha/\beta}$ is less than unity if the β phase grows faster than α, greater than unity if the α phase grows faster than β, and one if the growth rates are the same where APBs will propagate to the surface.

- Using $Al_{0.2}GaP$ marker layers where APDs can be suppressed just at $10\ nm$ from the GaP/Si interface [137][54][48] as shown in Figure 1.15.

The GaP microdisk samples used for experiments in this thesis are grown on a vicinal 6°-off Si (001) substrate to facilitate the tuning of the imbalance in the growth rates of APDs, thanks to the adjustment of growth temperature and V/III ratio. Also, $Al_{0.2}GaP$ layers are appropriately positioned in the first few nanometers of the growth to annihilate a large part of very small domains ($< 10\,nm$). These combined techniques will tailor the spatial distribution of APDs instead of their complete annihilation towards realizing relaxed random quasi phase matching assisted nonlinear frequency conversions. Further details on these topics are included in section 1.5.3 and chapter 3.

1.5.1 Characterization of APDs

To understand the characteristics of APDs spontaneously formed in a GaP/Si epilayer, some parameters of their distribution should be introduced. The two important quantities under concern are,

- Characteristic width (C_W) or equivalently correlation length ($\mathcal{L}_c$)
- Mean polarity ($P_{APD,mean}$)

The characteristic width corresponds to the mean distance between two adjacent APBs along the in-plane direction (perpendicular to the growth direction). In other words, it is linked to the mean APD size known as correlation length ($\mathcal{L}_c$). The mean polarity is defined as the spatial average of the local polarity distribution $P(r)$ (either $+1$ or -1) present in the GaP epilayer due to the formation of APDs at position r. There are several experimental techniques used to detect the presence and sizes of APDs including anisotropic etching [138], X-ray diffraction (XRD) [139], dark field transmission electron microscopy (TEM) [140], scanning electron microscopy (SEM) [141], atomic force microscopy (AFM) [142], reflectance anisotropy spectroscopy (RAS) [143][144], etc. The detection of APDs distribution

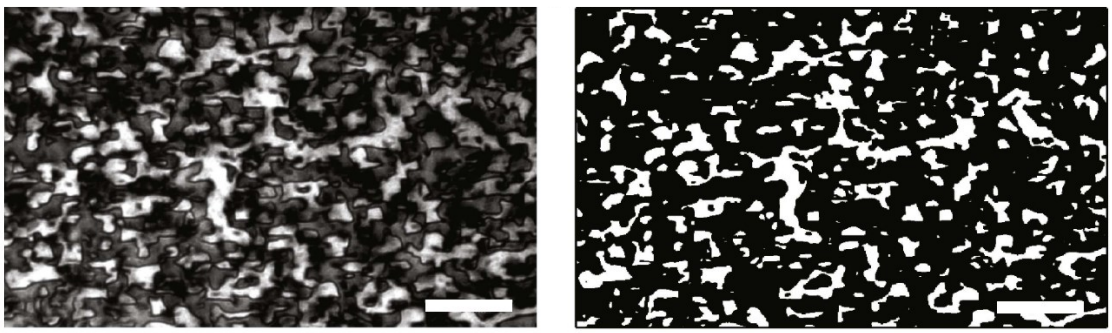

Figure 1.16: (a) The dark field TEM on the $g = (002)$ diffraction peak of a 20 nm thick GaP/Si sample grown by molecular beam epitaxy. (b) Binarized image after applying a threshold mask in (a). The scale bars are $50\,nm$ long. Image: Courtesy of Ref.[34].

in GaP/Si samples investigated in this thesis exploited a GaP etch solution combined with SEM surface observations where the morphology of the GaP surface will be closely related to APBs and through AFM studies where the trenches corresponding to APBs are visible as height contrast, see section 3.2 for further details.

In order to explain the numerical procedures for obtaining the APDs distribution parameters, let's consider a plan-view TEM micrograph in (002) dark field conditions in which the intensity strongly depends on local polarity inversions [145] (see Figure 1.16(a)). The bright and dark areas in this greyscale image are identified as the presence of APDs of opposite polarity. To clearly define the borders between APDs a threshold mask to the micrograph is applied to obtain a purely black and white image (Figure 1.16(b)). In this way, APDs of polarity $+1$ can be assigned to white areas and -1 for black areas. The spatial Fourier transform of this binarized image has an amplitude peak centered around the spatial frequency (f_s) equal to zero whose half width at half maximum (HWHM) from a Lorentzian fit is related to the mean APD size. The Fourier transform of $P(r)$ is given by:

$$F(P(r))(f_s) = \frac{1}{\pi}\frac{\frac{A}{2\pi C_W}}{f_s^2 + \left(\frac{1}{2\pi C_W}\right)^2} \qquad \text{Eq. 1.72}$$

with a $1/\pi C_W$ HWHM for the Lorentzian fit. If the autocorrelation of the binarized APDs image is modeled as a decreasing exponential profile in the form $A\exp(-|x|/\mathcal{L}_c)$, then the characteristic width is associated with the correlation length. The Fourier transform of this exponential function in the space of spatial frequencies is written as:

$$F_{\mathrm{AC}}(f_s) = \int_{-\infty}^{+\infty} A e^{-\frac{|x|}{\mathcal{L}_c}} e^{-i2\pi f_s x} dx = \frac{\frac{2A}{\mathcal{L}_c}}{\left(\frac{1}{\mathcal{L}_c}\right)^2 + (2\pi f_s)^2} \qquad \text{Eq. 1.73}$$

with a Lorentzian HWHM of $1/\pi\mathcal{L}_c$. According to the Wiener-Khinchin theorem, it is the same as the squared Fourier transform magnitude of the APDs image, thus the Fourier transform profile of the APDs takes the form:

$$F_{APD}(f_s) = \frac{B}{\sqrt{(2\pi f_s)^2 + \left(\frac{1}{\mathcal{L}_c}\right)^2}} \qquad \text{Eq. 1.74}$$

with a HWHM of $\sqrt{3}/\pi\mathcal{L}_c$ where B is a constant. Comparing the HWHM values of Eq. 1.72 and Eq. 1.74, we can express the correlation length in terms of characteristic width by:

$$\mathcal{L}_c = C_W \times \sqrt{3} \qquad \text{Eq. 1.75}$$

More details related to these calculations can be found in Ref.[61]. The spatial mean of the sample's polarity distribution can be deduced by averaging the ± 1 polarities of the contrast threshold-based image, $P_{APD,mean} = \langle P(r) \rangle$. For an entirely black image the $P_{APD,mean} = -1$, and for a completely white image $P_{APD,mean} = +1$. If an image contains the same number of white and black areas (the same number of domains are oriented in opposite directions) then the $P_{APD,mean} = 0$. So, a single-phase APDs free GaP epilayer expects $P_{APD,mean} = \pm 1$. The uncertainties for determining the mean polarity and the correlation length lie in the choice of thresholding. Once the APDs distribution is analyzed, it will be interesting to investigate their effect on the potential applications of the GaP/Si platform such as in nonlinear optics since the GaP polarity and thus the $\chi^{(2)}$ susceptibility is locally reversed.

1.5.2 Efficiency of frequency doubling in a microdisk with APDs

The APDs are expected to propagate through the epilayer towards the surface if no annihilation technique is applied [127], [146]–[148]. These defects will thus strongly interfere with the natural $\bar{4}$-symmetry of GaP crystal and disturb the $\bar{4}$-QPM for nonlinear frequency conversions such as SHG. The presence of APDs leads to the spatial evolution of the nonlinear susceptibility tensor component d_{14} as:

$$d_{14}(r) = d_{14} \times P(r) \qquad \text{Eq. 1.76}$$

Inserting Eq. 1.76 in Eq. 1.64, the overlap integral between the pump and the SH WGMs can be rewritten by additionally integrating over φ in cylindrical coordinates:

$$\begin{aligned} \widetilde{K}_{\pm} = \frac{\mp 1}{2\varepsilon_0 \omega_{\mathrm{SH}} n_p^4} \int_{-\frac{h}{2}}^{\frac{h}{2}} \tilde{Z}_{\mathrm{SH}} \tilde{Z}_p^2 \int_0^R \int_0^{2\pi} d_{14}(r,\varphi) \\ \times e^{\mathrm{i}(\Delta m \pm 2)\varphi} r \tilde{\psi}_{\mathrm{SH}} \left(\frac{m_p}{r} \tilde{\psi}_p \pm \frac{\mathrm{d}\tilde{\psi}_p}{\mathrm{d}r} \right)^2 \mathrm{d}r\mathrm{d}\varphi\mathrm{d}z \end{aligned} \qquad \text{Eq. 1.77}$$

Then, the SHG efficiency given by Eq. 1.67 will take the form:

$$\begin{aligned} \eta = P_{\mathrm{in}} \left| \widetilde{K}_- + \widetilde{K}_+ \right|^2 \times \frac{\alpha_{\mathrm{SH}}^2 (1 - |t_{\mathrm{SH}}|^2)}{(1 - \alpha_{\mathrm{SH}} |t_{\mathrm{SH}}|)^2} \\ \times \left[\frac{\alpha_p^2 \left(1 - |t_p|^2\right)}{\left(1 - \alpha_p |t_p|\right)^2} \right]^2 \end{aligned} \qquad \text{Eq. 1.78}$$

Let's consider that the APDs are controlled to occupy a thickness of h_{APD} within the microdisk thickness of h along the z-axis perpendicular to the microdisk plane. The overlap integral can then be modified to obtain:

$$\tilde{K}_{\pm} = \frac{\mp 1}{2\varepsilon_0 \omega_{\mathrm{SH}} n_p^4} \int_{-\frac{h}{2}}^{\frac{h}{2}} \tilde{Z}_{\mathrm{SH}} \tilde{Z}_p^2 \int_0^R \int_0^{2\pi} d_{14}(z, \mathrm{r}, \varphi) \times e^{\mathrm{i}(\Delta m \pm 2)\varphi} r \tilde{\psi}_{\mathrm{SH}} \left(\frac{m_p}{r} \tilde{\psi}_p \pm \frac{\mathrm{d}\tilde{\psi}_p}{\mathrm{d}r} \right)^2 \mathrm{d}r\mathrm{d}\varphi\mathrm{d}z \qquad \text{Eq. 1.79}$$

where the function $d_{14}(z, \mathrm{r}, \varphi)$ takes into account the inhomogeneities of the nonlinear susceptibility tensor component due to the APDs in the GaP layer thickness. It has been proposed that such APDs engineered GaP/Si microdisks could break the parity selection rules [54].

The evolution of SHG efficiency in GaP/Si microdisks according to the characteristic parameters of the APDs distribution is already reported theoretically by Guillemé et al. [34]. They modeled a doubly resonant strict $\bar{4}$-QPM configuration and numerically synthesized realistic APD distributions with $25\ \mu m^2$ areas from the real experimental TEM image containing APD distribution patterns ($\mathcal{L}_c = 10 \pm$

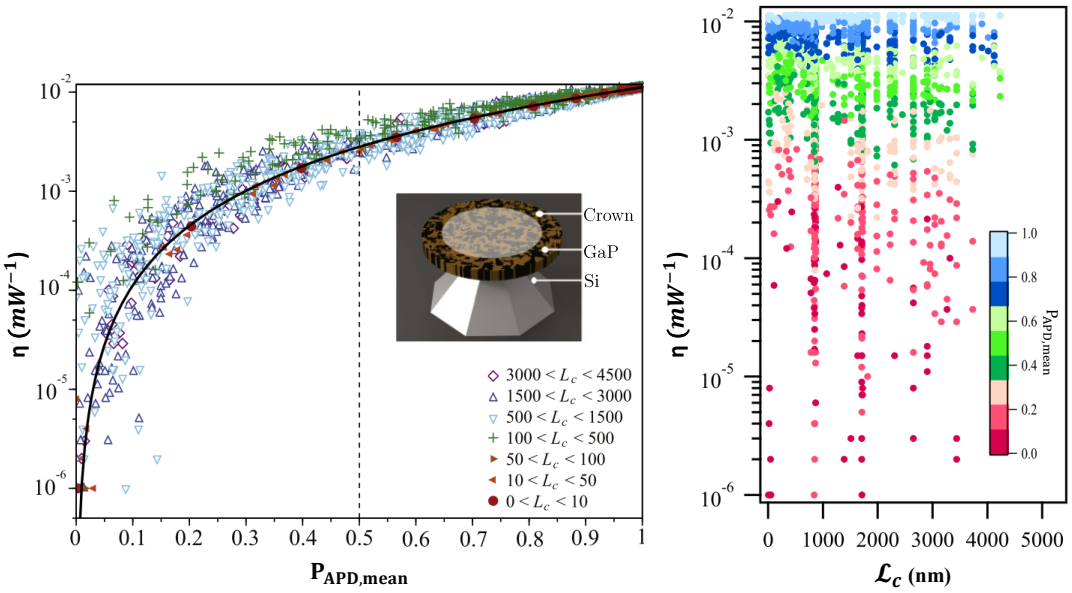

(a) (b)

Figure 1.17: Evolution of calculated SHG efficiency with parameters of artificial APD distributions. $\mathbf{P_{APD,mean}}$ is varied from **0** to **1**. The dashed vertical line corresponds to $\mathbf{P_{APD,mean}}$ of Figure 1.16 and the black solid curve is a parabolic fit that shows quadratic dependence of the conversion efficiency based on Eq. 1.77 and Eq. 1.78 (maximum value of $\mathbf{10^{-2}\ mW^{-1}}$ for strict $\bar{4}$-QPM). Inset: Sketch of a GaP/Si microdisk with APDs in the GaP layer. (b) $\boldsymbol{\mathcal{L}_c}$ is varied from **~10 nm** to **~4 µm**. In (a) and (b), the mean polarity is calculated only on the **20** % external crown (unshaded area of the inset). Images (modified): Courtesy of Ref.[34].

$2\,nm,\ P_{APD,mean} = 0.5 \pm 0.1\,nm)$. The $\mathcal{L}_c$ and $P_{APD,mean}$ of their artificial distributions are controlled by adjusting the HWHM of the Lorentzian and threshold mask of binarization, respectively. This investigation revealed that strict $\bar{4}$-QPM based SHG efficiency can drop two orders of magnitude when $P_{APD,mean}$ is varied from 1 (single phase GaP crystal without APDs) to 0.1 ($10\,\%$ imbalance between ± 1 APDs) as depicted in Figure 1.17(a). In addition, the finite size of the microdisk can affect the conversion efficiency through the sampling of the APD distribution depending on the values of $\mathcal{L}_c$ ($< 100\,nm$ shows the least standard deviation in comparison to the cases $> 1500\,nm$). Moreover, Figure 1.17(b) from their work concludes that there is no significant variation for the conversion efficiency while $\mathcal{L}_c$ is varied for a fixed $P_{APD,mean}$. These findings suggest at the first glance that the natural random distribution of APDs is detrimental to efficient strict $\bar{4}$-QPM based SHG in a GaP/Si platform. This is wrong: the nonlinear frequency conversion now appears out of the strict $\bar{4}$-QPM condition as detailed in the next section 1.5.3.

1.5.3 Random Quasi Phase Matching

In Eq. 1.77, expanding $d_{14}(r, \varphi)$ in the azimuthal Fourier series, the $\bar{4}$-QPM condition gets strongly modified by the presence of APDs. It should thus read as $\Delta m \pm 2 - M_{APD} = 0$ where specific spatial frequency components M_{APD} of $d_{14}(r)$

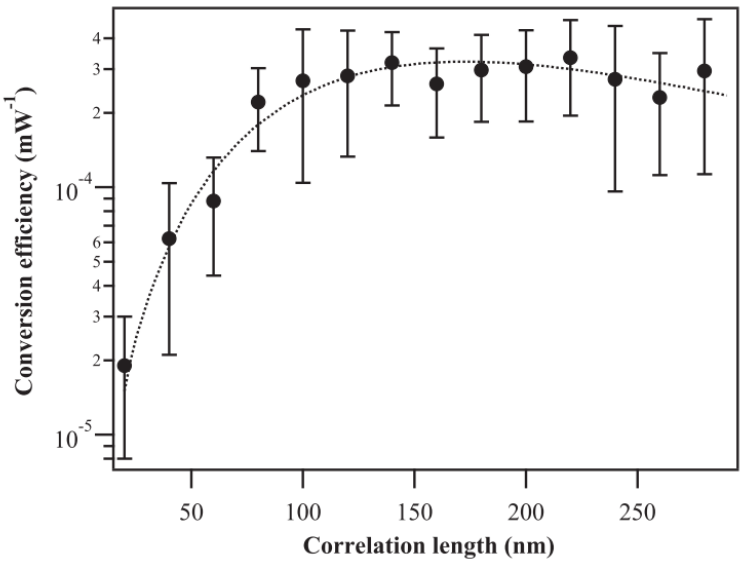

Figure 1.18: The dependence of calculated SHG conversion efficiency on $\mathcal{L}_c$ in a GaP/Si microdisk with radius $2.01\,\mu m$, thickness $178\,nm$ and $|\Delta m| = 8$. The error bars illustrate the standard deviation of efficiency for each class of $\mathcal{L}_c$ with $P_{APD,mean} = 0$. The dotted curve is a fit based on Eq. 1.77. Image: Courtesy of Ref.[34].

can compensate for any cases far from the reach of strict $\bar{4}$-QPM known as random quasi phase matching (RQPM) [69], as reported in the same theoretical work of Guillemé et al. mentioned in section 1.5.2. Figure 1.18 shows a build-up of the SHG conversion efficiency while $\mathcal{L}_c$ is varied in a GaP/Si microdisk for doubly resonant modes with $|\Delta m| = 8$. This indicates that the phase matching is assisted by randomly distributed APDs. This technique allows relaxed SHG phase matching in exchange for lower conversion efficiency just one to two orders of magnitude below the ideal $\bar{4}$-QPM (in the order of $10^{-5}\,mW^{-1}$ for $\mathcal{L}_c{\sim}50\,nm$ and $10^{-4}\,mW^{-1}$ in the best case where $\mathcal{L}_c{\sim}200\,nm$), see Figure 1.19(a). This process is not only competitive in efficiency but also it makes possible to find many experimental geometrical configurations (thickness and radius combinations) for SHG achieving RQPM in comparison to ideal $\bar{4}$-QPM. Reciprocally, a single geometry can lead to the demonstration of RQPM at different wavelengths using various Δm values (see Figure 1.19(b)). However, APD correlation length must be carefully tailored by specific growth strategies for optimized RQPM [131][129]. Thus, the GaP/Si platform is a suitable candidate for the realization of efficient broadband nonlinear photonic devices despite APDs.

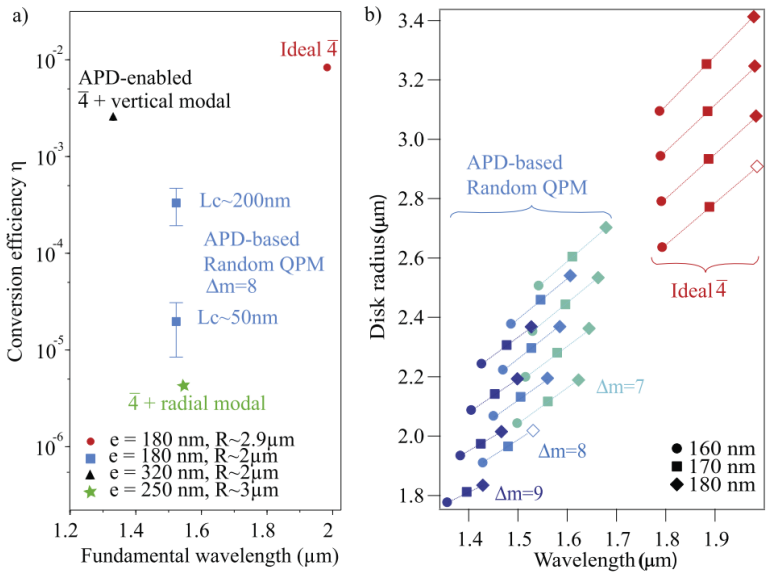

Figure 1.19: Comparison of RQPM with other QPM schemes. (a) Calculated SHG conversion efficiencies for 4 different QPM schemes such as ideal $\bar{4}$-QPM (red circle), APD assisted vertical modal QPM + $\bar{4}$-QPM (dark triangle) [54], RQPM (blue square) and radial modal QPM + $\bar{4}$ -QPM (green star) [58]. (b) Geometrical configurations available for microdisks with RQPM and ideal $\bar{4}$-QPM. Images (modified): Courtesy of Ref.[34].

1.6 Deeper insight on optical losses in GaP/Si microdisk

An optical resonator is always prone to losses from its design, material and fabrication parameters. The microresonator utilizes its long effective path length to achieve performance enhancements, hence understanding the loss mechanisms and their minimization is crucial. To classify these losses with a focus on our GaP/Si microdisks, there is first an inevitable radiation loss due to the curvature of microdisks (Q_{rad}). In addition, the roughness of the surface (Q_S) and the sidewalls (edge) (Q_R) formed during fabrication generates additional losses. Finally, losses due to the absorption in the GaP volume by tailored APBs (Q_{APD}) are also a concern. Thus, the general expression Eq. 1.43 for intrinsic quality factor can be expressed as:

$$\frac{1}{Q_i} = \frac{1}{Q_{rad}} + \frac{1}{Q_S} + \frac{1}{Q_R} + \frac{1}{Q_{APD}} \qquad \text{Eq. 1.80}$$

In the following sections, we will describe in detail the losses Q_{rad}, Q_R and Q_{APD}. They are the primary interest for this thesis and Q_S is made negligible with prolonged polishing of the GaP surface (detailed in Appendix A).

1.6.1 Curvature induced radiation losses

In the resonator cavity, the WGMs are inherently lossy due to the curvature. This loss can be attributed to the tunneling or coupling of the azimuthally guided mode into radiation modes known as radiation losses [149]. To parameterize and understand this loss in more detail, let's recall the dispersion relation for TE and TM modes in a microdisk (Eq. 1.34). As discussed under section 1.3.1, solving it for k gives complex eigen frequencies of WGMs whose imaginary part defines the continuous decay rate of energy confined within the resonator (Q_i). For a given value of m and refractive index ratio $n = n_1/n_2$ (in the case of our suspended microdisk, $n_1 = n_{eff}$ of GaP and $n_2 = n_{air}$), multiple radial mode solutions exist at discrete k values characterized by two parameters, the normalized radius $X = 2\pi r n_1/\lambda$ and Q_i. Now, rewriting the dispersion relation for TE and TM modes in normalized form yields:

$$\begin{aligned} n\frac{J'_m[AX]}{J_m[AX]} - \frac{H'^{(2)}_m[AX/n]}{H^{(2)}_m[AX/n]} &= 0 \qquad \text{TM modes} \\ \frac{J'_m[AX]}{J_m[AX]} - n\frac{H'^{(2)}_m[AX/n]}{H^{(2)}_m[AX/n]} &= 0 \qquad \text{TE modes} \end{aligned} \qquad \text{Eq. 1.81}$$

where $A = (1 - i/2Q_i)$. Solving for the complex roots of Eq. 1.81, generalized plots of the bending limited intrinsic Q-factor (Q_{rad}) as a function of X can be obtained, see Figure 1.20. The TE modes around $1.55\,\mu m$ in our $250\,nm$ thick GaP microdisks ($n_{eff} = 2.5$) with the smallest radius $\sim 2\,\mu m$ ($X \sim 20$) can even possess Q_{rad} larger than 10^6. However, for TM modes having $n_{eff} = 1.5$, even the largest

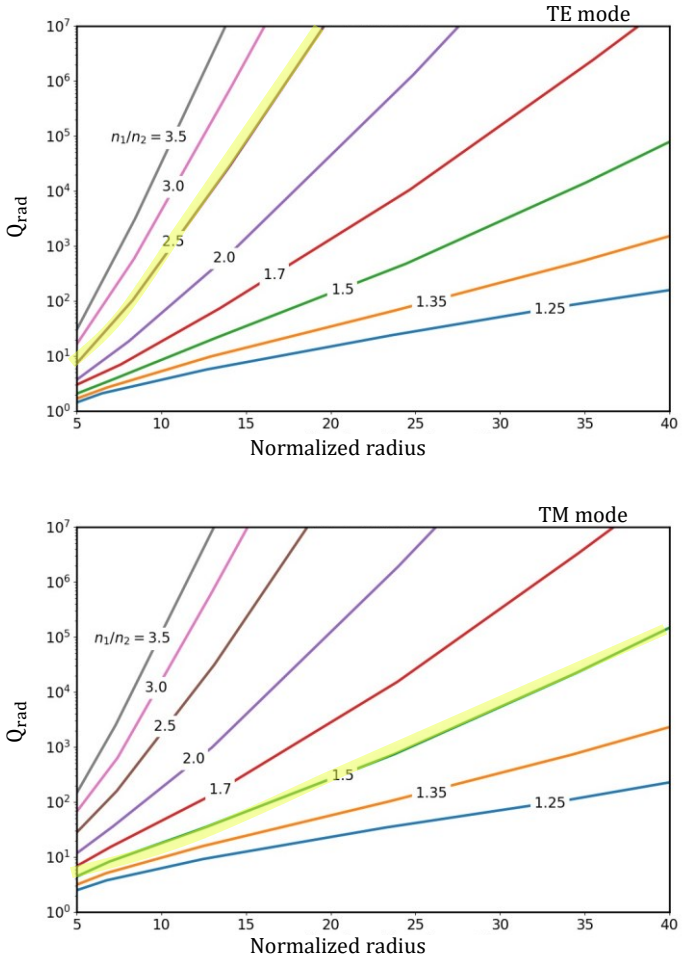

Figure 1.20: Bending limited intrinsic Q-factor of the lowest order radial TE and TM WGMs of a microdisk as a function of normalized radius and refractive index contrast (family of diagonal lines). The shaded diagonal curves (yellow) represent our samples. Image (modified): Courtesy of Ref.[95].

microdisks of radius ~3.5 μm (X~21) only lead to a maximum Q_{rad} in the range of 10^2 for the same wavelength. The bending loss increases as the index contrast is decreased. This effect is more severe on thin microdisks that have a small n_{eff}, reducing the refractive index contrast. The Q_{rad} drops due to the curvature when the radius of the microdisks is reduced. A higher refractive index contrast can combat the increase in bending induced losses while reducing radius. The better radial confinement of larger radii microdisks yields negligible bending induced losses. From another point of view, the bigger microdisks pull the WGMs away from the edge. Thus, by varying the size of microdisks, one can find a way to separate sidewall roughness induced losses (see section 1.6.2) from volume losses (refer section 1.6.3).

1.6.2 Roughness induced scattering losses

A common loss mechanism in microdisks is the scattering from the sidewall roughness due to the deviations from the ideal disk geometry resulting from the imperfect fabrication process. The microdisk resonators in the WGM regime are evaluated using the Volume Current Method (VCM) [150] to estimate the edge scattering losses. An analysis of microdisk roughness using this method is already reported in Ref.[91]. To explain the investigation performed in chapter 3, we will only refer to relevant expressions based on Ref.[151][152].

The dielectric perturbation on the microdisk edge introduces polarization currents induced by the confined field, contributing to outwardly scattered fields in analogy with microwave electronics. Calculating the surface parallel and surface perpendicular current contributions gives the current density in the presence of dielectric perturbation. Then, far field vector potential sourced by this current density can be obtained. Expressing the far field Poynting vector in terms of the vector potential allows for calculating the far field total scattered power and the corresponding attenuation factor. The microdisk modes are most affected by perturbations in the azimuthal direction in which the propagation vector dominates. In general, the etch process tends to produce uniform corrugations along the microdisk height (Z-direction) and it can be represented in a nearly one-dimensional way along the arc length (X_p), see Figure 1.21. Applying Gaussian statistics, the roughness can be characterized by two parameters, the RMS value

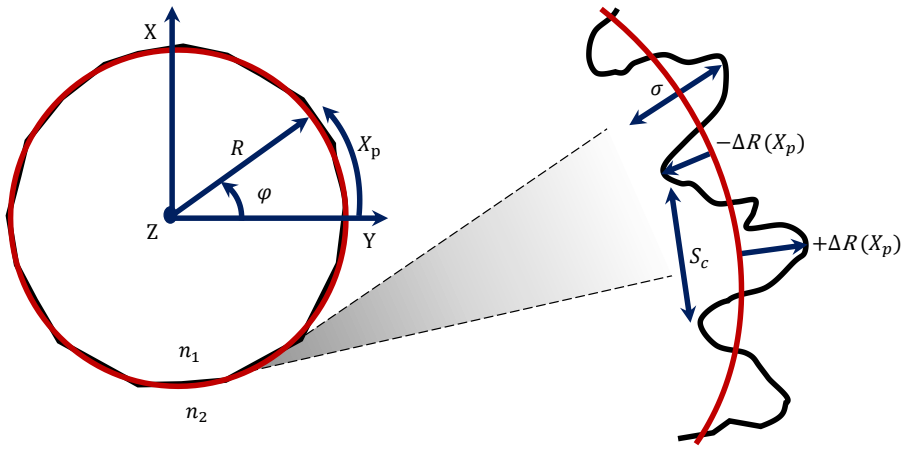

Figure 1.21: Schematic of the microdisk with edge roughness in cylindrical coordinates (top view). The red circle indicates the ideal circular curvature of the microdisk and the right-hand side displays a zoom on the corrugations. The symbols (R, φ, Z) denote the radius, angle and height of the microdisk, respectively. The radial variations at the border between the two dissimilar refractive indices n_1 and n_2 are labeled as $\pm\Delta R(X_p)$.

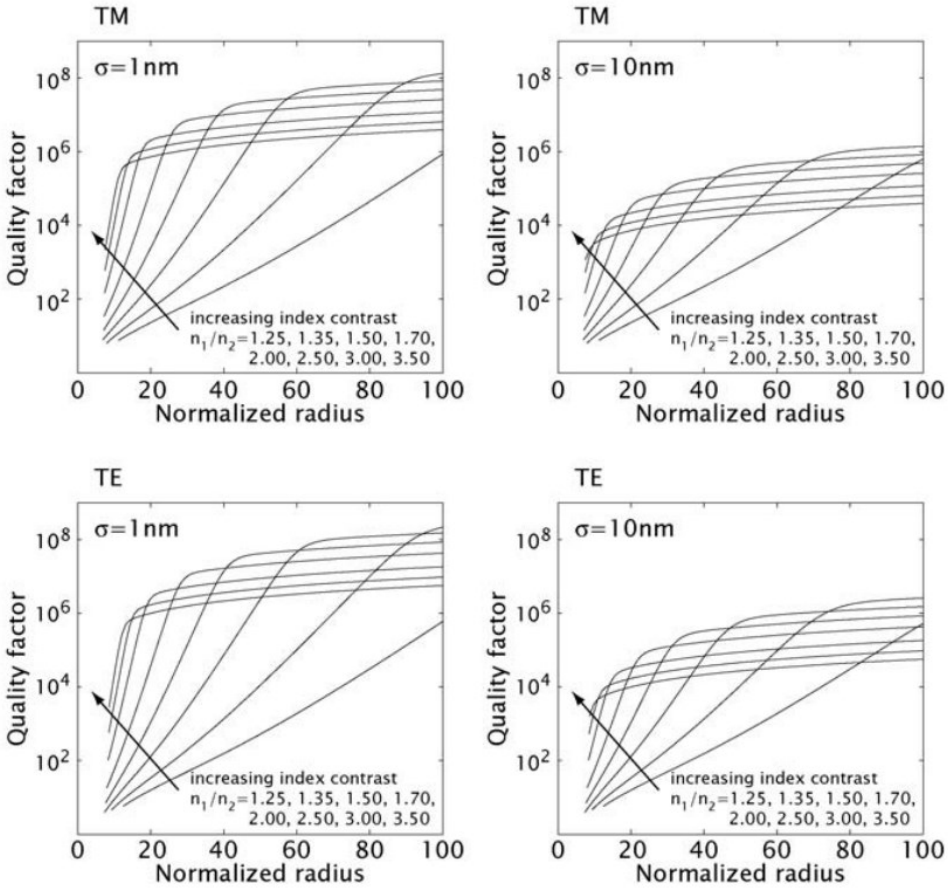

Figure 1.22: Evolution of Q-factor limited by Q_{rad} and Q_R for two different values of roughness and various refractive index ratio. The parameters are $\lambda = 1.55\ \mu m$, $d = 300\ nm$, $n_2 = 1$, $S_c = 75\ nm$. Image: Courtesy of Ref.[152].

(σ) and its correlation length (S_c) [153]. Then, the Gaussian correlation function for etching induced roughness is given by:

$$C(X_p) = \sigma^2 e^{-\pi\left(\frac{X_p}{S_c}\right)^2} \qquad \text{Eq. 1.82}$$

where $C(0) = \sigma^2$ and S_c is within a factor of $\sqrt{\pi/4\ln 2} = 1.064$ of a FWHM definition. From the definition of the Q-factor (see section 1.3.2.1), we can model the loss contribution along the resonator circumference (L) in the form of $exp(-\alpha L)$. Then, the associated Q-factor which is independent of radius can be written [152]:

$$Q_R = \frac{n_{eff.grp} k}{\alpha_R} \qquad \text{Eq. 1.83}$$

where α_R is the optical loss induced attenuation factor. Using Eq. 1.83, a working expression for the quality factor associated with edge scattering can be derived for thin microdisks with a thickness (d) less than the wavelength (λ) as [152]:

$$Q_R^{TE/TM} = \frac{1}{\frac{16\pi^3}{3m}\left(1-\frac{1}{n^2}\right)^2 \xi^2 \ell_c \Gamma_z \delta} \qquad \text{Eq. 1.84}$$

where the parameters are defined as normalized roughness $\xi = n_1\sigma/\lambda$, normalized correlation length $\ell_c = n_1 S_c/\lambda$, Γ_z is the vertical confinement factor defined by the ratio of power vertically confined to the total power guided, normalized thickness $\delta = d/\lambda$ and m is the azimuthal number. Analyzing Eq. 1.84 show that the Q_R is independent of radius and polarization in the thin microdisk regime. The competition between bending loss and edge scattering loss is shown in Figure 1.22. Maintaining a higher Q_{rad} value while decreasing the radius is possible by increasing the refractive index contrast as we described in section 1.6.1 (see Figure 1.20). For larger radii, the Q_{rad} is insignificant and Q_R dominates, leading to the Q-factor becoming independent of radius. Thus, there is a trade-off between Q_{rad} and Q_R while designing practical microdisk devices as reported in Ref.[151].

1.6.3 Interfacial defects induced volume losses

Finally, we are concerned about volume losses due to optical absorptions in the GaP layer. As mentioned in section 1.5.1, the GaP/Si platform is prone to interfacial defects such as APBs, which should be annihilated or controlled to make it useful for practical applications. The stacking faults and microtwins are other structural defects that can appear when growing a III-V material onto Si [154]. In our research team, we developed a growth procedure limiting the occurrence of such defects to less than **2 %** in volume (checked by pole figures as reported in Ref.[137]). In comparison, from the distribution of APBs in our sample and the limitation of their lateral influence to the charge localization [51] we can estimate the density of APBs to be more than **10 %** of the volume. Contrary to APBs, it has not been

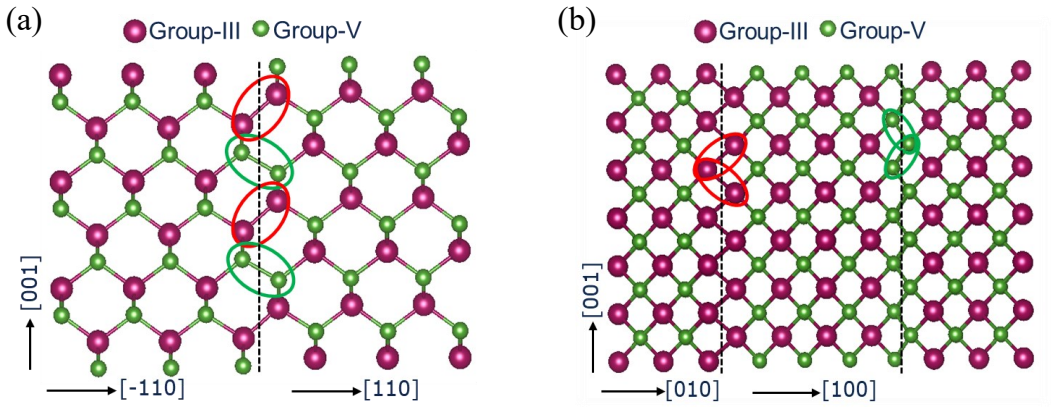

Figure 1.23: Schematic of (a) St-APBs and (b) NSt-APBs atomic configuration.

reported any study on the influence of microtwins and stacking faults on optical absorption. Therefore, we neglected any additional contributions to the volumic optical losses and considered only the loss induced by APBs for the work presented in this thesis.

In the heteroepitaxy of III-V/Si, different compositions of APBs can appear. Stoichiometric APBs (St-APBs) have the same amount of III-III bonds and V-V bonds, while non-stoichiometric APBs (NSt-APBs) have different amounts of III-III bonds and V-V bonds. In extreme cases, NSt-APBs can feature only III-III or V-V bonds. This is schematically illustrated in Figure 1.23. It has been theoretically reported by Tea et al. [51] that APBs lead to bandgap reduction based on a pure St-APBs model for GaP/Si growth. Recently, Chen et al. [47] calculations show there is no bandgap reduction for pure III-III and V-V NSt-APBs in the GaP/Si sample. Instead, they result in a constant density of states within the whole bandgap. Hence, APBs absorption induced volume losses will be impacted by the APBs compositions present in the sample. As for roughness losses, the APDs induced Q-factor can be linked with an attenuation factor α_{APD}:

$$Q_{APD} = \frac{n_{eff.grp} k}{\alpha_{APD}} \qquad \text{Eq. 1.85}$$

The experimental assessment of APBs induced losses in the volume of the GaP layer is presented in chapter 3 in detail.

Summary

In nonlinear optics, an efficient SHG requires the interacting waves to obey the energy and momentum conservations along with the polarization selection rules. The efficiency of frequency doubling gets enhanced by using materials with large nonlinear susceptibility, long interaction length and high pump intensity. The micron scaled structures like microdisks can confine light by TIR to form WGMs. They possess characteristics like large loaded Q-factor and small mode volume to demonstrate the nonlinear frequency mixing at the chip level. The GaP microdisks grown on Si possess interesting qualities. The GaP has an indirect wide bandgap which prevents TPA at the telecom band and offers high power operation for nonlinear photonics. The competitive 2nd order nonlinear susceptibility, material symmetry ($\bar{4}$-QPM) and large refractive index offered by the GaP complement its performance as a nonlinear device. Moreover, the least lattice mismatch with Si favors the photonic integration of GaP based devices onto a chip. Defects called APDs formed during epitaxy, if tailored, can be used to relax the phase matching condition. This phase matching called random QPM in GaP/Si microdisks has competitive efficiency in comparison to the natural symmetry offered $\bar{4}$-QPM. The Q-factor of the GaP/Si microdisks can be impacted by many loss contributions

such as the inherent bending related radiation losses, fabrication roughness induced scattering losses and the emerging APBs generated volume losses.

2 Instrumentation for optical characterization of microdisks

Introduction

This chapter is dedicated to describing the main experimental components of the thesis. In the first part, we discuss the optical modes propagating in a standard single mode fiber in order to understand their evolution while fabricating a taper with minimal loss and maximum evanescent field. Later, a detailed procedure for the fabrication of dimpled fiber taper, an on-chip testing probe is included with its performance optimization. Thereafter, we will illustrate the experimental setup and characterization of microdisks at different wavelength regimes, short-wave infrared (SWIR) and near-infrared (NIR) corresponding to $1.4 - 3\ \mu m$ and $0.75 - 1.4\ \mu m$, respectively. This will help us to investigate the losses in the random crystal polarity engineered GaP/Si photonic platform as described in chapter 3 and a prerequisite for frequency doubling experiments in GaP based microdisks as demonstrated in chapter 4. A detailed description of the theory included in this chapter can be found in Ref.[61], [155]–[158].

2.1 Evanescent field coupling techniques

An important element in the characterization of a microresonator is the method by which the light is injected and extracted from the cavity. There are many coupling methods developed out of which commonly used couplers are prisms [159][160], angle polished fibers [161] and tapered optical fibers [162]. All these methods are utilizing the energy transfer between a WGM cavity and coupler guided modes evanescent fields as illustrated by schematics in Figure 2.1. After the first demonstration of adiabatically tapered fibers, they are the most widely used devices for coupling due to their significant advantages over other techniques [163][164][165][33][58][166]. They possess high efficiency, versatility, and maneuverability over other methods. In addition, they occupy less on-chip space and reduce the noise of the signal carried in the fundamental mode by filtering

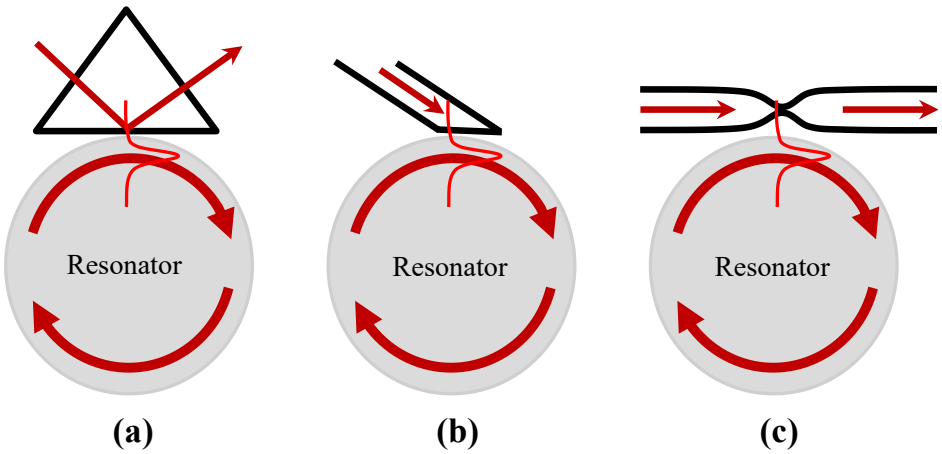

Figure 2.1: Different coupling methods for energy exchange between a WGM cavity and an evanescent field tail from (a) prism coupler, (b) angled polished fiber and (c) straight tapered fiber.

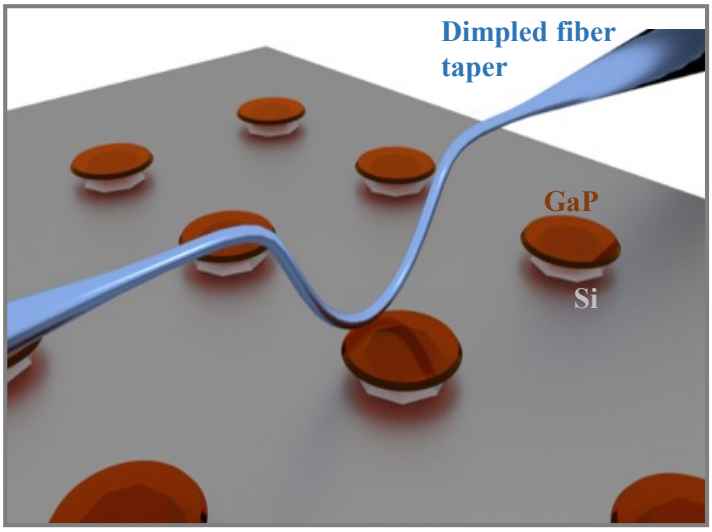

Figure 2.2: A 3D illustration of a dimpled fiber taper selectively coupled to an on-chip GaP/Si microdisk.

higher order leaky modes. Practically, straight fiber tapers are cheap, easy to fabricate and well suited for coupling to a stand-alone off-chip device [162].

Drastic improvements in state-of-the-art nanofabrication technologies are now able to fabricate small size, delicate nanostructures on-chip. They require a reliable testing probe of comparable size. The straight fiber tapers are not good as a wafer-scale probe for micron-scale photonic components due to their macroscopic arms extending from the tapered region. It can lead to unnecessary coupling to the

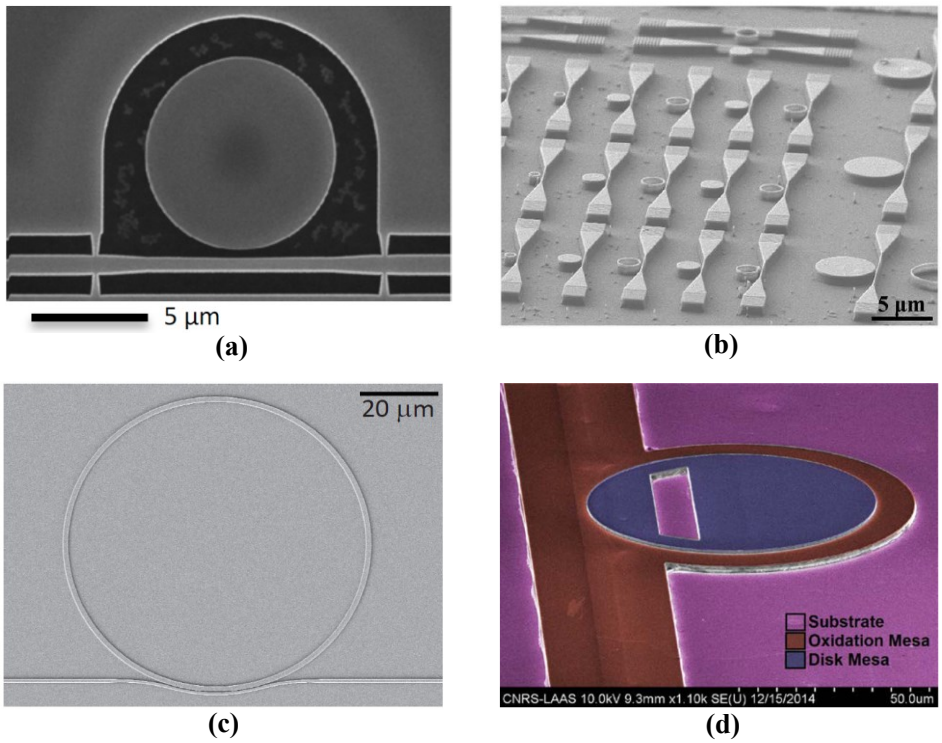

Figure 2.3: SEM images of integrated coupler-microresonator systems. (a) An $8\ \mu m$ diameter nitride microdisk with a suspended side-coupled bus waveguide. (b) GaP waveguide-integrated ring/disk resonators with out-of-plane grating couplers on the etched diamond substrate. (c) An $80\ \mu m$ diameter Si_3N_4microring resonator with a pulley waveguide. (d) A $75\ \mu m$ diameter GaAs microdisk vertically coupled to a buried oxide access waveguide. Images: Courtesy of Ref.[22], Ref.[23], Ref.[24] and Ref.[25], respectively.

substrate and accidental damage to the structures. However, an on-chip coupling can be managed if the devices are elevated above the chip surface or the sample itself is cleaved in bars [167][168]. In our case, employing the latter method requires complex manipulations during fabrication such as thinning the substrate and cleaving it into strips with only one raw of the microdisk. Different types of curved fiber tapers are now developed for coupling tightly spaced in-plane resonators [169][170]. In a recent technique, such a fiber taper is realized by introducing a small "depression" region into the thinnest part of a straight fiber taper, known as a dimpled fiber taper. They can be effectively utilized to study any individual resonator without affecting others [171][172], see Figure 2.2. It possesses all the advantages of a straight taper. Even after fabrication, the tension in the dimpled

fiber taper can be mechanically increased to modify the amplitude of the depression region in order to limit fluctuations in the taper-microdisk gap. This will reduce the broadband noise to a level comparable to its straight taper counterparts [171]. It's a simple, cheap, nondestructive local probe for the optical characterization of devices at the wafer scale. However, despite the advantages possessed by dimpled fiber tapers as a testing probe for densely packed microcavities, they are not suitable for on-chip integration. Integrated optical links have also progressively emerged in parallel as dedicated on-chip testing structures with evanescent field coupling towards the realization of PICs [173][174]. A few of the recently developed integrated coupling schemes include side-coupled suspended bus waveguides [22], waveguide-grating structures [23], pulley waveguides [24] and vertically coupled buried access waveguides [25] as shown in Figure 2.3.

2.1.1 Dynamics of fiber taper modes

To better understand the fabrication of a fiber taper, it is worth mentioning the evolution of modes propagating through a standard step-index optical fiber [175]. This will help us later to describe the guiding of light in a tapered optical fiber, the strength of the evanescent field present at its waist region for coupling with a microresonator and energy exchange between different fiber taper modes that could lead to losses. A tapered step-index fiber implies that the core is negligible and the light is guided by the cladding-air interface in the thinnest region. Considering the cladding-air interface as the core-cladding of a cylindrical step-index fiber, the former can be treated in an analogy [176]. Thus, solving the Helmholtz equation for the electromagnetic field distribution of the guided modes according to the boundary conditions given by Maxwells equations at the core-cladding interface results in a well-known expression (complete solution can be found in Ref.[155][77]):

$$\left[\frac{J'_m(T)}{TJ_m(T)}+\frac{K'_m(S)}{SK_m(S)}\right]\left[\frac{J'_m(T)}{TJ_m(T)}+\frac{1}{n_{co}}\frac{K'_m(S)}{SK_m(S)}\right]=\left(\frac{m\beta}{kn_{co}}\right)^2\left(\frac{V}{TS}\right)^4 \qquad \text{Eq. 2.1}$$

with parameters $T=(\mathrm{d}/2)(k^2{n_{co}}^2-\beta^2)^{1/2}$, $S=(\mathrm{d}/2)(\beta^2-{n_{cl}}^2k^2)^{1/2}$ and $V=(2\pi/\lambda)(\mathrm{d}/2)({n_{co}}^2-{n_{cl}}^2)^{1/2}$. The J_m and K_m are the Bessel function and the modified Bessel function respectively with primes for the function derivatives, m is the mode number (non-negative integer), $d/2$ is the fiber core radius, β is the propagation constant of the existing modes, k is the propagation constant in vacuum, n_{co} and n_{cl} are the refractive indices of core and cladding respectively, λ is the wavelength of light propagating through the fiber and V is the normalized frequency (or V-number) which is a dimensionless quantity that determines the number of modes a fiber can support. The eigenvalue equation (Eq. 2.1) for β (characteristic equation of any mode in an optical fiber) can be solved for each value of m which yields a set of discrete propagation constants for the guided modes propagating in an optical fiber at a fixed diameter and excitation wavelength.

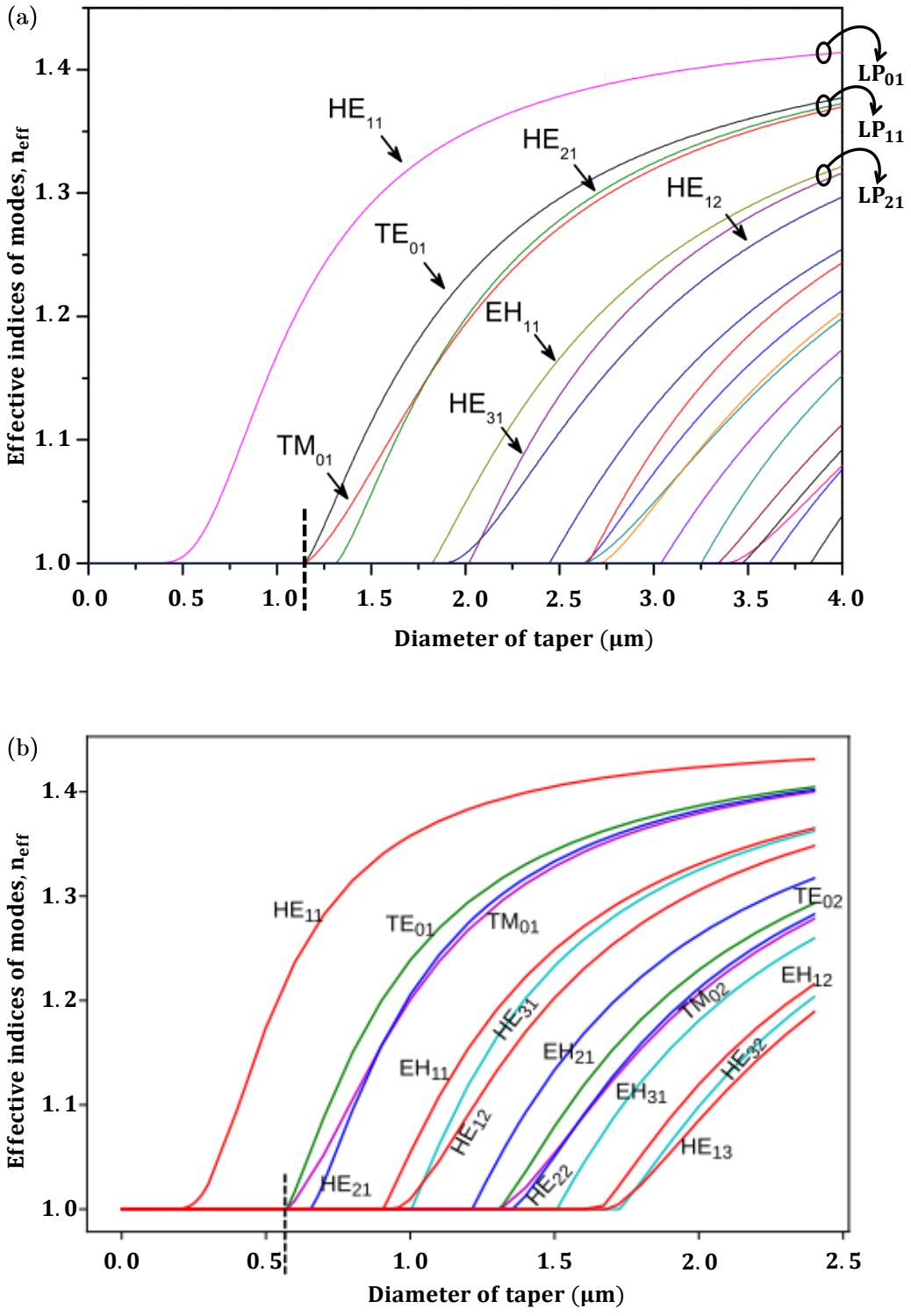

Figure 2.4: The propagation of modes in an optical fiber. (a) Tapering at a wavelength of 1.55µm. Image (modified): Courtesy of Ref.[156]. (b) Tapering at a wavelength of 0.78 µm. Image (modified): Courtesy of Ref.[166]. The cut-off diameters are also marked by a black dashed line.

Depending on the values of m, these modes are categorized as transverse electric/magnetic (TE_{0j}/TM_{0j}) for $m = 0$ and hybrid (HE_{mj}/EH_{mj}) for $m > 0$, where j is a positive integer. The HE_{11} is the fundamental mode [155] and a step-index fiber always supports this mode despite its physical diameter. These general solutions are valid for both scenarios, a weakly guiding step-index fiber ($n_{co} - n_{cl} \ll 1$) and a strongly guiding fiber taper waist ($n_{co} \approx n_{cl}$). However, the number of solutions gets reduced to half in the weakly guiding regime, because the β values of hybrid modes ($HE_{m+1,j}$ and $EH_{m-1,j}$) have degenerated in this approximation. This leads to the superposition of hybrid modes to linearly polarized modes (LP_{mj}) like HE_{11} becomes LP_{01} [177].

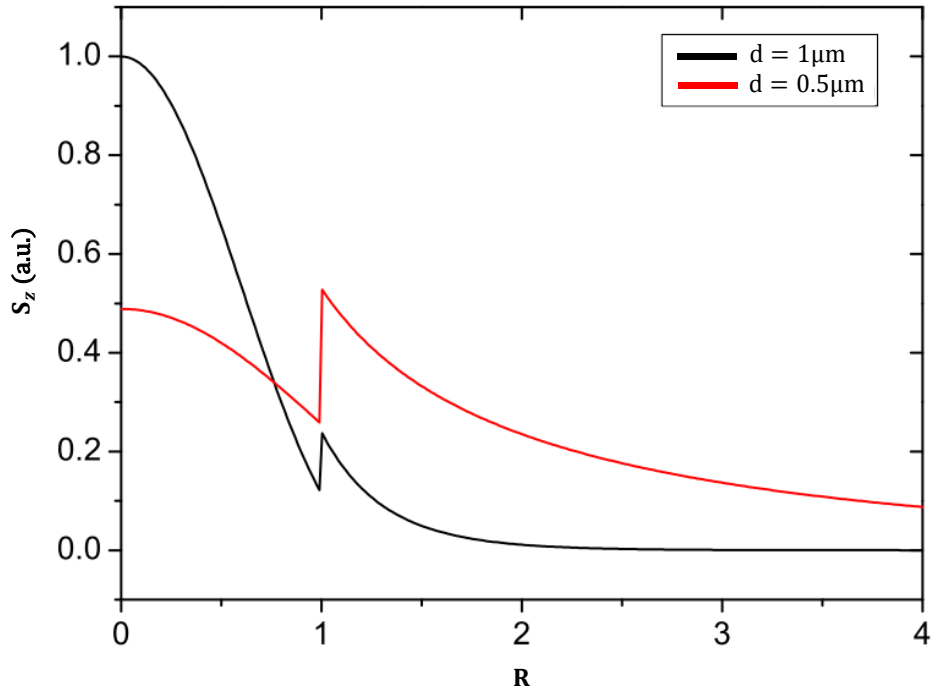

Figure 2.5: Amplitude variation for the Poynting vector of HE_{11} mode versus R for two different fiber taper diameters. Image (modified): Courtesy of Ref.[156].

Once the values of β are found numerically, then the effective refractive index of modes (normalized propagation constant) can be defined as $n_{eff} = \beta/k$. In the case of a tapered optical fiber, it is relevant to analyze the existence of modes as a function of its diameter while tapering for different wavelengths of interest. Every single mode optical fiber waveguide should possess a V-number $< V_0 = 2.405$. Thus from the definition of normalized frequency, for a value of V_0 in a standard step-index fiber, an analytic expression for a single mode cut-off diameter (d_c) can be derived in the weakly guiding approximation [72]:

$$d_c = \frac{2.405\lambda}{\pi\sqrt{n_{co}^2 - n_{cl}^2}} \qquad \text{Eq. 2.2}$$

Numerically solving Eq. 2.2 for a propagating wavelength of $\lambda = 1.55\ \mu m$ through a silica optical fiber having $n_{co} = 1.45$ and $n_{cl} = 1$ can result in a $d_c < 1.145\ \mu m$ as illustrated in Figure 2.4(a). The parameter d_c indicates that only the lowest order hybrid mode HE_{11} can survive below this critical diameter (see section 2.2.1 for a detailed numerical evaluation of d_c). In other words, the taper becomes a multimode above d_c and the number of existing modes will start to vary as $\sim V^2$. In addition, if the waist diameter is large, the light is mostly confined inside the fiber with $n_{eff} \sim n_{co}$. Once waist diameter decreases, the n_{eff} approaches n_{cl} and the evanescent field increases in the air cladding. The d_c also varies with the wavelengths of light propagating through the fiber. For comparison, it's worth noticing that the d_c will become almost half ($\sim 0.570\ \mu m$) for the same refractive index parameters at a wavelength of propagation $\lambda = 0.78\ \mu m$ as presented in the Figure 2.4(b). The expression for d_c given in Eq. 2.2 is also useful as the end of tapering criterion which comes in handy while fabricating the taper (see section 2.2.1). For our experiments, we have fabricated such thin fiber tapers supporting only HE_{11} mode with negligible losses to simplify the optical characterization of microdisks.

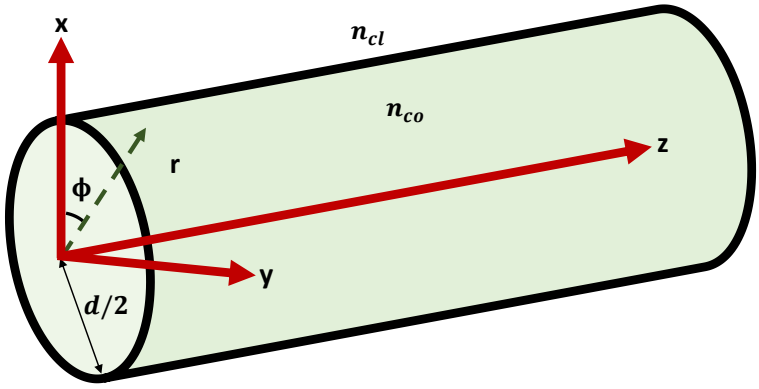

Figure 2.6: Schematic of the fiber taper section in cylindrical coordinates (r,ϕ,z). The light is propagated along the z-direction.

After identifying the fiber taper modes, we are now interested in analyzing the evanescent field available for coupling to a microresonator and then quantifying it. From the electromagnetic profile of HE_{11} mode (see Ref.[155] for the mathematical solution), the evolution of the Poynting vector component corresponds to the HE_{11} energy flow along the fiber taper axis (S_z) can be illustrated as a function of the radial dimension R (see Figure 2.5). The parameter R is defined as the ratio of the radial position r with respect to the core radius $d/2$, thus $R = 1$ at the core-

cladding interface (see Figure 2.6). It is clear that when the fiber taper diameter is appropriately reduced, a large evanescent field tail can be made available at the cladding region [178][179]. To quantify the evanescent field, the fraction of power available at the fiber taper exterior can be obtained from the expression:

$$\eta_{exterior} = 1 - \left(\frac{\int_{-\pi}^{\pi} \int_{d/2}^{+\infty} rS_z d\phi dr}{\int_{-\pi}^{\pi} \int_{0}^{+\infty} rS_z d\phi dr} \right) \qquad \text{Eq. 2.3}$$

The variation of $\eta_{exterior}$ according to the fiber taper diameter is shown in Figure 2.7. A fiber taper carrying a wavelength of $1.55\ \mu m$ has only $20\ \%$ of its field available as evanescent up to $d_c \sim 1\ \mu m$. Thereafter, further reducing the diameter can lead to a sharp increase in the evanescent field. However, in practice, care must be taken to have an optimal evanescent field without breaking the fiber taper during fabrication.

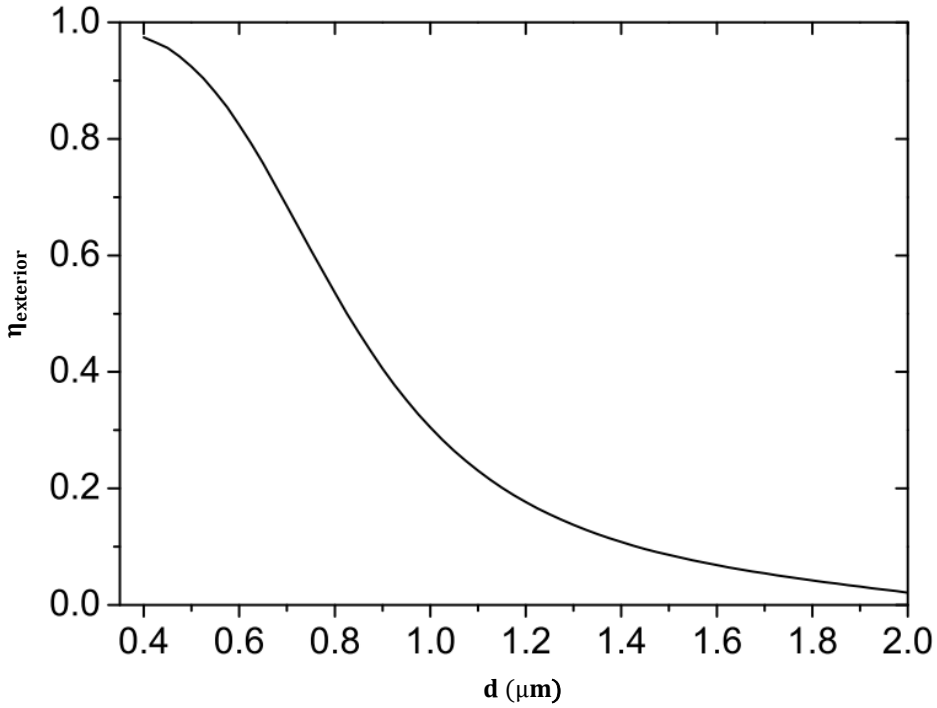

Figure 2.7: Fraction of power in the form of an evanescent field present at the exterior of the fiber taper while varying the diameter. Image (modified): Courtesy of Ref.[156].

2.1.2 Adiabatic fiber taper profiling

Once fabricated, a fiber taper has three regions: an undisturbed part with the original diameter (d_0), a transition section where the diameter decreases/increases to form a slope and the waist where the diameter is thinnest ($n_{cl} = 1$) as shown in

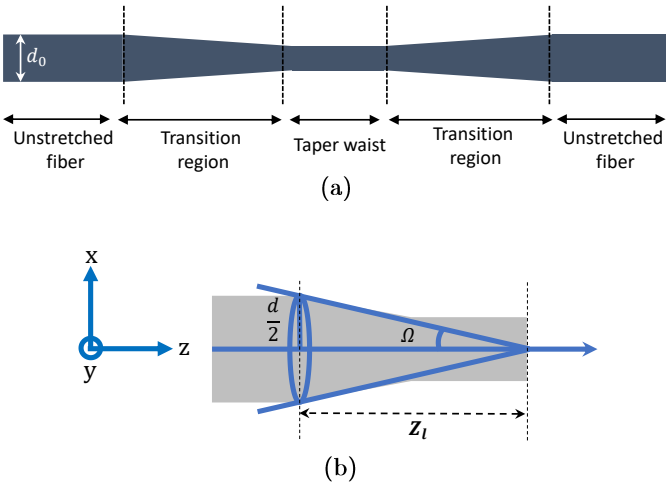

Figure 2.8: Schematic of (a) different regions in a fiber taper and (b) fiber taper transition region labeled with fiber taper angle. The local fiber taper length scale Z_l and local fiber taper angle $\Omega(z)$ can be considered as the height and apex angle of a right circular cone with the base matching the cross-section of the fiber taper core with the local radius $d/2(z)$. The $Z_l \approx d/2(z)/\Omega(z)$ for $\Omega(z) \ll 1$, where z is the distance along the fiber taper.

Figure 2.8(a). The desired scenario is that only HE_{11} (LP_{01}) mode carries the major power through the fiber taper. This will prevent higher order fiber taper modes from getting undesirably coupled to resonator modes leading to noise in the signal. A smooth fiber taper transition profile is the key parameter for achieving this state and the fiber taper must be fabricated as adiabatic (obeying the slowness criterion) [155][180]. To define this criterion, a fiber taper angle ($\Omega(z)$) can be expressed as (see Figure 2.8(b)):

$$\Omega(z) = \frac{d}{2}(z) \times \frac{(\beta_1(z) - \beta_2(z))}{2\pi} \qquad \text{Eq. 2.4}$$

where $\beta_1(z)$ and $\beta_2(z)$ are the propagation constants of fundamental and dominant local coupling modes in the fiber taper, $(d/2)(z)$ is the fiber taper core radius. A fiber taper becomes adiabatic if the fiber taper angle is made small enough everywhere (less than the right side of Eq. 2.4) so that the fundamental mode HE_{11} (LP_{01}) has negligible power loss while propagating through the fiber taper length. The axial symmetry of the fiber taper restricts the fundamental mode to couple only with the higher order modes of the same azimuthal symmetry (HE_{1j} (LP_{0j}) modes), such as predominantly to the HE_{12} (LP_{02}) mode. If the fiber taper transition is not smooth or steep (non-adiabatic case), then the taper angle will change abruptly. This will result in a power transfer from the fundamental mode to other closer higher order modes with different azimuthal symmetries (LP_{11}). Thus, the fiber taper experiences higher loss. In a nutshell, Eq. 2.4 mandates that

the fiber taper angle should be kept sufficiently small while reducing the fiber taper core radius by ensuring a gradual transition region in order to obtain a lossless adiabatic fiber taper. In practice, the fiber tapers adiabatic profiling can be disturbed due to fabrication imperfections or bent and adequate care during fabrication is necessary.

2.2 Dimpled fiber tapers for coupling on-chip devices

In our research activities, we are interested in WGMs possessing large Q-factors ($\geq 10^4$) for nonlinear frequency conversion processes like SHG. Since they have a very weak radiative part which makes the coupling of light into the WGM micro-resonators and its detection hardly possible in free space. To characterize disks with μm/nm dimensions, it is practically easier to make an optical link between the resonator and the optical setup using tapered fibers due to the merits they possess. In a good configuration, they can transfer the total incoming power to the micro-resonator mode [99]. In addition, by controlling the gap between the optical waveguide and resonator the coupling efficiencies can be adjusted [181][165]. In the case of closely packed nanostructures in a planar geometry, using a straight tapered optical fiber for coupling to a particular one without disturbing all others will be an extremely challenging task. This is the case with us, where each sample contains 880 microdisks arranged in 88×10 matrix format. Microdisks are separated by $500\ \mu m$ along the row and $50\ \mu m$ along the column. Along with a nano precise positioning system we have thus chosen to use dimpled fiber tapers throughout the thesis for direct coupling to our microdisks at the lowest point of the dimpled region.

The whole process of fabricating a dimpled fiber taper consists of two main stages. First one for the fabrication of a straight fiber taper and then in the next step creating a “dimple” (curvature) in the thinnest part of the straight fiber taper. A detailed procedure is given in the following sections.

2.2.1 Fabrication of straight fiber tapers

A commercially available single mode fiber (Corning SMF-28e) is utilized to fabricate a taper. It can be done either through hydrofluoric acid etching [182][183] or heat-and-pull method [184]–[187]. In our laboratory, the latter method is followed for fabrication. The schematic of this inbuilt fiber taper fabrication setup is shown in Figure 2.9 and a photograph is in Figure 2.13(a). Initially, the fiber coating is stripped in a small portion typically $5\ cm$ long which will later go into the flame after cleaning with ethanol. Now, both arms of this stripped length are held by fiber holders fixed into motorized translational stages (Thorlabs MTS50/M-Z8, $50\ mm$ travel range) with their motion precisely controlled by a servo (apt-dc, Thorlabs)-computer combo system. A $1\ mW$ of power from a tunable laser (Tunics plus, Photonetics) at a wavelength of $1550\ nm$ is transmitted through the fiber. The

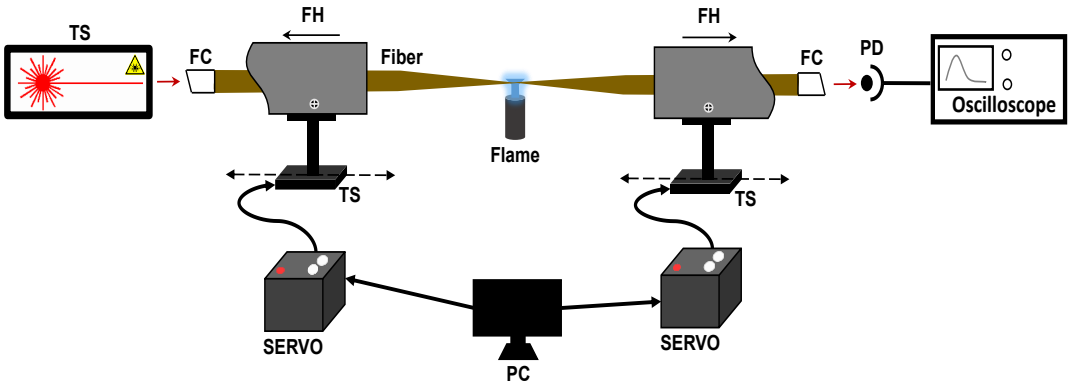

Figure 2.9: Schematic of the straight tapered optical fiber fabrication setup.
TS: Tunable laser source, FH: Fiber holder, TS: Translational stage, PC: Computer control, PD: Photodetector, FC: Fiber connector.

output end of this fiber is connected to a photodiode (New Focus MODEL 2053) which is plugged into an oscilloscope (Tektronix TDS2024B) for monitoring the fiber transmission. The stripped portion is then heated by a butane torch (DREMEL VERSAFLAME) with a flame of diameter $5\,mm$ (known as hot-zone [188]) at $1200\,°C$ [189]. The temperature is ideal because the fiber becomes ductile at $1100\,°C$ and can melt at $1700\,°C$. In the initial stages of pulling, the tapering is controlled by keeping a lower speed of $0.3\,mm/s$ for the translational stages moving in opposite directions. This will keep the transmission from dropping abruptly. After a few seconds $(\sim 20\,s)$, the speed is increased to $1\,mm/s$ to prevent distortion of the tapering part by the blow from the flame. As the tapering progresses the fiber transmission changes to oscillations due to interference between various modes propagating inside the fiber [189] (see section 2.1.1 for details). Once the taper reaches d_c the oscillation changes back into a stable transmission, as shown by the taper transmission profile for $1550\,nm$ in Figure 2.10. Thus, the oscillations are handy to determine when the pulling must be stopped. The pulling is then quickly stopped and the flame is immediately removed. This last step should be done simultaneously to avoid any further heating or pulling. Otherwise, it may lead to the breaking of the fiber taper and/or a major loss ($> 50\,\%$) in transmission. In the latter case, it will not be good enough to undergo the next stage of processing for a dimpled fiber taper, a more delicate structure. This experimental setup is capable of fabricating straight fiber tapers with $80 - 95\,\%$ transmission.

In practice, the oscillations in the oscilloscope due to mode beating indicate that energy is exchanged between the fundamental fiber mode and higher order modes. This observation is in contradiction with the adiabatic criterion, an ideal case that should be ensured while pulling (see section 2.1.2). However, there can be other distortions that break this condition. In our case, the turbulence in the flame

due to a short burst in the gas flow can slightly bend the fiber to distort its cylindrical symmetry. This will lead to energy transfer even though the slope of the tapered region is smooth. Stray air currents in the fiber taper fabrication environment should be also blocked. We have prevented it with a box encapsulating the fabrication setup. To overcome the stability issues of flame, a ceramic micro-heater can be employed [186]. This will improve the reproducibility of the fiber taper fabrication. A hydrogen-oxygen torch with a comparably cleaner flame than a butane torch can be used in the current system for obtaining a taper with a better transmission [190].

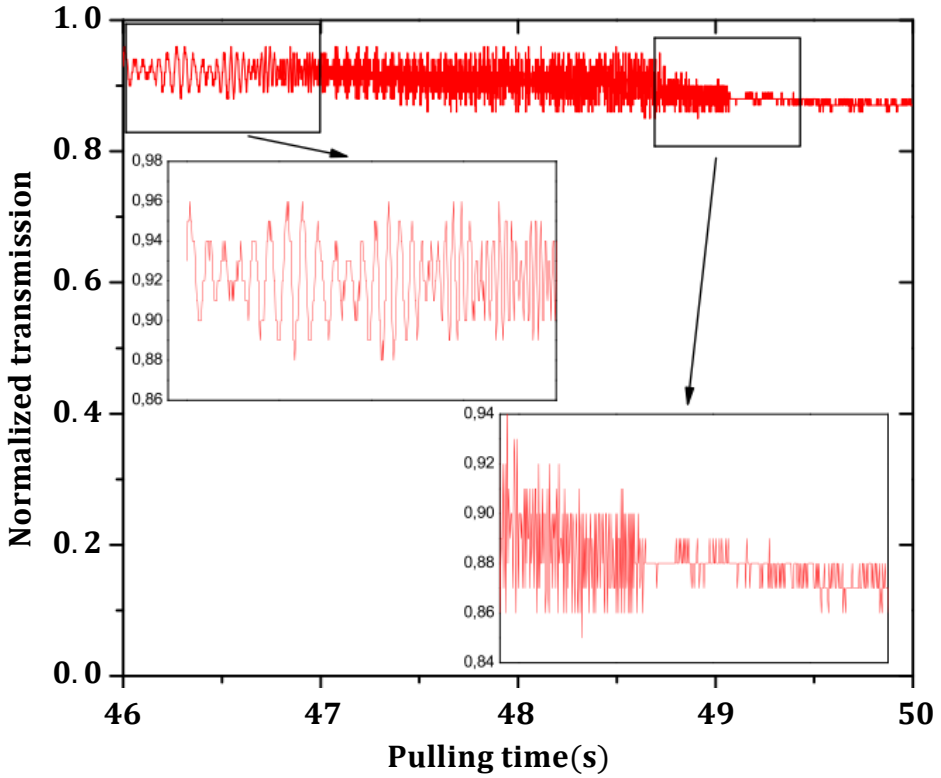

Figure 2.10: Normalized transmission profile of a fiber taper during pulling. Left inset: zoom on the beating pattern generated due to the interaction of multimodes. Right inset: zoom on the beating oscillations when the taper changes from multimode to single mode around 49 *s*. Image (modified): Courtesy of Ref.[156].

One can choose to fabricate a fiber taper for the desired wavelength of interest by sending that wavelength through the fiber and tapering it. The exponential decrease in the unstretched fiber diameter d_0 placed in a hot-zone length of L (stationary flame) for pulling over a time t with a constant speed of pulling v according to the conservation of mass is given by [188][189]:

$$d = d_0 e^{-\frac{vt}{L}} \qquad \text{Eq. 2.5}$$

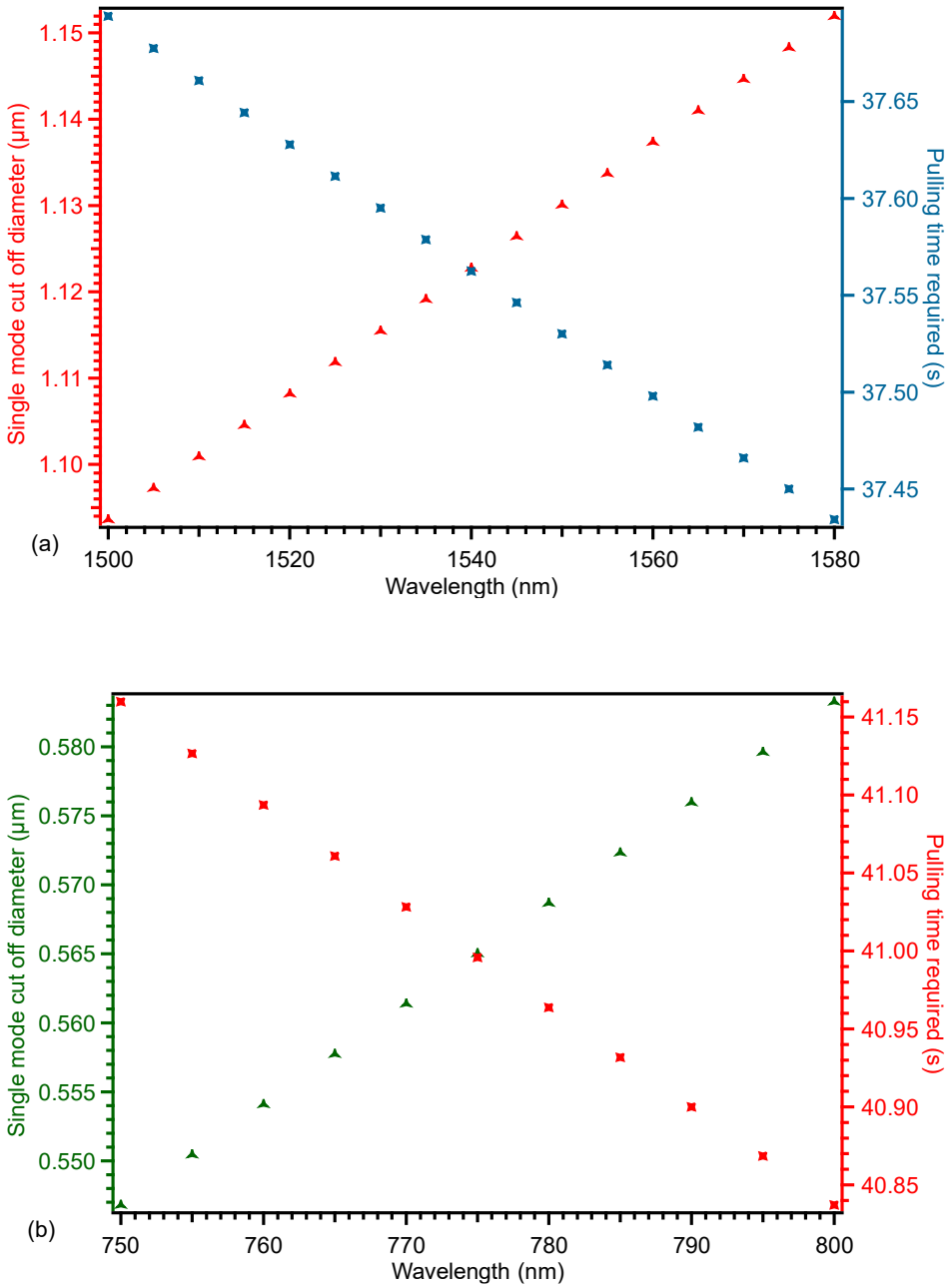

Figure 2.11: The single mode cut-off diameter and corresponding heat-pulling time required to fabricate an optimized fiber taper at the wavelength of interest (a) SWIR regime (b) NIR regime.

For calculations, let's consider the experimental setup values of heat-pulling parameters mentioned at the beginning of this section 2.2.1 along with $V_0 = 2.405$, $n_{co} = 1.45$. Using Eq. 2.2 and Eq. 2.5, the cut-off diameter and required time duration of pulling are determined for fabricating optimized fiber tapers in the SWIR and/or NIR wavelength regimes as depicted in Figure 2.11. According to this investigation, the fiber taper fabricated by us for the transmission studies in the SWIR regime (described in section 2.3.1) will possess a $d_c = 1.130\ \mu m$ for single

mode operation at $\lambda = 1.55\ \mu m$. It is realized by pulling the fiber for $37.53\ s$ duration. For the studies in NIR regime (described in section 2.3.4), the d_c of the fiber taper takes a value of $0.565\ \mu m$ at $\lambda = 0.775\ \mu m$ which is achieved by a longer pulling duration of $41.00\ s$.

Interestingly, a NIR band optimized fiber taper can also be used for SWIR regime operation simultaneously, but we can expect larger losses for fundamental mode carried SWIR power. This is evident from comparing the HE_{11}mode curves in the plots shown in Figure 2.4 (see section 2.1.1). For a fiber taper with $0.565\ \mu m$ diameter, the effective index for SWIR band becomes close to 1 resulting in a propagation prone to scattering due to imperfections, dusts etc. On the other hand, a fiber taper of diameter $1.130\ \mu m$ is a multimode in the NIR band with a very small evanescent field for coupling (see section 2.2.3 for details).

2.2.2 Fabrication of dimpled fiber tapers

Once a straight tapered optical fiber is fabricated with enough transmission ($> 80\ \%$), it can be converted into a dimpled fiber taper. The schematic of the experimental setup is given in Figure 2.12 and a photograph is in Figure 2.13(b). To make a curvature at the waist, a mold is initially prepared with $\sim 5\ cm$ long fiber piece (Corning SMF-28e). About $3\ cm$ of its coating is stripped and cleaned with ethanol. Later, this stripped region is dipped into Alumina and heated using a micro torch filled with oxygen and butane to form a mold. Then the mold is fixed onto a vertical translational stage and carefully aligned to touch the thinnest part of the straight fiber taper from the bottom. The fiber taper is then bent around the mold. Thereafter, the mold is gradually raised manually and the tension on the fiber taper is adjusted using motorized translational stages. Once the stretching of the fiber taper is completed by forming a curved region, an oscillating micro torch fixes it permanently. Now, the mold is gradually lowered along with adjusting the

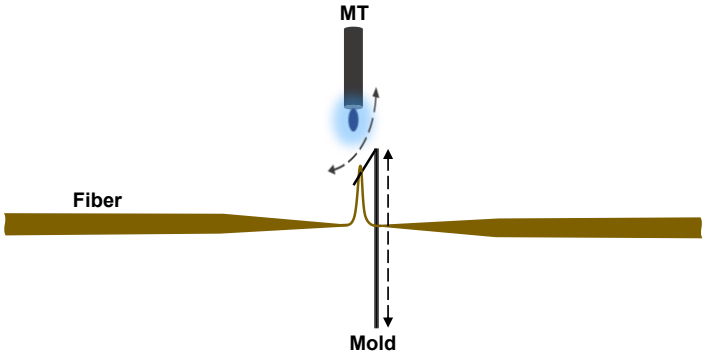

Figure 2.12: Schematic of the process for dimpling a straight tapered optical fiber. MT: Micro torch.

tension on the dimpled taper. At the end of this relaxation process, the mold will be removed carefully without sticking to the dimpled taper, thanks to the Alumina coating. A photograph of such a fabricated dimpled taper is shown in Figure 2.13(c) with a red arrow pointing towards the "dimpled" region. Once fabricated they have a curvature with a diameter of $125\ \mu m$ and can be fixed onto a homemade U-shaped support with a mechanical controller for varying the tension and further transport into the optical injection bench [191]. Regardless of the advantages the dimpled taper possesses, the fabrication process is time consuming due to its delicate nature and the multiple steps involved. In addition, the lack of controllability while coupling due to the electrostatic force leads to difficulty in the repeatable measurements.

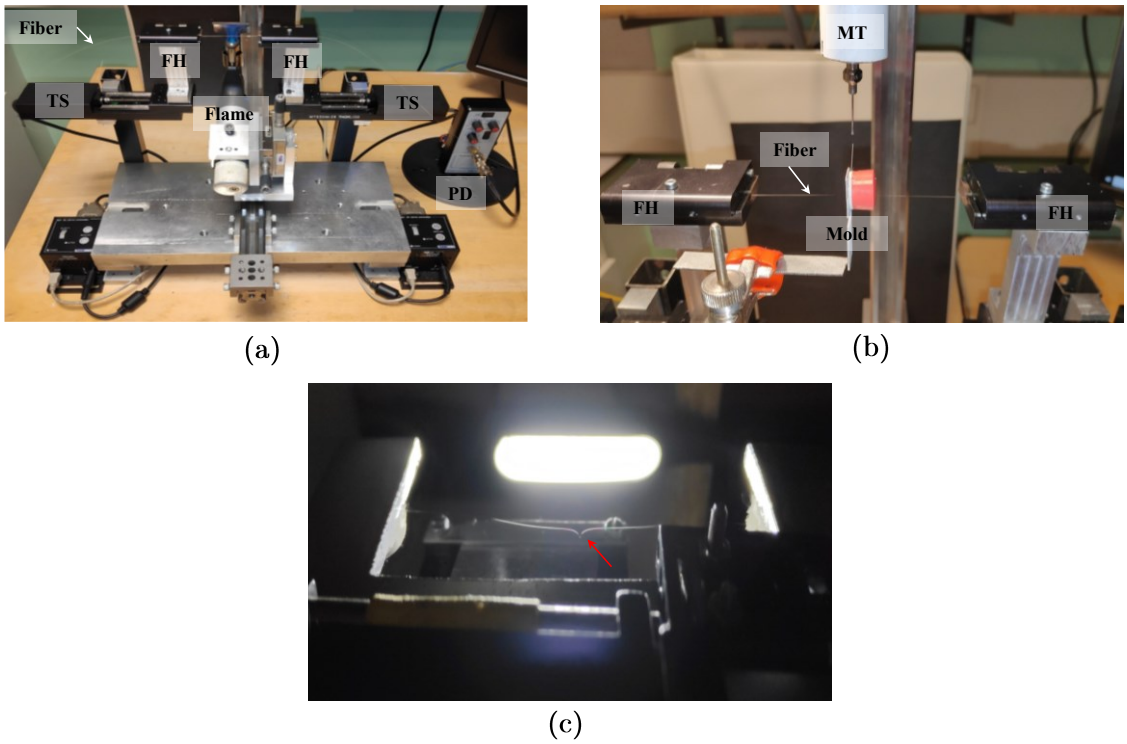

(a) (b)

(c)

Figure 2.13: Photographs of (a) straight tapered optical fiber fabrication setup, (b) dimple tapered optical fiber fabrication setup and (c) dimple tapered optical fiber fixed in a support illuminated by white light. FH: Fiber holder, TS: Translational stage, MT: Micro torch.

2.2.3 Optimized fiber tapers for the wavelength of interest

Tapering a fiber allows to have a sufficient evanescent field around its waist for a particular wavelength of light propagating through it. Such a fiber taper with negligible loss can be fabricated and approached to an optical resonator for selectively exciting the cavity modes if the taper profiling is performed

adiabatically. Then, an overlap occurs between the strongly guided fundamental mode in the taper and the resonator mode for efficiently injecting/extracting the light, known as transmission spectroscopy (see details in section 2.3).

A fiber taper optimized for a specific wavelength of interest can characterize optical cavities efficiently [172]. However, an efficient coupling may require large spectral tolerance. In the case of nonlinear studies of microdisks such as SHG (see chapter 4 for details), the pump will be in the SWIR range ($1.5 - 1.6\ \mu m$) and therefore the SH signal will be generated in the NIR range ($750 - 800\ nm$). It is possible to use separately optimized fiber tapers for each field involved in this experimental situation, one for injecting the pump and the other for extracting the SH signal [61]. In practice, the multiple fiber tapers can lead to a challenging coupling process in terms of the fragility of the fiber tapers and fluctuations in the coupling efficiency to desired resonances while optimizing their positions. It is complex to manipulate two fiber tapers in our case over many on-chip microdisks with small radii of $2 - 3.5\ \mu m$ only in the two-dimensional (2D) matrix. To ease our experiments, single fiber tapers are carefully optimized through fabrication with suitable diameters for coupling both wavelengths of interest as discussed in section 2.2.1. Further discussion on the suitability of a single fiber taper for nonlinear experiments is given in section 2.3.2.

2.3 Linear characterization of GaP based microdisks

In this thesis work, two kinds of suspended microdisks based on GaP ($GaP/Al_{0.7}GaP/GaP$ and GaP/Si) have been investigated. Their fabrication, realized in the OHM team, using NanoRennes technological facilities is described in Appendix A. The $GaP/Al_{0.7}GaP/GaP$ microdisks are fabricated to demonstrate nonlinear frequency doubling with strict $\bar{4}$-QPM. A detailed analysis of their nonlinear properties is provided in chapter 4. The GaP/Si microdisks contain tailored APDs. They are fabricated to realize RQPM based nonlinear frequency conversions. A quantitative analysis of the loss contribution in such microdisks is presented in chapter 3 and the first insight into their nonlinear optical properties is given in chapter 4. The linear characterization setups and the typical transmission responses of these microdisks are described here onwards.

2.3.1 Experimental setup for characterizing microdisks: SWIR regime

An inbuilt optical injection bench adapted to the sample's geometry is used for the characterization of the microdisks as illustrated in the schematic Figure 2.14. A photograph of the setup is also shown in Figure 2.15. Using this approach, one can identify the whispering gallery modes and measure their quality factors. In addition, the investigation of different nonlinear interactions is also possible (see

chapter 4 for more details). The traditional scanning method is utilized to experimentally measure the Q-factor of resonances defined in Eq. 1.41. The GaP/Si samples used in our investigation contain several hundreds of suspended microdisks arranged in a matrix pattern in the order of increasing size. On the other hand, the GaP/$Al_{0.7}$GaP/GaP sample contains only a one-dimensional (1D) array of suspended microdisks.

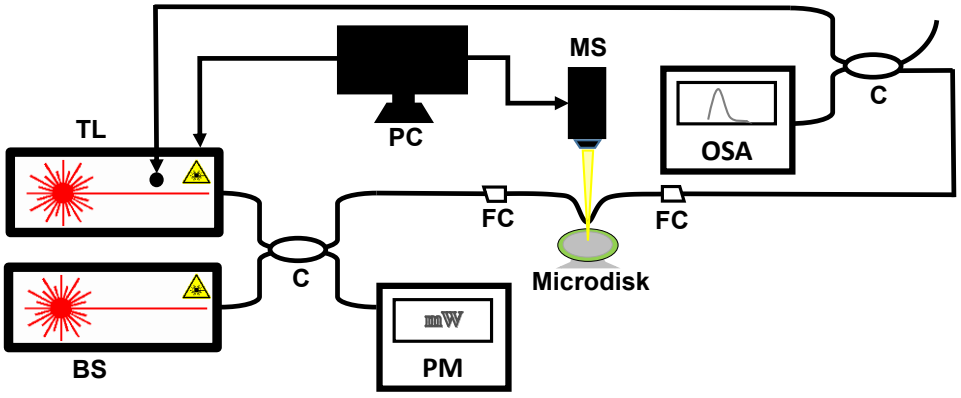

Figure 2.14: Schematic of the experimental setup used for the linear characterization of microdisks in the SWIR regime.
TL: Tunable laser, BS: Broad spectrum source, C: Coupler, PM: Power meter, OSA: Optical spectrum analyzer, FC: Fiber connector, MS:Microscope, PC: Computer control.

The system mainly consists of a $50\times$ objective microscope (Nikon CFI60 TU Plan Epi ELWD) controlled by three servo motors providing $50\,nm$ accuracy in positioning the microscope with respect to the microdisk or fiber taper. Directly above the sample, an access dimpled fiber taper is then mounted on a piezoelectric stage (PI, P-611.3S NanoCube) with a positioning accuracy of $0.2\,nm$. The sample support is attached to linear translational stages with micrometer accuracy and an angular adjustment stage. The fiber taper is then carefully lowered towards a specific microdisk and aligned for coupling with the help of the microscope. The initial movement of the fiber taper is controlled by the translational stages, but for a final approach to the microdisk the piezoelectric stage is used for precision. For wavelength sweep, a $1\,mW$ narrowband $(<200\,kHz)$ tunable laser source (Agilent 8164A Lightwave Measurement System) is injected into the resonator through the fiber taper. The laser tuning ranges from $1510-1583\,nm$ with the best resolution of $8.1\,pm$. The transmission resonance spectrum is recorded with the help of an inbuilt power sensor module integrated into the tunable laser itself. Initially, a reference transmission spectrum of the fiber taper is collected from the sensor without coupling to the microdisk. In the next step, the transmission spectrum of the coupled system is captured. Then a ratio of the latter with respect to the former

gives us the normalized transmission spectrum, which is a characteristic of the coupled microdisk only. A broad spectrum source (HiGHWAVE) is also adapted within the setup along with OSA (Anritsu, MS9710B) to monitor fiber taper-microdisk coupling. The manipulation of the dimpled fiber taper in the vicinity of the microdisk requires great accuracy. Hence, an insulator box for the characterization setup blocking air currents and nano-mechanical controls for the taper position are used.

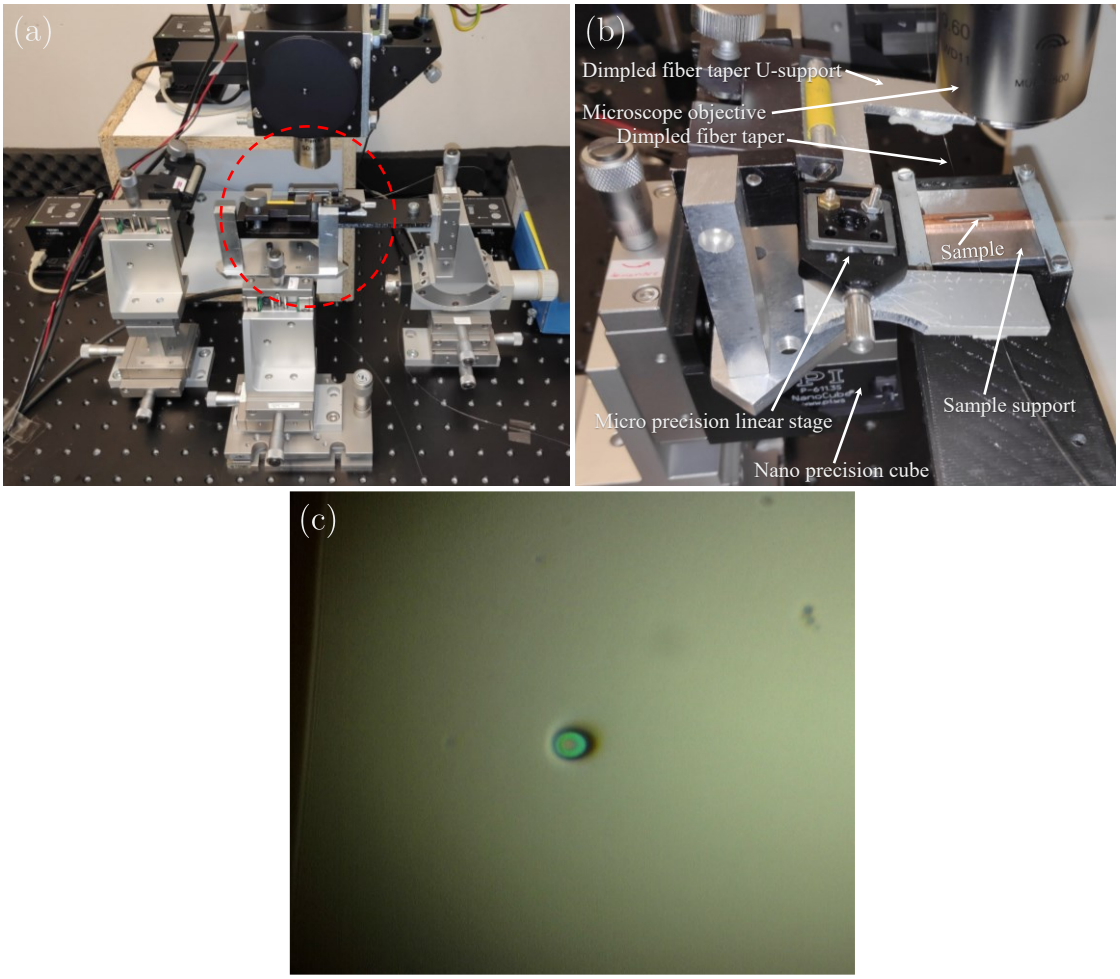

Figure 2.15: (a) Photograph of the experimental setup. (b) An enlarged view of the coupling region red circled in (a). (c) Typical microscope view of a GaP/Si microdisk having $2\ \mu m$ radius.

2.3.2 Transmission measurements: SWIR regime

The GaP/$Al_{0.7}$GaP/GaP microdisks presented here are only $130\ nm$ thick as compared to the $250\ nm$ thick GaP/Si microdisks. The typical transmission spectra of these microdisks are shown in Figure 2.16. As the dimpled fiber taper approaches the close proximity of the microdisk resonator, resonance peaks are gradually

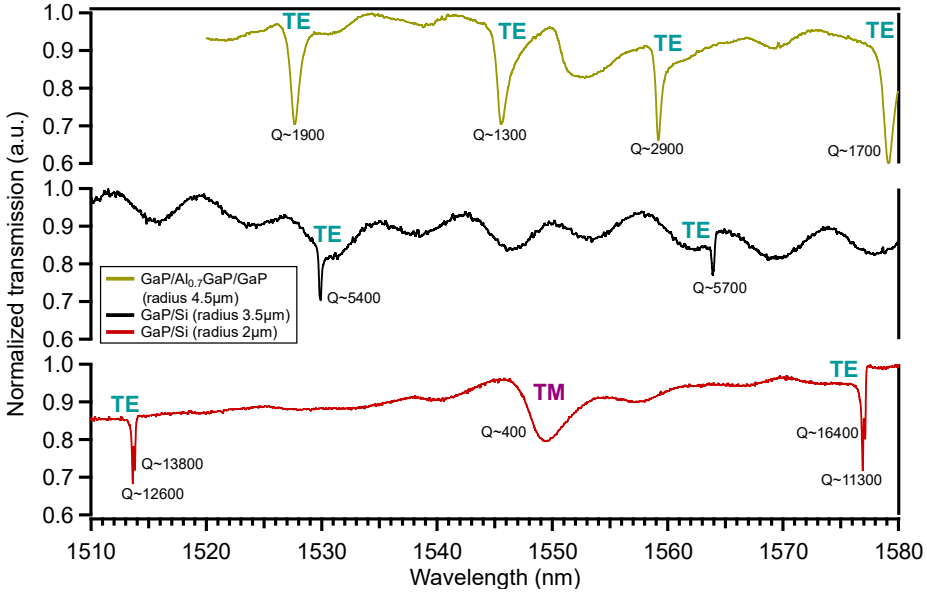

Figure 2.16: Typical transmission spectra of $GaP/Al_{0.7}GaP/GaP$ microdisks with a $4.5\ \mu m$ radius and GaP/Si microdisks with radii of $2\ \mu m$, $3.5\ \mu m$ in the SWIR band.

revealed. However, even after touching the microdisk and despite the coupling position adjustments, the normalized transmission of resonances never reached zero. This can be seen from the ordinates in Figure 2.16 for both kinds of microdisk samples exploited in this thesis. As described in Ref.[95], the large effective refractive index contrast of dimpled fiber taper and microdisk makes critical-coupling and over-coupling very unlikely to occur in our case. Six years separate the fabrication of the $GaP/Al_{0.7}GaP/GaP$ microdisks (2013) and one of the GaP/Si microdisks (2019), during which the fabrication process evolved a lot passing from photolithography to e-beam lithography and the etching from wet to dry etching. As mentioned above, these different fabrication processes are described in Appendix A (section A.1 and section A.2). In the transmission spectra, the GaP/Si microdisks show Q-factors in the order of 10^4 while $GaP/Al_{0.7}GaP/GaP$ microdisks are in the order of 10^3. This Q-factor drop can be qualitatively explained by the different microdisk rim roughness introduced by the different fabrication processes. As discussed in section 1.6.1 (Figure 1.20), the TE mode of a $130\ nm$ thick microdisk with $n_{eff} = 2$ has a bending limited intrinsic Q-factor in the range $10^4 - 10^5$ for a radius of $2\ \mu m$. Thus, the difference in microdisk thickness is not an issue in the Q-factor drop. These $GaP/Al_{0.7}GaP/GaP$ microdisks after incorporating with $GaPN_{0.02}$ quantum wells and following a similar fabrication process as that of GaP/Si microdisks reported a better Q-factor of 10000 [192].

In the transmission spectra of GaP/Si, we have observed only a small number of WGMs within the wavelength span of the tunable laser. They are mainly $p = 1$

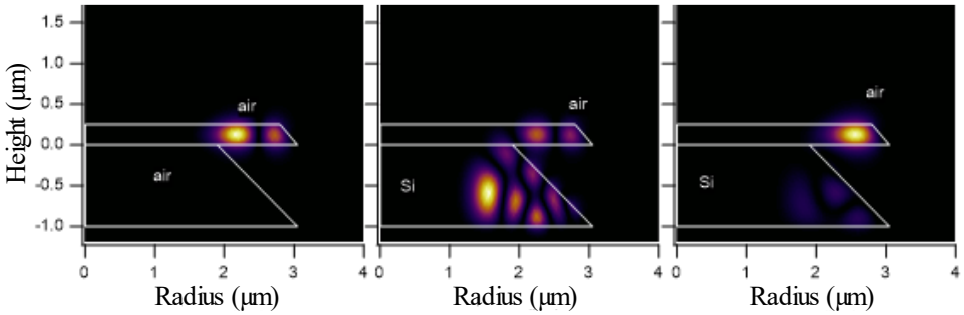

(a) (b) (c)

Figure 2.17: FEM simulations of WGMs in a GaP microdisk coupled to the pedestal type of (a) air at $p = 2$, (b) Si at $p = 2$ and (c) Si at $p = 1$.

TE, TM modes identified from the FSR calculation of WGMs with the radial quantum number 1. In general, the air-cladded GaP membranes are single mode for both TE and TM modes in the vertical direction ($q = 1$) around $1550\,nm$ for thicknesses below $270\,nm$. The GaP/Si microdisks with $250\,nm$ thickness lead the TE modes to experience a larger effective refractive index than the TM modes. Thus, for TM modes the Q_{rad} is limited to a few 10^2 while for TE modes it can be theoretically in the order of 10^6, even for a $2\,\mu m$ radius microdisk as described in section 1.6.1. We can observe this effect in the transmission spectra of GaP/Si microdisks where the TE modes have larger Q-factors. The presence of a Si pedestal (undercutting distance is not more than $1\,\mu m$) can prevent the existence of TE and TM modes of higher radial orders. This is attributed to the lack of optical confinement between the GaP microdisk and Si pedestal which leads to the coupling of higher order modes to the pedestal, as shown clearly by FEM simulations in Figure 2.17. The geometry of the system in simulations is taken as close as possible to fabricated microdisks. In Figure 2.17(a), the material of the pedestal has been considered as air and a TE mode with radial index $p = 2$ (azimuthal index: $m = 20$ at $1579\,nm$) is identified. The simulation is performed again by replacing the pedestal material with Si where we have observed a strong coupling between the field in the pedestal and the $p = 2$ WGM, see Figure 2.17(b). To ensure the convergence of the simulation, the Si pedestal is not open onto a Si substrate but suspended in the air. Thus, we cannot estimate the Q-factor decrease straightforwardly. In the real sample, the optical power coupled to the pedestal is lost into the substrate. In comparison, when we perform this simulation with a radial order $p = 1$ mode and Si pedestal in the same wavelength range, the coupling almost disappears as can be seen in Figure 2.17(c). On the other hand, we have observed a comparatively smaller FSR with a denser number of modes in the transmission spectra of GaP/$Al_{0.7}$GaP/GaP microdisks. They are identified as TE modes where TM modes are not supported in the SWIR band due to the small

geometrical parameters of the microdisks. The larger undercutting distance for GaP/$Al_{0.7}$GaP/GaP microdisks ($\sim 1.8\,\mu m$) and the cladding behavior of the $Al_{0.7}$GaP pedestal due to its lower refractive index compared with GaP can confine TE modes of higher radial orders. The GaP/$Al_{0.7}$GaP/GaP microdisks investigated in this thesis are recorded with $p = 2$ TE modes (see Figure 4.1 for mode indexation in section 4.1.1), while $p = 3$ is reported for the active GaP/$Al_{0.7}$GaP/GaP microdisks [192].

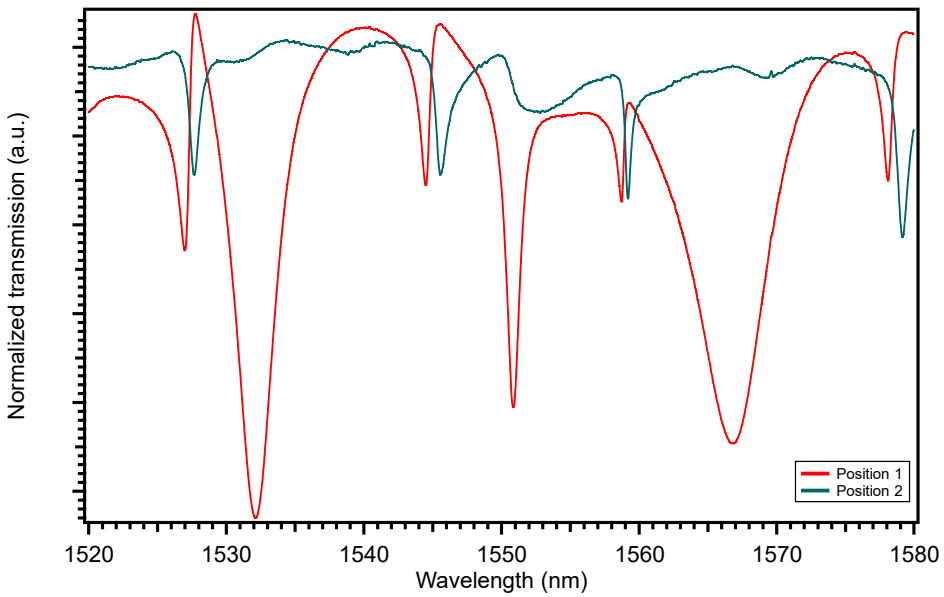

Figure 2.18: The sensitivity of transmission spectra to the fiber taper coupling positions for a 4.5 µm GaP/$Al_{0.7}$GaP/GaP microdisk in the SWIR band.

In our experiments, the fiber taper will always touch the microdisk due to the electrostatic force of attraction. The fiber taper-microdisk coupling positions can influence the transmission spectra by shifting the resonances in the range of a few nanometers and modifying the coupling strength of resonances. In the specific case illustrated in Figure 2.18, the spectral position of a resonance located at $1544.48\,nm$ changes $\sim 1.1\,nm$ while slightly moving the fiber taper to another location. This effect can be attributed to the local change in the effective refractive index of the microdisk experienced by the resonances. It is particularly useful for microdisks with fabrication flaws in their geometrical parameters to tune their resonances to achieve the doubly resonant condition for efficient frequency conversion. The appearance and disappearance of specific resonances can also occur while relocating the fiber taper as can be seen at $1550.88\,nm$ by comparing both spectra. Thus, the optimized coupling of fiber taper to a particular resonance can lead to non-optimized coupling to other resonances. As briefly discussed in section

2.2.3, this is a drawback for the nonlinear experiments with only one fiber taper used to inject the pump and extract the generated nonlinear signals. The optimization of fiber taper for efficiently coupling the pump in the SWIR band leads to non-optimized couplings in the NIR and VIS bands. Hence, the simultaneous transmission measurement in the non-optimized bands becomes out of reach. In addition, trying to optimize the fiber taper position in the SWIR band results in a shift of the desired resonances in all bands including SWIR. Consequently, it leads to discrepancies between the theoretical indexation of the resonances and the experimental spectra in all wavelength bands under investigation. In the remaining part of this chapter 2, we will restrict ourselves to the GaP/Si microdisks for the sake of clarity unless otherwise specified.

The measured FSR of our GaP/Si microdisks helps us to calculate the real radii they possess. From the transmission studies, an FSR of $63\ nm$ is obtained for our smallest microdisk while the largest microdisk shows an FSR of $32\ nm$. In Figure 2.19, the curve represents a fit on the experimentally measured FSR values as a function of the target microdisks radii giving a scaling factor of 0.95 ± 0.01. This factor corresponds to the fabrication tolerance in the radii and their real values are computed using Eq. 1.46. Such a variation is acceptable according to our fabrication process.

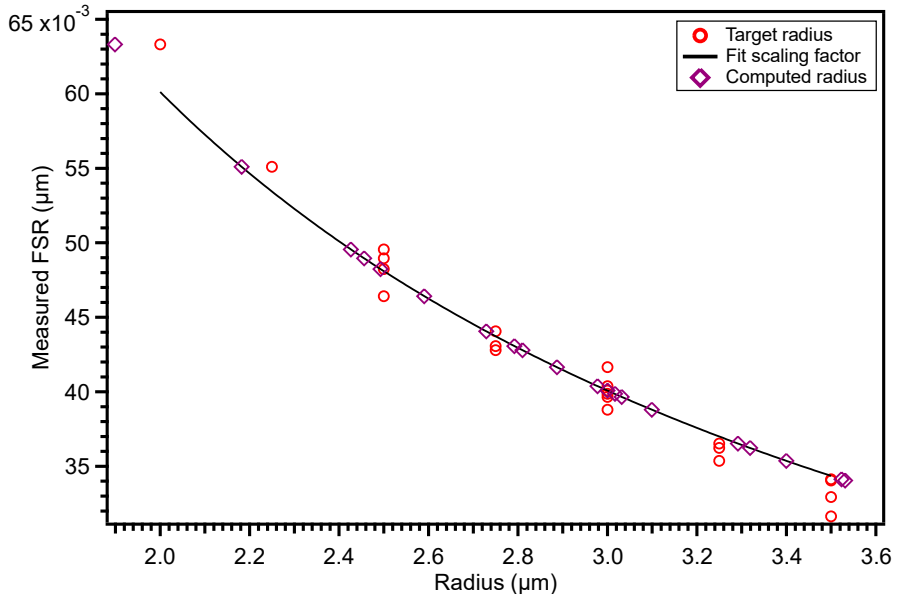

Figure 2.19: FSR distribution of GaP/Si microdisks as a function of radius.

2.3.3 Mode splitting of SWIR regime resonances

In most of the GaP/Si microdisks transmission spectra, splitting in the resonance peak is observed for the TE modes. This can be attributed to the typical backscattering coupling due to the lifting of the degeneracy of clockwise and counter-clockwise propagating modes in the microdisk [87][88][89] (see section 1.3.3.3 for a theoretical description). A zoom on the high resolution transmission spectrum of a GaP/Si microdisk of $2\ \mu m$ radius (see Figure 2.16) is given in Figure 2.20 where the doublet mode that appeared on a resonance peak is clearly observable.

The rate of photons backscattering in the microdisk is determined by doublet splitting value $\Delta\lambda$. The photons life time in the cavity is quantified by the individual linewidths $\delta\lambda_l$ (left mode) and $\delta\lambda_r$ (right mode) of the doublet. A double Lorentzian fit will give us individual modes loaded quality factors of $Q_l = 11338$ and $Q_r = 16353$ for linewidths $\delta\lambda_l = 139\,pm$ and $\delta\lambda_r = 96\,pm$, respectively. Then, a mode coupling optical quality factor (Q_β) is given by the expression:

$$Q_\beta = \frac{\lambda}{\Delta\lambda} \qquad \text{Eq. 2.6}$$

where λ is the center wavelength of the resonance. We have measured $Q_\beta = 7510$ for a splitting of $\Delta\lambda = 210\,pm$. This is in the same order of magnitude of Q_β value that could be calculated from the measured short-scale sidewall roughness component [92][91] (see section 3.3 for details).

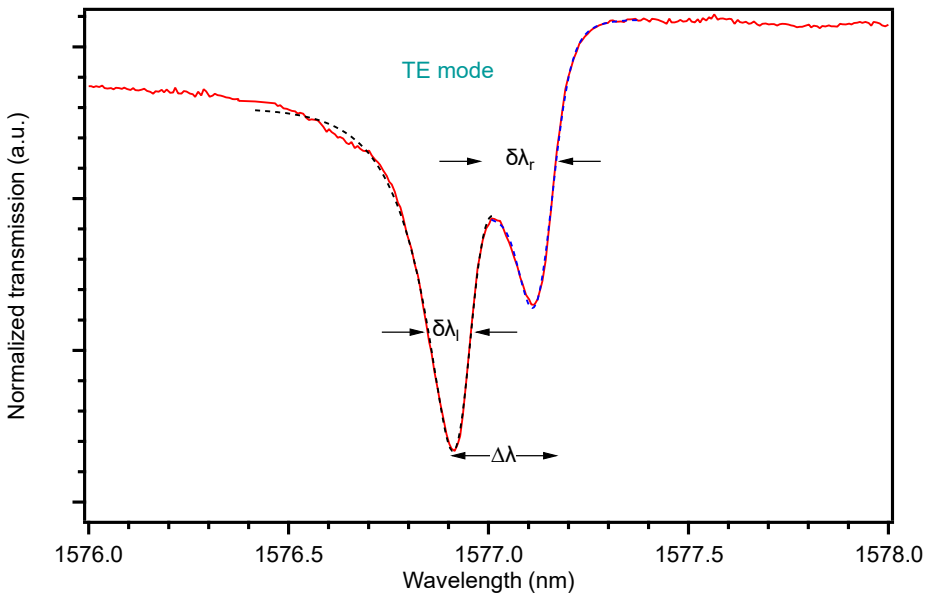

Figure 2.20: Splitting observed in the resonance peak. The black dashed line represents a double Lorentzian fit.

2.3.4 Experimental setup for characterizing microdisks: NIR regime

The investigation of the properties of our microdisks in the NIR regime is inevitable for their application as a frequency up-converter. Transmission spectra are collected using the same inbuilt optical injection bench (illustrated in Figure 2.15), but with a slightly different configuration as depicted in the schematic Figure 2.21.

The dimpled fiber taper (optimized for $775\,nm$ with $d_c = 0.565\,\mu m$) is carefully aligned for coupling to a specific microdisk with the help of the microscope as explained in section 2.3.1. Thereafter, a broadband visible source (BLMS mini-SUPERLUM, 6.2 mW, HIGH mode) is injected into the microdisk. The transmitted light through the dimpled fiber taper from the cavity is then collected using the OSA. A power meter (PM100D, S120C sensor, Thorlabs) is also used at the output end of the dimpled taper for assisting fiber taper-microdisk coupling. The OSA is operated in 3 different resolutions of $1\,nm$, $0.2\,nm$ and $0.07\,nm$ (device limit). The resolution of $1\,nm$ is utilized at the beginning of data acquisition to identify the optimal coupling position by observing the resonance peaks with less noise. Here also we have collected both reference and measurement transmission spectra for extracting the resonance response of the coupled microdisk at each OSA resolution to calculate Q-factors.

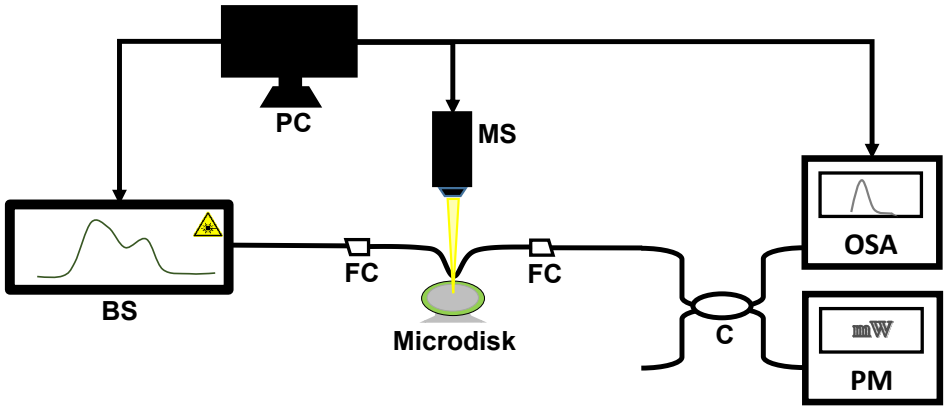

Figure 2.21: Schematic of the experimental setup used for the linear characterization of microdisks in the NIR regime.
BS: Broad spectrum source, C: Coupler, PM: Power meter, OSA: Optical spectrum analyzer, FC: Fiber connector, MS: Microscope, PC: Computer control.

2.3.5 Transmission measurements: NIR regime

A typical NIR transmission spectrum of a $2\,\mu m$ radius GaP/Si microdisk is shown in Figure 2.22(a). The 3 spectra in this plot correspond to different OSA

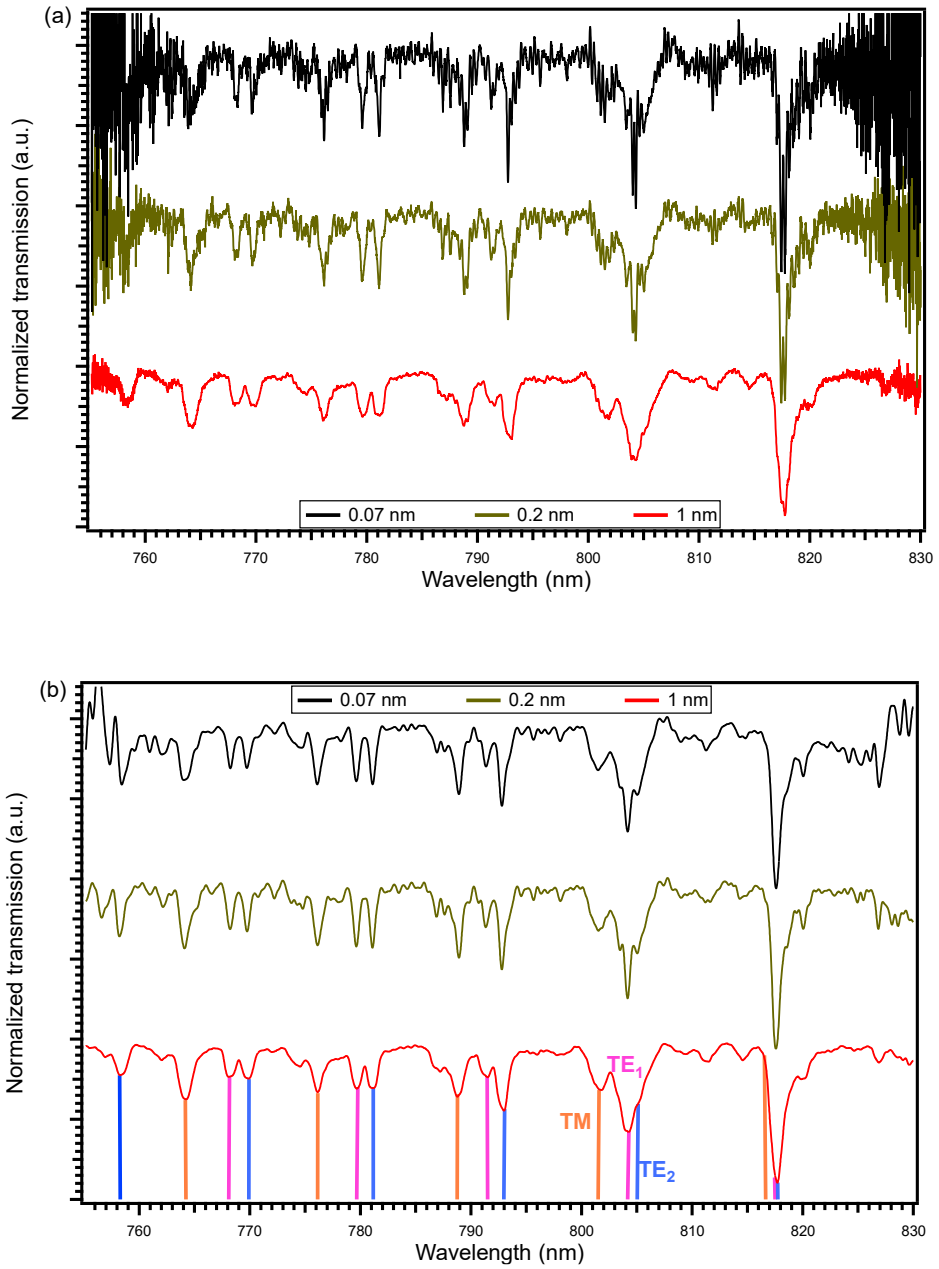

Figure 2.22: The NIR transmission spectra of a GaP/Si microdisk at different OSA resolutions (a) before and (b) after low pass frequency filtering.

resolutions captured at the same dimpled fiber taper-microdisk coupling position. The resolution is increased for each acquisition towards the limit, then the spectra became noisier with indistinguishable resonances. These high frequency oscillations may be due to the response of a millimeter sized cavity formed within the setup itself during experiments predicted by their measured FSR value. It was unable to get rid of them completely during the experiments, however, a digital low pass frequency filter is later applied to clean the spectra which also broadens the true

resonances as shown in Figure 2.22(b). These ambiguities made the NIR spectra analysis quite challenging in terms of precisely measuring the Q-factors, wavelength detunings, mode splittings and mode indexing. To compensate for the broadening induced by the digital filter, we have mimicked microdisk resonance with a known FWHM and applied the same filter to calculate the broadening that occurred. The measurements after filter broadening compensation reveal that the microdisks of radii $2-2.25\ \mu m$ at $0.07\ nm$ OSA resolution can possess NIR Q-factors in the range of 10^2-10^3. A maximum Q-factor of 3600 is measured for a microdisk of radius $2.25\ \mu m$. The comparison of spectra in the SWIR and NIR bands allows us to identify the resonant microdisks, eligible for SHG experiments. A group of such microdisks is identified along with detuning between their pump and SH resonance wavelengths as included in Table 3. In addition, despite the low Q-factor values of NIR resonances, their broad linewidth can increase the chance of spectral overlap between the interacting modes to enhance the nonlinear frequency conversion efficiency [33][193].

r	λ_{pump}	Q_{pump}	m_{pump}	λ_{SHG}	Q_{SHG}	FWHM	Δ	Δ_{norm}
2	1563.73	2177	17	783.4	1623	0.5	-3.0	6.2
2	1568.63	4038	17	784.7	2241	0.4	-0.7	2.1
2	1577.12	16353	17	789.7	1597	0.5	-2.3	4.6
2	1529.57	4317	17	764.2	757	1.0	1.3	1.2
2	1555.31	4688	17	781.2	1873	0.4	-7.1	16.9
2	1556.66	6247	17	782.6	802	1.0	-8.6	8.8
2.25	1529.13	8905	20	764.6	1270	0.6	-0.1	0.1
2.25	1542.93	8752	20	772.9	3581	0.2	-2.8	13.1

Table 3: A list of GaP/Si microdisks suitable for SHG.
Microdisk radius: r(µm), Pump resonance wavelength: $\lambda_{pump}(nm)$, Pump resonance Q-factor: Q_{pump}, Azimuthal number of the pump resonance: m_{pump}, SHG resonance wavelength: $\lambda_{SHG}(nm)$, SHG resonance Q-factor: Q_{SHG}, Full width at half maximum of the SHG resonance:FWHM(nm), Resonance wavelength detuning $(\lambda_p - 2\lambda_{SH}) : \pm\Delta(nm)$, Normalized resonance wavelength detuning $(|\Delta|/FWHM)$:Δ_{norm}.

2.3.6 Estimation of Q-factors: NIR regime

The true spectrum of the microdisk is broadened while measuring with OSA. Thus, to estimate the real loaded Q-factors of the GaP/Si microdisks in the NIR band, a convolution model is fit into the experimentally measured FWHM values of the resonances after filter broadening compensation at different OSA resolutions as presented in Figure 2.23. We can consider that the measured resonance spectrum is the convolution of the characteristic broadening of the microdisk cavity and the response function of the OSA. In the design of this theoretical model, the microdisks broadening is approximated to a gaussian profile for the sake of simpler calculations. The broadening induced by the OSA is considered to be a gaussian too. The curves in Figure 2.23 correspond to the convoluted FWHM values for different resonance linewidths as a function of the OSA resolution. From a group of data points at different OSA resolutions, we found a qualitative agreement between the experimental results with the theoretical model. At higher resolutions of the OSA, we observe a stabilization of the experimental linewidths measured. This is similar to the behavior of resonances of linewidths between 0.58-$0.34\ nm$ corresponding to Q-factors between 1400 and 2300. We can also notice a few experimental outliers from the theoretical model fit. Probably they are the low Q-factor modes of different polarization or the higher order modes involved in the measurements. It is also possible for measurement discrepancies to occur at lower OSA resolutions.

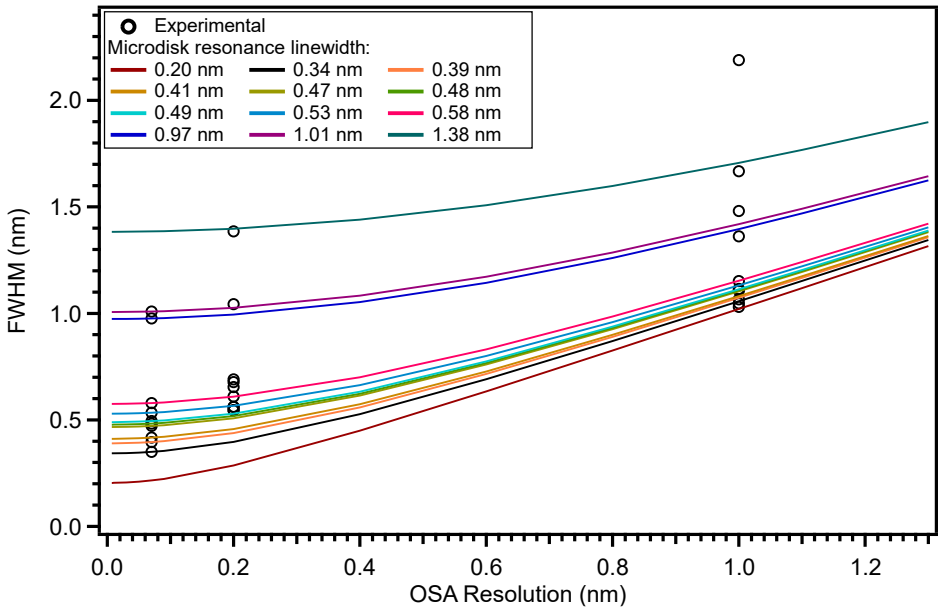

Figure 2.23: The convolution model fit on the experimental FWHM of resonances extracted from the broadened transmission spectrums of $2\ \mu m$ radius GaP/Si microdisks in the NIR regime.

Summary

This chapter described the instruments and experimental configurations required for characterizing the microdisks. Merits for evanescent field coupling of light with a microresonator using fiber taper are briefly explained. The transformation of different modes propagating in a standard optical fiber while tuning its diameter is then investigated for tapering a fiber adiabatically allowing single mode operation. The evanescent field surrounding the fiber taper available for coupling is also illustrated. The fabrication of optimized straight fiber tapers and their on-chip counterparts dimpled fiber tapers are described in detail. The optical injection setups and coupling procedures are explained to extract the transmission spectra of microdisks in the SWIR and NIR wavelength bands. The mode families are identified and the characteristic parameters of the microdisk such as Q-factors, FSR and mode splittings are determined. In the next chapter, we will take advantage of these measurements for investigating losses in our GaP/Si microdisks focused on estimating APD induced losses [48].

3 Loss analysis of APD engineered GaP/Si microdisks

Introduction

This chapter presents the loss analysis conducted on the results obtained from the experimental characterization of the GaP/Si microdisks shown in chapter 2. In the first step, we briefly describe the monolithic heteroepitaxial growth and technological processing of GaP microdisks on Si substrates with tailored APDs. After identifying APDs distribution, their characteristic parameters are extracted. The contribution of different losses to the total intrinsic quality factor of the microdisk is then statistically assessed with a special focus on lateral roughness and APBs absorption induced losses. This investigation provides critical feedback on the fabrication quality control and leads to an experimental estimation of the loss generated by APBs in the GaP/Si devices. They are vital information for the fabrication of future nonlinear photonic components based on this platform [48].

3.1 Fabrication of random crystal polarity engineered GaP/Si microdisks

The fabrication is not one of my doctoral research objectives and only the details required for this thesis are included. The devices under scrutiny in this chapter were fabricated by the OHM research group (Optoelectronics Heteroepitaxy and Materials) located in Rennes using the facilities of the NanoRennes Technological platform from the RENATECH+ network. The OHM team has expertise in making defect-tailored photonic components. We have also triggered collaborations with the C2N laboratory (Isabelle Sagnes) and the Ghent university Photonics research group (Bart Kuyken) for the fabrication of more advanced samples such as fully integrated GaP-on-insulator photonic waveguides or polarity-engineered photonic resonators. The Institut Foton uses Molecular-beam epitaxy (MBE) and C2N uses Metal-Organic Vapour Phase Epitaxy (MoVPE) for sample preparation.

At Institut Foton, random crystal polarity engineered GaP layers are grown on vicinal Si substrates with a miscut. The fabrication process follows Migration Enhanced Epitaxy (MEE) with suitable temperature and V/III ratio along with marker layers for controlling APDs as introduced in section 1.5. The rough GaP surface obtained right after growth is polished to achieve acceptable levels for fabricating quality photonic devices. The sample is then used to quantitatively study the APDs characteristics (see section 3.2). Also, suspended GaP microdisks on Si are technologically processed for transmission experiments and loss analysis (see section 2.3 and section 3.3). A detailed growth procedure and technological processing are given in Appendix A.

3.2 APB development process

It is crucial to understand the distribution of APDs in the grown GaP/Si samples for the assessment of the loss imposed by them. This characterization is carried out on a sample piece that was not used for the technological processing of the microdisk. After the chemical mechanical polishing (CMP) process (see step 2 described in Appendix A), the sample is dipped for a few seconds into a GaP Etch commercial solution to reveal the APBs. Thereafter, SEM and AFM study is conducted to identify the domains of opposite polarity and statistically analyze the crystal polarity distribution. The SEM image is shown in Figure 3.1. From the fast etching of APBs on the polished surface, a network of valleys becomes clearly visible. APBs are then tracked using a graphics tablet to create a binarized image. The minority domains obtained with this technique are highlighted in red in Figure 3.1. The autocorrelation function of the binarized image is then computed as shown in Figure 3.2. As discussed in section 1.5.1, the size of the minority domains can be directly obtained from the exponential decay of the central peak. Also, the mean distance between the homophase domains is identified from the distance between

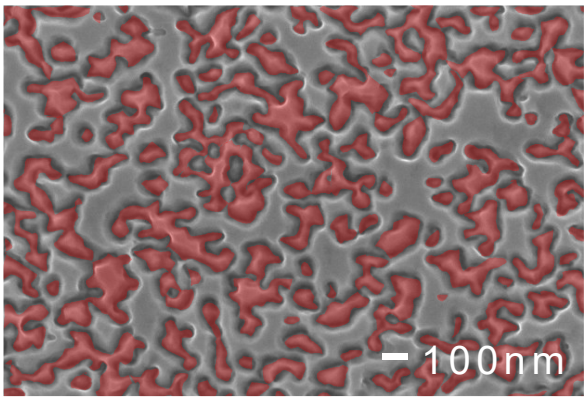

Figure 3.1: SEM image of APDs distribution in the grown GaP/Si film.

the satellite peaks. In our sample, the average size for minority domains ($\mathcal{L}_c$) is found to be $90 \pm 5\,nm$ and the mean distance between them is $250 \pm 60\,nm$. The average polarity in the sample ($P_{APD,mean}$) is measured to be 0.3 by integrating the binarized surface. This implies to say that $65\,\%$ of the surface is occupied by $+1$ domains and $35\,\%$ by -1 domains. This is in good agreement with the geometrical dimensions of the domains reported above. A similar value for the $P_{APD,mean}$ is already reported for an APD height tailored GaP/Si microdisk [54]. According to the discussion under sections 1.5.2 and 1.5.3, a mean polarity of 0.3 and a correlation length of $90\,nm$ can lead to a SHG conversion efficiency in the order of $10^{-3}\,\mathrm{mW}^{-1}$ for a $Q_i = Q_{cpl} = 10^4$ [34].

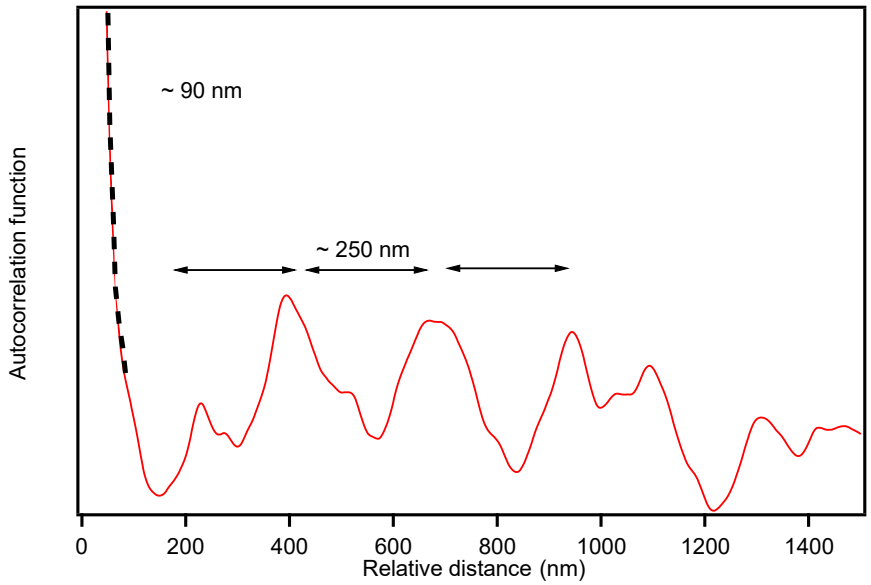

Figure 3.2: Autocorrelation function calculated from the APD distribution of GaP/Si film shown in Figure 3.1.

3.3 Statistical analysis of loss contributions in the SWIR regime

The next objective is to analyze the various forms of optical losses occurring in GaP/Si microdisk cavities technologically processed from this crystal polarity engineered platform. Such an investigation based on the quality factors of WGMs in the microdisks allows the quantitative assessment of losses due to roughness and controlled APDs induced volume losses.

The SWIR transmission study was conducted on 37 microdisks of increasing radii varying from $2 - 3.5\,\mu m$. A top Q-factor of 1.6×10^4 is obtained for the first time in literature for a GaP microdisk monolithically grown on Si with tailored antiphase domain distribution [48]. For the loss inspection, we will restrict ourselves

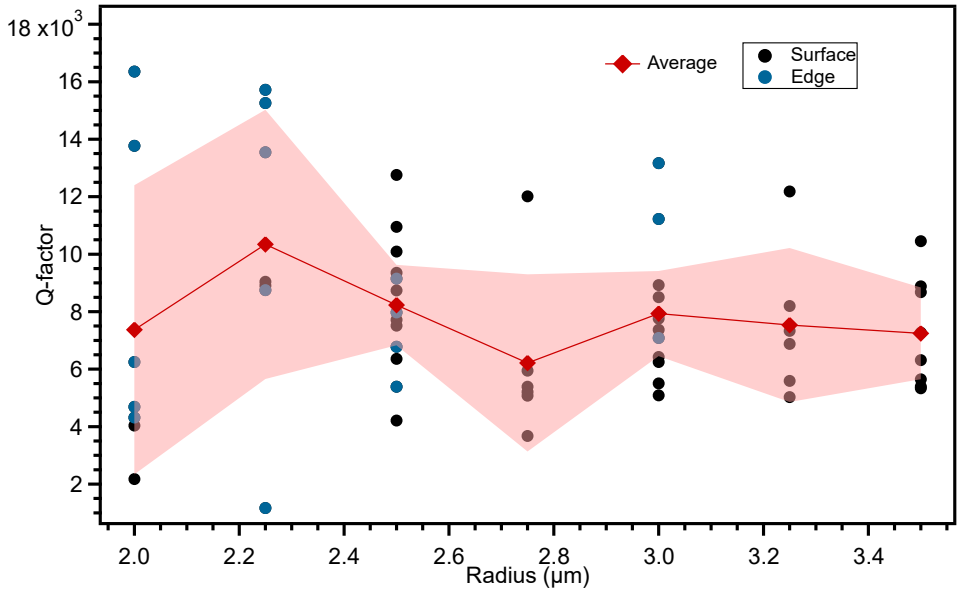

Figure 3.3: Evolution of GaP/Si microdisk Q-factors as a function of radius. The dimpled fiber taper coupling positions on each microdisk to find under-coupling conditions are labeled with circular markers in black (surface-coupling either close to the edge or the center of the disk) and blue (edge-coupling to the disk). The average Q-factor is in red and the confidence interval is in pink.

to the Q-factors of TE modes. Each microdisk spectrum shows one or two of these resonances within the transmission spectral span. The experimental Q-factors measured for 59 WGMs with $p = 1$ (described in section 2.3.1) can be statistically distributed according to the microdisk radii as displayed in Figure 3.3. In our experiments, the fiber taper-microdisk energy exchange is considered to be under-coupled as described in section 2.3.2 [95]. Thus, the loaded Q-factors provide a reasonable estimation of the intrinsic Q-factors of the microdisks as per Eq. 1.44 by neglecting the coupling Q-factor term ($Q_i < Q_{cpl}$). In fact, the intrinsic Q-factors are slightly underestimated with this assumption. The averaged Q-factor ($\bar{Q}$) is deduced from the red curve with diamond markers in the plot as 8×10^3 with a confidence interval of $25 - 75$ % (shaded region in Figure 3.3). This average value is close to the Q-factors reported in the previous works from our team on GaP/$Al_{0.7}$GaP/GaP microdisks fabricated using similar technological processing as that of GaP/Si microdisks at the Institut Foton [192]. There is no significant variation in the average Q-factor observed with increasing microdisk radius. As discussed in section 1.6.1, the Q_{rad} must increase with the radius. This reveals that all Q-factors are limited by some other loss contributions considering the under-coupled microdisk. In addition, the confidence interval is found to be getting narrower with the increase in microdisk size. An explanation for these findings will

be unveiled by deeply analyzing Eq. 1.80, where the intrinsic Q-factors can be altered by Q_S, Q_{rad}, Q_R and Q_{APD}. The prolonged CMP process justifies to neglect the Q_S term involvement and we also neglected loss contributions from other structural defects of the microdisk for this analysis as explained in section 1.6.3.

3.3.1 Sidewall roughness induced scattering losses

One of the main optical losses that occur in microdisks is due to their rough sidewalls, after bending induced losses as discussed in section 1.6. In our samples, this loss contribution can be severe because of the lift-off process we have used to

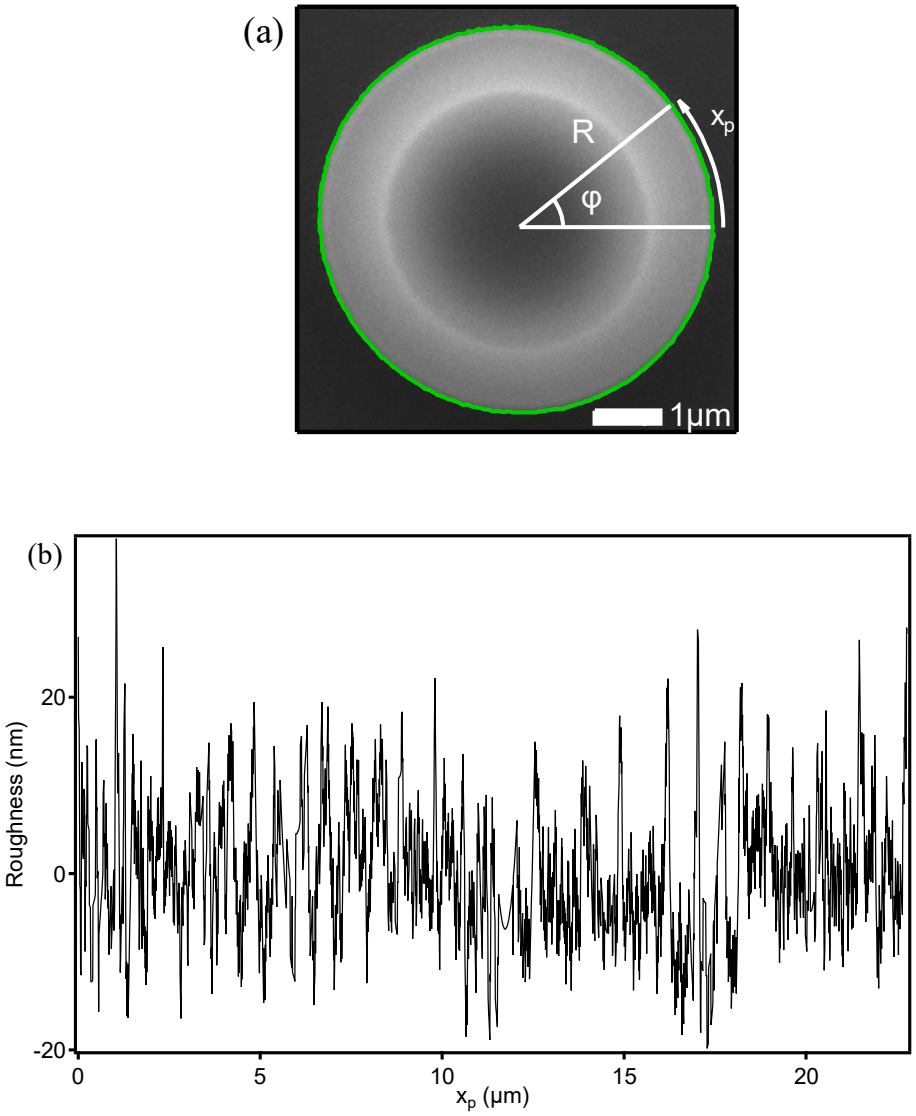

Figure 3.4: (a) SEM view of a GaP/Si microdisk from which edge roughness is obtained. (b) Extracted lateral roughness profile of microdisks.

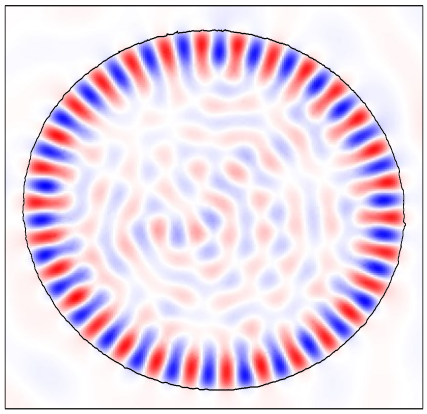

Figure 3.5: FEM simulation of TE WGM in a GaP/Si microdisk with a roughness profile shown in Figure 3.4(b).

define the disks during technological processing (Appendix A, step 4 in section A.1). This method can generate more roughness than metal-free masking [194].

To deeply analyze this loss contribution, SEM images of our GaP/Si microdisks are collected as shown in Figure 3.4(a). We have then extracted the lateral roughness profile as a function of the perimeter position (Figure 3.4(b)) given by:

$$X_p = R\varphi \qquad \text{Eq. 3.1}$$

where R is the average microdisk radius and φ is the azimuthal angle. The roughness obtained in this analysis is only limited by the $5\,nm$ resolution of the SEM microscopy conducted. The roughness profiles can be fed to a finite element method (FEM) environment to get a direct estimation of Q_R on individual roughness distribution, see Figure 3.5. The simulation gives a Q-factor of 3×10^4 for a TE WGM at $1.57\,\mu m$. The scattering of light is observed both inside and outside of the microdisk which is inevitable due to the sidewall roughness. However, this Q-factor value does not account for the loss induced by the presence of the Si pedestal.

A statistical examination of the lateral roughness is then carried out to get a deeper insight into the formation of this prominent loss contribution. The autocorrelation function of the sidewall roughness, plotted in Figure 3.6, reveals the existence of two roughness components in our microdisks, hereafter called short-scale and long-scale components. The short-scale component is identified from the fast decaying central peak of the autocorrelation function and the long-scale component appears in the form of satellite peaks. The exponential decay of the short-scale component is typical of random roughness with correlation length $S_{c,short} = 70 \pm 5\,nm$. Contrarily, the long-scale component corresponds to a pseudo-periodical topology with a pseudo-period (or roughness correlation length)

$S_{c,long} = 650 \pm 50\,nm$. Utilizing Eq. 1.82, these components are found to have individual roughness of $\sigma_{short} = \sigma_{long} = 5\,nm$ RMS, leading to a combined roughness (σ_{comb}) of $7\,nm$ RMS. Measuring RMS roughness in the order of $5 - 7\,nm$ is consistent with a resolution of the SEM image in the range of $5\,nm$. Indeed, a $7\,nm$ RMS topology shows peak-to-peak variations above $30\,nm$ (see Figure 3.4(b)).

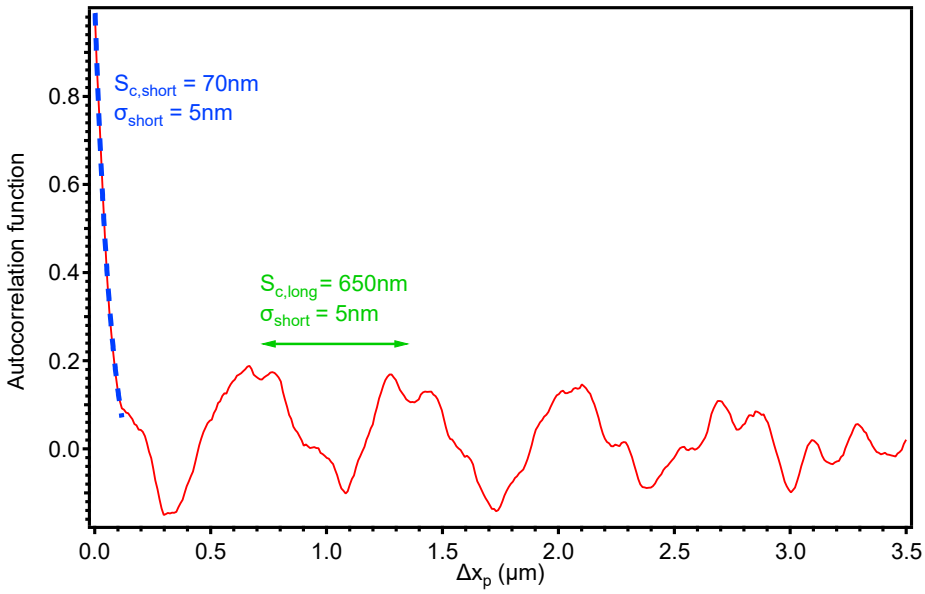

Figure 3.6: Autocorrelation function of the lateral roughness profile shown in Figure 3.4(b).

It has been previously reported the studies on the impact of microdisk sidewall structural imperfections using both an arbitrary number of subwavelength scatters approach [92] and a volume current method for distributed roughness (see section 1.6.2) [91][151][152]. The theoretical dependence of the roughness induced contribution Q_R as a function of the roughness correlation length S_c is shown in Figure 3.7 (red). This curve is plotted using Eq. 1.84 (based on the analysis proposed in Ref.[152]) for a thin microdisk of radius $2\,\mu m$ supporting TE modes and a fixed roughness of $\sigma = 5\,nm$ RMS. It is clear from the plot that the lateral roughness present in our GaP/Si microdisk samples results in a Q_R contribution from 10^5 to 10^4 in agreement with the FEM simulation (see Figure 3.5). The effect of the short-scale roughness component will only lead to Q-factors around 10^5. However, such a calculation is in principle valid only for random roughness with the gaussian profile. This is not the case with the long-scale component which is quasi-periodic. The estimated impact of the latter is thus overestimated and it can be considered as the "worst case" situation. Notably, more detailed approaches show that the impact of a quasi-periodic roughness on the Q-factors of resonances strongly depends on the commensurability of the resonance azimuthal order and

the corrugation order of the roughness [151][152]. The value of 10^4 of Q_R at $S_{c,long}$ thus cannot account solely for the experimental average value of 8000. In addition, the pseudo-period obtained is only one order of magnitude smaller than the perimeter of the microdisks under investigation. Consequently, the roughness distribution can vary significantly from one microdisk to another, affecting the Q-factors differently. This accounts for the narrowing of the large confidence interval as the radius increases. Although the sidewall roughness is attributed to the technological processing of the microdisks, we cannot completely rule out the possibility of any correlation with the presence of APBs in our sample, even if their typical dimensions ($100 - 150\,nm$) fit neither the short-scale nor the long-scale correlation length. To finish with, the independence of the average Q-factor with the microdisks radii shown in Figure 3.3 agrees with the dominance loss contributions in the form of Eq. 1.83 and Eq. 1.85 where the loss is modeled by an exponential decay, compared to radiation losses in the Q-factor values, as illustrated for example in Figure 1.22.

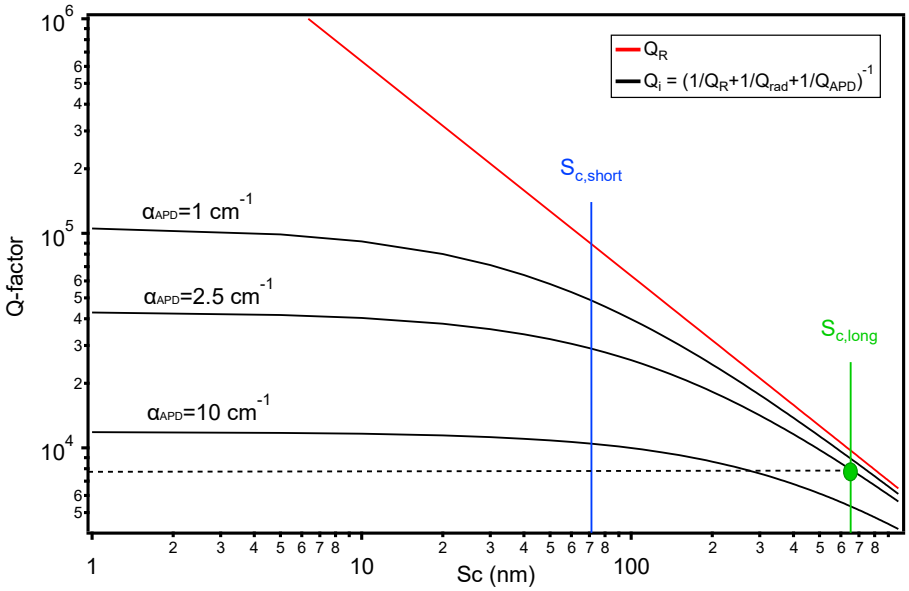

Figure 3.7: Theoretical evolution of Q_R as a function of S_c (red line) and dependence of Q_i on different values of APB's induced volumic losses (black-solid curves). The green circle at the long-scale roughness component represents the matching point of the experimental $\bar{Q}$ (black dashed line) and Q_i for an APD-induced volumic loss corresponds to $\alpha_{APD} = 2.5\,cm^{-1}$.

3.3.2 APBs absorption induced volume losses

In Figure 3.7, it appears that accounting only for the bending and sidewall roughness induced losses in our samples is insufficient to explain the drop in the

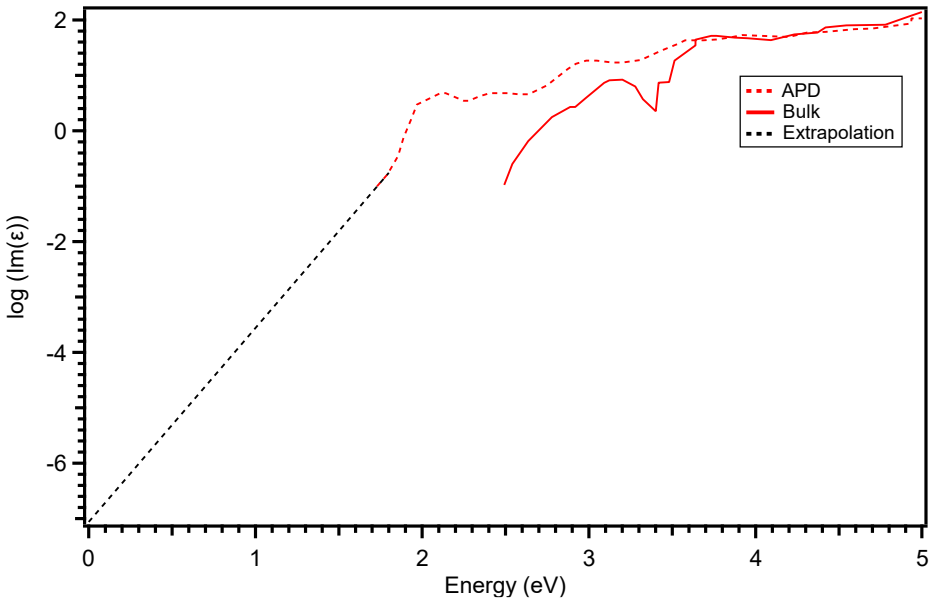

Figure 3.8: Imaginary part of the dielectric function (log scale) versus Γ optical bandgap energy of GaP in bulk form (solid-red), with APBs (dashed-red) and its exponential tail extrapolation (dashed-black). Image (modified): Courtesy of Ref.[51].

measured average intrinsic Q-factor down to 8×10^3. Therefore, a third contribution to the loss can be introduced. It could be due to the absorption induced by the APBs tailored in the volume of the GaP layer. A theoretical investigation by Tea et al. [51] had been already published some years ago to estimate to which extent APBs can modify the bulk optoelectronic properties of GaP. Their calculations, performed on stoichiometric APBs containing both cations and anions, revealed that the APB planes can trap charge carriers and thus act as deep level centers. In turn, the absorption properties are found to be significantly modified especially within the bandgap of GaP. A redshift of the bandgap edge of $0.7\ eV$ is to be expected so that the exponential tail of the electronic contribution to the dielectric constant can still affect absorption at $1.55\ \mu m$ ($0.8\ eV$). This is shown in the work by Tea et al., see Figure 3.8 where the imaginary part of ε has been calculated in log scale as a function of the photon energy. The dielectric constant calculation was then limited to values above 0.1. It illustrates that strong absorption can occur at much lower photon energies of $\sim 1.7\ eV$ ($717\ nm$) for GaP with APBs in comparison to $\sim 2.5\ eV$ ($497\ nm$) for its bulk form. In addition, extrapolating this calculation with an exponential tail to $1.55\ \mu m$ gives an induced attenuation factor $\alpha_{APD} = 2\pi \times Im(\varepsilon)/\lambda n_{eff.grp}$ in the $1\ cm^{-1}$ order of magnitude for a measured APBs density of $8000\ mm^{-1}$.

The impact of APBs induced Q-factor on the Q_i for different attenuation values of α_{APD} is included in Figure 3.7 by rewriting Eq. 1.80 as:

$$\frac{1}{Q_i} = \frac{1}{Q_{rad}} + \frac{1}{Q_R} + \frac{\alpha_{APD}}{n_{eff.grp} k} \qquad \text{Eq. 3.2}$$

This analysis found that a value of $\alpha_{APD} \sim 2.5 \pm 0.2\ cm^{-1}$ allows matching perfectly between the experimental $\bar{Q}$ and the Q_i at $S_{c,long}$. This attenuation corresponds to a linear loss ($10\alpha_{APD}/\ln 10$) of $10 \pm 1\ dB\ cm^{-1}$ for the measured APBs density. The APB-limited Q_i is then calculated to be 4.5×10^4. We believe an order of magnitude in the range of 10^4 is a good first assessment of the APBs related losses. All loss contributions are summarized in Table 4. There has recently been an experimental demonstration of SHG in GaP nano-waveguides grown on III-V substrates with losses in the same range [195]. It ensures that our novel platform is compatible with the realization of practical individual nonlinear devices, especially at the lowest cost because of the Si substrate and the minimal III-V material deposition. In order to develop larger integrated photonic circuits in this defect tailored GaP/Si platform, the GaP membrane needs to be transferred onto dielectric substrates [38] and the technological processing must be refined to achieve APB-limited optical losses.

Loss contribution	Q-factor value	Details
Bending	$Q_{rad} > 10^6$	Theoretical, TE mode (Section 1.6.1, Figure 1.20)
Surface roughness	$Q_s \sim 10^6$	Theoretical, VCM, TE mode, $\sigma = 1\ nm$ RMS, $S_c = 75\ nm$ (Section 1.6.2, Figure 1.22)
Sidewall roughness	$Q_R \sim 10^4 - 10^5$	$S_{c,short} = 70\ nm$, $S_{c,long} = 650\ nm$, $\sigma_{comb} = 7\ nm$ RMS (Section 3.3.2, Figure 3.7)
APBs	$Q_{APD} \sim 10^4$	$\alpha_{APD} = 2.5\ cm^{-1}$ APB density $= 8000\ mm^{-1}$ (Section 3.3.2, Figure 3.7)

Table 4: Loss contributions associated with GaP/Si microdisks leading to an average intrinsic Q-factor of 8000.

3.4 APBs induced volume losses: NIR regime

As we mentioned in section 1.6.3, Tea et al. work is based only on stoichiometric APBs. The extrapolation of their work (see Figure 3.8) shows that the value of extinction coefficient $k_{ec} = Im(\varepsilon)/2n_{eff.grp}$ is multiplied by 550. Accounting for the factor of 2 in the wavelength, the value of $\alpha_{APD} = 4\pi k_{ec}/\lambda$ at $0.775\ \mu m$ should be 1100 times larger than the one at $1.55\ \mu m$. Thus, the stoichiometric APBs limited Q-factor (Q_{St}) at $775\ nm$ wavelength should be 1100 times smaller than at $1.55\ \mu m$, namely $Q_{St}(775\ nm) = 250$. This value is smaller than the NIR regime Q-factors ($\sim 10^3$) experimentally measured (see section 2.3.5). It suggests that the pure St-APBs-model is insufficient to explain our GaP/Si microdisks. Hence, a mixing of St-APBs and NSt-APBs could be considered with a constant density of states for NSt-APBs through the whole band gap and no shift of the band gap edge as for St-APBs [47]. Therefore, a different spectral dependence of the volume losses must be expected. However, Ref.[47] does not provide any calculation of the dielectric constant to go further in the modelization of the phenomenon. The understanding of the impact of APBs on the linear properties of confined modes thus requires further experimental and theoretical investigations in the future.

Summary

We have briefed the fabrication of APDs controlled monolithic GaP/Si microdisks and statistically analyzed various loss contributions limiting their performance in detail. The APDs distribution in the specific sample under scrutiny shows a mean polarity of 0.3 for $90\ nm$ sized minority domains with a $250\ nm$ distance between them on average. This should ensure a nonlinear frequency doubling efficiency of $10^{-3}\ mW^{-1}$, just one order of magnitude smaller than the ideal $\bar{4}$-QPM scenario in the absence of APDs. The roughness generated at the microdisk sidewalls during fabrication can result in two orders of magnitude optical losses. We found two roughness components possessing an individual RMS roughness of $5\ nm$, the random short-scale and the pseudo-periodical long-scale, that affect the intrinsic Q-factors with a roughness correlation length of $70\ nm$ and $650\ nm$, respectively. The latter is observed to be more severe in our GaP/Si microdisks in comparison which reduces the Q-factors down to 10^4 instead of 10^5 by the former. Further analysis to understand the measured average intrinsic Q-factors of 8000 estimated APBs induced linear losses in the GaP/Si platform based devices at $1.55\ \mu m$ to $10\ dB/cm$ ($\alpha_{APD} = 2.5\ cm^{-1}$). In addition, the difference between the measured NIR regime Q-factors and that predicted by the pure St-APBs theoretical model suggests that APBs in our samples have a composition of St-APBs and NSt-APBs. The loss analysis results give valuable feedback for the fabrication improvements of the random crystal polarity engineered GaP/Si

platform and promise its capabilities for the future development of integrated nonlinear photonic components at the manufacturer level.

4 Nonlinear frequency conversion in monolithically integrated GaP microdisks

Introduction

This chapter discusses the realization of nonlinear frequency conversions in GaP microdisks. The ultimate goal of this thesis was to demonstrate nonlinear effects based on random QPM in GaP/Si microdisks. The linear characterization of these microdisks in the SWIR and NIR regimes ensured their performance as a nonlinear frequency converter and their APDs distribution was tailored to favor random QPM. In this chapter, we first investigate SHG in GaP/$Al_{0.7}$GaP/GaP microdisks. In addition to the validation of our optical setup, this study is the opportunity to explore a microdisk design where strict $\bar{4}$-QPM should occur. In the second part, we explore the nonlinear properties of our GaP/Si microdisks and compare them to the properties of microdisks grown on native substrates.

4.1 Demonstrating strict $\bar{4}$-QPM in GaP/$Al_{0.7}$GaP/GaP microdisks

In a GaP/$Al_{0.7}$GaP/GaP platform, the GaP microdisks are technologically processed with $Al_{0.7}$GaP pedestals on a GaP substrate. The spontaneous emergence of interfacial defects such as APDs will not occur in these samples due to the use of native substrates. In addition, the lattice parameters of both GaP and $Al_{0.7}$GaP materials are sufficiently close to ensure defect free growth. Their detailed fabrication is described in Appendix A, section A.2. These microdisks were made by the OHM research group a few years ago, from which their technological processing evolved in the later years as briefed for recently fabricated GaP/Si microdisks (Appendix A, section A.1) [48]. Hence, they possess slightly low Q-factor values as mentioned in section 2.3.2.

4.1.1 Mode indexation and QPM schemes

The transmission study was conducted on a GaP/$Al_{0.7}$GaP/GaP microdisk with a radius of $4.5\ \mu m$ and a thickness of $130\ nm$. In the SWIR band, we used the experimental setup described to linearly characterize the microdisk samples (see Figure 2.14 in section 2.3.1). The spectrum obtained is shown in Figure 4.1 and a fit to the resonant mode at $1547.71\ nm$ gives a Q-factor of 2100 ± 100 as given in Figure 4.1(inset). We will take advantage of this mode (pump resonance) to inject power into the microdisk for SHG. The TM modes are not supported in this wavelength regime due to the small thickness and radius of the microdisk. In the NIR band, the transmission characteristics are obtained using the experimental setup illustrated in Figure 2.21 (section 2.3.4) with OSA resolution set to $0.2\ nm$. We are not only able to extract the TM spectrum of the microdisk (see Figure 4.2) but also the TE resonances in the NIR region (not shown for the sake of clarity). The fit for TM resonant modes close to the half wavelength of pump mode (SH resonance) presented in Figure 4.2(inset) gives Q-factors of 810 at $772.0\ nm$ and 1785 at $775.1\ nm$.

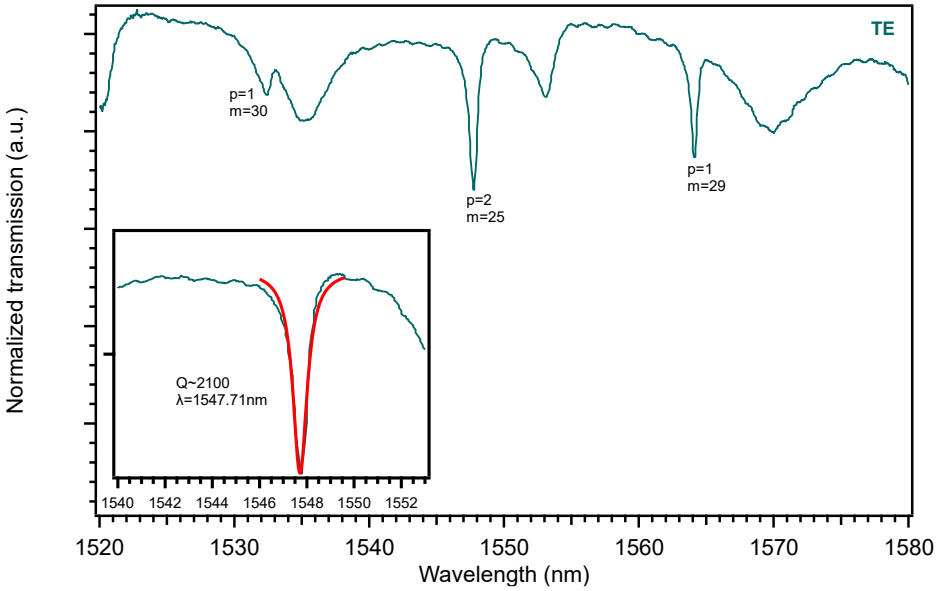

Figure 4.1: The SWIR transmission spectrum of GaP/$Al_{0.7}$GaP/GaP microdisk. Inset: The Q-factor extracted from the pump resonance.

The mode indexation can be used to predict the pump and SH resonances involved in the SHG. Therefore, FEM simulations are initially conducted in the SWIR to match the experimental FSR of the resonances with minor adjustments over the geometrical parameters of the microdisk under investigation, in good agreement with its SEM characterization. Later, these values are used within

simulations in the NIR range leading to the indexation of resonances as shown in Figure 4.1 and Figure 4.2. It seems that the TE mode ($p = 2,\ m = 25$) at $1547.71\,nm$ and the TM mode ($p = 2,\ m = 52$) at $775.1\,nm$ can satisfy the strict $\bar{4}$-QPM condition $m_{SH} - 2m_p = +2$, but with a wavelength detuning of $2.4\,nm$ comparable to the work reported by Kuo et al. [33]. In addition, this configuration will involve pump and SH resonances with radial orders $p = 2$. This could impact the efficiency of the SHG phenomenon compared to strict $\bar{4}$-QPM with $p = 1$ resonances. In the following section 4.1.2, we will discuss the method used to demonstrate the nonlinear interaction between these modes for frequency doubling.

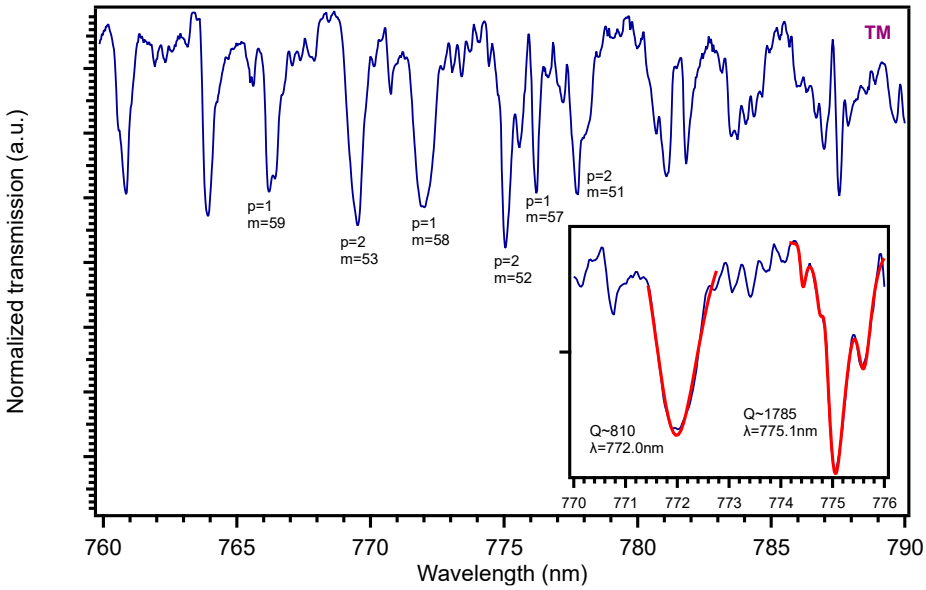

Figure 4.2: The TM transmission spectrum of GaP/$Al_{0.7}$GaP/GaP microdisk in the NIR regime. Inset: The Q-factors extracted from two resonant modes.

4.1.2 Experimental setup for nonlinear characterization

An experimental setup is configured to pump the GaP/$Al_{0.7}$GaP/GaP microdisk with high power for the generation of nonlinear signals as depicted in Figure 4.3. This system consists of a narrowband ($< 200\,kHz$) tunable laser source (Agilent 8164A Lightwave Measurement System) for wavelength sweeps in the SWIR region ($1544.4 - 1545.6\,nm$). The laser output is then pulse modulated using an acousto-optic modulator (AOM) (AA Opto-Electronic) for peak power enhancement. The AOM is driven by an RF driver (AA Opto-Electronic) which is controlled by a digital pulse generator (DG535, Stanford research systems, Inc.) producing square waves of pulse-width $3\,\mu s$ and frequency of $100\,kHz$. An Erbium-Doped Fiber Amplifier (EDFA) (Amonics) is operated thereafter for amplifying the

pulsed signals to obtain a peak pump power of $32 - 219\,mW$ recorded by a power meter (EXFO, FPM-300). The average power (thus the peak power) is varied by changing the current supplied to the internal pump laser diodes of EDFA. The power is injected into the microdisk pump resonant mode through a dimpled fiber taper. The fiber taper-microdisk coupling is assisted by the $50\times$ magnifying microscope and precision linear-angular stages as discussed in section 2.3.1 with a detailed description of coupling steps. Once the SHG is detected, the pump polarization is optimized by a polarization controller to maximize the nonlinear output. The generated signals are collected from the microdisk through the same dimpled fiber taper and spectrally resolved using a spectrometer (StellarNet Inc, BLUE-Wave UVIS-50) with a fixed resolution of $1.6\,nm$ and an operational range of $285 - 1136\,nm$. The power measurements are performed by a silicon photodiode power sensor (S130VC, Thorlabs) associated with a short wavelength pass ($<$ $800\,nm$) filter (FES0800, Thorlabs). An OSA (MS9710B, Anritsu) connected at the output end of the dimpled fiber taper monitors the pump transmission profiles. The power of the nonlinearly interacting signals mentioned hereafter is defined by the peak power in the fiber taper immediately before the coupling region and after loss compensation.

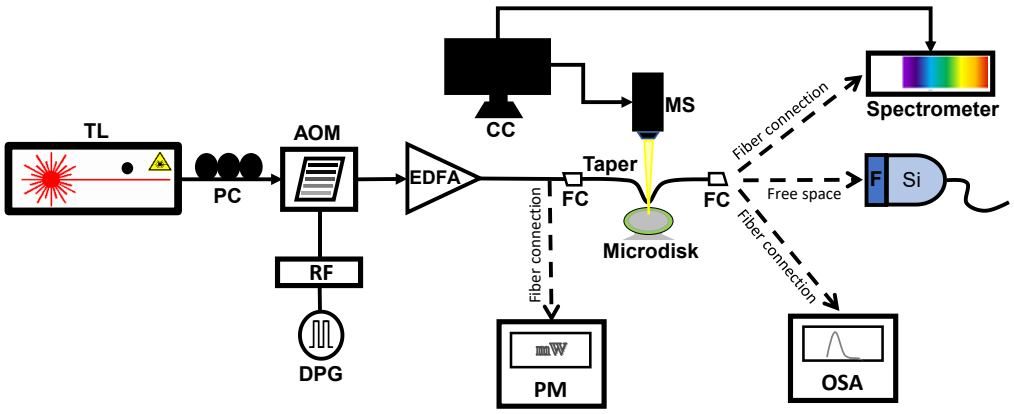

Figure 4.3: Schematic of the experimental setup used for the nonlinear characterization of microdisks. TL: Tunable laser, PC: Polarization controller, AOM: Acousto-optic modulator, RF: RF driver, DPG: Digital pulse generator, EDFA: Erbium Doped Fiber Amplifier, PM: Power meter, FC: Fiber connector, MS: Microscope, CC: Computer control, OSA: Optical Spectrum Analyzer, F: Short wavelength pass filter, Si: Silicon photodiode power sensor.

4.1.3 SHG by $\bar{4}$-QPM

Nonlinear emissions are observed by positioning the laser close to the $(p = 2, m = 25)$ pump resonance as shown in Figure 4.4. The signals generated in our case are SHG close to half of the pump wavelength and a higher order generation of around one-third of the pump wavelength. Once the SHG is detected in the spectrometer, the TE pump polarization is explicitly optimized using a polarization controller for better signal strength. In addition, the coupling is adjusted by moving the fiber taper for delivering pump power efficiently into the microdisk. In this coupling condition, the SH resonance is weakly coupled to the fiber taper and transmission measurement in the NIR regime is out of reach (see section 2.3.2 in chapter 2 for details). Also, the relocation of the fiber taper may create a complex situation since it leads to the spectral shift of both pump and SH resonances. The energy mismatch between them can be positively or negatively impacted as a result [33]. Finally, the pump wavelength is also scanned at the maximum power to find the maximized nonlinear output. After these experimental optimizations, we found that the maximum SHG is observed when the pumping wavelength is at $1545\ nm$.

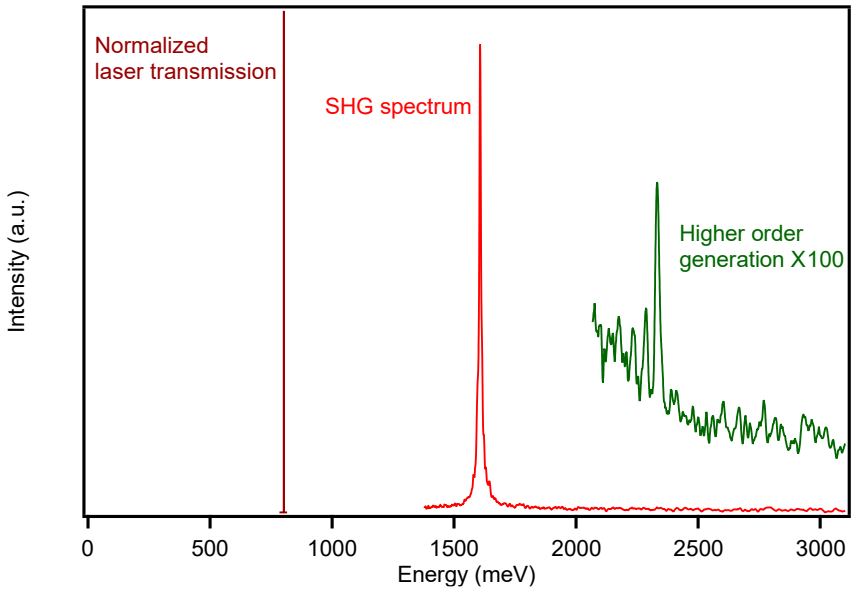

Figure 4.4: Intensity spectra of the pump laser line, SHG and higher order generation received at the output of the fiber taper. The SHG and higher order generation are recorded at $50\ ms$ and $500\ ms$ integration time, respectively.

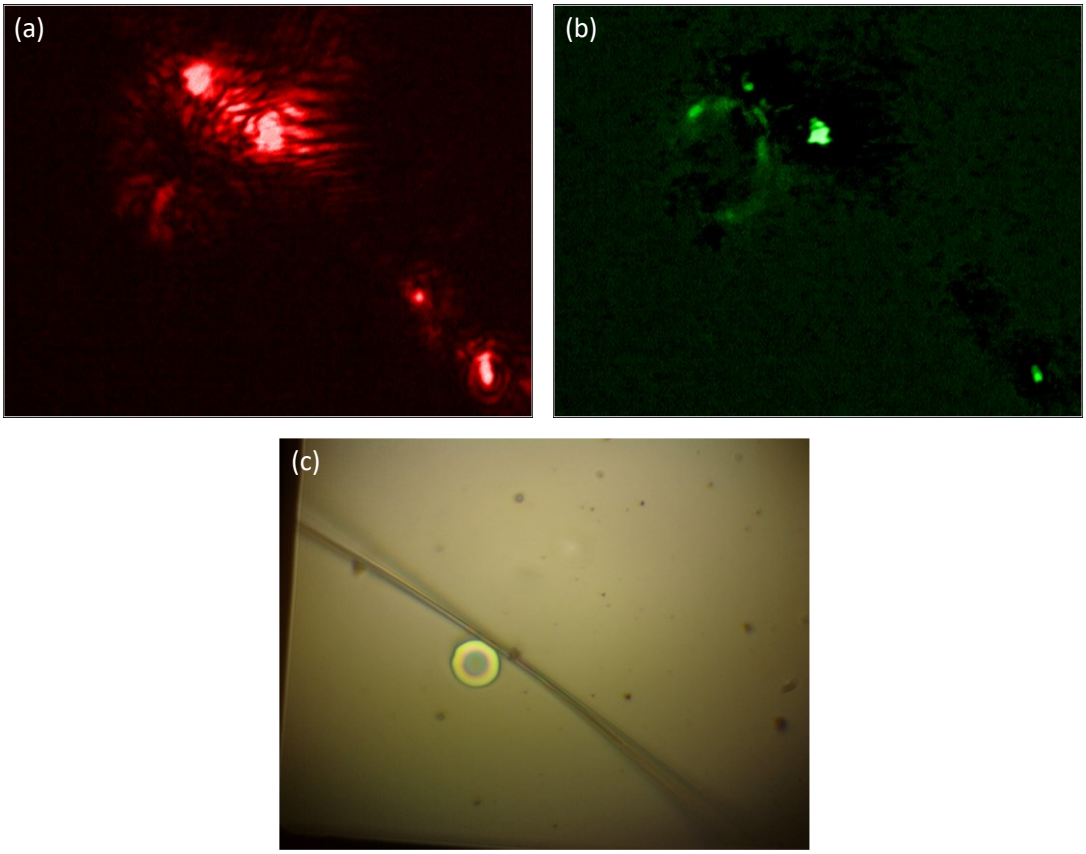

Figure 4.5: Image of (a) SHG and (b) higher order generation at a maximum pump power of $219\ mW$ obtained by digitally processing the microscope captured RGB image without gamma correction. (c) Coupled fiber taper-microdisk system used for frequency upconversion.

Once the frequency conversion occurs the microscope camera captures any visible colors emerging from the microdisk. The naked eye can also detect the color glows in the microdisk depending on the signal strength. We have not only observed a strong red glow but also a light shade of green as can be seen in Figure 4.5(a), (b). We preferred to adjust the fiber taper position to the top edge of the microdisk for better measurement stability, repeatability and increased coupling, as displayed in Figure 4.5(c). Notice that the fiber taper has few diffusion points that may occur while tapering, but they are far from the coupling zone. As we mentioned in section 4.1.1, the SH resonance which can be involved in the SHG process by $\bar{4}$-QPM is a $(p = 2,\ m = 52)$ WGM. However, we cannot completely rule out the participation of the $(p = 1,\ m = 58)$ resonant mode at $772.0\ nm$ in this nonlinear frequency conversion which is also seemingly closer to the half wavelength of pump mode with an initial wavelength detuning of $3.7\ nm$. Fano profiles are often observed in our GaP/$Al_{0.7}$GaP/GaP microdisk samples which can indeed lead to a large coupling of the observed resonances to other modes via the fiber taper [196][197][61].

The discrepancy of the wavelength measured for the SHG at $771.5 \pm 0.4\,nm$ with the theoretical value can be attributed to the calibration issues of the spectrometer which is optimized for the wavelength range $400 - 700\,nm$. The higher order generated at $531.4 \pm 0.4\,nm$ is however far ($\sim 16\,nm$) from the expected direct third harmonic generation (THG) wavelength, slightly above the band gap edge of GaP. We assume its origin as the sum frequency generation, either between the EDFA background and the SHG signal or between the EDFA pumping peak and tail of the SHG signal. In general, it is challenging to achieve the proper combination of phase matching considering the strong chromatic dispersion of the GaP material and resonance distribution at the THG wavelength. The existing experimental setups do not have a tunable laser that is capable of accessing this visible wavelength range for transmission spectroscopy. Therefore, it was difficult to further investigate this detuned signal. The requirement of handling a very thin fiber taper with a cut-off diameter of less than $573\,nm$ for this wavelength band increases the experimental complexity. In addition, it is practically impossible during the nonlinear frequency conversion experiments to ensure an efficient fiber taper-microdisk coupling simultaneously at all wavelengths of interest for a particular coupling location as discussed in section 2.3.2. It is worth noticing that the simultaneous presence of SHG and direct THG was already observed in the GaP microcavity [198]. Recently, it has been reported for the coexistence of direct THG and cascaded SFG as THG signal along with the SHG while pumping at the telecom window [199].

4.1.4 SHG efficiency

Comparing the spectra of the generated nonlinear signals (Figure 4.4 in section 4.1.3), the SFG is found to be more than two orders of magnitude smaller than the SHG obtained. Therefore, it does not impact significantly the SHG power measurements and we neglected its contribution for further analysis in this work. A photodiode power sensor combined with a short wavelength pass filter is utilized to measure the power of the frequency doubled signal generated as a function of pump power. This system can block any pump residuals from reaching the sensor. A log-log plot corresponding to this measurement is given in Figure 4.6. We have observed theoretical quadratic power dependence for SHG at low pump powers up to $69\,mW$. Thereafter, a deviation larger than quadratic occurs until the pump power reaches $113\,mW$ where the SHG power evolution returns to satisfy again almost a quadratic law. This behavior can be attributed to the pump power induced shift in the cavity resonance due to the thermo-optic effect [200][201][202]. In our case, the pump wavelength is fixed close to the longer wavelength side of the cavity pump resonance. The cavity starts to heat up once the pump power gets sufficiently high and the resonance shifts to longer wavelengths due to the thermo-optic effect induced refractive index change. At this stage, the resonance experiences an

improved overlap with the pump wavelength and the intracavity energy increases to observe an over quadratic behavior. Finally, this effect ends at very high pump powers and the curve recovers quadratic. It occurs when the shift in resonance begins to slip away from the pump wavelength. Similar non-quadratic behavior was reported for SHG in GaAs photonic crystal cavities [203]. The intracavity photothermal temperature tuning of cavity resonances for efficient SHG by achieving double resonance was already reported for GaP microdisks [58]. The thermo-optic effect we have recorded can be further confirmed by scanning the pump wavelength at different pump powers in the increasing and decreasing wavelength directions as shown in Figure 4.7. The redshift of the cavity resonance and asymmetric response obtained thus validate the hypothesis of a photothermal effect [200][201]. However, bistability behavior is not evidenced in our experiment as we do not satisfy the bistability condition due to the moderately high Q-factors of the resonances [81]:

$$|\Delta_{bistability}| > \frac{\sqrt{3}}{2}\delta\lambda \qquad \text{Eq. 4.1}$$

where $\Delta_{bistability}$ is the detuning between the pump resonance and pump wavelength, and $\delta\lambda$ is the FWHM of the pump resonance. Note that bistability is rather a drawback as far as nonlinear frequency conversion of high frequency data flux is concerned.

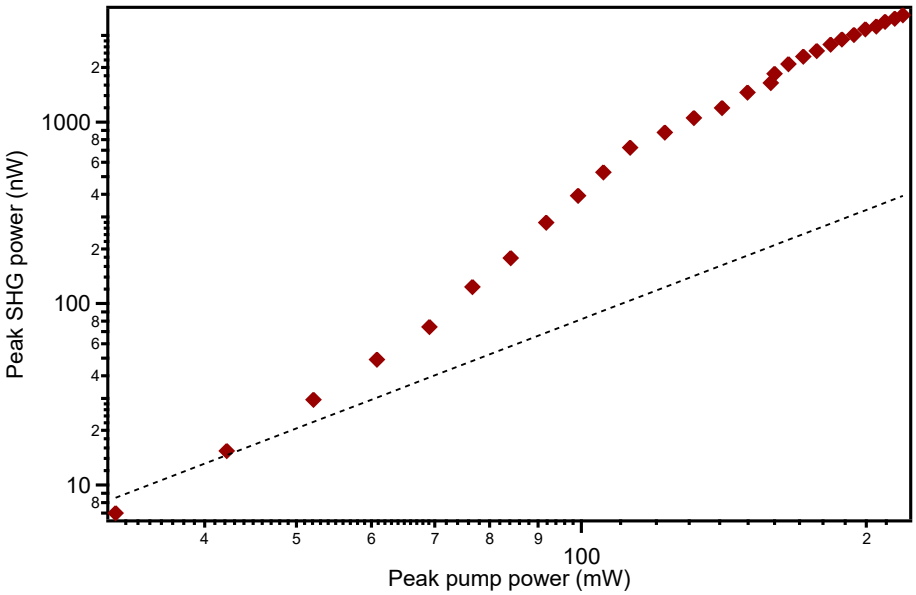

Figure 4.6: The double log plot describes the evolution of SHG power with pump power. The pump power is increased from $\mathbf{32 - 219\ mW}$. The dashed line represents ideal quadratic behavior.

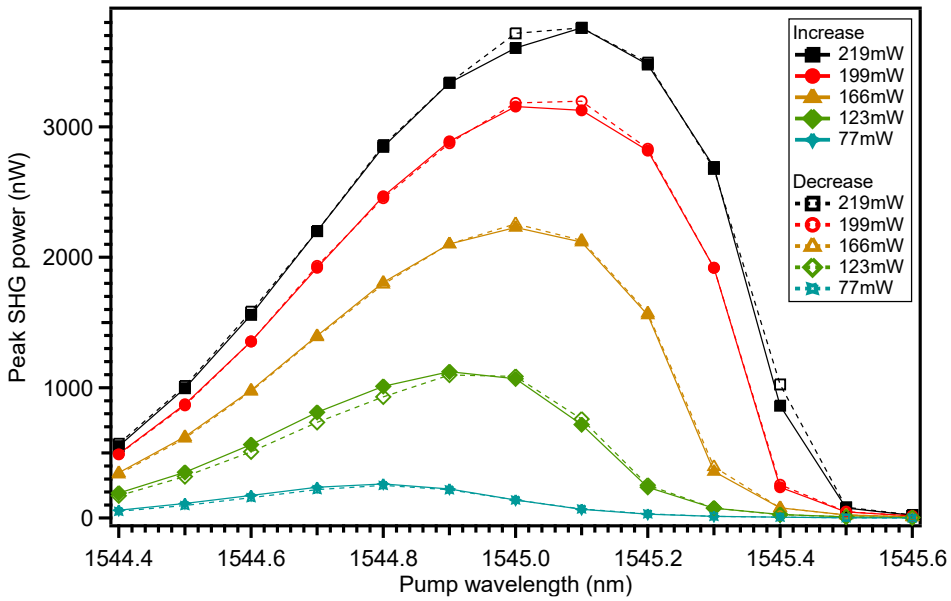

Figure 4.7: The variation of SHG power while detuning the pumping wavelength from the pump resonance in both forward and backward directions at different pump powers.

It is possible to model the over quadratic response and recovery of quadratic variation in Figure 4.6 along with the asymmetric shape of the curves in Figure 4.7 using CMT. We have considered the coupled mode equations of the pump and SH modes as described in Ref.[204]. The thermo-optic effect is introduced by incorporating the normalized thermo-optic coefficients of GaP, $3.4 \times 10^{-5}\, K^{-1}$ for the pump mode and $2.9 \times 10^{-5}\, K^{-1}$ for the SH mode [205][58]. Also, the detuning of these interacting modes with the pumping wavelength is considered. The qualitative plots thus obtained under the critical-coupling assumption for both modes are shown in Figure 4.8. The low Q-factor of the pump mode predicted by Figure 4.8 indicates that we have slightly overestimated it experimentally. However, residual bistability can be observed in Figure 4.8(b) at high pump powers even for this low Q-factor, probably due to the critical-coupling assumption [205]. Otherwise, the experimental coupling configuration is far from the critical-coupling regime. The SH mode in this model inherited the details of the shorter wavelength resonance shown in Figure 4.2(inset). The CMT model validates our experimental observations by recreating them as the mode dynamics of the cavity itself and thus an argument over the possibility of any experimental artifacts is nullified.

The observed nonlinear frequency doubling process is further analyzed to determine the conversion efficiency by taking into account external losses such as the transmission loss of the fiber taper in the SWIR and NIR bands, fiber connector loss in the SWIR band, filter transmission response for the SHG wavelength and

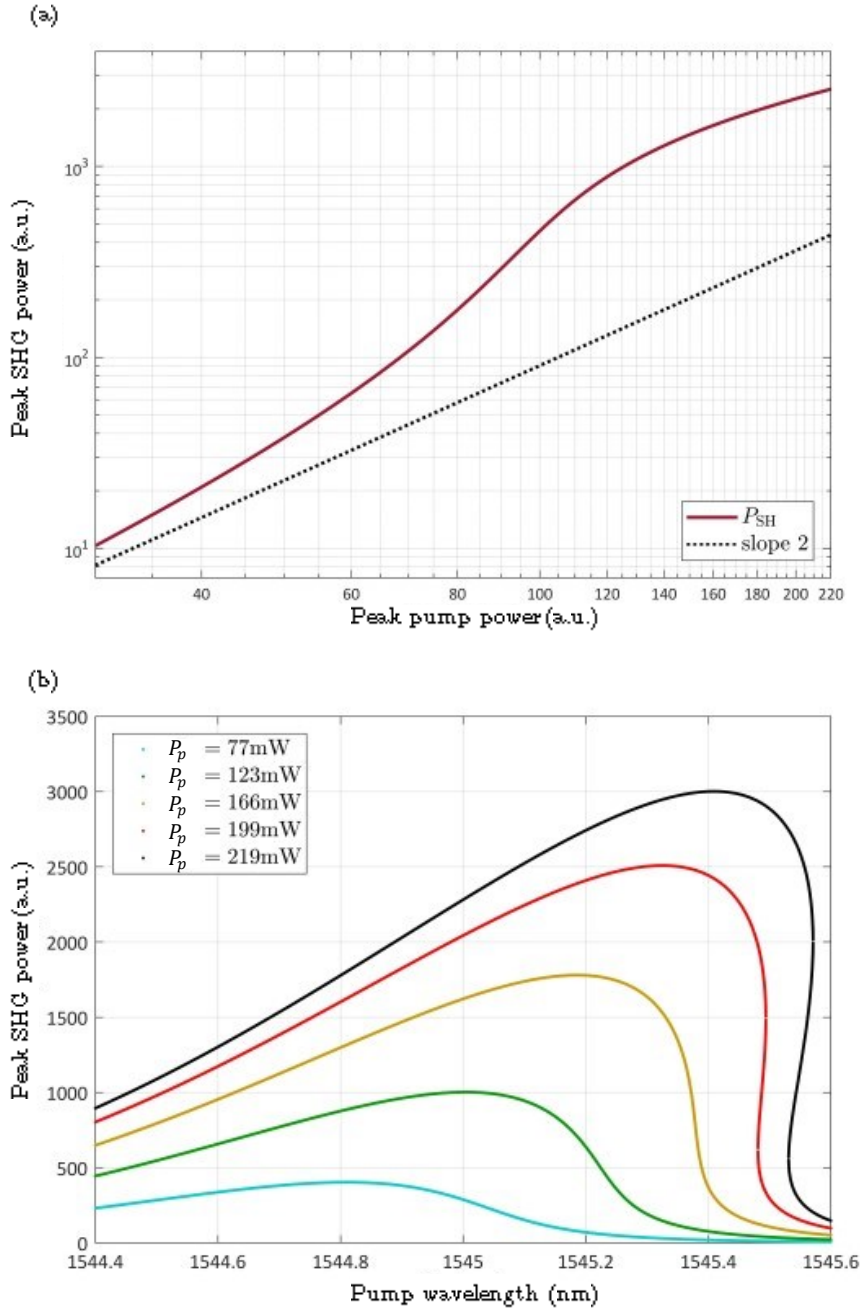

Figure 4.8: The CMT model showing the evolution of (a) SHG power with the pump power ($\mathbf{32-219}\,\boldsymbol{mW}$) and (b) SHG power as a function of the pumping wavelength for different pump powers. The parameters are pump mode at $\mathbf{1544.54}\,\boldsymbol{nm}$ with a Q-factor of **1500**, SH mode at $\mathbf{771.99}\,\boldsymbol{nm}$ with a Q-factor of **800**, and the pumping wavelength at $\mathbf{1545.1}\,\boldsymbol{nm}$. $\boldsymbol{P_{SH}}$: Peak SHG power and $\boldsymbol{P_p}$: Peak pump power.

the divergence of the SHG signal arriving in front of the power sensor area. We measured a peak pump power of $219\ mW$ and SH signal power of $4\ \mu W$ in the fiber taper immediately before the coupling region, giving a normalized external conversion efficiency of $8.14 \times 10^{-3}\ \%W^{-1}$. It is important to compare this result with a similar work reported by Lake et al. [58] in GaP microdisks. In their work, the normalized external conversion efficiency of $38\ \%W^{-1}$ was obtained for a $\bar{4}$-QPM coupled to radial modal QPM configuration with the pump resonance ($p = 1,\ m = 27,\ Q_i = 1.1 \times 10^5$) at $1545\ nm$ and SH resonance ($p = 3, m = 56, Q_i = 9600$) at $772.2\ nm$. In addition, photo-thermal temperature tuning is utilized to achieve a doubly resonant cavity. Recalling our case, the telecom to visible wavelength conversion is demonstrated between a pump resonance ($p = 2, m = 25, Q_i = 2100$) at $1547.71\ nm$ and SH resonance ($p = 2, m = 52, Q_i = 1785$) at $775.1\ nm$. As discussed in section 1.4.2, the TM polarized SH field (E_{SH}) can result from the square of either the spin up (E_+^2) or spin down (E_-^2) component of the pump field according to the TSAM formalism. Thus, the overlap coefficient given by Eq. 1.64 can be directly attributed to the overlap integral of these components involved in the SHG process [40][95][96][97][98]. The radial profiles of these components for different radial number configurations are shown in Figure 4.9(a), (b) and (c). The resulting field overlap is given in Figure 4.9(d). The combination of components E_+^2 and E_{SH} with $p = 1$ has the best overlap as shown in Figure 4.9(a). Nevertheless, this nonlinear interaction corresponding to additional $+2$ quanta is forbidden due to strong material and structural dispersions [39][40][95]. Then, the next possible combination involves E_-^2 and E_{SH} components with $p = 1$, which corresponds to additional -2 quanta [40][95]. In our frequency doubling process, strict $\bar{4}$-QPM is achieved with the pump and SH field sharing the same radial confinement number of 2 as given in Figure 4.9(b). If this configuration is far from being the optimal case of strict $\bar{4}$-QPM compared to the $p = 1$ case (see Figure 4.9(d)) [39], the inner lobe of the SH resonance keeps a nonnegligible overlap with squared E_+ and E_- components. Comparing now to the case of Ref. [58], there is a strong negative contribution in the E_{SH} component close to the maximum of E_+^2 and E_-^2 components in Figure 4.9(c). This is evident in their field overlap depicted in Figure 4.9(d). Calculating the conversion efficiency in all SHG configurations with the same Q-factors and normalizing it with the $p = 1\ K_+^2$ case, the impact of the Q-factor can be removed to investigate the effect of field overlap. Analyzing this normalized conversion efficiency presented in Figure 4.9(e), the overlap coefficient in our case can offer a conversion efficiency of just one order of magnitude below the best possible configuration and a factor of 20 better than the work by Lake et al. The Q-factor difference between these two works corresponds to a factor of 12000 in the conversion efficiency which would raise the conversion of the $p = 2$ strict $\bar{4}$-QPM scheme to about $100\ \%W^{-1}$. This is still below the factor 20 predicted by our calculation but it is already a very promising result. It is reported by Kuo et al. [94] work that a $\sim 5\ nm$ detuning can lead to a ~ 1000 drop

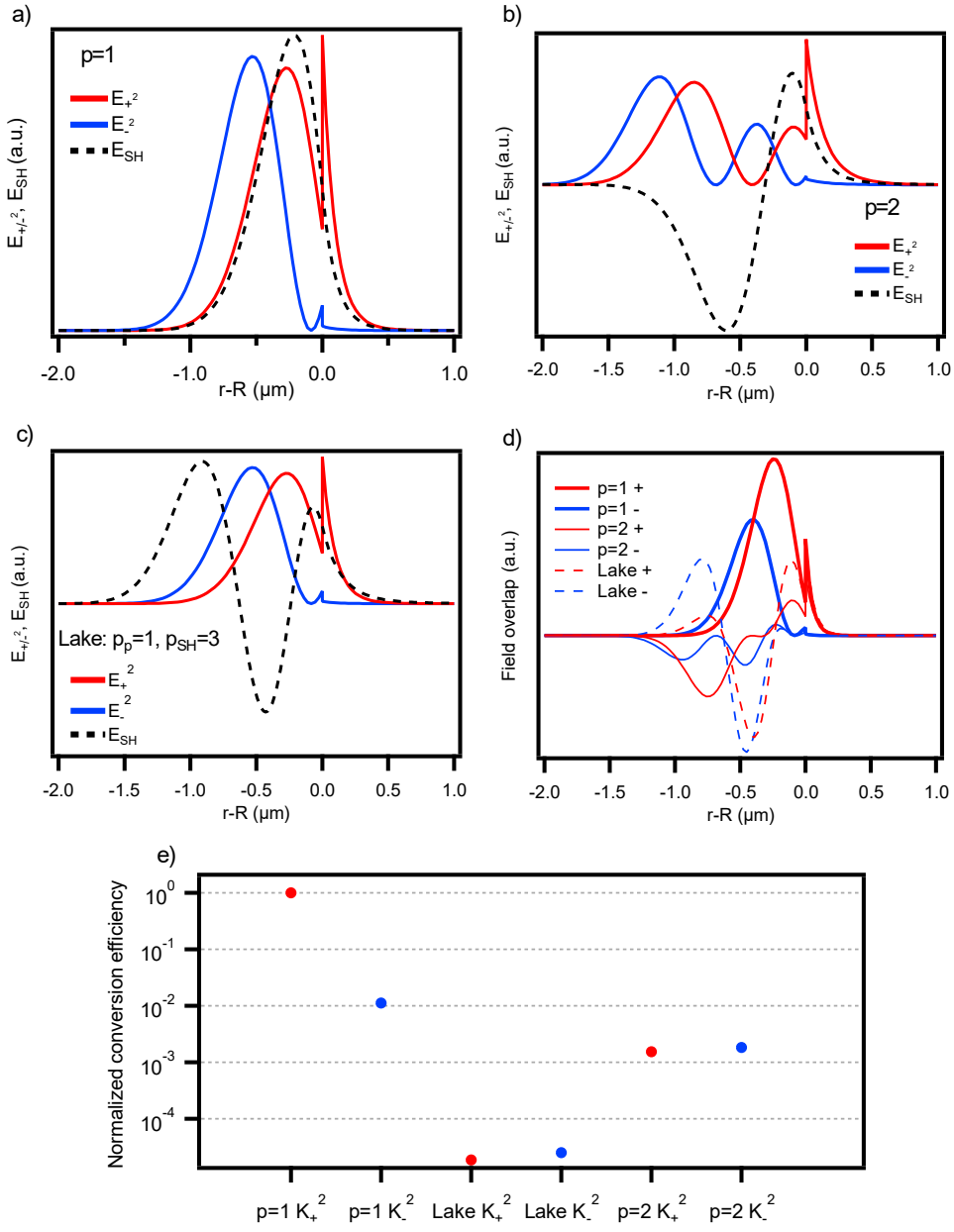

Figure 4.9: Radial profiles of the components $\boldsymbol{E_+^2}$, $\boldsymbol{E_-^2}$ and $\boldsymbol{E_{SH}}$ for different SHG configurations. (a) Strict $\bar{\boldsymbol{4}}$-QPM with $\boldsymbol{p = 1}$. (b) Strict $\bar{\boldsymbol{4}}$-QPM with $\boldsymbol{p = 2}$. (c) Lake et al. case. (d) Field overlap of the components $\boldsymbol{E_+^2}$, $\boldsymbol{E_-^2}$ and $\boldsymbol{E_{SH}}$. (e) Normalized conversion efficiency associated with each configuration. r: radial position and R: microdisk radius.

in the conversion efficiency. Considering that our cavity is non-doubly resonant with an initial detuning of $2.4\,nm$, the remaining factor of 8 can be explained with a factor of 2 for detuning and 4 for all the uncertainties. Such a comparison indicates that our microdisk does not achieve a doubly resonant state even using thermo-optic tuning of the resonances, probably due to limited pump laser power.

This investigation finally suggests that we should be able to find an experimental configuration with $p = 1$ in this system giving much better efficiency, provided that Q-factors can be also improved along with achieving a double resonance. In the following section 4.2, this successfully demonstrated experimental setup is utilized for the nonlinear characterization of GaP/Si microdisks which possess better Q-factors and RQPM capability for relaxed efficient frequency conversions.

4.2 Nonlinear characterization of APDs tailored GaP/Si microdisks

The GaP/Si microdisks linearly characterized in chapter 2 provides a set of microdisks suitable for the nonlinear frequency conversions (see Table 3 in section 2.3.5). In comparison with GaP/$Al_{0.7}$GaP/GaP microdisks, they possess larger Q-factors in the order of 10^3-10^4 for pump resonances and 10^2-10^3 for SH resonances. Thus, we could expect conversion efficiencies close to the one observed for the GaP microdisks of section 4.1. However, it was difficult to identify the polarization and the indexation of modes in the NIR regime due to the existence of much denser modes and the recorded "messy" spectra due to the larger thickness of our GaP/Si microdisks compared to the investigated GaP/$Al_{0.7}$GaP/GaP microdisks as illustrated in chapter 2. This prevents us from predicting the RQPM nonlinear dynamics directly. Nonetheless, it is practically possible to pump the TE resonances of these microdisks in the SWIR regime while monitoring the NIR/visible regime with a detector to uncover any frequency conversions [199]. We chose a $250\,nm$ thick GaP/Si microdisk of radius $2\,\mu m$ and followed the same coupling procedures using a dimpled fiber taper for the nonlinear experiment as explained in section 4.1.2. The SWIR transmission response of this specific microdisk is shown in Figure 4.10(a). The pumping performed at a maximum power of $219\,mW$ on a TE resonance ($p = 1$) at $1555.71\,nm$ is found to be generating a pale green glow at the microdisk edge in the form of WGMs. In the expected SHG regime, we could not apparently notice any signal and our microscope setup lacks a dedicated color filter. Despite this observation, it was unable to collect the signal into a spectrometer and power meter using the same injection fiber taper as successfully carried out for the GaP/$Al_{0.7}$GaP/GaP microdisk. In order to enhance the signal by injecting high pump power, the tunable laser-EDFA system in the setup (see Figure 4.3) is replaced with a picosecond laser (PriTel). Its primary output is

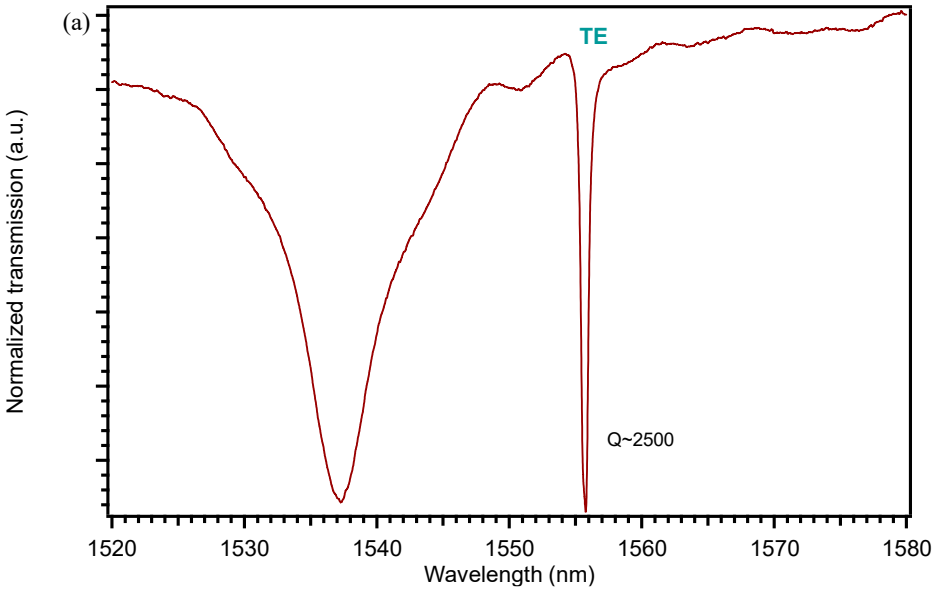

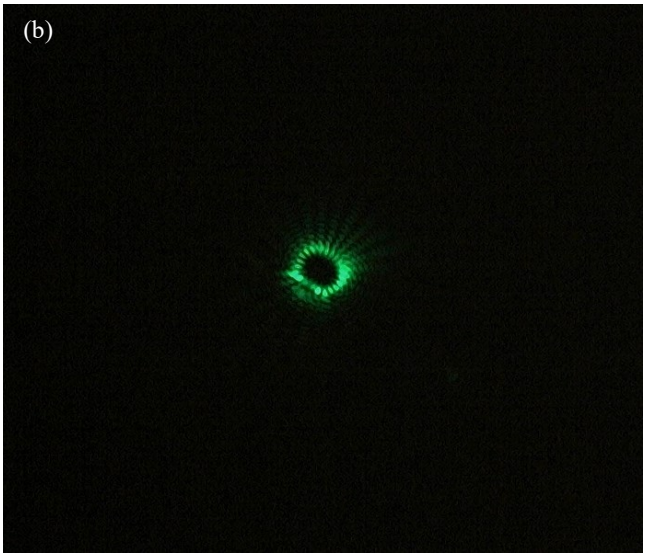

Figure 4.10: (a) SWIR transmission spectrum of a GaP/Si microdisk used for nonlinear investigations. (b) RGB image of the green signal captured by the microscope.

followed by a polarization controller directly connected to the input end of the fiber taper. The OSA is now connected to the secondary output of the laser to monitor spectral pump profiles. The laser is operated at a $10\,ps$ pulse width and $20\,MHz$ repetition rate. The peak pump power can be tuned from $400\,mW$ to $3.4\,W$ by varying the current supplied to the internal diode laser of the picosecond laser. We observed the same green signal but with high intensity as shown in Figure 4.10(b). Around 26 lobes are roughly countable from the edge of the microdisk, similar to WGMs in the SWIR regime. If the image is processed for RGB layers, they show

identical patterns. Once the polarization and the fiber taper-microdisk coupling location are optimized for the TE pump, maximum signal strength is observed when the pump laser wavelength is at $1555.08\,nm$. The coupling of this magnificent signal from the microdisk towards the detectors went unsuccessful again with a single fiber taper. The non-optimized coupling of fiber taper for NIR and visible regions in comparison to the pump injection could be a possible reason for this inability (see section 2.3.2). As mentioned above, the GaP/Si microdisks are thicker than GaP/$Al_{0.7}$GaP/GaP microdisks, which also complicates the coupling of these modes. Moreover, the requirement of a very thin diameter for the highly fragile dimpled fiber taper to operate in single mode at these wavelengths is also a practical constraint (see section 2.2.1).

A series of microscope images are captured by tuning the pump wavelength across with maximum power. Furthermore, the pump power is increased by fixing the pumping wavelength close to the longer wavelength side of the cavity pump resonance. These images are then processed as plotted in Figure 4.11. The evolution of the generated signal with pump wavelength is found to be resonantly enhanced. The variation with the pump power seems linear in the $1-3\,W$ range. The observed signal intensity grows ~ 5.5 times for the range $0.5-1\,W$. At low power (below $0.5\,W$), the experiment is limited by the low sensitivity of the microscope camera. It is thus practically difficult to extract the nonlinearity exponent of the evolution at low powers. A blueshift for the pump resonance and photodegradation of its Q-factor is noticed in some of our GaP/Si microdisks during the prolonged pumping at a high power of $3.4\,W$ [206][207]. This is an indication of free carrier generation induced refractive index change and the heating effects damaging the microdisk internally. However, it is hasty to conclude at this stage the origin of the generated visible signal without spectra and proper power evolution investigations over several decades using a power meter. Such a study would be especially important because APB planes present in the GaP/Si microdisks can act as deep-level traps for charge carriers within the forbidden gap modifying the absorption properties [51] as discussed in section 3.3.2 and the high power operation can simultaneously excite various nonlinear effects in the medium [208]. At this stage, three plausible scenarios can be drawn to explain the observed signal:

- The large thickness of the GaP/Si microdisks under scrutiny prevents the second harmonic signal from being collected by the dimpled fiber taper used. Only poorly confined higher order nonlinear signals, as observed in section 4.1.3 for GaP microdisks on native substrates, can be recorded through the microscope setup.
- APBs induced absorption in the band gap of GaP/Si generates carriers that are further excited towards the GaP conduction band due to the very high field density within the microdisk, leading to band gap edge

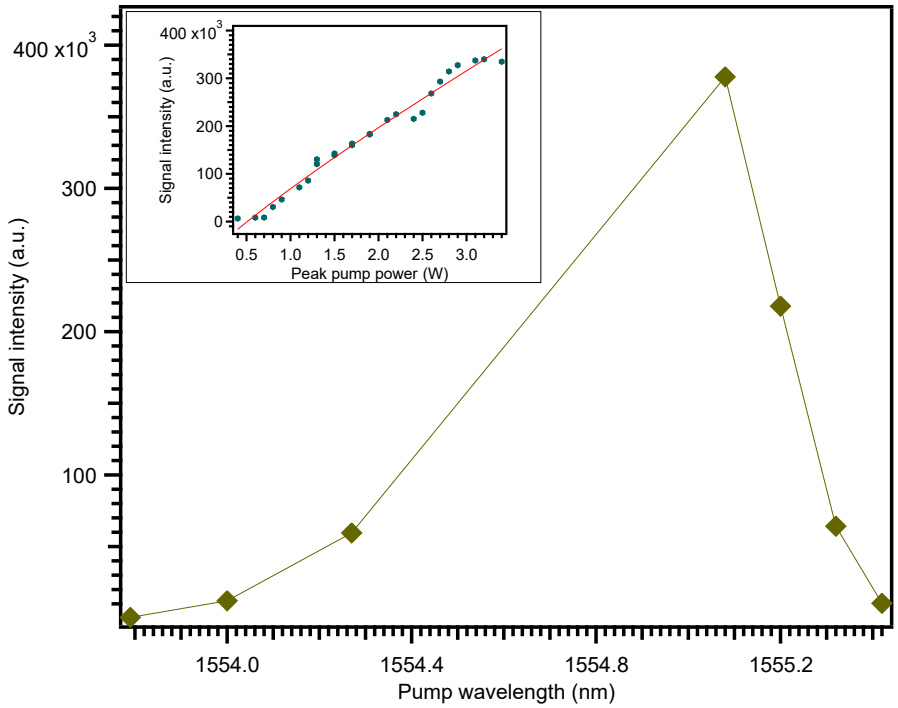

Figure 4.11: The intensity of the generated signal as a function of the pump wavelength and pump power (inset). The asymmetric curve obtained while scanning the pump wavelength reveals the thermo-optic effect induced pump resonance shift in the microdisk. In the inset, the curve seems roll off at high pump powers probably due to distortion of the pump resonance or its large shift resulting in decoupling from the laser.

emission. Spectral analysis of the observed signal should allow us to conclude this hypothesis.

- If the second order QPM is still out of reach despite the RQPM in GaP/Si microdisks that could offer SHG and thus a cascaded THG, then the possibility of phase matched direct THG due to the $\chi^{(3)}$ nonlinearity at high power operations could not be ruled out.

Finally, we should emphasize the high damage threshold of most GaP/Si microdisks, standing $3.4\,W$ peak powers of pulsed excitation. This is particularly promising for high power applications based on GaP photonics.

Summary

In this chapter, we have discussed the nonlinear characterization of very thin GaP/$Al_{0.7}$GaP/GaP microdisks to investigate strict $\bar{4}$-QPM. A strict $\bar{4}$-QPM is demonstrated only between resonances with radial order $p = 2$, far from being an optimal configuration. Still, the calculation shows this configuration is more

promising than most other $\bar{4}$-QPM coupled to modal configurations reported so far. Experimentally, our system remains limited due to the small Q-factors of the resonances in the GaP/$Al_{0.7}$GaP/GaP microdisks fabricated compared to the state-of-the-art and we could not find a doubly resonant configuration. As far as GaP/Si microdisks are concerned, their nonlinear characterization for investigating random QPM reveals emission in the green wavelength range, similar to the SFG signal observed in GaP microdisks on native substrates. However, no nonlinear emission is coupled to the dimpled fiber taper used in this experiment. Further investigation will be needed to identify the origin of this emission.

Conclusion

In this work, we have reported the optical loss analysis and the demonstration of the SHG process in monolithically integrated suspended GaP microdisks. Two types of microdisk samples were investigated, GaP/Si and GaP/$Al_{0.7}$GaP/GaP. The GaP/Si sample contains thick microdisks fabricated recently with e-beam lithography and dry-etching stages which contain tailored APDs due to polar on non-polar epitaxy enabling RQPM for the SHG process. The GaP/$Al_{0.7}$GaP/GaP sample of thin microdisks was fabricated a few years ago using photolithography and wet-etching steps to demonstrate the $\bar{4}$-QPM assisted SHG process. The samples were characterized linearly and nonlinearly using optimized optical fiber tapers offering a large evanescent field considering under-coupling. The transmission spectroscopy in the SWIR (NIR) regime reveals that the Q-factors of the GaP/Si microdisks are in the order of $\sim 10^4$ ($\sim 10^3$) while GaP/$Al_{0.7}$GaP/GaP microdisks are in the order of $\sim 10^3$ ($\sim 10^2 - 10^3$), probably due to the difference in the fabrication process.

The performance of optical devices carved out of these platforms is dependent on various optical losses. We have investigated loss contributions in the GaP/Si microdisks statistically using Q-factors measured in the SWIR band with an average value of 8×10^3. Other than the inevitable bending induced losses ($Q_{rad} > 10^6$) and the negligible polished surface roughness ($< 1\,nm$ RMS) induced losses ($Q_R \sim 10^6$), the main optical loss contributors identified are the radius independent sidewall roughness scattering and tailored APBs absorption. We found two roughness components with individual RMS roughness of $5\,nm$, the random short-scale and the pseudo-periodical long-scale, that are affecting the intrinsic Q-factors of the microdisks with a roughness correlation length of $70\,nm$ and $650\,nm$, respectively. Using VCM, the long-scale component is found to be more severely affecting our GaP/Si microdisks which reduces the Q-factors down to 10^4 instead of 10^5 by the short-scale component. However, such a calculation based on Gaussian statistics is an overestimation for the long-scale component. The APDs distribution in the specific GaP/Si sample under scrutiny shows a mean polarity of 0.3 for $90\,nm$ sized minority domains with a $250\,nm$ distance between them on average. Further loss analysis revealed that the APBs optical absorption in the volume of the GaP layer is leading to a linear loss of $10\,dB/cm$ corresponding to an optical attenuation factor $\alpha_{APD} = 2.5\,cm^{-1}$ [48]. This is in agreement with the optical attenuation theoretically predicted by Tea et al. for the measured APBs density of $8000\,mm^{-1}$ through a pure St-APBs model in GaP/Si samples with a

bandgap reduction of $\sim 0.7\, eV$. However, calculations for Q-factors in the NIR regime based on this model suggest that our GaP/Si sample is probably a composition of St-APBs and NSt-APBs. A different spectral dependence of the APBs induced optical loss should be expected in such cases since NSt-APBs do not lead to band gap reduction but has a constant density of states in the whole band gap as calculated by Chen et al.

The nonlinear characterization of GaP/$Al_{0.7}$GaP/GaP microdisks revealed SHG with a pump at telecom wavelength assisted by strict $\bar{4}$-QPM. The experimental configuration investigated is far from optimal due to the modest Q-factors of our microdisks but the strict $\bar{4}$ nonlinear scheme observed, involving radial number modes $p = 2$ is the most efficient scheme reported so far in III-V zinc-blende microdisks. It also suggests that it is possible to find the best case $p = 1$ strict $\bar{4}$-QPM configurations in these microdisks. The comparison of our results with the literature also indicates that the investigated microdisk cannot achieve double resonance even using thermo-optic effects, probably due to limited pump laser power. As we could not satisfy the bistability condition with moderately high Q-factors, there is no bistability behavior observed.

The nonlinear response of APD-tailored GaP/Si microdisks shows strong green emission with a high power damage threshold. However, we couldn't spectrally assess it, probably due to the strongly confined lower order nonlinear signal in the thick GaP/Si microdisk that does not get coupled to the fiber taper or the coupling is not at a good location to receive the signal. The origin of this signal is not clarified, although, the presence of APBs can act as deep centers trapping charge carriers with a reduced bandgap and a very high field density may lead to band gap edge emission.

To sum up, the loss analysis suggests a refinement of the fabrication process to reach APBs limited optical losses with Q-factors in the 50000 range. In addition, a model accounting for different APBs in the GaP layer must be considered for future investigations to completely understand the spectral dependence of the APBs absorption losses. Furthermore, the experimentally estimated APBs induced loss is found to be compatible with demonstrating efficient RQPM based nonlinear devices, especially at the lowest cost because of the Si substrate and the minimal III-V material deposition. A completely integrated microdisk-waveguide structure is essential in the next stage to work close to the real PIC models and to overcome practical difficulties of fiber taper like fragility, contact induced resonance shifts, variations in the coupling efficiencies and unreliable conversion efficiencies. Fabricating large Q-factor GaP/$Al_{0.7}$GaP/GaP microdisks will achieve better conversion efficiencies provided double resonance conditions can be met, either through fabrication or tuning later like utilizing the thermo-optic effect. In a nutshell, this thesis takes us one more step toward realizing GaP based wavelength converters and future defect tailored PICs.

Appendix A

A.1 Fabrication of GaP microdisks on a Si substrate

Here we describe the GaP/Si microdisks epitaxy step-by-step as depicted in the schematic in Figure A.1.

Step 1: Preparation of Si substrate and growth of GaP layer

One of the primary concerns in the fabrication is to prepare the substrate for the growth process. For that purpose, the Si substrate is initially chemically treated

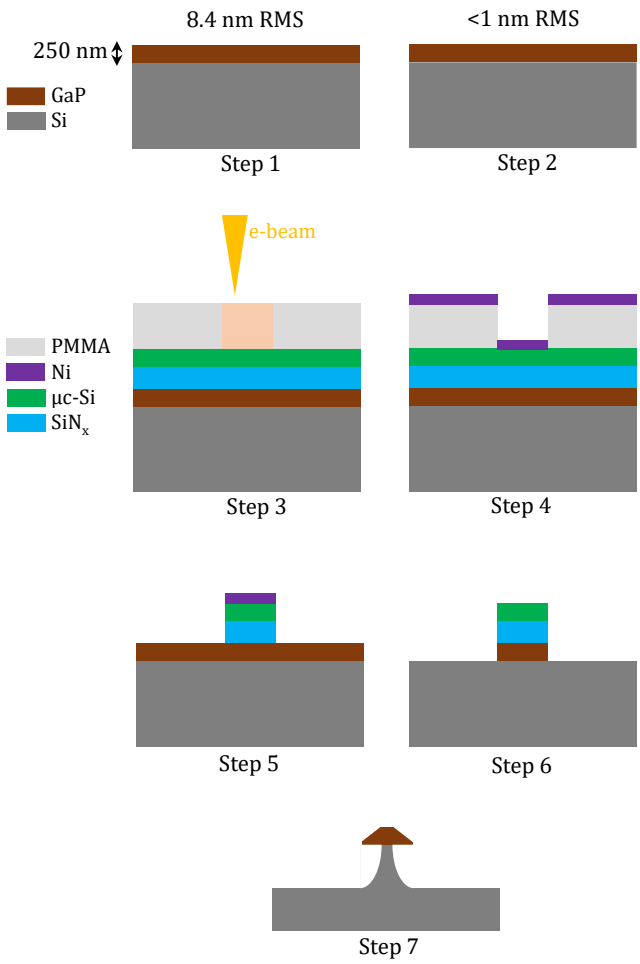

Figure A.1: Different steps involved in the monolithic heteroepitaxial growth and technological processing of GaP microdisks on Si pedestal.

with HF-1%/UV-O_3/HF-1% [209]. Then it is loaded into the MBE chamber, heated at $800\,℃$ for hydrogen desorption and cooled down to GaP growth temperature. Thereafter, a $10\,nm$ thick layer of GaP is first grown on the substrate using MEE at $350\,℃$. The temperature is then gradually increased from $580-660\,℃$ and the GaP layer thickness is grown to $400\,nm$ finally.

To tailor the APDs a vicinal 6°-off (001) Si substrate is chosen for the fabrication. Also, the grown III-V layer contains three $2\,nm$ thick $Al_{0.2}GaP$ wells. They are located at $10\,nm$, $35\,nm$ and $50\,nm$ from the Si interface. As discussed under section 1.5, suitably combining the fine control of V/III ratio (slightly above 1 in our case) and growth temperature on a vicinal substrate the spatial distribution of minority domains with a size in the $100\,nm$ range is engineered [43][54].

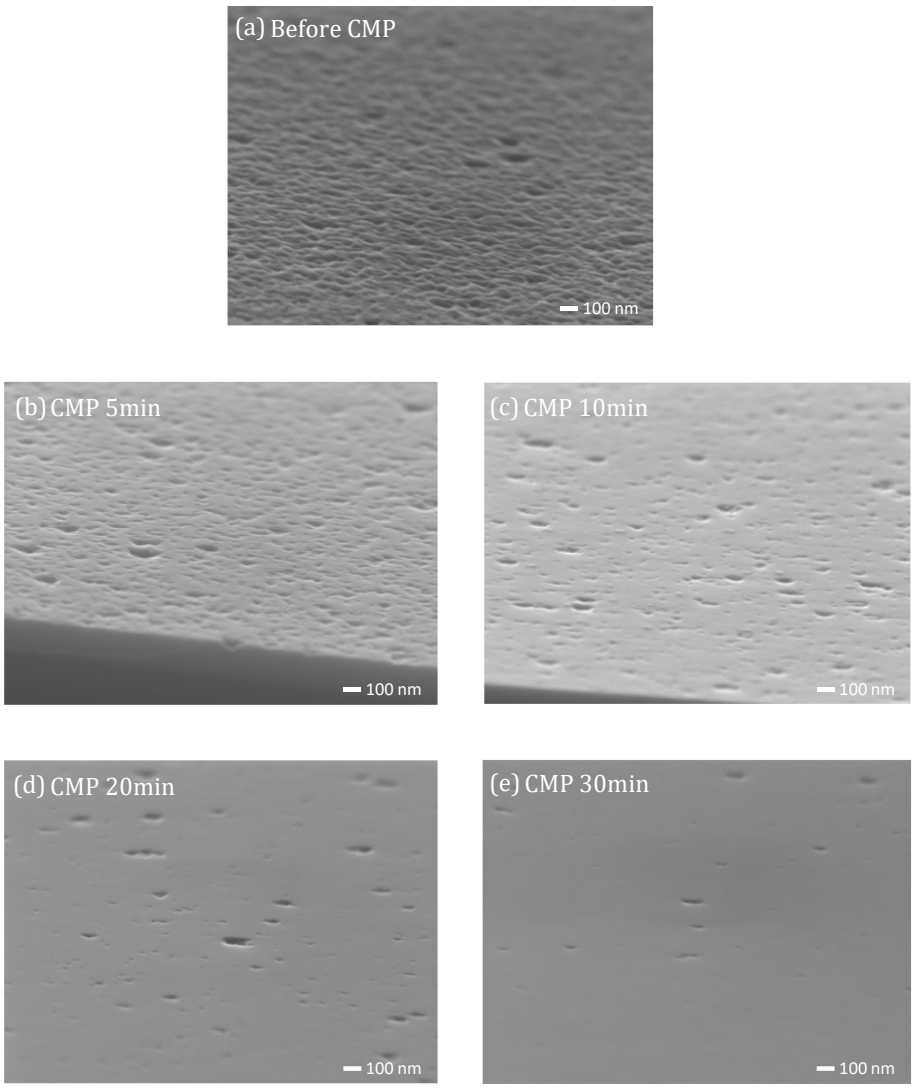

Figure A.2: The SEM images of GaP film grown on Si (a) before CMP (b-e) after CMP of 5, 10, 20 and 30 *minutes*, respectively.

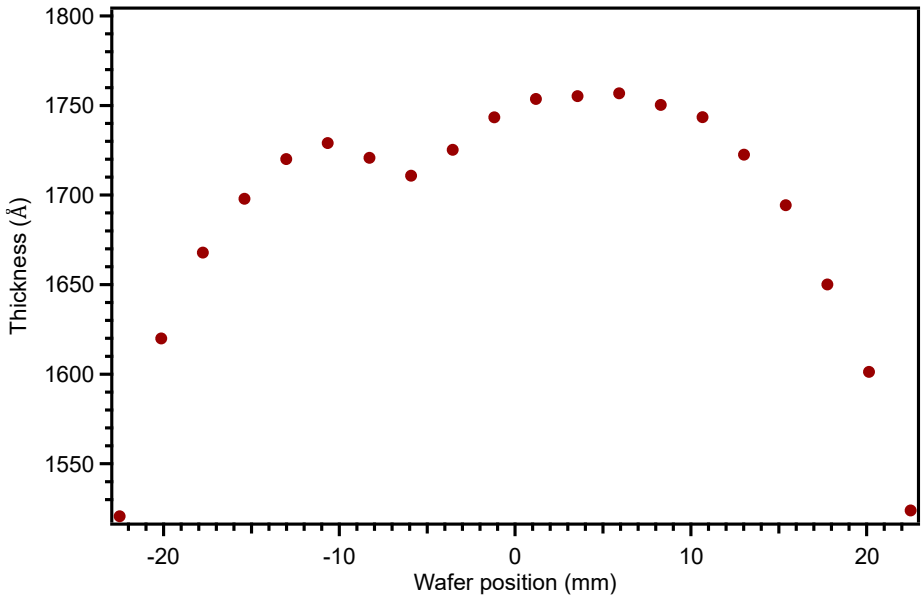

Figure A.3: The thickness gradient introduced by CMP on the epilayer with an initial thickness of 200 nm.

Step 2: Chemical Mechanical Polishing (CMP) of the GaP surface

The sample right after the formation of the GaP layer shows a surface roughness of $8.4\,nm$ RMS. This is a typical value of III-V/Si epilayers with emerging APDs [210][211]. Such a roughness in the platform is not at all suitable for realizing photonic components. To overcome this situation, the GaP surface undergoes a CMP process using phosphoric acid at $1\,\%$ and rubber pads. Figure A.2 shows the SEM images of the sample surface after CMP for a certain duration. A $30\,min$ polishing of the GaP layer leads to the removal of a $100\,nm$ thickness and thereby ensures a flat surface with a low concentration of surface defects (see Figure A.2(e)). For a prolonged CMP of $1\,hour$, a $250\,nm$ thick GaP layer remains to obtain a surface roughness as low as below $1\,nm$ RMS. The thickness profile of the sample from ellipsometry showing wedge formation after the CMP is given in Figure A.3. At the Institut Foton, the same CMP process is also carried out on other samples with results validating that the surface roughness is below $1\,nm$ RMS [212]. The emerging APDs can strongly affect the surface roughness of GaP/Si epilayers [127]. However, a direct correlation between the sample topography and the crystal polarity distribution remains unproved. After the CMP process our sample is then cut into two pieces. One part is utilized for understanding APDs distribution (see section 3.2) and the other portion is used for the technological processing of the suspended microdisks as described in the following steps.

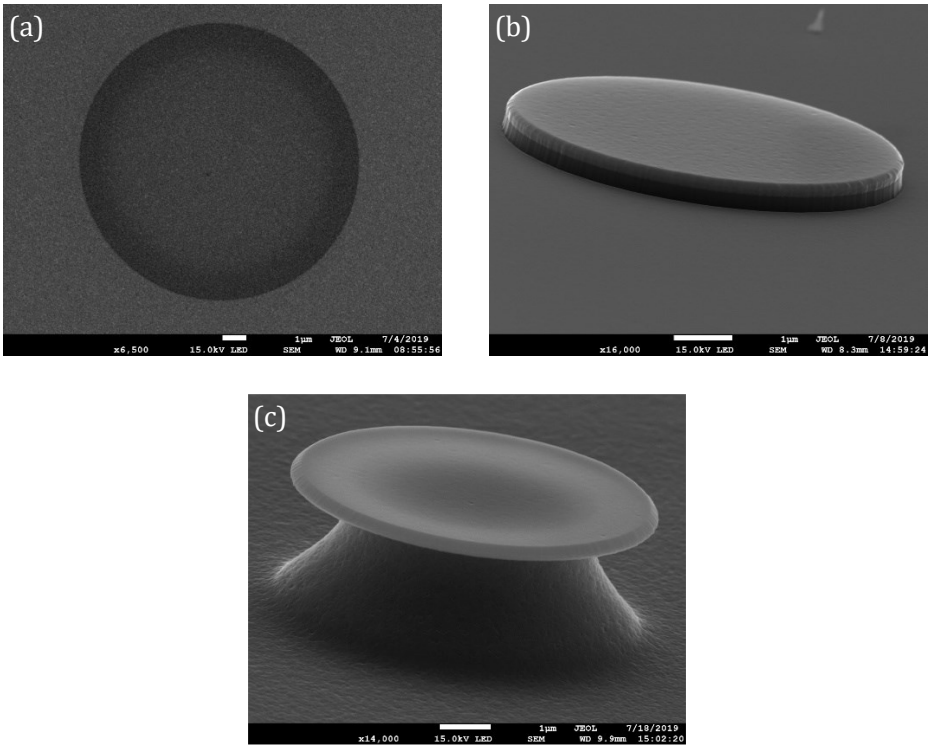

Figure A.4: The SEM images of different steps in the technological processing of GaP/Si microdisks (a) after Ni lift-off (b) during dry etching of GaP (c) final GaP microdisk with Si pedestal.

Step 3: Growth of mask layers and e-beam lithography

At this stage, a mask over the GaP layer is formed by depositing SiN_x, doped microcrystalline Si (µc-Si) that facilitates charge distribution during e-beam lithography and poly methyl methacrylate (PMMA) in this order respectively. Later, lithography is performed using JEOL SEM + Xenos e-beam module and PMMA developed to imprint a negative of the disk patterns onto the PMMA.

Step 4: Ni deposition and PMMA lift-off

This step includes Ni deposition and PMMA lift-off which will define a hard mask for the microdisks. The process is generally known as Ni lift-off. The SEM image of the sample after the Ni lift-off process is shown in Figure A.4(a). The most recent GaP/Si microdisk samples are fabricated with Hydrogen Silsesquioxane (HSQ) resist which can produce a rim roughness as low as the one offered by Ni lift-off, but with less number of steps involved. However, these samples were not investigated in this work.

Step 5: Dry etching of doped µc-Si /SiNx

Now using CF_4 inductively coupled plasma-reactive ion etching (ICP-RIE) the doped µc-Si/SiN_x stacked layers are etched. The Ni layer is then removed with HNO_3.

Step 6: Dry etching of the GaP

The disk pattern is then completely transferred into the GaP layer with the help of Cl_2/Ar ICP-RIE. The SEM image of the sample at this stage is shown in Figure A.4(b).

Step 7: Isotropic dry etching of Si

The remaining mask layers are removed using CF_4 ICP-RIE. Finally, the GaP microdisks are partially released by under-etching the Si substrate with isotropic SF_6 RIE. This process creates a Si pedestal for the GaP microdisk and also results in the formation of a wedge shape (bevel) on the GaP microdisk rims [192]. The SEM image of a completely grown GaP microdisk with a Si pedestal is shown in Figure A.4(c).

A.2 Fabrication of GaP microdisks on a GaP substrate

As mentioned in section 2.3.2 and section 4.1, the fabrication process followed by the Institut Foton has advanced a lot from the 2013 samples. However, those former steps are described here to understand the GaP/$Al_{0.7}$GaP/GaP microdisks investigated in this thesis, see Figure A.5.

A $1\ \mu m$ thick $Al_{0.7}$GaP sacrificial layer is first grown on a GaP substrate which will serve later to define the microdisk pedestal. The top GaP layer is then deposited with a thickness varying from $150 - 250\ nm$ depending on the target thickness (the GaP/$Al_{0.7}$GaP/GaP samples studied in this work were targeted at $150\ nm$ and we believe a small under-etching happened on the microdisk itself during the pedestal etching). In comparison, the GaP/$Al_{0.7}$GaP/GaP microdisks used in Ref.[192] (containing $GaPN_{0.02}$ quantum wells) is $200\ nm$ thick. Later, S1805 resist and a SiN_x hard mask ($65\ nm$ thick) is deposited. The SUSS MicroTec MJB4 photolithography tool is then used to define the microdisk structure. After developing the resist, buffered hydrofluoric acid (BHF) solution etches the hard mask transferring the microdisk pattern. The wet etching of the GaP and $Al_{0.7}$GaP layers are performed using a GaP Etch commercial solution which can etch the $Al_{0.7}$GaP faster than the GaP. Thus, in the same etching process, the GaP microdisk is defined and the $Al_{0.7}$GaP pedestal is formed. The SEM image of such a microdisk is also included in Figure A.5.

The fabrication of GaP/$Al_{0.7}$GaP/GaP samples that have undergone an upgraded process after 2013 is described in Ref.[192][61]. The e-beam lithography is utilized in this case to define the microdisk geometry using a SU8 negative

photoresist and a SiN_x hard mask. Instead of complete wet etching stages, the Cl_2/Ar ICP-RIE dry etching is performed for the vertical etching of both GaP and $Al_{0.7}GaP$ layers. Finally, lateral wet etching is adopted for the pedestal formation using hydrofluoric acid (HF) solution.

The rim roughness analysis of GaP/$Al_{0.7}$GaP/GaP microdisks conducted in Ref.[61] shows that the former samples have a direct RMS roughness of $24\ nm$ as compared to $22\ nm$ for the latter samples. For both kinds of samples, subtraction of the long-scale waviness contribution gives RMS roughness of $10\ nm$. This is one order of magnitude larger than what has been reported for GaAs [194].

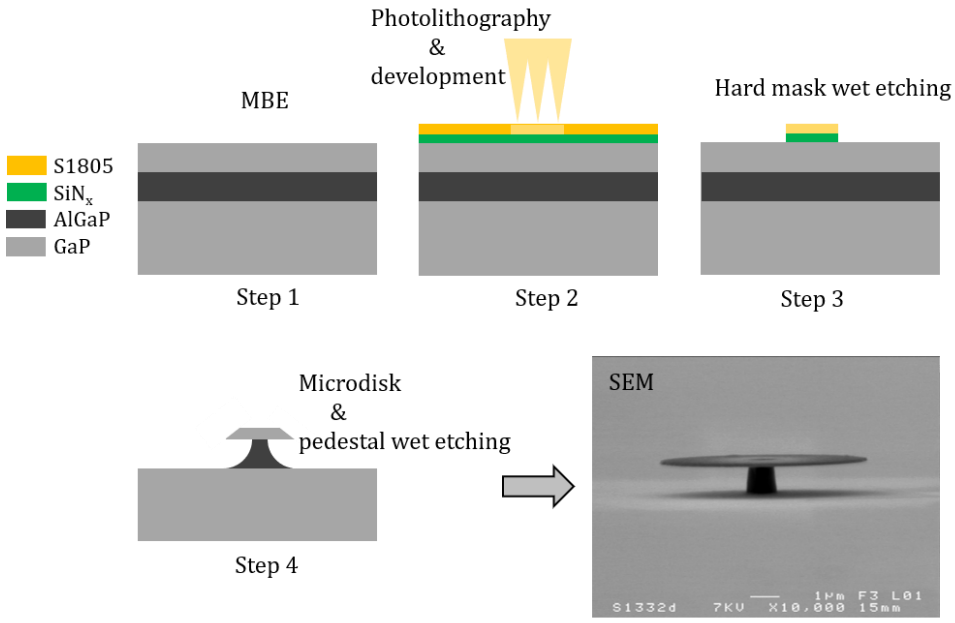

Figure A.5: Different steps involved in the heteroepitaxial growth and technological processing of GaP/$Al_{0.7}$GaP/GaP microdisks.

Appendix B

List of publications and conferences related to this thesis

- **Rasool Saleem-Urothodi**, Julie Le Pouliquen, Tony Rohel, Rozenn Bernard, Christelle Pareige, Alejandro Lorenzo-Ruiz, Alexandre Beck, Antoine Létoublon, Olivier de Sagazan, Charles Cornet, Yannick Dumeige, Yoan Léger*. Loss assessment in random crystal polarity gallium phosphide microdisks grown on silicon. Optics Letters, Optical Society of America - OSA Publishing, 2020, 45 (16), pp.4646. ⟨10.1364/OL.399935⟩. ⟨hal-02926153⟩
- **Rasool Saleem-Urothodi**, Julie Le Pouliquen, Tony Rohel, Rozenn Bernard, Christelle Velly-Pareige, Alejandro Lorenzo-Ruiz, Alexandre Beck, Antoine Létoublon, Olivier de Sagazan, Charles Cornet, Yannick Dumeige, Yoan Léger*. Optical losses in GaP microdisks on Si with controlled random polarity. 17è Journées de la Matière Condensée (JMC 17), Aug 2021, Rennes (virtual), France. ⟨hal-03402730⟩
- **Rasool S Urothodi**, Julie Le Pouliquen, Tony Rohel, Rozenn Bernard, Christelle Velly-Pareige, Alejandro Lorenzo-Ruiz, Alexandre Beck, Antoine Létoublon, Olivier de Sagazan, Charles Cornet, Yannick Dumeige, Yoan Léger*. High-Quality Factor Zinc-Blende III-V Microdisks on Silicon for Nonlinear Photonics. Compound Semiconductor Week 2021 (CSW 2021), May 2021, Stockholm, France. ⟨hal-03285528⟩
- **Rasool Saleem-Urothodi**, Julie Le Pouliquen, Tony Rohel, Rozenn Bernard, Christelle Pareige, Alejandro Lorenzo-Ruiz, Alexandre Beck, Antoine Létoublon, Olivier de Sagazan, Charles Cornet, Yannick Dumeige, Yoan Léger*. Crystal-polarity engineered gallium phosphide microdisks grown on silicon. IOP conference- PHOTON2020, Sep 2020, virtual, United Kingdom. ⟨hal-03032794⟩

Appendix C

Résumé en Français

Un résonateur optique à modes de galerie est une microscopique structure cylindrique présentant un indice de réfraction élevé vis-à-vis de son environnement, de façon que la lumière reste piège en son sein par réflexion totale interne le long du cylindre [17]–[21].

Si la phase de l'onde lumineuse est conservée après un tour au sein du résonateur, des interférences constructives donnent lieu aux modes de galerie (WGM), comme le montre la condition de résonance:

$$2\pi n_{\text{eff}} R = m\lambda \qquad \text{Eq. C.1}$$

où λ est la longueur d'onde de résonance de l'onde lumineuse, R le rayon du résonateur, m un entier et n_{eff} l'indice de réfraction effectif du mode optique. Chaque mode de galerie peut alors être décrit par la combinaison d'un nombre quantique azimutal (m), radial (p) et planaire (q). Les résonateurs optiques à mode de galerie confinent la lumière dans un très petit volume (échelle micron-nano) pendant une longue durée, constituant une plate-forme idéale pour améliorer les interactions lumière-matière non linéaires. Ils peuvent avoir différentes géométries comme des disques, des anneaux, des sphères, des tores, etc. Les microrésonateurs sont l'un des principaux composants des circuits photoniques intégrés (PICs) [14], [22]–[25]. Ils permettent de réaliser différentes fonctions optiques [14], [24], [34], [26]–[33] laissant présager le développement de PICs ultra-rapides, bas-coût, et hautement intégrés [10]. Leurs performances peuvent être améliorées par l'identification et l'optimisation de leurs pertes optiques. La sélection des matériaux de fabrication de ces structures est un véritable challenge, dépendant non-seulement des contraintes technologiques mais surtout des applications visées.

Le semi-conducteur binaire III-V GaP est entré dans l'industrie photonique dans les années 1960 sous la forme de diodes électroluminescentes vertes mais n'a pas eu le même développement que le GaAs ou le GaN en raison de sa bande interdite indirecte [37]. Récemment, le GaP a vu un regain d'intérêt en tant que matériau potentiel pour des dispositifs nanophotoniques nonlinéaires [14][23][38]. Il a de nombreux avantages pour concurrencer ses homologues commerciaux (GaAs, $LiNbO_3$, InP, etc.) tels qu'une large bande interdite indirecte de $2{,}24\ eV$ empêchant l'absorption de deux photons à $1{,}55\ \mu m$ permettant un processus de doublement de fréquence de puissance élevée, une susceptibilité non linéaire de second ordre

compétitive ($d_{14} = 28{,}5\ pmV^{-1}$) dans la bande C, un symétrie cubique non centrosymétrique de type zinc-blende offrant une symétrie $\bar{4}$ pour offrant un quasi-accord de phase naturel où la susceptibilité non linéaire subie par les photons s'inverse naturellement à chaque quart de tour autour de l'axe [001] [39][40], le plus grand indice de réfraction linéaire (> 3) parmi les matériaux III-V transparents dans le visible pour un confinement optique élevé et un indice de réfraction non linéaire élevé ($\sim 10^{-17}\ m^2W^{-1}$) pour la réalisation de processus non linéaires du troisième ordre [14]. De plus, son faible désaccord de maille avec le Si [41] permet l'intégration monolithique de GaP sur des substrats Si, laissant présager une capacité d'intégration à grande échelle, à bas coût et compatible aux technologies CMOS [2] pour le développement de la photonique non linéaire sur silicium [34][54][48].

En exploitant les propriétés des matériaux GaP et Si, des résonateurs à microdisques suspendus monolithiquement intégrés de GaP/Si, GaP/$Al_{0.7}$GaP/GaP ont été fabriqués et sont caractérisés dans cette thèse. Les échantillons de GaP/Si contenant des microdisques épais sont les structures les plus récentes fabriquées à l'institut FOTON, obtenus par lithographie par faisceau d'électrons, gravure sèche et polissage mécano-chimique [48]. Les échantillons GaP/$Al_{0.7}$GaP/GaP à microdisques minces ont été fabriqués il y a quelques années par photolithographie et gravure humide. Compte tenu de l'épitaxie d'un matériau polaire sur un matériau non-polaire impliquée dans le cas des microdisques GaP épitaxiés sur Si, des défauts cristallins appelés domaines d'antiphase (APD) se forment dans la couche de GaP, menant à une inversion locale dans l'ordre d'empilement des plans atomiques [43]–[46]. D'un APD à l'autre, les plans atomiques Ga seront opposés aux plans atomiques P et vice versa. Ce sont des régions où la polarité du réseau est localement inversée et les jonctions formées entre les domaines d'antiphase adjacents sont appelées parois d'antiphase (APB). La formation d'APDs/APBs peut être attribuée à différents scénarios, tel que la croissance du GaP sur une surface de Si avec des terrasses monoatomiques [49]. Les APDs sont donc des défauts de croissance présentant généralement une distribution spatiale aléatoire et se propageant le long de l'axe de croissance dans toute la couche épitaxiale, ce qui peut impacter les performances de dispositifs réalisés dans cette plateforme. Jusqu'ici, poussés par la réalisation de lasers sur silicium, les efforts de recherches ont principalement visé à l'annihilation des APDs faveur [43], [48]–[50], [54], [123], [129], [135], [136]. Une distribution d'APDs est caractérisée par une longueur de corrélation ($\mathcal{L}_c$) et une polarité moyenne ($P_{APD,mean}$). $\mathcal{L}_c$ correspond à la distance moyenne entre les deux APB adjacentes selon la direction dans le plan (perpendiculaire à la direction de croissance). En d'autres termes, il s'agit de la taille moyenne d'une APD. La polarité moyenne est définie comme la moyenne spatiale de la distribution de polarité de la couche épitaxiée en raison. Dans cette thèse, les APBs sont mises en évidence par révélation chimique sur des couches polies et imagerie électronique à balayage. Une image binarisée est ensuite traitée

numériquement en identifiant les domaines minoritaires et la fonction d'autocorrélation correspondante est calculée. La taille des domaines minoritaires est directement obtenue à partir de la décroissance exponentielle du pic central. La distance moyenne entre les domaines homophasés est extraite de la distance entre les pics satellites. La distribution des APD dans l'échantillon GaP/Si étudié dans cette thèse montre une polarité moyenne de $0{,}3$ pour les domaines minoritaires de $90\,nm$ avec une distance moyenne de $250\,nm$ entre eux. Une telle distribution aléatoire de polarité cristalline va nécessairement avoir un impact important sur les processus optiques non linéaire du second ordre.

Dans un microdisque de symétrie zinc-blende, exempt de défaut, lors d'un processus non linéaire du second ordre, le quasi-accord de phase naturel, dit $\bar{4}$, aboutit à une condition spécifique sur la différence entre nombres azimutaux des modes produits et des modes entrants, Δm: $\Delta m = \pm 2$. Cette condition, assurant la conservation du moment cinétique, et la conservation de l'énergie avec la présence de résonances aux longueurs d'ondes entrantes et produites sont particulièrement difficiles à obtenir simultanément de manière expérimentale car elle sont extrêmement exigeantes sur les paramètre géométriques des structures. Jusqu'ici, l'accord de phase naturel strict n'avait jamais été observé dans les microdisques zinc-blende tel que GaP ou GaAs et le processus était toujours couplé à un quasi-accord de phase modal, diminuant l'efficacité du phénomène [58][33]. L'apparition d'une distribution de polarité cristalline aléatoire dans des microdisques zinc-blende peut donc être considéré comme un moyen de relâcher cette contrainte. Dans les microdisques de GaP/Si à polarité cristalline aléatoire, la condition d'accord de phase devient: $\Delta m = \pm 2 + M_{APD}$, où le dernier élément correspond à une composante de fréquence spatiale de la distribution d'APD, permettant de compenser le désaccord de phase entre les modes impliqués. Cette configuration spécifique est appelée quasi-accord de phase aléatoire [34]. Au démarrage de cette thèse, aucune évaluation expérimentale des pertes induites par les APD dans les microdisques GaP/Si et des propriétés non linéaires de ces dispositifs n'avait été publiée à notre connaissance. Cette thèse répond donc à ces deux questionnements en comparant de manière expérimentale la démonstration du quasi-accord de phase aléatoire à celle du quasi-accord de phase $\bar{4}$ strict dans les microdisques GaP/Si et GaP/GaP respectivement.

L'un des aspects importants de la réalisation de dispositifs photoniques intégrés est la minimisation des pertes optiques au sein des dispositifs qui empêchent ceux-ci d'atteindre les performances souhaitées malgré les avantages de cette géométrie de cavité. Le paramètre qui quantifie les pertes dans un microrésonateur est le facteur de qualité Q défini comme 2π fois le rapport de l'énergie totale stockée dans la cavité à l'énergie dissipée par cycle [77]. Dans le domaine de Fourier, la distribution de fréquence de l'énergie optique dans la cavité prend la forme d'une

raie lorentzienne et le facteur Q peut être mesuré à partir du spectre de transmission du WGM comme suit:

$$Q = \frac{\omega}{\Delta\omega} = \frac{\lambda}{\Delta\lambda} \qquad \text{Eq. C.2}$$

où λ est la longueur d'onde de résonance. Les paramètres $\Delta\omega$ et $\Delta\lambda$ dans l'Eq. C.2 sont les largeurs à mi-profondeur de la lorentzienne dans l'espace des fréquences ou des longueurs d'onde respectivement Pour obtenir ces spectres en transmission, un laser accordable fonctionnant dans la longueur d'onde d'intérêt est couplé aux microdisques à travers le champ évanescent d'une fibre optique amincie et la réponse est enregistrée à l'aide d'un capteur de puissance. La fabrication d'une fibre amincie droite consiste à chauffer une partie d'une fibre monomode standard et à l'étirer avec une vitesse contrôlée pendant une certaine durée [184]–[187]. Après avoir atteint un diamètre critique pour une longueur d'onde d'intérêt particulière, un fonctionnement monomode peut être où le mode présente un champ évanescent très étendu hors de la fibre, permettant le couplage au résonateur. Plus précisément, nous avons utilisé des fibres amincies coudées [171][172] dont la courbure est obtenue par moulage [162]. Ces dispositifs, présentant les mêmes avantages que les fibres amincies droites [99][181][165] permettent en outre un couplage sélectif à des microdisques densément distribués sur une puce photonique. Il existe deux types de mécanismes de pertes contrôlant le facteur Q d'un microrésonateur, les pertes extrinsèques (Q_{cpl}) et intrinsèques (Q_i). Le Q_{cpl} est associé au couplage du microrésonateur avec des guides d'ondes d'accès à proximité tels que les fibres amincies pour l'excitation sélective de modes. Le Q_i est lié aux paramètres physiques du microrésonateur. La somme des pertes intrinsèques et extrinsèques donne le facteur Q chargé ou total (Q_{loaded}) du microrésonateur tel que:

$$Q_{\text{loaded}}^{-1} = Q_{\text{cpl}}^{-1} + Q_{\text{i}}^{-1} \qquad \text{Eq. C.3}$$

Les études de transmission dans le régime SWIR (NIR) révèlent que les facteurs Q des microdisques GaP/Si sont de l'ordre de $\sim 10^4 (\sim 10^3)$ tandis que les microdisques GaP/$Al_{0.7}$GaP/GaP sont de l'ordre de $\sim 10^3 (\sim 10^2 - 10^3)$. La différence de facteurs Q de ces différents échantillons peut être attribuée à la différence dans leur processus de fabrication. Ceci est en accord avec les mesures de cathodoluminescence effectuées il y a quelques années sur des microdisques GaP/$Al_{0.7}$GaP/GaP actifs réalisés suivant une procédure de fabrication similaire à celle des microdisques GaP/Si de cette these [192]. Le développement de composants photoniques dans la plateforme GaP/Si nécessite une bonne compréhension des mécanismes de perte optique et de leur optimisation. Cette thèse présente donc l'analyse expérimentale des pertes optiques dans les microdisques GaP/Si qui seront ensuite utilisés dans les expériences de conversion de fréquences non linéaire.

Linear characterization of GaP/Si microdisks

Dans les microdisques GaP/Si, le Q_i peut être affecté par les pertes par radiation liées à la courbure du résonateur (Q_{rad}), la diffusion Rayleigh par la surface rugueuse des parois du disque (Q_R) et l'absorption due aux APB formés dans le volume GaP (Q_{APD}). Par conséquent, l'Eq. C.3 pour le facteur Q total peut s'écrire:

$$Q_{\text{loaded}}^{-1} = Q_{\text{cpl}}^{-1} + Q_{\text{rad}}^{-1} + Q_{\text{R}}^{-1} + Q_{\text{APD}}^{-1} \qquad \text{Eq. C.4}$$

En considérant un régime de sous-couplage pour le système fibre amincie-microdisque ($Q_{cpl} >> Q_i$) [95] et sachant que le processus de polissage mécano-chimique prolongé de la surface du microdisque GaP/Si garantit une surface de l'échantillon d'une rugosité de l'ordre d' $1\,nm$ RMS, nous avons analysé statistiquement les facteurs Q intrinsèques expérimentaux de nombreux microdisques présentant un rayon de 2 à $3{,}5\,\mu m$ dans la bande SWIR afin d'estimer les contributions des pertes par radiation, de celles associées à la rugosité latérale et de celles associées aux APBs. Le facteur Q intrinsèque moyen de 8×10^3 s'avère indépendant du rayon, contrairement au Q_{rad} , ce qui confirme l'impact prépondérant d'autres contributions aux pertes. Dans nos échantillons, la contribution des pertes induites par la rugosité des bords peut être sévère en raison du processus de décollement du masque de Ni utilisé pour définir les disques lors de la fabrication. Cette méthode peut générer plus de rugosité que le masquage sans métal [194]. A partir de l'image MEB d'un microdisque GaP/Si, nous avons extrait le profil de rugosité latérale de nos microdisques. Les valeurs de rugosité RMS (σ) et sa longueur de corrélation (S_c) sont alors obtenues par autocorrélation du profil. Nous avons trouvé deux composantes de rugosité avec une rugosité RMS individuelle de $5\,nm$: une première contribution aléatoire à petite échelle ($S_{c,short} = 70\,nm$) et une contribution quasi-périodique à grande échelle ($S_{c,long} = 650\,nm$). En utilisant l'approche de courant en volume (VCM) [151][152], les pertes induites par cette rugosité latérale peuvent être estimées:

$$Q_R^{TE/TM} = \frac{1}{\frac{16\pi^3}{3m}\left(1-\frac{1}{n^2}\right)^2 \xi^2 \ell_c \Gamma_z \delta} \qquad \text{Eq. C.5}$$

où le Q_R est déterminé par le contraste d'indice de réfraction n, la rugosité normalisée ξ, la longueur de corrélation normalisée ℓ_c, la hauteur de disque normalisée δ, le facteur de confinement vertical Γ_z et le nombre azimutal m. L'analyse montre que (voir Figure C.6) la composante à grande échelle affecte plus sévèrement nos microdisques GaP/Si que la composante à petite échelle (réduction du facteur Q a 10^4 et 10^5, respectivement). Cependant, un tel calcul basé sur des statistiques gaussiennes et non une quasi-périodicité tend à surestimer la composante à grande échelle. La valeur moyenne des facteur Q observés nécessite donc de prendre en considération des pertes dans le volume du GaP qui peuvent

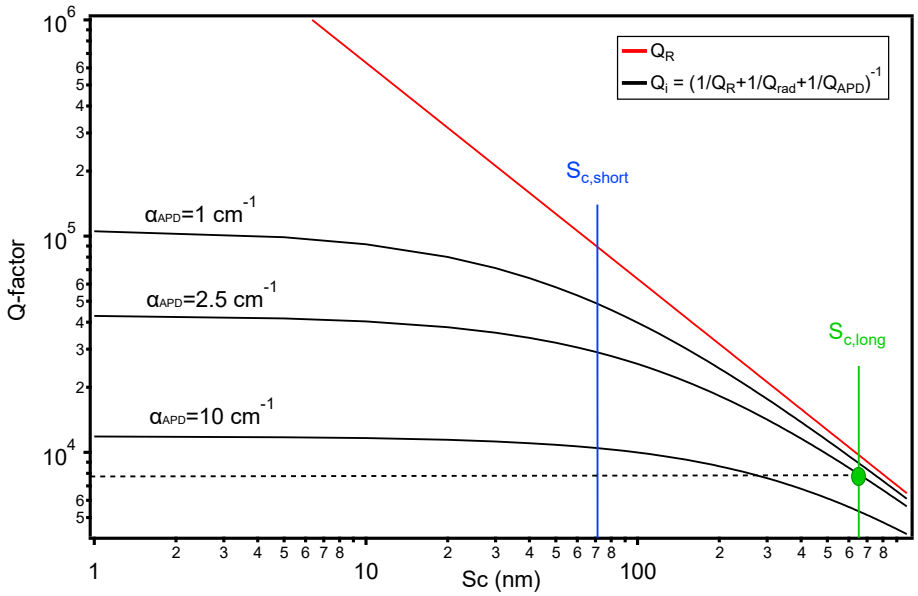

Figure C.6: Évolution théorique de Q_R en fonction de S_c (ligne rouge) et du Q_i limité par absorpotion par les APBs pour différentes valeurs d'atténuation α_{APD} (courbes pleines noires). Le cercle vert indique le point de correspondance entre le Q_i moyen (ligne pointillée noire) et le Q_i limité d'APB pour $\alpha_{APD} = 2.5\ cm^{-1}$.

provenir des APBs apparues pendant la croissance. En effet, les calculs atomistiques de Tea et al. montrent que les APBs pourraient provoquer une réduction de la bande interdite de l'ordre de $0.7\ eV$ [51]. En reliant l'absorption par les APBs dans le volume de la couche GaP à la définition du facteur Q, une expression pour Q_{APD} peut être écrite:

$$\frac{1}{\mathrm{Q_{APD}}} = \frac{\alpha_{APD}}{n_{eff.grp}k} \qquad \text{Eq. C.6}$$

où k est le vecteur d'onde, $n_{eff.grp}$ l'indice de groupe effectif et α_{APD} est le coefficient d'absorption linéique du matériau. La contribution de pertes liées aux APBs peut ainsi être estimée à une valeur de l'ordre de $10 \pm 1\ dB/cm$ ce qui correspond à un coefficient d'absorption $\alpha_{APD} = 2{,}5 \pm 0{,}2\ cm^{-1}$ pour la densité APBs mesurée $8000\ mm^{-1}$ [48]. Le calcul montre ainsi que le facteur Q intrinsèque limité par les APBs est de $4{,}5 \times 10^4$. En d'autres termes, si la principale contribution de perte reste la diffusion de la rugosité des parois latérales, l'absorption par les APB dans la couche GaP reste non négligeable avec des facteurs Q limites entre 10000 et 100000. Cette estimation de perte est en accord avec l'atténuation optique théoriquement prédite par Tea et al. qui se base uniquement sur la formation d'APB dites stœchiométriques (St-APBs, comprenant autant de cation que d'anions) dans la couche de GaP/Si. Cependant ce modèle mène à une surestimation très forte des pertes induites par les APBs dans le régime NIR

(facteurs Q inférieurs à 250 au lieu des valeurs mesurées autour de 10^3). Nous savons à présent que d'autres types d'APBs, non-stœchiométriques (St-APBs), apparaissent vraisemblablement durant la croissance et présentent une signature spectrale très différente de celle St-APBs, à savoir une faible densité d'état semi-métallique constante à travers la bande interdite plutôt qu'une réduction de celle-ci, comme démontré par par Chen et al. [47]. Une caractérisation expérimentale plus poussée de l'influence des APBs sera un passage obligé pour le développement de la plateforme GaP/Si. Notons que récemment, la SHG a été démontrée dans des nano-guides d'ondes de GaP à orientation de polarité cristalline contrôlée. Les pertes optiques totales mesurées dans ces dispositifs sont de l'ordre de $10\,dB/cm$ pour une densité d'APBs bien moindre, en cohérence avec nos observations [195]. Les microdisques de GaP/Si fabriqués apparaissent donc comme compatible à la démonstration de phénomène de conversion de fréquences non linéaire.

Processus non linéaires du second ordre dans les microdisques de GaP/$Al_{0.7}$GaP/GaP and GaP/Si

L'exploitation des paramètres du matériau GaP peut favoriser les performances optiques non linéaires. Plusieurs démonstrations de conversion de fréquences optiques dans les microrésonateurs GaP ont donc déjà été publiées [14][58]. De tels phénomènes restent à démontrer dans le cas des microdisques GaP monolithiquement intégrés sur substrats Si, a fortiori s'ils reposent sur le quasi-accord de phase aléatoire par l'intermédiaire d'une distribution d'APDs. Dans ce travail de thèse nous comparons les caractérisations non linéaires des microdisques GaP/$Al_{0.7}$GaP/GaP et GaP/Si.

L'identification des schémas d'interaction non linéaires est cruciale pour comprendre la dynamique non linéaire elle-même. Dans le cas d'un microdisque GaP à symétrie cristallographique $\bar{4}3m$, la génération d'un SHG polarisé TM est attendue pour une pompe polarisée TE [39]. La possibilité de réaliser un quasi-accord de phase $\bar{4}$ strict (à indice radial constant) ou accompagné d'un QPM modal (changement des indices radiaux et/ou planaires) dépend des paramètres géométriques du résonateurs. Comme mentionné ci-dessus, le quasi-accord de phase $\bar{4}$ strict, nécessitant des disques très fins de l'ordre de $130\,nm$, n'avait jamais été observé [39][61]. C'est dans ce but qu'ont été développés les microdisques GaP/$Al_{0.7}$GaP/GaP étudiés dans cette thèse. En comparaison, les microdisques GaP/Si réalisés présentent une épaisseur de l'ordre de $250\,nm$, offrant un confinement optique plus fort et surtout permettant le recours au processus de quasi-accord de phase aléatoire, plus tolérant quant à la condition d'égalité sur les nombres azimutaux des résonances impliquées, comme proposé théoriquement par Guillemé et al. [54][34]. Dans ces deux types d'échantillons, plusieurs microdisques présentant des résonances offrant un facteur de qualité suffisant et un décalage en

énergie minimale pour la SHG ont été étudiés en régime non linéaire. Les résultats les plus pertinents sont exposés dans ce travail.

I. Strict $\bar{4}$-QPM in GaP/$Al_{0.7}$GaP/GaP microdisks

Le montage d'injection optique non linéaire consiste en l'utilisation d'un laser accordable modulé en amplitude, couplé à un EDFA en régime de saturation, permettant l'injection optique au sein des microdisques par le biais d'une fibre amincie coudée. Les signaux non linéaires générés sont collectés par la même fibre et enregistrés à l'aide d'un spectromètre et d'une photodiode. Un microscope permet de visualiser le processus de couplage et de contrôler la diffusion de toute émission nonlinéaire dans le visible à la surface du microdisque.

L'injection dans un microdisque GaP/$Al_{0.7}$GaP/GaP de $4.5\,\mu m$ de rayon à la longueur d'onde télécom de $1545\,nm$ a permis la génération d'un signal de seconde harmonique à 771.5 ± 0.4 nm. Le spectre d'intensité de ce processus SHG est représenté en Figure C.7. L'interaction non-linéaire est observée entre les résonances ($p = 2$, $m = 25$, TE) pour le mode fondamental et ($p = 2$, $m = 52$, TM) pour le mode SH, dont les facteurs de qualité sont de 2100 et 1785, respectivement. Il s'agit donc bien d'un processus en quasi-accord de phase $\bar{4}$ strict où il n'y a pas de modification des indices de confinements radiaux et planaires. C'est la première démonstration de ce phénomène pour les microdisques III-V zinc blende. Cependant, la configuration observée n'est toujours pas la configuration optimale car elle implique des résonances dont l'indice de confinement radial est supérieur à 1. Cette démonstration suggère néanmoins qu'une condition en quasi-accord de phase $\bar{4}$ strict avec $p = 1$ est accessible expérimentalement dans ce type de microdisques.

L'évolution de la puissance du signal de SH en fonction de la puissance pic du laser de pompe ($32 - 219\,mW$) a été suivi à l'aide d'une photodiode. Une dépendance quadratique est observée à faible et haute puissance de pompe alors qu'une évolution sur-quadratique est visible à puissances intermédiaires. Ce comportement peut être attribué au décalage en longueur d'onde induit par des effets thermo-optiques dans la cavité [200][201][202]. Ces effets ont même été utilisés pour accorder le processus en énergie par les décalage simultanés des résonances de pompe et de SH [58]. Dans notre cas, le laser de pompe est positionné spectralement proche du flanc haute longueur d'onde de la résonance d'injection. L'échauffement de la cavité quand la puissance de pompe devient suffisamment haute provoque un décalage des résonances vers les longueurs d'onde plus élevées par la modification de l'indice de réfraction. La résonance a alors un meilleur recouvrement avec le laser de pompe et l'énergie intracavité augmente produisant l''évolution sur-quadratique. Au-delà d'une certaine puissance de pompe le décalage en longueur d'onde de la résonance ne mènerait qu'à une baisse du recouvrement avec le laser; l'effet thermo-optique cesse.

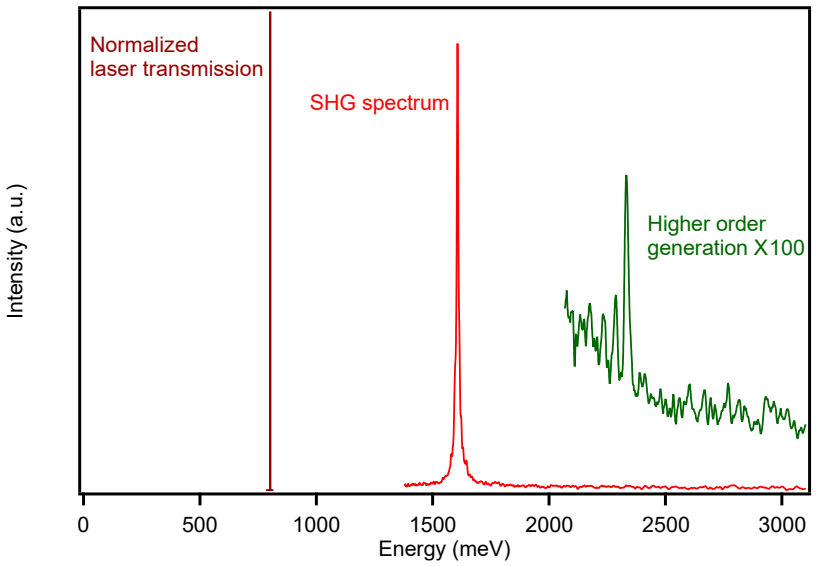

Figure C.7: Spectres d'intensité des signaux impliqués dans le processus SHG. Le SHG et la génération d'ordre supérieur (négligeable) sont enregistrés à $50\,ms$ et $500\,ms$ de temps d'intégration, respectivement.

Cet effet thermo-optique est également confirmé par le comportement de la SHG est étudié lors du balayage en longueur d'onde de la pompe, pour différentes puissances d'injection. Un décalage dans le rouge de la résonance de SHG et une forme asymétrique sont observés, en accord avec la littérature [200][201]. Aucun effet de bistabilité n'est en revanche observé dans notre système car la condition de bistabilité n'est pas respectée du fait des facteurs de qualités modestes des résonances utilisées [81].

L'efficacité de conversion non linéaire externe normalisée obtenue expérimentalement ($8.14 \times 10^{-3}\,\%W^{-1}$) est significativement plus basse que celle rapportée par Lake et al. [58] dans des microdisques de GaP suspendus ($38\,\%W^{-1}$). La comparaison de nos mesures avec ce travail montre que l'efficacité de conversion mesurée dans notre cas est fortement limitée par la valeur des facteurs de qualité (d'un facteur 12000). Nous confirmons ainsi expérimentalement que la configuration non-linéaire utilisée, avec quasi-accord de phase $\bar{4}$ strict, offre un bien meilleur recouvrement non-linéaire des champs, d'un facteur 20 en théorie. Expérimentalement, le décalage en énergie de $2.4\,nm$ entre les résonances fondamentales et SH utilisées n'est certainement pas compensé par l'effet thermo-optique ce qui explique la différence entre les efficacités de conversion. Notons enfin que la méthode de couplage par fibre amincie est loin d'offrir un couplage critique pour le mode fondamental et le mode de SH. A l'avenir, l'intégration du couplage devrait encore permettre d'améliorer les efficacités de conversion de ces dispositifs.

En résumé, nos microdisques fins de GaP/$Al_{0.7}$GaP/GaP ont permis de démontrer pour la première fois un schéma de SHG en quasi-accord de phase $\bar{4}$ strict. Cette configuration pourrait être plus performante si les facteurs de qualités de ces microdisques fins peuvent être améliorés dans le futur. Cette étude nous a également permis de valider le montage expérimental pour l'étude des microdisques de GaP/Si.

II. Vers la conversion de fréquence non linéaire dans les microdisques de GaP/Si

Les expériences d'injection non linéaire ont été menée sur un microdisque de GaP/Si de $2\,\mu m$ de rayon, sur une résonance aux longueur d'onde télécom de polarisation TE avec indice radial ($p = 1$) et un facteur de qualité $Q = 3200$. Dans le NIR, l'indexation des modes est rendue difficile du fait de densité spectrale de modes à ces longueurs d'onde pour des disques épais ($250\,nm$). De manière surprenante, la réponse nonlinéaire du microdisque montre une émission assez forte dans le vert, visible par diffusion via le microscope de contrôle du montage. Le seuil de dommage des microdisques GaP/Si est particulièrement élevé (autour de $3.4\,W$) alors qu'un laser picoseconde a été utilisé dans ces expériences pour atteindre les régimes de puissances maximaux disponibles au laboratoire. Ce seuil de dommage est particulièrement prometteur pour les applications non linéaires haute-puissance. Nous n'avons cependant pas pu caractériser davantage l'émission non linéaire car il nous a été impossible de collecté ce signal via la fibre de couplage. Probablement du fait du très faible champ évanescent à ces longueurs d'onde dans le microdisque et dans la fibre amincie. La Figure C.8 montre l'image de l'amission non linéaire obtenue par le microscope de contrôle.

Ces images de microscope ont été utilisées pour caractériser au mieux le phénomène observé, et notamment son évolution en fonction de la longueur d'onde et de la puissance de pompe. La variation de l'émission avec la puissance de pompe, entre $400\,mW$ et $3.4\,W$, semble linéaire sur plus de deux octaves de puissance. Cependant, il est difficile de sonder une éventuelle non linéarité de l'évolution à basse puissance d'injection, notamment du fait de la sensibilité limitée de la caméra utilisée.

Un décalage vers le bleu de la résonance de la pompe et une photodégradation du facteur de qualité est observé sur quelques disques étudiés suite à une injection prolongée à haute puissance ($3.4\,W$) [206][207]. C'est l'indication d'une génération de porteurs libres provoquant un changement d'indice de réfraction et d'effets thermiques induisant des dommages sur le disque. Il parait prématuré de conclure à ce stade sur l'origine de l'émission verte observée, notamment sans caractérisation spectrale de ce signal et sans évolution en puissance sur plusieurs décades. Ces études seront déterminantes dans le futur afin de savoir si ce signal provient bien d'effets aux second ordre cascadés, d'effets du troisième ordre ou d'une émission de bord de bande interdite induite par l'absorption de porteurs par les APBs.

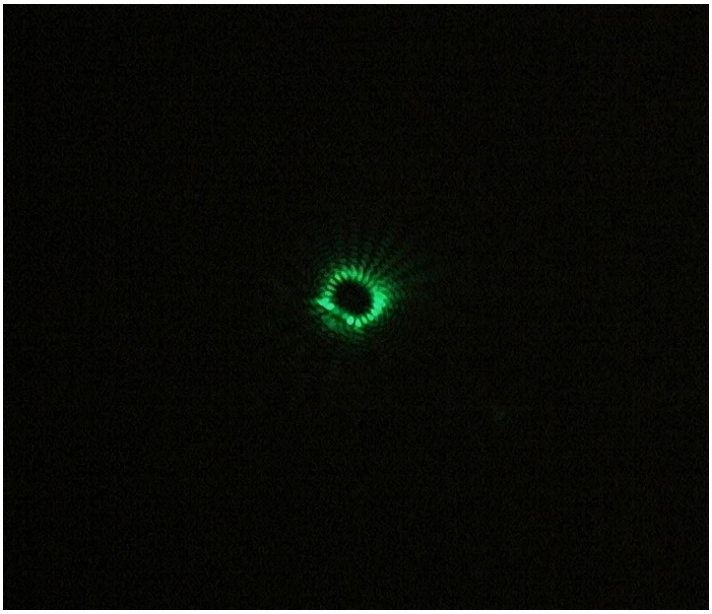

Figure C.8: Image RGB du signal vert capturé par le microscope.

Expérimentalement, si le montage existant peut être amélioré pour effectuer simultanément une spectroscopie d'injection et de transmission non linéaire pour tous les régimes de longueur d'onde d'intérêt, alors plus d'informations pourront être mises à disposition pour évaluer les signaux observés. La dynamique des modes pourra alors être mieux explorée. Nous devons également nous diriger vers un couplage intégré des microdisques qui permettra un meilleur contrôle du régime d'injection, une plus grande stabilité expérimentale de l'injection et une plus grande simplicité de mise en œuvre pour un couplage différencié entre différentes plages de longueur d'onde.

Conclusion

Pour conclure, l'analyse des pertes optiques au sein des microdisques de GaP/Si montre que l'amélioration du procédé de fabrication de ces dispositifs devrait permettre d'atteindre des facteurs de qualités de plusieurs dizaines de milliers, limités vraisemblablement par l'absorption par les parois d'antiphase des couches III-V/Si. L'estimation de l'impact de cette source de pertes est cruciale pour le développement futur d'applications non linéaires basées sur la plateforme GaP/Si. Ces résultats montrent également que l'impact des APBs sur les pertes optiques dépend très probablement de leur stœchiométrie.

La SHG avec quasi-accord de phase $\overline{4}$ strict a été démontré pour la première fois dans les microdisques III-V zinc blende, au sein de microdisques fins de GaP/$Al_{0.7}$GaP/GaP. Malgré des facteurs de qualité modeste lié au processus de

fabrication, nous démontrons une efficacité de conversion prometteuse validant cette voie de recherche. Une émission non linéaire a également été observée dans les microdisques de GaP monolithiquement intégrés sur Si, révélant des seuils de dommage particulièrement élevés. Les principales voies d'amélioration de ces dispositifs reposent à présent sur leur intégration au sein de PICs afin de stabiliser le couplage optique à ces structures et d'en optimiser le régime. En un mot, cette thèse nous fait faire un pas de plus vers la réalisation de convertisseurs de longueur d'onde à base de GaP et de futurs PIC III-V intégrés sur silicium.

Bibliography

[1] G. E. Moore, "Cramming more components onto integrated circuits, Reprinted from Electronics, volume 38, number 8, April 19, 1965, pp.114 ff.," *IEEE Solid-State Circuits Soc. Newsl.*, vol. 11, no. 3, pp. 33–35, Sep. 2006, doi: 10.1109/N-SSC.2006.4785860.

[2] G. Fisher, M. R. Seacrist, and R. W. Standley, "Silicon Crystal Growth and Wafer Technologies," *Proc. IEEE*, vol. 100, no. Special Centennial Issue, pp. 1454–1474, May 2012, doi: 10.1109/JPROC.2012.2189786.

[3] D. Thomson *et al.*, "Roadmap on silicon photonics," *J. Opt.*, vol. 18, no. 7, p. 073003, Jul. 2016, doi: 10.1088/2040-8978/18/7/073003.

[4] R. Soref, "The Past, Present, and Future of Silicon Photonics," *IEEE J. Sel. Top. Quantum Electron.*, vol. 12, no. 6, pp. 1678–1687, Nov. 2006, doi: 10.1109/JSTQE.2006.883151.

[5] M. Lipson, "Guiding, modulating, and emitting light on Silicon-challenges and opportunities," *J. Light. Technol.*, vol. 23, no. 12, pp. 4222–4238, Dec. 2005, doi: 10.1109/JLT.2005.858225.

[6] M. Seifried *et al.*, "Monolithically Integrated CMOS-Compatible III–V on Silicon Lasers," *IEEE J. Sel. Top. Quantum Electron.*, vol. 24, no. 6, pp. 1–9, Nov. 2018, doi: 10.1109/JSTQE.2018.2832654.

[7] Z. Peng *et al.*, "A Non-Volatile Tunable Ultra-Compact Silicon Photonic Logic Gate," *Nanomaterials*, vol. 12, no. 7, p. 1121, Mar. 2022, doi: 10.3390/nano12071121.

[8] C. Shirpurkar *et al.*, "Photonic crystal resonators for inverse-designed multi-dimensional optical interconnects," *Opt. Lett.*, vol. 47, no. 12, p. 3063, Jun. 2022, doi: 10.1364/OL.461272.

[9] S. Assefa, W. M. J. Green, A. Rylyakov, C. Schow, F. Horst, and Y. A. Vlasov, "Monolithic integration of silicon nanophotonics with CMOS," in *IEEE Photonics Conference 2012*, Sep. 2012, pp. 626–627, doi: 10.1109/IPCon.2012.6358777.

[10] C. Sun *et al.*, "Single-chip microprocessor that communicates directly using light," *Nature*, vol. 528, no. 7583, pp. 534–538, Dec. 2015, doi: 10.1038/nature16454.

[11] J.-F. Song *et al.*, "Silicon photonic integrated circuits with electrically

programmable non-volatile memory functions," *Opt. Express*, vol. 24, no. 19, p. 21744, Sep. 2016, doi: 10.1364/OE.24.021744.

[12] W. Bogaerts *et al.*, "Programmable photonic circuits," *Nature*, vol. 586, no. 7828, pp. 207–216, Oct. 2020, doi: 10.1038/s41586-020-2764-0.

[13] M. C. Estevez, M. Alvarez, and L. M. Lechuga, "Integrated optical devices for lab-on-a-chip biosensing applications," *Laser Photon. Rev.*, vol. 6, no. 4, pp. 463–487, Jul. 2012, doi: 10.1002/lpor.201100025.

[14] D. J. Wilson *et al.*, "Integrated gallium phosphide nonlinear photonics," *Nat. Photonics*, vol. 14, no. 1, pp. 57–62, Jan. 2020, doi: 10.1038/s41566-019-0537-9.

[15] W. Xie, C. Xiang, L. Chang, W. Jin, J. Peters, and J. E. Bowers, "Silicon-integrated nonlinear III-V photonics," *Photonics Res.*, vol. 10, no. 2, p. 535, Feb. 2022, doi: 10.1364/PRJ.446898.

[16] W. Bogaerts *et al.*, "Nanophotonic waveguides in silicon-on-insulator fabricated with CMOS technology," *J. Light. Technol.*, vol. 23, no. 1, pp. 401–412, Jan. 2005, doi: 10.1109/JLT.2004.834471.

[17] J. W. S. B. Rayleigh, "The theory of sound," *Macmillan co.*, vol. 2, 1877.

[18] J. W. S. Rayleigh, "The Problem of the Whispering Gallery," *Sci. Pap.*, vol. 5, p. 617, 1912.

[19] Lord Rayleigh, "CXII. The problem of the whispering gallery," *London, Edinburgh, Dublin Philos. Mag. J. Sci.*, vol. 20, no. 120, pp. 1001–1004, Dec. 1910, doi: 10.1080/14786441008636993.

[20] R. D. Richtmyer, "Dielectric Resonators," *J. Appl. Phys.*, vol. 10, no. 6, pp. 391–398, Jun. 1939, doi: 10.1063/1.1707320.

[21] G. Mie, "Beiträge zur Optik trüber Medien, speziell kolloidaler Metallösungen," *Ann. Phys.*, vol. 330, no. 3, pp. 377–445, 1908, doi: 10.1002/andp.19083300302.

[22] I. Roland *et al.*, "Near-infrared III-nitride-on-silicon nanophotonic platform with microdisk resonators," *Opt. Express*, vol. 24, no. 9, p. 9602, May 2016, doi: 10.1364/OE.24.009602.

[23] N. Thomas, R. J. Barbour, Y. Song, M. L. Lee, and K.-M. C. Fu, "Waveguide-integrated single-crystalline GaP resonators on diamond," *Opt. Express*, vol. 22, no. 11, p. 13555, Jun. 2014, doi: 10.1364/OE.22.013555.

[24] Q. Li, M. Davanço, and K. Srinivasan, "Efficient and low-noise single-photon-level frequency conversion interfaces using silicon nanophotonics," *Nat. Photonics*, vol. 10, no. 6, pp. 406–414, Jun. 2016, doi: 10.1038/nphoton.2016.64.

[25] S. Calvez *et al.*, "Vertically Coupled Microdisk Resonators Using AlGaAs/AlOx Technology," *IEEE Photonics Technol. Lett.*, vol. 27, no. 9, pp. 982–985, May 2015, doi: 10.1109/LPT.2015.2405031.

[26] F. Vollmer and L. Yang, "Review Label-free detection with high-Q microcavities: a review of biosensing mechanisms for integrated devices," *Nanophotonics*, vol. 1, no. 3–4, pp. 267–291, Dec. 2012, doi: 10.1515/nanoph-2012-0021.

[27] T. J. Kippenberg and K. J. Vahala, "Cavity Opto-Mechanics," *Opt. Express*, vol. 15, no. 25, p. 17172, Mar. 2007, doi: 10.1364/OE.15.017172.

[28] S. M. Spillane, T. J. Kippenberg, and K. J. Vahala, "Ultralow-threshold Raman laser using a spherical dielectric microcavity," *Nature*, vol. 415, no. 6872, pp. 621–623, Feb. 2002, doi: 10.1038/415621a.

[29] B. E. Little, S. T. Chu, H. A. Haus, J. Foresi, and J.-P. Laine, "Microring resonator channel dropping filters," *J. Light. Technol.*, vol. 15, no. 6, pp. 998–1005, Jun. 1997, doi: 10.1109/50.588673.

[30] D. V. Strekalov, C. Marquardt, A. B. Matsko, H. G. L. Schwefel, and G. Leuchs, "Nonlinear and quantum optics with whispering gallery resonators," *J. Opt.*, vol. 18, no. 12, p. 123002, Dec. 2016, doi: 10.1088/2040-8978/18/12/123002.

[31] T. Aoki *et al.*, "Observation of strong coupling between one atom and a monolithic microresonator," *Nature*, vol. 443, no. 7112, pp. 671–674, 2006, doi: 10.1038/nature05147.

[32] M. Pöllinger and A. Rauschenbeutel, "All-optical signal processing at ultra-low powers in bottle microresonators using the Kerr effect," *Opt. Express*, vol. 18, no. 17, p. 17764, Aug. 2010, doi: 10.1364/OE.18.017764.

[33] P. S. Kuo, J. Bravo-Abad, and G. S. Solomon, "Second-harmonic generation using -quasi-phasematching in a GaAs whispering-gallery-mode microcavity," *Nat. Commun.*, vol. 5, no. 1, p. 3109, May 2014, doi: 10.1038/ncomms4109.

[34] P. Guillemé *et al.*, "Second harmonic generation in gallium phosphide microdisks on silicon: from strict 4^{-} to random quasi-phase matching," *Semicond. Sci. Technol.*, vol. 32, no. 6, p. 065004, Jun. 2017, doi: 10.1088/1361-6641/aa676d.

[35] Z. Zhou, B. Yin, and J. Michel, "On-chip light sources for silicon photonics," *Light Sci. Appl.*, vol. 4, no. 11, pp. e358–e358, Nov. 2015, doi: 10.1038/lsa.2015.131.

[36] M. Tang *et al.*, "Integration of III-V lasers on Si for Si photonics," *Prog. Quantum Electron.*, vol. 66, pp. 1–18, Aug. 2019, doi: 10.1016/j.pquantelec.2019.05.002.

[37] M. H. Pilkuhn and L. M. Foster, "Green Luminescence from Solution-grown Junctions in GaP Containing Shallow Donors and Acceptors," *IBM J. Res. Dev.*, vol. 10, no. 2, pp. 122–129, Mar. 1966, doi: 10.1147/rd.102.0122.

[38] M. Billet *et al.*, "Gallium phosphide-on-insulator integrated photonic structures fabricated using micro-transfer printing," *Opt. Mater. Express*, Aug. 2022, doi: 10.1364/OME.461146.

[39] Y. Dumeige and P. Féron, "Whispering-gallery-mode analysis of phase-matched doubly resonant second-harmonic generation," *Phys. Rev. A*, vol. 74, no. 6, p. 063804, Dec. 2006, doi: 10.1103/PhysRevA.74.063804.

[40] A. Lorenzo-Ruiz and Y. Léger, "Generalization of Second-Order Quasi-Phase Matching in Whispering Gallery Mode Resonators Using Berry Phase," *ACS Photonics*, vol. 7, no. 7, pp. 1617–1621, Jul. 2020, doi: 10.1021/acsphotonics.0c00393.

[41] H. Mori, M. Ogasawara, M. Yamamoto, and M. Tachikawa, "New hydride vapor phase epitaxy for GaP growth on Si," *Appl. Phys. Lett.*, vol. 51, no. 16, pp. 1245–1247, Oct. 1987, doi: 10.1063/1.98693.

[42] E. A. Fitzgerald *et al.*, "Monolithic III-V/Si Integration," *ECS Trans.*, vol. 16, no. 10, pp. 1015–1020, Oct. 2008, doi: 10.1149/1.2986863.

[43] C. Cornet *et al.*, "Zinc-blende group III-V/group IV epitaxy: Importance of the miscut," *Phys. Rev. Mater.*, vol. 4, no. 5, p. 053401, May 2020, doi: 10.1103/PhysRevMaterials.4.053401.

[44] G. Aminoff and B. Broomé, "Strukturtheoretische Studien über Zwillinge. I.," *Zeitschrift für Krist. - Cryst. Mater.*, vol. 80, no. 1–6, pp. 355–376, Dec. 1931, doi: 10.1524/zkri.1931.80.1.355.

[45] D. B. Holt, "Antiphase boundaries in semiconducting compounds," *J. Phys. Chem. Solids*, vol. 30, no. 6, pp. 1297–1308, Jun. 1969, doi: 10.1016/0022-3697(69)90191-7.

[46] K. Morizane, "Antiphase domain structures in GaP and GaAs epitaxial layers grown on Si and Ge," *J. Cryst. Growth*, vol. 38, no. 2, pp. 249–254, May 1977, doi: 10.1016/0022-0248(77)90305-0.

[47] L. Chen *et al.*, "Epitaxial III–V/Si Vertical Heterostructures with Hybrid 2D-Semimetal/Semiconductor Ambipolar and Photoactive Properties," *Adv. Sci.*, vol. 9, no. 2, p. 2101661, Jan. 2022, doi: 10.1002/advs.202101661.

[48] R. Saleem-Urothodi *et al.*, "Loss assessment in random crystal polarity gallium phosphide microdisks grown on silicon," *Opt. Lett.*, vol. 45, no. 16, p. 4646, Aug. 2020, doi: 10.1364/OL.399935.

[49] H. Kroemer, "Polar-on-nonpolar epitaxy," *J. Cryst. Growth*, vol. 81, no. 1–4, pp. 193–204, Feb. 1987, doi: 10.1016/0022-0248(87)90391-5.

[50] R. Kaplan, “LEED study of the stepped surface of vicinal Si (100),” *Surf. Sci.*, vol. 93, no. 1, pp. 145–158, Mar. 1980, doi: 10.1016/0039-6028(80)90052-7.

[51] E. Tea *et al.*, “Theoretical study of optical properties of anti phase domains in GaP,” *J. Appl. Phys.*, vol. 115, no. 6, p. 063502, Feb. 2014, doi: 10.1063/1.4864421.

[52] S. Chen *et al.*, “Electrically pumped continuous-wave III–V quantum dot lasers on silicon,” *Nat. Photonics*, vol. 10, no. 5, pp. 307–311, May 2016, doi: 10.1038/nphoton.2016.21.

[53] C.-J.-A. Cornet, Y. Léger, and C. Robert, *Integrated lasers on silicon*. Amsterdam London: Elsevier ISTE Press, 2016.

[54] P. Guillemé *et al.*, “Antiphase domain tailoring for combination of modal and 4^{-}-quasi-phase matching in gaGuillemé, Pllium phosphide microdisks,” *Opt. Express*, vol. 24, no. 13, p. 14608, Jun. 2016, doi: 10.1364/OE.24.014608.

[55] T. H. Mairnan, “Stimulated optical radiation in ruby,” *Nature*, vol. 4736, pp. 493–494, 1960.

[56] P. A. Franken, A. E. Hill, C. W. Peters, and G. Weinreich, “Generation of Optical Harmonics,” *Phys. Rev. Lett.*, vol. 7, no. 4, pp. 118–119, Aug. 1961, doi: 10.1103/PhysRevLett.7.118.

[57] K. Rivoire, Z. Lin, F. Hatami, W. T. Masselink, and J. Vučković, “Second harmonic generation in gallium phosphide photonic crystal nanocavities with ultralow continuous wave pump power,” *Opt. Express*, vol. 17, no. 25, p. 22609, Dec. 2009, doi: 10.1364/OE.17.022609.

[58] D. P. Lake, M. Mitchell, H. Jayakumar, L. F. dos Santos, D. Curic, and P. E. Barclay, “Efficient telecom to visible wavelength conversion in doubly resonant gallium phosphide microdisks,” *Appl. Phys. Lett.*, vol. 108, no. 3, p. 031109, Jan. 2016, doi: 10.1063/1.4940242.

[59] S. M. Hendrickson, A. C. Foster, R. M. Camacho, and B. D. Clader, “Integrated nonlinear photonics: emerging applications and ongoing challenges [Invited],” *J. Opt. Soc. Am. B*, vol. 31, no. 12, p. 3193, Dec. 2014, doi: 10.1364/JOSAB.31.003193.

[60] R. W.Boyd, *Nonlinear optics*, 3rd ed. Amsterdam ; Boston: Academic Press, 2008.

[61] P. Guillemé, “Génération de seconde harmonique dans les microdisques de phosphure de gallium intégrés sur silicium,” 2016.

[62] D. A. Kleinman, “Nonlinear Dielectric Polarization in Optical Media,” *Phys. Rev.*, vol. 126, no. 6, pp. 1977–1979, Jun. 1962, doi: 10.1103/PhysRev.126.1977.

[63] P. D. Maker, R. W. Terhune, M. Nisenoff, and C. M. Savage, “Effects of Dispersion and Focusing on the Production of Optical Harmonics,” *Phys. Rev. Lett.*, vol. 8, no. 1, pp. 21–22, Jan. 1962, doi: 10.1103/PhysRevLett.8.21.

[64] J. E. Midwinter and J. Warner, “The effects of phase matching method and of uniaxial crystal symmetry on the polar distribution of second-order non-linear optical polarization,” *Br. J. Appl. Phys.*, vol. 16, no. 8, pp. 1135–1142, Aug. 1965, doi: 10.1088/0508-3443/16/8/312.

[65] J. A. Armstrong, N. Bloembergen, J. Ducuing, and P. S. Pershan, “Interactions between Light Waves in a Nonlinear Dielectric,” *Phys. Rev.*, vol. 127, no. 6, pp. 1918–1939, Sep. 1962, doi: 10.1103/PhysRev.127.1918.

[66] M. M. Fejer, G. A. Magel, D. H. Jundt, and R. L. Byer, “Quasi-phase-matched second harmonic generation: tuning and tolerances,” *IEEE J. Quantum Electron.*, vol. 28, no. 11, pp. 2631–2654, 1992, doi: 10.1109/3.161322.

[67] L. E. Myers, W. R. Bosenberg, G. D. Miller, R. C. Eckardt, M. M. Fejer, and R. L. Byer, “Quasi-phase-matched 1064-µm-pumped optical parametric oscillator in bulk periodically poled LiNbO_3,” *Opt. Lett.*, vol. 20, no. 1, p. 52, Jan. 1995, doi: 10.1364/OL.20.000052.

[68] K. Pantzas *et al.*, “Continuous-Wave Second-Harmonic Generation in Orientation-Patterned Gallium Phosphide Waveguides at Telecom Wavelengths,” *ACS Photonics*, vol. 9, no. 6, pp. 2032–2039, Jun. 2022, doi: 10.1021/acsphotonics.2c00156.

[69] M. Baudrier-Raybaut, R. Haïdar, P. Kupecek, P. Lemasson, and E. Rosencher, “Random quasi-phase-matching in bulk polycrystalline isotropic nonlinear materials,” *Nature*, vol. 432, no. 7015, pp. 374–376, Nov. 2004, doi: 10.1038/nature03027.

[70] R. Savo *et al.*, “Broadband Mie driven random quasi-phase-matching,” *Nat. Photonics*, vol. 14, no. 12, pp. 740–747, Dec. 2020, doi: 10.1038/s41566-020-00701-x.

[71] M. Hermouet, “Optomechanical silicon microdisk resonators for biosensing in liquid,” Université Grenoble Alpes, 2019.

[72] M. Borselli, “High-Q microresonators as lasing elements for silicon photonics,” 2006.

[73] S. Mariani, “Three-wave mixing in semiconductor whispering gallery mode microcavities,” 2014.

[74] J. E. Heebner, “Nonlinear optical whispering gallery microresonators for photonics,” 2003.

[75] K. R. Hiremath, “Coupled mode theory based modeling and analysis of

circular optical microresonators," 2005.

[76] C. Baker, "On-chip nano-optomechanical whispering gallery resonators," 2013.

[77] J. D. Jackson, *Classical electrodynamics*, 2d ed. New York: Wiley, 1975.

[78] K. Okamoto, *Fundamentals of optical waveguides*. San Diego: Academic Press, 2000.

[79] R. Gao *et al.*, "Broadband highly efficient nonlinear optical processes in on-chip integrated lithium niobate microdisk resonators of Q-factor above 10^8," *New J. Phys.*, vol. 23, no. 12, p. 123027, Dec. 2021, doi: 10.1088/1367-2630/ac3d52.

[80] A. Yariv, "Coupled-mode theory for guided-wave optics," *IEEE J. Quantum Electron.*, vol. 9, no. 9, pp. 919–933, Sep. 1973, doi: 10.1109/JQE.1973.1077767.

[81] H. A. Haus, *Waves and fields in optoelectronics*. Englewood Cliffs, NJ: Prentice-Hall, 1984.

[82] H. A. Haus and W. Huang, "Coupled-mode theory," *Proc. IEEE*, vol. 79, no. 10, pp. 1505–1518, 1991, doi: 10.1109/5.104225.

[83] C. Arlotti, O. Gauthier-Lafaye, A. Monmayrant, and S. Calvez, "Achromatic critically coupled racetrack resonators," *J. Opt. Soc. Am. B*, vol. 34, no. 11, p. 2343, Nov. 2017, doi: 10.1364/JOSAB.34.002343.

[84] Y. Dumeige, S. Trebaol, L. Ghişa, T. K. N. Nguyên, H. Tavernier, and P. Féron, "Determination of coupling regime of high-Q resonators and optical gain of highly selective amplifiers," *J. Opt. Soc. Am. B*, vol. 25, no. 12, p. 2073, Dec. 2008, doi: 10.1364/JOSAB.25.002073.

[85] T. Kamalakis and T. Sphicopoulos, "Frequency Dependence of the Coupling Coefficients and Resonant Frequency Detuning in a Nanophotonic Waveguide-Cavity System," *IEEE J. Quantum Electron.*, vol. 42, no. 8, pp. 827–837, Aug. 2006, doi: 10.1109/JQE.2006.877298.

[86] V. S. Il'chenko and M. L. Gorodetskii, "Thermal Nonlinear Effects in Optical Whispering Gallery Microresonators," *LASER Phys.*, vol. 2, no. 6, pp. 1004–1009, 1992.

[87] D. S. Weiss, V. Sandoghdar, J. Hare, V. Lefèvre-Seguin, J.-M. Raimond, and S. Haroche, "Splitting of high-Q Mie modes induced by light backscattering in silica microspheres," *Opt. Lett.*, vol. 20, no. 18, p. 1835, Sep. 1995, doi: 10.1364/OL.20.001835.

[88] B. E. Little, J.-P. Laine, and S. T. Chu, "Surface-roughness-induced contradirectional coupling in ring and disk resonators," *Opt. Lett.*, vol. 22,

no. 1, p. 4, Jan. 1997, doi: 10.1364/OL.22.000004.

[89] M. L. Gorodetsky, A. D. Pryamikov, and V. S. Ilchenko, "Rayleigh scattering in high-Q microspheres," *J. Opt. Soc. Am. B*, vol. 17, no. 6, p. 1051, 2000, doi: 10.1364/josab.17.001051.

[90] T. J. Kippenberg, S. M. Spillane, and K. J. Vahala, "Modal coupling in traveling-wave resonators," *Opt. Lett.*, vol. 27, no. 19, p. 1669, Oct. 2002, doi: 10.1364/OL.27.001669.

[91] M. Borselli, T. J. Johnson, and O. Painter, "Beyond the Rayleigh scattering limit in high-Q silicon microdisks: theory and experiment," *Opt. Express*, vol. 13, no. 5, p. 1515, 2005, doi: 10.1364/opex.13.001515.

[92] Q. Li, A. A. Eftekhar, Z. Xia, and A. Adibi, "Unified approach to mode splitting and scattering loss in high-Q whispering-gallery-mode microresonators," *Phys. Rev. A*, vol. 88, no. 3, p. 033816, Sep. 2013, doi: 10.1103/PhysRevA.88.033816.

[93] P. S. Kuo, W. Fang, and G. S. Solomon, "4¯-quasi-phase-matched interactions in GaAs microdisk cavities," *Opt. Lett.*, vol. 34, no. 22, p. 3580, Nov. 2009, doi: 10.1364/OL.34.003580.

[94] P. S. Kuo and G. S. Solomon, "On- and off-resonance second-harmonic generation in GaAs microdisks," *Opt. Express*, vol. 19, no. 18, p. 16898, Aug. 2011, doi: 10.1364/OE.19.016898.

[95] A. Lorenzo-Ruiz, "Nonlinear photonics integrated devices based on GaP," 2021.

[96] C. Ciret *et al.*, "Full Vectorial Modeling of Second Harmonic Generation in III-V-on-insulator Nanowires," *Opt. Express*, vol. 28, no. 21, pp. 31584–31593, Jan. 2020, doi: 10.1364/OE.402150.

[97] R. Y. Chiao and Y.-S. Wu, "Manifestations of Berry's Topological Phase for the Photon," *Phys. Rev. Lett.*, vol. 57, no. 8, pp. 933–936, Aug. 1986, doi: 10.1103/PhysRevLett.57.933.

[98] A. Tomita and R. Y. Chiao, "Observation of Berry's Topological Phase by Use of an Optical Fiber," *Phys. Rev. Lett.*, vol. 57, no. 8, pp. 937–940, Aug. 1986, doi: 10.1103/PhysRevLett.57.937.

[99] A. Yariv, "Universal relations for coupling of optical power between microresonators and dielectric waveguides," *Electron. Lett.*, vol. 36, no. 4, p. 321, 2000, doi: 10.1049/el:20000340.

[100] E. Gil-Santos, C. Baker, A. Lemaître, C. Gomez, G. Leo, and I. Favero, "Scalable high-precision tuning of photonic resonators by resonant cavity-enhanced photoelectrochemical etching," *Nat. Commun.*, vol. 8, pp. 1–7, 2017, doi: 10.1038/ncomms14267.

[101] I. Shoji, T. Kondo, A. Kitamoto, M. Shirane, and R. Ito, "Absolute scale of second-order nonlinear-optical coefficients," *J. Opt. Soc. Am. B*, vol. 14, no. 9, p. 2268, Sep. 1997, doi: 10.1364/JOSAB.14.002268.

[102] D. N. Nikogosyan, *Nonlinear Optical Crystals: A Complete Survey*. New York: Springer-Verlag, 2005.

[103] E. D. Palik, *Handbook of Optical Constants of Solids*. Burlington: Elsevier, 1985.

[104] J. Václavík and D. Vápenka, "Gallium Phosphide as a material for visible and infrared optics," *EPJ Web Conf.*, vol. 48, p. 00028, May 2013, doi: 10.1051/epjconf/20134800028.

[105] A. Lorenzo-Ruiz, Y. Leger, C. Cornet, and A. Beck, "THz surface phonon polariton generation in GaP photonic waveguide," in *2019 44th International Conference on Infrared, Millimeter, and Terahertz Waves (IRMMW-THz)*, Sep. 2019, vol. 2019-Septe, pp. 1–2, doi: 10.1109/IRMMW-THz.2019.8873756.

[106] C. D. Salzberg and J. J. Villa, "Infrared Refractive Indexes of Silicon Germanium and Modified Selenium Glass*," *J. Opt. Soc. Am.*, vol. 47, no. 3, p. 244, Mar. 1957, doi: 10.1364/JOSA.47.000244.

[107] S. Adachi, "Optical dispersion relations for GaP, GaAs, GaSb, InP, InAs, InSb, Al x Ga 1− x As, and In 1− x Ga x As y P 1− y," *J. Appl. Phys.*, vol. 66, no. 12, pp. 6030–6040, Dec. 1989, doi: 10.1063/1.343580.

[108] A. S. Barker and M. Ilegems, "Infrared Lattice Vibrations and Free-Electron Dispersion in GaN," *Phys. Rev. B*, vol. 7, no. 2, pp. 743–750, Jan. 1973, doi: 10.1103/PhysRevB.7.743.

[109] D. E. Zelmon, D. L. Small, and D. Jundt, "Infrared corrected Sellmeier coefficients for congruently grown lithium niobate and 5 mol% magnesium oxide –doped lithium niobate," *J. Opt. Soc. Am. B*, vol. 14, no. 12, p. 3319, Dec. 1997, doi: 10.1364/JOSAB.14.003319.

[110] J. Pastrňák and L. Roskovcová, "Refraction Index Measurements on AlN Single Crystals," *Phys. status solidi*, vol. 14, no. 1, pp. K5–K8, 1966, doi: 10.1002/pssb.19660140127.

[111] C. Kittel, *Introduction to solid state physics*, 8th ed. Hoboken, NJ: Wiley, 2005.

[112] J. S. Blakemore, "Semiconducting and other major properties of gallium arsenide," *J. Appl. Phys.*, vol. 53, no. 10, pp. R123–R181, Oct. 1982, doi: 10.1063/1.331665.

[113] W. M. Haynes, D. R. Lide, and T. J. Bruno, *CRC Handbook of Chemistry and Physics*. CRC Press, 2016.

[114] B. G. Streetman and S. Banerjee, *Solid state electronic devices*, 5th ed. Upper Saddle River, N.J: Prentice Hall, 2000.

[115] A. R. Zanatta, "The optical bandgap of lithium niobate (LiNbO3) and its dependence with temperature," *Results Phys.*, vol. 39, p. 105736, Aug. 2022, doi: 10.1016/j.rinp.2022.105736.

[116] M. Feneberg, R. A. R. Leute, B. Neuschl, K. Thonke, and M. Bickermann, "High-excitation and high-resolution photoluminescence spectra of bulk AlN," *Phys. Rev. B*, vol. 82, no. 7, p. 075208, Aug. 2010, doi: 10.1103/PhysRevB.82.075208.

[117] J. E. Ayers, T. Kujofsa, P. Rago, and J. Raphael, *Heteroepitaxy of Semiconductors: Theory, Growth, and Characterization*, Second Edi. CRC Press, 2016.

[118] M. Levinshtein, S. Rumyantsev, and M. Shur, *Handbook Series on Semiconductor Parameters*, vol. 1. WORLD SCIENTIFIC, 1996.

[119] T. Soga, T. Jimbo, and M. Umeno, "Dislocation generation mechanisms for GaP on Si grown by metalorganic chemical vapor deposition," *Appl. Phys. Lett.*, vol. 63, no. 18, pp. 2543–2545, Nov. 1993, doi: 10.1063/1.110427.

[120] Y. Takagi, Y. Furukawa, A. Wakahara, and H. Kan, "Lattice relaxation process and crystallographic tilt in GaP layers grown on misoriented Si(001) substrates by metalorganic vapor phase epitaxy," *J. Appl. Phys.*, vol. 107, no. 6, p. 063506, Mar. 2010, doi: 10.1063/1.3310479.

[121] O. Skibitzki *et al.*, "GaP collector development for SiGe heterojunction bipolar transistor performance increase: A heterostructure growth study," *J. Appl. Phys.*, vol. 111, no. 7, p. 073515, Apr. 2012, doi: 10.1063/1.3701583.

[122] S. Almosni, "Growth, structural and electro-optical properties of GaP/Si and GaAsPN/ GaP single junctions for lattice-matched tandem solar cells on silicon," 2015.

[123] I. Lucci *et al.*, "Universal description of III-V/Si epitaxial growth processes," *Phys. Rev. Mater.*, vol. 2, no. 6, p. 060401, Jun. 2018, doi: 10.1103/PhysRevMaterials.2.060401.

[124] I. Lucci, "Surface and interface contributions to III-V / Si hetero-epitaxial growth : Theory and Experiments," 2019.

[125] T. T. Nguyen, "Sillicon photonics based on monolithic integration of III-V nanostructures on silicon," 2013.

[126] Y. Wang, "Structural analyses by advanced X-ray scattering on GaP layers epitaxially grown on silicon for integrated photonic applications," 2018.

[127] A. C. Lin, M. M. Fejer, and J. S. Harris, "Antiphase domain annihilation

during growth of GaP on Si by molecular beam epitaxy," *J. Cryst. Growth*, vol. 363, pp. 258–263, Jan. 2013, doi: 10.1016/j.jcrysgro.2012.10.055.

[128] B. Kunert, I. Németh, S. Reinhard, K. Volz, and W. Stolz, "Si (001) surface preparation for the antiphase domain free heteroepitaxial growth of GaP on Si substrate," *Thin Solid Films*, vol. 517, no. 1, pp. 140–143, 2008, doi: 10.1016/j.tsf.2008.08.077.

[129] K. Volz *et al.*, "GaP-nucleation on exact Si (001) substrates for III/V device integration," *J. Cryst. Growth*, vol. 315, no. 1, pp. 37–47, Jan. 2011, doi: 10.1016/j.jcrysgro.2010.10.036.

[130] T. J. Grassman *et al.*, "Nucleation-related defect-free GaP/Si(100) heteroepitaxy via metal-organic chemical vapor deposition," *Appl. Phys. Lett.*, vol. 102, no. 14, p. 142102, Apr. 2013, doi: 10.1063/1.4801498.

[131] T. J. Grassman *et al.*, "Control and elimination of nucleation-related defects in GaP/Si(001) heteroepitaxy," *Appl. Phys. Lett.*, vol. 94, no. 23, p. 232106, Jun. 2009, doi: 10.1063/1.3154548.

[132] M. Henzler and J. Clabes, "Structural and Electronic Properties of Stepped Semiconductor Surfaces," *Jpn. J. Appl. Phys.*, vol. 13, no. S2, p. 389, Jan. 1974, doi: 10.7567/JJAPS.2S2.389.

[133] R. Fischer, N. Chand, W. Kopp, H. Morkoç, L. P. Erickson, and R. Youngman, "GaAs bipolar transistors grown on (100) Si substrates by molecular beam epitaxy," *Appl. Phys. Lett.*, vol. 47, no. 4, pp. 397–399, Aug. 1985, doi: 10.1063/1.96179.

[134] R. M. Sieg, S. A. Ringel, S. M. Ting, E. A. Fitzgerald, and R. N. Sacks, "Anti-phase domain-free growth of GaAs on offcut (001) Ge wafers by molecular beam epitaxy with suppressed Ge outdiffusion," *J. Electron. Mater.*, vol. 27, no. 7, pp. 900–907, Jul. 1998, doi: 10.1007/s11664-998-0116-1.

[135] Y. Takagi, H. Yonezu, K. Samonji, T. Tsuji, and N. Ohshima, "Generation and suppression process of crystalline defects in GaP layers grown on misoriented Si(100) substrates," *J. Cryst. Growth*, vol. 187, no. 1, pp. 42–50, Apr. 1998, doi: 10.1016/S0022-0248(97)00862-2.

[136] T. J. Grassman *et al.*, "Toward Metamorphic Multijunction GaAsP/Si Photovoltaics Grown on Optimized GaP/Si Virtual Substrates Using Anion-Graded GaAsyP1-y Buffers," in *2009 34th IEEE Photovoltaic Specialists Conference (PVSC)*, Jun. 2009, no. 001, pp. 002016–002021, doi: 10.1109/PVSC.2009.5411489.

[137] Y. Ping Wang *et al.*, "Quantitative evaluation of microtwins and antiphase defects in GaP/Si nanolayers for a III–V photonics platform on silicon using

a laboratory X-ray diffraction setup," *J. Appl. Crystallogr.*, vol. 48, no. 3, pp. 702–710, Jun. 2015, doi: 10.1107/S1600576715009954.

[138] P. N. Uppal and H. Kroemer, "Molecular beam epitaxial growth of GaAs on Si(211)," *J. Appl. Phys.*, vol. 58, no. 6, pp. 2195–2203, Sep. 1985, doi: 10.1063/1.335987.

[139] A. Létoublon *et al.*, "X-ray study of antiphase domains and their stability in MBE grown GaP on Si," *J. Cryst. Growth*, vol. 323, no. 1, pp. 409–412, May 2011, doi: 10.1016/j.jcrysgro.2010.10.137.

[140] I. Németh, B. Kunert, W. Stolz, and K. Volz, "Ways to quantitatively detect antiphase disorder in GaP films grown on Si(001) by transmission electron microscopy," *J. Cryst. Growth*, vol. 310, no. 23, pp. 4763–4767, Nov. 2008, doi: 10.1016/j.jcrysgro.2008.07.105.

[141] A. Georgakilas *et al.*, "Generation and annihilation of antiphase domain boundaries in GaAs on Si grown by molecular beam epitaxy," *J. Mater. Res.*, vol. 8, no. 8, pp. 1908–1921, Aug. 1993, doi: 10.1557/JMR.1993.1908.

[142] H. Döscher *et al.*, "In situ antiphase domain quantification applied on heteroepitaxial GaP growth on Si(100) ," *J. Vac. Sci. Technol. B, Nanotechnol. Microelectron. Mater. Process. Meas. Phenom.*, vol. 28, no. 4, p. C5H1-C5H6, 2010, doi: 10.1116/1.3466529.

[143] H. Döscher *et al.*, "Indirect in situ characterization of Si(100) substrates at the initial stage of III–V heteroepitaxy," *J. Cryst. Growth*, vol. 315, no. 1, pp. 16–21, Jan. 2011, doi: 10.1016/j.jcrysgro.2010.08.017.

[144] H. Döscher and T. Hannappel, "In situ reflection anisotropy spectroscopy analysis of heteroepitaxial GaP films grown on Si(100)," *J. Appl. Phys.*, vol. 107, no. 12, p. 123523, Jun. 2010, doi: 10.1063/1.3357391.

[145] I. Németh, "Transmission electron microscopic investigations of heteroepitaxial III/V semiconductor thin layer and quantum well structures," 2008.

[146] T. Matsushita, T. Yamamoto, and T. Kondo, "Epitaxial Growth of Spatially Inverted GaP for Quasi Phase Matched Nonlinear Optical Devices," *Jpn. J. Appl. Phys.*, vol. 46, no. No. 17, pp. L408–L410, Apr. 2007, doi: 10.1143/JJAP.46.L408.

[147] X. Yu, L. Scaccabarozzi, A. C. Lin, M. M. Fejer, and J. S. Harris, "Growth of GaAs with orientation-patterned structures for nonlinear optics," *J. Cryst. Growth*, vol. 301–302, no. SPEC. ISS., pp. 163–167, Apr. 2007, doi: 10.1016/j.jcrysgro.2006.11.315.

[148] I. Németh, B. Kunert, W. Stolz, and K. Volz, "Heteroepitaxy of GaP on Si: Correlation of morphology, anti-phase-domain structure and MOVPE growth

conditions," *J. Cryst. Growth*, vol. 310, no. 7–9, pp. 1595–1601, 2008, doi: 10.1016/j.jcrysgro.2007.11.127.

[149] A. W. Snyder and J. D. Love, "Tunnelling leaky modes on optical waveguides," *Opt. Commun.*, vol. 12, no. 3, pp. 326–328, Nov. 1974, doi: 10.1016/0030-4018(74)90026-1.

[150] M. Kuznetsov and H. Haus, "Radiation loss in dielectric waveguide structures by the volume current method," *IEEE J. Quantum Electron.*, vol. 19, no. 10, pp. 1505–1514, Oct. 1983, doi: 10.1109/JQE.1983.1071758.

[151] J. E. Heebner, T. C. Bond, and J. S. Kallman, "Generalized formulation for performance degradations due to bending and edge scattering loss in microdisk resonators," *Opt. Express*, vol. 15, no. 8, p. 4452, 2007, doi: 10.1364/OE.15.004452.

[152] J. Heebner, R. Grover, and T. A. Ibrahim, *Optical Microresonators: Theory, Fabrication, and Applications*, vol. 138, no. 8. New York, NY: Springer New York, 2008.

[153] M. Borselli, K. Srinivasan, P. E. Barclay, and O. Painter, "Rayleigh scattering, mode coupling, and optical loss in silicon microdisks," *Appl. Phys. Lett.*, vol. 85, no. 17, pp. 3693–3695, Oct. 2004, doi: 10.1063/1.1811378.

[154] V. Narayanan, S. Mahajan, K. J. Bachmann, V. Woods, and N. Dietz, "Stacking faults and twins in gallium phosphide layers grown on silicon," *Philos. Mag. A*, vol. 82, no. 4, pp. 685–698, Mar. 2002, doi: 10.1080/01418610208243196.

[155] A. W. Snyder and J. D. Love, *Optical Waveguide Theory*. Boston, MA: Springer US, 1984.

[156] V. Huet, "Étude et réalisation de lignes à retard optique intégrées dans des micro-résonateurs à modes de galerie en verres actifs dopés erbium," Université Rennes 1, 2015.

[157] M. Cai, "Optical Fiber Taper Coupled Glass Microsphere Resonators," 2001.

[158] A. Coillet, "Microfibres pour l'optique non linéaire," 2011.

[159] V. B. Braginsky, M. L. Gorodetsky, and V. S. Ilchenko, "Quality-factor and nonlinear properties of optical whispering-gallery modes," *Phys. Lett. A*, vol. 137, no. 7–8, pp. 393–397, May 1989, doi: 10.1016/0375-9601(89)90912-2.

[160] W. von Klitzing, R. Long, V. S. Ilchenko, J. Hare, and V. Lefèvre-Seguin, "Tunable whispering gallery modes for spectroscopy and CQED experiments," *New J. Phys.*, vol. 3, pp. 14–14, Aug. 2001, doi: 10.1088/1367-2630/3/1/314.

[161] V. S. Ilchenko, X. S. Yao, and L. Maleki, "Pigtailing the high-Q microsphere

cavity: A simple fiber coupler for optical whispering-gallery modes," *Opt. Lett.*, vol. 24, no. 11, p. 723, Jun. 1999, doi: 10.1364/OL.24.000723.

[162] J. C. Knight, G. Cheung, F. Jacques, and T. A. Birks, "Phase-matched excitation of whispering-gallery-mode resonances by a fiber taper," *Opt. Lett.*, vol. 22, no. 15, p. 1129, Aug. 1997, doi: 10.1364/OL.22.001129.

[163] Ming Cai, G. Hunziker, and K. Vahala, "Fiber-optic add-drop device based on a silica microsphere-whispering gallery mode system," *IEEE Photonics Technol. Lett.*, vol. 11, no. 6, pp. 686–687, Jun. 1999, doi: 10.1109/68.766785.

[164] M. Cai and K. Vahala, "Highly efficient optical power transfer to whispering-gallery modes by use of a symmetrical dual-coupling configuration," *Opt. Lett.*, vol. 25, no. 4, p. 260, Feb. 2000, doi: 10.1364/OL.25.000260.

[165] T. J. A. Kippenberg, "Nonlinear Optics in Ultra-high-Q Whispering-Gallery Optical Microcavities," 2004.

[166] M. Gaira and C. S. Unnikrishnan, "Integrated end-to-end instrumentation for the study of whispering gallery modes in dynamic liquid micro-cavities coupled to sub-micron tapered fibers," *EPJ Tech. Instrum.*, vol. 8, no. 1, p. 2, Dec. 2021, doi: 10.1140/epjti/s40485-020-00062-3.

[167] K. Srinivasan, P. E. Barclay, M. Borselli, and O. J. Painter, "An optical-fiber-based probe for photonic crystal microcavities," *IEEE J. Sel. Areas Commun.*, vol. 23, no. 7, pp. 1321–1329, Jul. 2005, doi: 10.1109/JSAC.2005.851212.

[168] G. Anetsberger *et al.*, "Near-field cavity optomechanics with nanomechanical oscillators," *Nat. Phys.*, vol. 5, no. 12, pp. 909–914, Dec. 2009, doi: 10.1038/nphys1425.

[169] L. Ding, P. Senellart, A. Lemaitre, S. Ducci, G. Leo, and I. Favero, "GaAs micro-nanodisks probed by a looped fiber taper for optomechanics applications," in *SPIE Photonics Europe*, Apr. 2010, p. 771211, doi: 10.1117/12.853985.

[170] Y. Ren, R. Zhang, C. Ti, and Y. Liu, "Tapered optical fiber loops and helices for integrated photonic device characterization and microfluidic roller coasters," *Optica*, vol. 3, no. 11, p. 1205, Nov. 2016, doi: 10.1364/OPTICA.3.001205.

[171] C. P. Michael, M. Borselli, T. J. Johnson, C. Chrystal, and O. Painter, "An optical fiber-taper probe for wafer-scale microphotonic device characterization," *Opt. Express*, vol. 15, no. 8, p. 4745, 2007, doi: 10.1364/OE.15.004745.

[172] B. D. Hauer, P. H. Kim, C. Doolin, A. J. MacDonald, H. Ramp, and J. P. Davis, "On-chip cavity optomechanical coupling," *EPJ Tech. Instrum.*, vol.

1, no. 1, p. 4, Dec. 2014, doi: 10.1140/epjti4.

[173] M. K. Chin and S. T. Ho, "Design and modeling of waveguide-coupled single-mode microring resonators," *J. Light. Technol.*, vol. 16, no. 8, pp. 1433–1446, 1998, doi: 10.1109/50.704609.

[174] A. Lorenzo-Ruiz, C. Cornet, A. Beck, and Y. Léger, "Dual wavelength evanescent coupler for nonlinear GaP-based microdisk resonators," *OSA Contin.*, vol. 3, no. 1, p. 43, Jan. 2020, doi: 10.1364/OSAC.3.000043.

[175] A. Yariv, *Optical electronics*, 4th ed. Philadelphia: Saunders College Pub, 1991.

[176] G. P. Agrawal, *Nonlinear fiber optics*, 3rd ed. San Diego: Academic Press, 2001.

[177] A. J. Fielding, K. Edinger, and C. C. Davis, "Experimental observation of mode evolution in single-mode tapered optical fibers," *J. Light. Technol.*, vol. 17, no. 9, pp. 1649–1656, 1999, doi: 10.1109/50.788571.

[178] J. Bures and R. Ghosh, "Power density of the evanescent field in the vicinity of a tapered fiber," *J. Opt. Soc. Am. A*, vol. 16, no. 8, p. 1992, Aug. 1999, doi: 10.1364/JOSAA.16.001992.

[179] P. N. Moar, S. T. Huntington, J. Katsifolis, L. W. Cahill, A. Roberts, and K. A. Nugent, "Fabrication, modeling, and direct evanescent field measurement of tapered optical fiber sensors," *J. Appl. Phys.*, vol. 85, no. 7, pp. 3395–3398, Apr. 1999, doi: 10.1063/1.369695.

[180] J. D. Love, W. M. Henry, W. J. Stewart, R. J. Black, S. Lacroix, and F. Gonthier, "Tapered single-mode fibres and devices. Part 1: Adiabaticity criteria," *IEE Proc. J Optoelectron.*, vol. 138, no. 5, p. 343, 1991, doi: 10.1049/ip-j.1991.0060.

[181] T. J. Kippenberg, S. M. Spillane, D. K. Armani, and K. J. Vahala, "Fabrication and coupling to planar high-Q silica disk microcavities," *Appl. Phys. Lett.*, vol. 83, no. 4, pp. 797–799, Jul. 2003, doi: 10.1063/1.1593833.

[182] E. J. Zhang, W. D. Sacher, and J. K. S. Poon, "Hydrofluoric acid flow etching of low-loss subwavelength-diameter biconical fiber tapers," *Opt. Express*, vol. 18, no. 21, p. 22593, Oct. 2010, doi: 10.1364/OE.18.022593.

[183] J.-P. Laine, B. E. Little, and H. A. Haus, "Etch-eroded fiber coupler for whispering-gallery-mode excitation in high-Q silica microspheres," *IEEE Photonics Technol. Lett.*, vol. 11, no. 11, pp. 1429–1430, Nov. 1999, doi: 10.1109/68.803068.

[184] G. Brambilla, V. Finazzi, and D. J. Richardson, "Ultra-low-loss optical fiber nanotapers," *Opt. Express*, vol. 12, no. 10, p. 2258, 2004, doi: 10.1364/OPEX.12.002258.

[185] J. M. Ward, D. G. O'Shea, B. J. Shortt, M. J. Morrissey, K. Deasy, and S. G. Nic Chormaic, "Heat-and-pull rig for fiber taper fabrication," *Rev. Sci. Instrum.*, vol. 77, no. 8, p. 083105, Aug. 2006, doi: 10.1063/1.2239033.

[186] L. Ding, C. Belacel, S. Ducci, G. Leo, and I. Favero, "Ultralow loss single-mode silica tapers manufactured by a microheater," *Appl. Opt.*, vol. 49, no. 13, p. 2441, May 2010, doi: 10.1364/AO.49.002441.

[187] L. Tong *et al.*, "Subwavelength-diameter silica wires for low-loss optical wave guiding," *Nature*, vol. 426, no. 6968, pp. 816–819, Dec. 2003, doi: 10.1038/nature02193.

[188] T. A. Birks and Y. W. Li, "The shape of fiber tapers," *J. Light. Technol.*, vol. 10, no. 4, pp. 432–438, Apr. 1992, doi: 10.1109/50.134196.

[189] F. Orucevic, V. Lefèvre-Seguin, and J. Hare, "Transmittance and near-field characterization of sub-wavelength tapered optical fibers," *Opt. Express*, vol. 15, no. 21, p. 13624, 2007, doi: 10.1364/OE.15.013624.

[190] J. M. Ward, A. Maimaiti, V. H. Le, and S. N. Chormaic, "Contributed Review: Optical micro- and nanofiber pulling rig," *Rev. Sci. Instrum.*, vol. 85, no. 11, p. 111501, Nov. 2014, doi: 10.1063/1.4901098.

[191] P. E. Barclay, K. Srinivasan, M. Borselli, and O. Painter, "Efficient input and output fiber coupling to a photonic crystal waveguide," *Opt. Lett.*, vol. 29, no. 7, p. 697, Apr. 2004, doi: 10.1364/OL.29.000697.

[192] P. Guillemé *et al.*, "Cathodoluminescence hyperspectral analysis of whispering gallery modes in active semiconductor wedge resonators," *Opt. Lett.*, vol. 43, no. 8, p. 1766, Apr. 2018, doi: 10.1364/OL.43.001766.

[193] Z. Hao *et al.*, "Sum-frequency generation in on-chip lithium niobate microdisk resonators," *Photonics Res.*, vol. 5, no. 6, p. 623, Dec. 2017, doi: 10.1364/PRJ.5.000623.

[194] D. Parrain *et al.*, "Origin of optical losses in gallium arsenide disk whispering gallery resonators," *Opt. Express*, vol. 23, no. 15, p. 19656, Jul. 2015, doi: 10.1364/OE.23.019656.

[195] A. P. Anthur *et al.*, "Second harmonic generation in gallium phosphide nano-waveguides," *Opt. Express*, vol. 29, no. 7, p. 10307, Mar. 2021, doi: 10.1364/OE.409758.

[196] U. Fano, "Effects of Configuration Interaction on Intensities and Phase Shifts," *Phys. Rev.*, vol. 124, no. 6, pp. 1866–1878, Dec. 1961, doi: 10.1103/PhysRev.124.1866.

[197] B.-B. Li *et al.*, "Experimental observation of Fano resonance in a single whispering-gallery microresonator," *Appl. Phys. Lett.*, vol. 98, no. 2, p. 021116, Jan. 2011, doi: 10.1063/1.3541884.

[198] K. Schneider, P. Welter, Y. Baumgartner, H. Hahn, L. Czornomaz, and P. Seidler, "Gallium Phosphide-on-Silicon Dioxide Photonic Devices," *J. Light. Technol.*, vol. 36, no. 14, pp. 2994–3002, Jul. 2018, doi: 10.1109/JLT.2018.2829221.

[199] B. McLaughlin, D. Lake, M. Mitchell, and P. Barclay, "Nonlinear optics in gallium phosphide cavities: simultaneous second and third harmonic generation," *J. Opt. Soc. Am. B*, May 2022, doi: 10.1364/JOSAB.455234.

[200] T. Carmon, L. Yang, and K. J. Vahala, "Dynamical thermal behavior and thermal self-stability of microcavities," *Integr. Photonics Res. Appl. Inf. Syst.*, vol. 12, no. 20, p. IWE4, 2005, doi: 10.1364/IPRA.2005.IWE4.

[201] X. Jiang and L. Yang, "Optothermal dynamics in whispering-gallery microresonators," *Light Sci. Appl.*, vol. 9, no. 1, p. 24, Dec. 2020, doi: 10.1038/s41377-019-0239-6.

[202] A. de Rossi, M. Lauritano, S. Combrié, Q. V. Tran, and C. Husko, "Interplay of plasma-induced and fast thermal nonlinearities in a GaAs-based photonic crystal nanocavity," *Phys. Rev. A*, vol. 79, no. 4, p. 043818, Apr. 2009, doi: 10.1103/PhysRevA.79.043818.

[203] S. Buckley, M. Radulaski, K. Biermann, and J. Vučković, "Second harmonic generation in photonic crystal cavities in (111)-oriented GaAs," *Appl. Phys. Lett.*, vol. 103, no. 21, p. 211117, Nov. 2013, doi: 10.1063/1.4833545.

[204] A. Rodriguez, M. Soljacic, J. D. Joannopoulos, and S. G. Johnson, "$\chi(2)$ and $\chi(3)$ harmonic generation at a critical power in inhomogeneous doubly resonant cavities," *Opt. Express*, vol. 15, no. 12, p. 7303, 2007, doi: 10.1364/OE.15.007303.

[205] A. Rasoloniaina, V. Huet, M. Thual, S. Balac, P. Féron, and Y. Dumeige, "Analysis of third-order nonlinearity effects in very high-Q WGM resonator cavity ringdown spectroscopy," *J. Opt. Soc. Am. B*, vol. 32, no. 3, p. 370, Mar. 2015, doi: 10.1364/JOSAB.32.000370.

[206] B. R. Bennett, R. A. Soref, and J. A. Del Alamo, "Carrier-induced change in refractive index of InP, GaAs and InGaAsP," *IEEE J. Quantum Electron.*, vol. 26, no. 1, pp. 113–122, 1990, doi: 10.1109/3.44924.

[207] H. S. Lee *et al.*, "Local tuning of photonic crystal nanocavity modes by laser-assisted oxidation," *Appl. Phys. Lett.*, vol. 95, no. 19, p. 191109, Nov. 2009, doi: 10.1063/1.3262961.

[208] F. Liu *et al.*, "Three-photon absorption and Kerr nonlinearity in undoped bulk GaP excited by a femtosecond laser at 1040 nm," *J. Opt.*, vol. 12, no. 9, p. 095201, Sep. 2010, doi: 10.1088/2040-8978/12/9/095201.

[209] Y. Ping Wang *et al.*, "Abrupt GaP/Si hetero-interface using bistepped Si

buffer," *Appl. Phys. Lett.*, vol. 107, no. 19, p. 191603, Nov. 2015, doi: 10.1063/1.4935494.

[210] W. Guo *et al.*, "Thermodynamic evolution of antiphase boundaries in GaP/Si epilayers evidenced by advanced X-ray scattering," *Appl. Surf. Sci.*, vol. 258, no. 7, pp. 2808–2815, Jan. 2012, doi: 10.1016/j.apsusc.2011.10.139.

[211] T. Nguyen Thanh *et al.*, "Structural and optical analyses of GaP/Si and (GaAsPN/GaPN)/GaP/Si nanolayers for integrated photonics on silicon," *J. Appl. Phys.*, vol. 112, no. 5, p. 053521, Sep. 2012, doi: 10.1063/1.4751024.

[212] L. Chen *et al.*, "Assessment of GaPSb/Si tandem material association properties for photoelectrochemical cells," *Sol. Energy Mater. Sol. Cells*, vol. 221, p. 110888, Mar. 2021, doi: 10.1016/j.solmat.2020.110888.

[213] E. F. Franchimon, K. R. Hiremath, R. Stoffer, and M. Hammer, "Interaction of whispering gallery modes in integrated optical microring or microdisk circuits: hybrid coupled mode theory model," *J. Opt. Soc. Am. B*, vol. 30, no. 4, p. 1048, Apr. 2013, doi: 10.1364/JOSAB.30.001048.

UNIVERSITÉ DE RENNES 1

Titre : Caractérisation linéaire et non linéaire de microdisques GaP monolithiquement intégrés sur substrats Si et GaP

Mots clés : Microrésonateurs GaP, photonique intégrée III-V, photonique silicium, domaines antiphase, pertes GaP/Si, SHG

Résumé : Cette thèse porte sur la caractérisation linéaire et non linéaire de microdisques de GaP intégrés sur substrats Si et GaP. Nos mesures de transmission optique dans les bandes SWIR et NIR démontrent que ces structures sont adaptées à l'étude de processus nonlinéaires tel que la génération de seconde harmonique (SHG). L'analyse statistique des facteurs de qualité permet d'identifier diverses pertes optiques affectant les microdisques GaP/Si à polarité cristalline aléatoire. Si la contribution principale aux pertes optiques reste la rugosité latérale des disques, une contribution non-négligeable provient de l'absorption par les parois d'antiphases (APBs) générées dans le GaP lorsqu'il est épitaxié sur Si, limitant le facteur de qualité de ces dispositifs à quelques dizaines de milliers.

Concernant les expériences d'optique non linéaire, un processus SHG basé sur un quasi-accord de phase strict est démontré pour la première fois, dans les microdisques GaP/GaP. Nous démontrons ainsi que, malgré les facteurs de qualités modestes de nos structures, l'optimisation des processus nonlinéaires dans les microdisques III-V est encore possible via la sélection rigoureuse du processus d'accord de phase. Dans le cas des des microdisques GaP/Si présentant un polarité cristalline aléatoire, la réponse nonlinéaire montre un comportement prometteur d'up-conversion à haute puissance, même s'il est difficile à ce stade de confirmer le processus en jeu.

Title : Linear and nonlinear characterization of monolithically integrated GaP microdisks on Si and GaP substrates

Keywords : GaP microresonators, III-V integrated photonics, silicon photonics, antiphase domains, GaP/Si loss, SHG

Abstract : This thesis investigates the linear and nonlinear characterization of monolithically integrated suspended GaP microdisks on Si and GaP substrates. In the linear studies, transmission measurements in the SWIR and NIR bands found microdisks suitable for the second harmonic generation (SHG). The statistical analysis of quality factors measured in the SWIR band identifies various optical losses affecting GaP/Si microdisks with random crystal polarity. If the main loss contribution still remains sidewall roughness scattering, the absorption by antiphase boundaries (APBs) in the GaP layer is found to be non-negligible, with limit quality factors between 10 000 and 100 000.

In the nonlinear optics experiments, a strict quasi-phase-matching based SHG process is demonstrated for the first time, in GaP/GaP microdisks for a pump in the telecom wavelength. Despite the modest quality factors of our structures, we thus demonstrate that optimization of the nonlinear conversion efficiency in III-V microdisks is still possible through the careful selection of the phase matching scheme at play in the nonlinear process. The nonlinear response of GaP/Si microdisks with random crystal polarity indicates promising nonlinear behavior towards high power frequency upconversion, despite the uncertainty on the process at play.